CYCLIC BEHAVIOR OF SHAPE MEMORY ALLOYS: MATERIAL CHARACTERIZATION AND OPTIMIZATION

A Thesis
Presented to
The Academic Faculty

by

Jason P. McCormick

In Partial Fulfillment
of the Requirements for the Degree
Doctor of Philosophy

School of Civil and Environmental Engineering
Georgia Institute of Technology
May 2006

CYCLIC BEHAVIOR OF SHAPE MEMORY ALLOYS: MATERIAL CHARACTERIZATION AND OPTIMIZATION

Approved by:

Dr. Reginald DesRoches, Advisor
School of Civil and Environmental Engineering
Georgia Institute of Technology

Dr. Roberto Leon
School of Civil and Environmental Engineering
Georgia Institute of Technology

Dr. Laurence Jacobs
School of Civil and Environmental Engineering
Georgia Institute of Technology

Dr. Kenneth Gall
School of Material Science and Engineering
Georgia Institute of Technology

Dr. Kimberly Kurtis
School of Civil and Environmental Engineering
Georgia Institute of Technology

Date Approved: March 31, 2006

ACKNOWLEDGEMENTS

Looking back over the years, I cannot imagine this journey reaching where it has without those who have been around me. It is with great appreciation that I thank all of those people who have been a part of it.

I would like to thank my advisor, Dr. Reginald DesRoches, for providing me the opportunity to pursue my goals and work on this project. Without his support, guidance, and advice this could not have come together as it has. The opportunities that he has allotted me both in guiding this research and beyond have been invaluable in setting the ground work for my future.

A special thanks goes out to Dr. Kenneth Gall for his collaboration in the material characterization study along with Jeff Tyber and Dr. Hans Maier. Without their input and work, the interdisciplinary nature of this study could not have been achieved. I would also like to thank Dr. Gall along with Dr. Laurence Jacobs, Dr. Roberto Leon, and Dr. Kimberly Kurtis for serving on my thesis advisory committee. Their encouragement and guidance throughout the course of my graduate studies is greatly appreciated.

A thank you also goes out to Special Metals for supplying much of the material used throughout this study.

Throughout my time at Georgia Tech, I have been extremely lucky to be surrounded by some of the greatest fellow graduate students who have provided not only technical advice but also their friendship. I would like to thank those whom I have had an opportunity to

share an office with over the years: Brian Smith, Justin Ocel, Matt Kahle, Dwight Dempsey, Walter Yang, Scott Canfield, Monique Hite, Laura Barbero-Buffa, Brad Penar, Jamie Padgett, and Masahiro Kurata. Many long hours have been spent together in that small office, but I cannot imagine spending them with a better group of people. A special thanks also goes out to those others who were always willing to lend their advice or provide an escape from my work Bryant Nielson, Leonardo Dueñas-Osorio, Adam Slapkus, Mauricio Lopez, Ben Mohr, Andy Maham, Brooke Ramage, and Frank Moon. I would be remiss if I forgot to thank the following undergraduates who worked so patiently with me during the course of this project: Laura Barbero-Buffa, Amanda Bezold, and Lisa Bolton.

I would like to thank Will Hughes and Diane Creighton for being great housemates and providing support, advice, and food as needed. Who would have known that Will and I would be living together five years later after being assigned an apartment together in the GLC.

The support from my parents and brother over the years is greatly appreciated. Without them I would not be where I am today. I cannot thank them enough for the support and confidence that they have had in me.

Finally, I would like to thank Laura Walz for her understanding, support, patience, and enduring love throughout the ups and downs of this whole process. Words cannot express how much I appreciate everything that she has done for me.

TABLE OF CONTENTS

LIST OF TABLES

LIST OF FIGURES

LIST OF SYMBOLS AND ABBREVIATIONS

SYMBOLS

$\mathbf{A}_f$ Austenite finish temperature

$\mathbf{A}_s$ Austenite start temperature

$\mathbf{E}_D$ Energy dissipated per cycle

$\mathbf{E}_i$ Initial elastic modulus (austenite modulus)

$\mathbf{E}_{S_o}$ Strain energy per cycle

$\mathbf{E}_{PL}$ Modulus during phase transformation

$\mathbf{F}_M$ Martensite force

$\mathbf{F}_{UL}$ Force at completion of reverse transformation

$\boldsymbol{H}$ Height of SDOF frame

$\mathbf{k}_i$ Initial stiffness (austenite stiffness)

$\mathbf{k}_M$ Stress-induced martensite stiffness

$\mathbf{k}_{PL}$ Loading/Unloading plateau stiffness

kk Trigger-line slope

$\boldsymbol{L}$ Length of SDOF brace

$\boldsymbol{L}_{SMA}$ Length of SMA element in SDOF brace

$\mathbf{M}_d$ Temperature at which SMA undergoes permanent plastic deformation upon yielding

$\mathbf{M}_f$ Martensite finish temperature

$\mathbf{M}_s$ Martensite start temperature

$\boldsymbol{n}$ Number of samples

$\boldsymbol{s}$ Sample standard deviation

$\boldsymbol{t}$ t-distribution

$\boldsymbol{T}$ Temperature

$\boldsymbol{V_Y}$ Coefficient of variation

$\boldsymbol{W}$ Width of SDOF frame

$\bar{\boldsymbol{x}}$ Sample mean

$\mathbf{X}_{mf}$ Displacement at end of loading plateau

$\mathbf{X}_{ms}$ Displacement at start of loading plateau

α Percentile value of the t-distribution

$\Delta\mathbf{H}$ Transformation latent heat

ε_o Transformational strain

ε_R Residual strain

ε_{SMA} Strain in SMA element

θ Inter-story drift angle

μ Mean

ξ_{eq} Equivalent viscous damping

σ Applied stress (Standard Deviation - Chapter 6)

σ_L Forward transformation stress

σ_M Martensite stress

σ_{UL} Reverse transformation stress

ABBREVIATIONS

A Austenite

AuCd Gold Cadmium

CsCl Cesium Chloride

DSC Differential Scanning Calorimetry

EBSD Electron Backscatter Diffraction

HRC Rockwell C hardness

K-S Test Kolmogorov-Smirnov Test

M Martensite

MANSIDE Memory Alloys for New Seismic Isolation and Energy Dissipation Devices

NC Number of training cycles

NiTi Nickel Titanium (Nitinol)

PDF Probability density function

R-phase Rhombohedral phase

SDOF Single Degree of Freedom

SL Strain level of training cycle

SMA Shape Memory Alloys

TEM Transmission Electron Microscopy

SUMMARY

Shape memory alloys (SMAs) are a unique metallic alloy which can undergo large deformations while reverting back to their undeformed shape through either the application of heat (shape memory effect) or the removal of the load (superelastic effect). These unique properties have led to the development of applications in the biomedical field (arterial stents), aerospace field (adaptive wings), and commercial industry (eyeglass frames). Recently, interest in the use of SMAs for seismic applications has increased. However, there is little connection between the materials studies on a microscopic level and the macroscopic full-scale behavior. Further, very few investigations have looked at the properties of large diameter bars typically used for structural engineering applications. This lack of information must be addressed before SMAs can be introduced to structural systems.

A multi-scale and multi-disciplinary approach is taken to explore the use of SMAs for applications in earthquake engineering. First, a materials characterization study is performed by studying precipitate formation, grain size, grain orientation, thermal transformation behavior, and strength. Cyclic uniaxial tensile tests on both coupon specimens and full-scale large diameter bars are then used to correlate the microstructural properties to the macroscopic mechanical behavior and provide a previously non-existent fundamental link between the nanometer scale structure up through the full-scale deformation response of large diameter NiTi bars. A variety of further experimental studies using NiTi wire are

performed in order to optimize their properties for seismic applications. The ability of mechanical training to stabilize NiTi cyclic properties, the ability of pre-straining to increase damping levels, and the influence of different types of earthquake loadings are considered. Based on the experimental findings, phenomenological mechanical models are developed. The OpenSEES computational platform is then used to evaluate the performance of innovative structural systems with shape memory alloys. One type of system evaluated includes an SMA bracing system used to modify the response of building systems during a seismic event and meet performance-based design criteria.

Overall, the results of this study have shown that the properties of NiTi SMAs can be modified for seismic applications through aging and deformation processing and optimized further through prior mechanical training or pre-straining. The analytical results show potential for the use of SMAs in seismic applications and provide areas for continued research.

CHAPTER I

INTRODUCTION

Shape memory alloys (SMAs) are a class of metallic alloys which have the ability to undergo large displacements while reverting back to their original undeformed shape through either the application of heat, shape memory effect, or the removal of the load, superelastic effect (Duerig et al., 1990a; Otsuka and Wayman, 1998). The ability of SMAs to recover their shape is, in part, due to the ordered crystalline structure between the austenite and martensite phases which allows the material to undergo a displacive (diffusionless) martensitic phase transformation as a result of temperature change or applied stress. Other microstructural features, such as the formation of precipitates, development of dislocations, and grain texturing also influence the properties of SMAs and promote the shape recovery process. On a macroscopic level, superelastic SMAs have been shown to develop a flag-shape hysteresis under cyclic axial loading, which can provide both recentering and supplemental energy dissipation as seen in Figure 1-1. Total recovery of axial deformation can be obtained for strains up to 6-9% with partial recovery being obtained for higher strain levels. These unique properties of SMAs have led to the development of a variety of applications for SMAs over the past two decades.

The biomedical, aerospace, and commercial fields have taken the most initiative in developing applications for SMAs. Several biomedical devices have taken advantage of the shape recovery process and excellent corrosion resistance of SMAs. Many of these

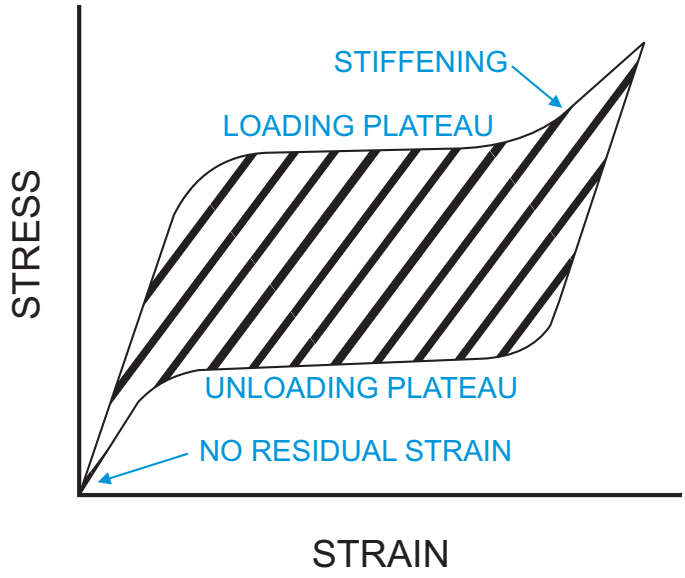

Figure 1-1: Idealized superelastic shape memory alloy stress-strain behavior

devices are used within the body, such as medical stents and orthodontic braces. Other biomedical devices use SMAs for applications outside the body in the area of orthopedics. The aerospace industry has taken advantage of the damping characteristics of SMAs by implementing them in both airplane wings and helicopter blades to reduce vibrations and increase control. Commercial industry has also developed many unique applications for SMAs such as eyeglass frames which can withstand day-to-day abuse and maintain their intended shape. Even many cell phone antennas are made of SMAs so as to take advantage of the recentering capability. As applications in these three areas have emerged, many other fields have started to look to take advantage of the properties of SMAs. In particular, the recentering and damping properties associated with SMAs has prompted interest in the civil engineering field for use of SMAs in seismic applications.

The repeatable recentering capability, formation of loading plateaus which limit force transfer to other members of the structure at intermediate strain levels, supplemental damping attributed to the flag-shape hysteresis, stiffening at large strain levels due to the formation of stress-induced martensite, and excellent low- and high-cycle fatigue properties are ideal properties for SMAs to be considered for earthquake engineering applications. These properties fit well with the needs of performance-based design currently used in the design of structural systems in earthquake prone areas. However, one of the key problems hindering the use of SMA devices in actual structures stems from a lack of effective knowledge transfer between the material science and structural engineering communities. Great strides in understanding the behavior and possible applications of SMAs, particularly NiTi, have been made in both fields, but the inability to effectively connect the research of both sides in a meaningful manner has limited further use of SMAs. Structural engineers typically have trouble deducing the mechanics at a microstructural level, while researchers in the materials science field are unfamiliar with the specific requirements of performance-based design of civil structures. Likewise, there exists a lack of knowledge of the mechanical properties of large diameter SMAs which may be more economical and convenient for structural applications, limited computational models to efficiently and accurately account for cyclic behavior of SMAs under earthquake loadings, and little understanding on how their behavior effects other members of a structural system.

1.1 Scope of Project

The cyclic properties of superelastic SMAs are sensitive to many variables which effect the internal microstructure of the material such as composition, heat treatment, and manufacturing process (Gall et al., 1999a). On a macroscopic level, loading rate and loading history tend to have a significant effect on the mechanical behavior of SMAs (Strnadel et al., 1995a,b). Presently, little has been done to connect both the microstructure of SMAs and macroscopic effects in a unified manner. Also, although several studies have been conducted on the mechanical behavior of SMAs, very few of these investigations have looked at bar sizes necessary for structural applications and loading levels or loading rates which are equivalent to those which would be sustained by structural members during an earthquake. Before SMAs can be used in practice for seismic response modification of structures, these concerns need to be addressed. The experimental portion of this study attempts to gain a better understanding of the cyclic behavior of SMAs by providing a fundamental and hierarchical link between the nanometer-scale structure of NiTi SMAs up through the mechanical behavior of large diameter specimens in terms of those properties important for structural applications. NiTi wires are also used to experimentally study variables particularly important to seismic applications and provide statistical information on the properties of NiTi to allow for more accurate modeling in structural reliability studies.

The ability to implement SMAs into structural and earthquake engineering practice is further complicated by the need to have accurate and easy to implement models accounting for the cyclic behavior of SMAs. An accurate model can allow for an initial study of the behavior of a building system using a SMA device for control of its response during a seismic

event. Further, more detailed studies of different building configurations can be undertaken to determine if the use of a SMA system provides a better response as compared to current conventional building systems. The analytical section of this study is used to determine the feasibility of SMA systems by addressing the following questions: (1) Can accurate models of SMA behavior be developed and implemented into structural engineering software, (2) How does the behavior of an SMA system compare to a conventional system, (3) What SMA parameters are most significant in effecting the response of a structural system during an earthquake, and (4) What is the optimal configuration of SMAs for a given structural system?

The main objective of this dissertation is to characterize the material behavior of NiTi superelastic SMAs while exploring the feasibility and optimal behavior of SMAs for use under a performance-based seismic design framework for the design and retrofit of structures in moderate to high seismic zones. By addressing the problems and questions presented, this objective is achieved.

1.2 Dissertation Outline

The content of the dissertation is organized into the following chapters:

- **Chapter 2:** An introduction to shape memory alloys and their behavior is presented. An overview of past studies conducted on material characterization of NiTi SMAs and their use in earthquake engineering applications is also discussed.

- **Chapter 3:** A multidisciplinary and multi-scale characterization of large diameter superelastic NiTi SMAs is undertaken to provide a link starting at the nano-scale

structure of NiTi leading up to the full-scale deformation response of NiTi bars. Specific focus is placed on the effect of loading levels and rates equivalent to those expected during an earthquake.

- **Chapter 4:** The results of experimental testing of superelastic NiTi SMA wire for seismic applications are presented. The effect of mechanical training, pre-straining, and near-field versus far-field type cycling is explored.

- **Chapter 5:** A study to determine probability distributions for specific NiTi SMA properties is presented based on data from tests conducted on NiTi wires. These properties considered are important for modeling SMA behavior and the distributions can be used for future analytical work.

- **Chapter 6:** Two analytical models are developed to represent the behavior of NiTi SMAs under uniaxial loading. The behavior of these models is compared through a simple SDOF study. Nonlinear time history analyses are conducted on both conventional structural systems and innovative systems implementing superelastic SMAs, and the responses of the different systems are compared.

- **Chapter 7:** Conclusions are presented along with recommendations for the use of superelastic NiTi SMAs for seismic applications in building systems based on the findings of this study. Suggestions for future research on the use of SMAs in seismic design and retrofit of structures also are made.

CHAPTER II

OVERVIEW OF SHAPE MEMORY ALLOYS

2.1 Shape Memory Alloys

2.1.1 Introduction to Shape Memory Alloys

Shape memory alloys are a group of metallic alloys which have the ability to undergo large deformations while reverting back to their original undeformed shape through either heating (shape memory effect) or removal of the load (superelastic effect). The ability of specific metallic materials to recover their shape was first discovered in the 1930's by Chang and Reid in Au-47.5 at%Cd (where at%Cd refers to the atom percent of Cd) (Otsuka and Wayman, 1998). Although shape memory was discovered in the 1930's, it was not until the discovery of shape memory properties in near equiatomic NiTi (also known as Nitinol) by Buehler and Wiley at the Naval Ordnance Laboratory that research into the mechanics and applications of shape memory alloys began (Melton, 1990). During the past two decades, several advances have been made in understanding the mechanisms associated with the shape memory and superelastic effects, their thermomechanical behavior, and the fabrication and production of SMAs leading to higher quality and more reliable materials at lower costs. These advances have prompted increased interest in the use of the material in a variety of engineering and commercial applications.

2.1.2 Basic Microstructure of Shape Memory Alloys

The crystalline structure of a material, in part, dictates the materials overall behavior. For this reason, it is important to have a basic understanding of the microscopic aspects of SMAs. This is true even for those looking to use them in large scale applications. Many authors have provided detailed information on the crystallography of SMAs since their discovery, which is used as the basis of this discussion (Otsuka and Shimizu, 1986; Otsuka and Wayman, 1998; Perkins, 1981; Wayman and Duerig, 1990). SMAs can typically be found in one of two stable phases, martensitic or austenitic. The martensitic phase receives its name due to the liberation of heat upon its formation and the austenitic phase is named after the parent phase of martensite in steels (Wayman and Duerig, 1990). In general, the martensitic phase is stable at low temperatures and under high stresses while the austenitic phase is stable at high temperatures and low stresses. The low symmetry martensitic phase is stable in either a multi-variant twinned form or a single variant detwinned form where the multi-variants represent a change in the orientation of the crystalline structure. Conversely, the austenitic phase only takes on a single form and tends to be harder and stronger (Wayman and Duerig, 1990). A two-dimensional general schematic view of the martensitic and austenitic phases can be seen in Figure 2-1.

The unique ability of SMAs to recover their shape is in part due to the ordered crystalline structure between the austenitic and martensitic phases. As a result, the ordering of the atoms in the martensitic phase and austenitic phase does not change. This ordering

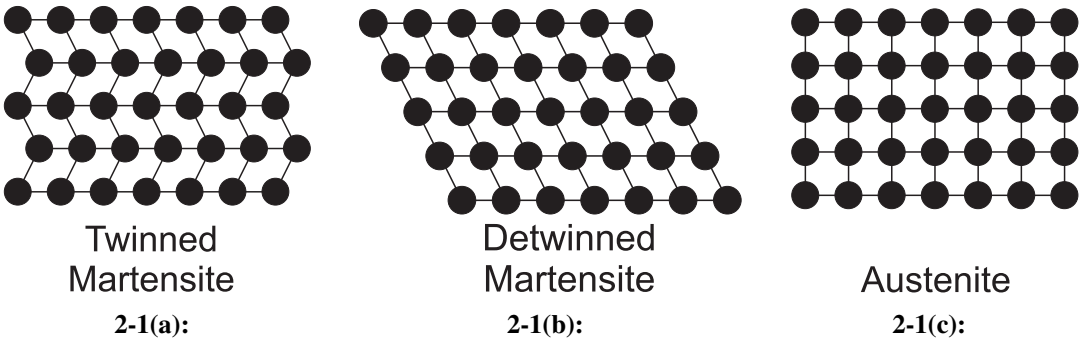

Figure 2-1: Schematic view of a typical SMA microstructure: (a) multi-variant twinned martensite, (b) single variant detwinned martensite, (c) austenite. (Adapted from Wayman and Duerig (1990))

allows the material to undergo a displacive (diffusionless) martensitic phase transformation either through a temperature change or the application of stress rather than the diffusional transformation associated with solid-state transformations of typical metals. The martensitic phase transformation takes place through both a lattice deformation (atomic movement) and lattice accommodation (invariant shear) process. The lattice deformation process consists of small atomic movements in either the austenite phase (Figure 2-1(c)) or twinned martensite phase (Figure 2-1(a)) layer by layer to create a single variant detwinned martensite structure (Figure 2-1(b)). This process consists only of a shape change (no volume change) with no permanent slip allowing the shape change to be reversible and providing the unique ability of SMAs to be able to undergo large deformations while returning to their original undeformed shape (Wayman and Duerig, 1990).

The martensite start temperature, M_s, martensite finish temperature, M_f, austenite start temperature, A_s, and austenite finish temperature, A_f, define the temperatures at which the phase transformations occur and result in hysteretic behavior during cooling and heating.

At temperatures below M_f, SMAs are in their twinned martensite phase while at temperatures above A_f, the SMAs are in their austenite phase. Significant property changes are associated with passing these transformation points and the transformation temperatures themselves are highly dependent on the composition and processing of the SMA (Melton, 1990).

2.1.3 Shape Memory Effect

As is mentioned in Section 2.1.1, there are two mechanisms by which the deformation of SMAs can be recovered, the shape memory effect and the superelastic effect. The shape memory effect occurs at temperatures below M_f, resulting in the SMA being in its twinned martensite form. Upon loading, the twinned martensite undergoes typical elastic deformation until the "yield" stress is reached at which point twin boundary movement occurs and detwinning initiates. After the completion of the phase transformation, further elastic deformation of the detwinned martensite occurs provided the critical slip stress has not been reached. Upon unloading, there remains residual strain which is recovered by heating the material above A_f causing a phase change to the high temperature austenite phase. Upon cooling, the structure returns to the original twinned martensite form with little or no residual strain (Wayman and Duerig, 1990). Figure 2-2 provides the stress-strain curve associated with the shape memory effect.

2.1.4 Superelastic Effect

The second means of shape recovery in SMAs is the superelastic effect. The superelastic effect occurs at temperatures above the A_f, resulting in the SMA being in its austenitic

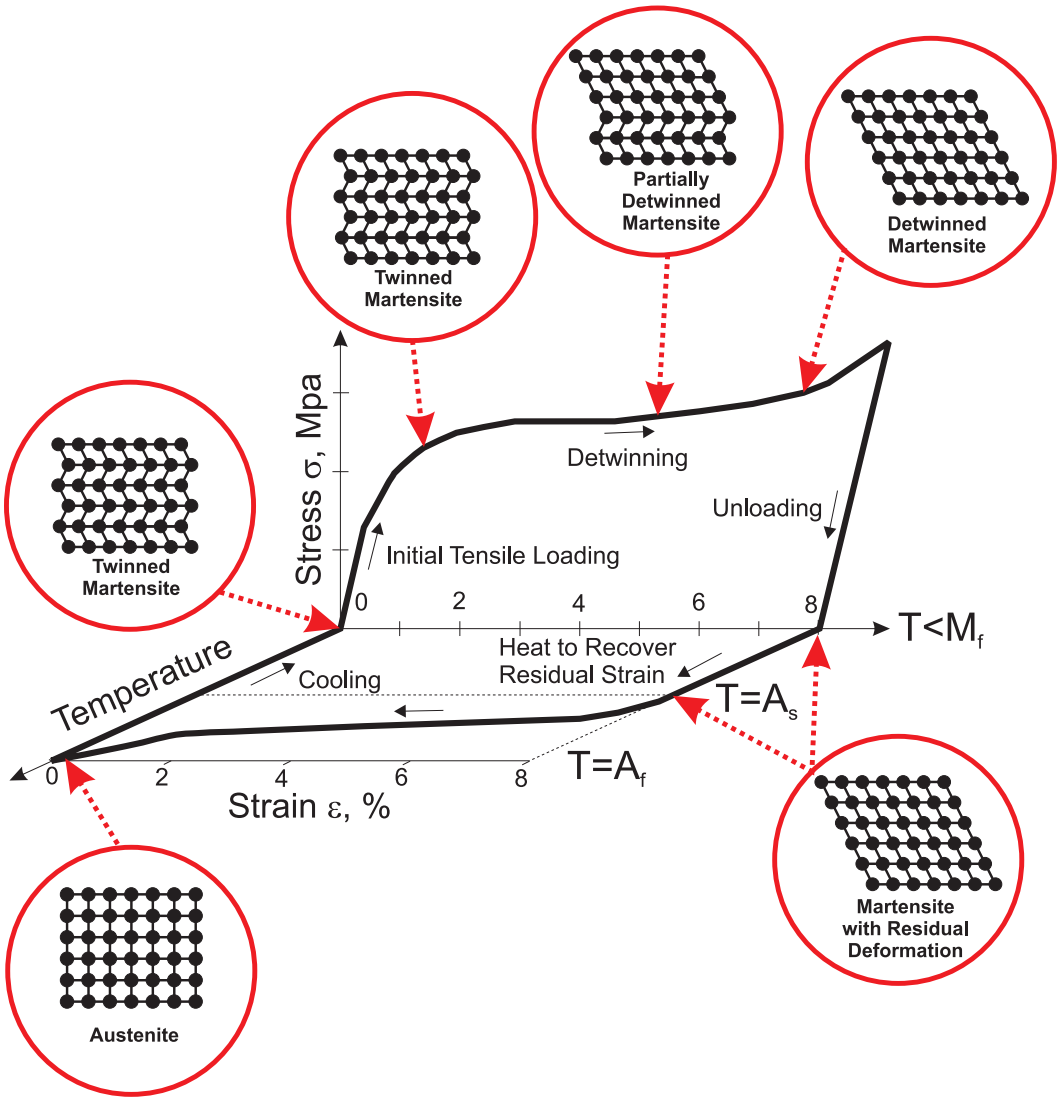

Figure 2-2: Typical stress-strain curve for an SMA undergoing the shape memory effect

phase at the start of loading. Upon loading, the austenite undergoes typical elastic deformation until the "yield" stress (stress at which martensite becomes stable) is reached. At this point, the martensitic phase transformation initiates. Detwinning then occurs along the stress plateau until the NiTi is in its fully detwinned martensite phase as is discussed in Section 2.1.2. After completion of the phase transformation, further elastic deformation can occur provided the critical slip stress has not been reached. Upon removal of the load, the detwinned martensite is no longer stable and reverts back to its original austenite phase. The energy driving this reverse transformation is the chemical free energy between the austenite phase and martensite phase (Tadaki et al., 1988). In order for the superelastic effect to occur, the critical slip stress must be above the critical stress to cause stress-induced martensite. If this is not true, permanent deformation occurs (Duerig and Zadno, 1990b). Figure 2-3 provides a schematic of the stress-strain curve associated with the superelastic effect.

2.1.5 Mechanical Behavior of Shape Memory Alloys

A further property to note is that the martensitic phase transformation is a thermoelastic process causing the mechanical behavior of SMAs to not only be dependent on stress and strain, but also temperature. The thermoelastic nature means that a decrease in the SMAs temperature equivalently acts as an increase in stress due to growth of martensitic plates causing an increase in internal stresses (Wayman and Duerig, 1990). This is the main contribution to the formation of the shape memory effect and the superelastic effect at different temperatures as can be seen from the three dimensional plot of stress, strain, and temperature in Figure 2-4. At a temperature above M_d, the stress to induce the martensitic

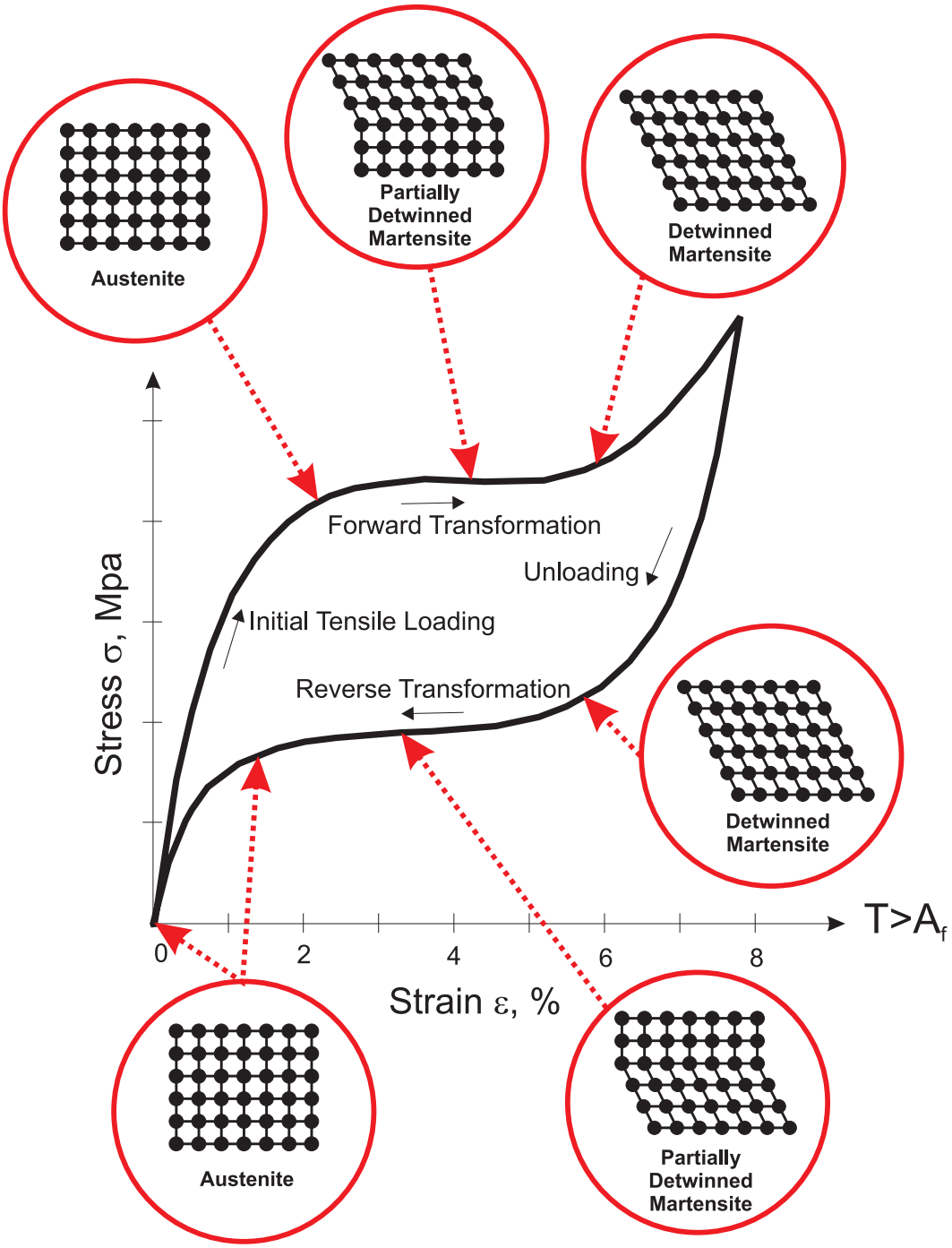

Figure 2-3: Typical stress-strain curve for an SMA undergoing the superelastic effect

transformation lies above the critical slip stress of the SMA resulting in permanent plastic deformation due to the thermoelastic nature of the material. This phenomenon has been labeled "ordinary plastic deformation" in Figure 2-4. Research has shown that the relationship between stress to induce martensite and temperature is linear and can be captured by the Clausius-Clapeyron equation shown in Equation 2.1:

$$\frac{d\sigma}{dM_s} = -\frac{\Delta H}{T\varepsilon_o} \tag{2.1}$$

The left side of Equation 2.1 refers to the change in stress with respect to a change in the martensite start temperature, while ΔH, T, and ε_o represent the transformation latent heat, temperature, and transformational strain, respectively. This relationship shows an increase in the difficulty to induce the martensitic phase transformation with an increase in temperature, which subsequently leads to an increase in the forward transformation stress, an increase in the reverse transformation stress, and deformation by permanent slip above a temperature M_d (Wayman and Duerig, 1990). This temperature effect needs to be considered when considering SMAs for applications which may experience a broad temperature range.

2.1.6 Applications of Shape Memory Alloys

The unique properties of SMAs, such as the shape recovery, hysteretic damping, good corrosion resistance, and biocompatibility, coupled with a significant reduction in price, higher quality, and better reliability has led to the development of several applications for SMAs in the biomedical, commercial, and aerospace fields. The ability to use SMAs to enhance

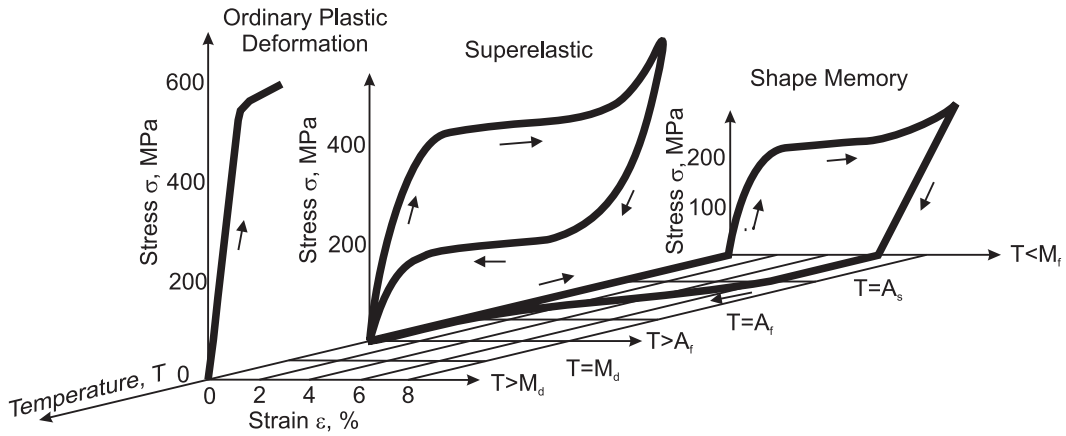

Figure 2-4: Three dimensional stress, strain, temperature relationship for the mechanical behavior of SMAs (DesRoches et al., 2004)

less invasive medical procedures has led to several developments in the medical field including: arterial stents, medical guide wires, catheters, orthodontic braces, and orthopedic prostheses (Duerig et al., 1990a). Commercial applications which have taken advantage of the superelastic properties of SMAs include eyeglass frames, cellular telephone antennas, and golf clubs (Asai and Suzuki, 2000; Hsu et al., 2000). The aerospace industry implemented SMAs in adaptive aircraft wings and smart helicopter blades for increased efficiency and reduced noise and vibration (Beauchamp et al., 1992; Chandra, 2001). The success of these applications has increased interest in the use of SMAs in other fields, such as for applications in the seismic resistant design and retrofit of civil engineering structures.

2.2 NiTi Shape Memory Alloys

2.2.1 Overview of NiTi Shape Memory Alloys

Although several different types of materials have shown shape memory properties, the most readily available and commercially used SMA in the United States is near-equiatomic

NiTi. For both this reason and the consistency of the properties and behavior of NiTi, it is the focus of the remainder of this dissertation. The following sections outline past research into the mechanical behavior of NiTi SMAs on both a microscopic and macroscopic level with an emphasis on those properties important for civil engineering and seismic applications. Before considering these efforts, it is important to know how the the nominal near-equiatomic NiTi SMA properties compare to those of a typical structural metal used in building and bridge systems.

Important properties for civil engineering applications are presented in Table 2-1 for structural steel, martensitic NiTi, and austenitic NiTi. A few things to note are the fact that the yield strength for martensite is lower than that of the austenite due to the difference in the microstructure between the two phases. The Young's modulus values for NiTi are less than that for structural steel due to the mobility of the twin boundaries in NiTi, particularly martensitic NiTi. The most important property for most applications is the ability of NiTi to recover strains up to approximately 8% providing a unique recentering capability to the material and limiting permanent deformations. Other mechanical properties such as ultimate tensile strength and elongation compare favorably to those of structural steel. NiTi also has excellent corrosion resistance which is due to the formation of a passive Titanium Oxide layer which limits surface diffusion over time. These properties have led to further studies of the mechanical behavior of SMAs for use in a variety of applications.

2.2.2 Material Characterization of NiTi

A basic materials characterization of NiTi provides an overview of the underlying nanoscale and microstructure properties of the material before looking at the properties of NiTi

Table 2-1: Properties of Structural Steel and NiTi SMAs

Property	Structural Steel	NiTi SMA	
		Martensitic	Austenitic
Density (g/cm^3)	7.85	6.45	6.45
Elastic Modulus (GPa)	200	21-41	30-83
Poisson's Ratio	0.27-0.30	0.33	0.33
Yield Strength (MPa)	248-517	70-140	195-690
Ultimate Tensile Strength (MPa)	448-827	895-1900	895-1900
Elongation at Failure (%)	20	5-50	5-50
Recoverable Elongation (%)	0.20%	up to 8%	up to 8%

SMAs on a macroscopic level. Nano-scale precipitates and the overall microstructure have a significant effect on the mechanical behavior of NiTi SMAs and can be used to explain their unique full-scale behavior. This section explores the underlying microstructure of NiTi SMAs under the context discussed in Section 2.1.2. Also, a short overview of past microstructural studies focusing on the effect which thermal processing, precipitates, texture, and overall microstructure have on the mechanical behavior of NiTi SMAs is presented in order to help gain a better understanding of the underlying mechanisms which effect the properties of large diameter bars used for civil and structural engineering applications.

2.2.2.1 Microstructure of NiTi Shape Memory Alloys

As mentioned, NiTi SMAs have a near-equiatomic composition and are made of an ordered intermetallic compound which allows for the occurrence of a displacive martensitic phase transformation. The primary crystalline structure associated with the martensitic phase is that of a B19' monoclinic geometry. Variants are associated with the twinned form as can be seen in Figure 2-5(a). The variants are seen as the change in direction in the crystalline structure. The phase transformation can also result in other martensitic phases, such as the

rhombohedral (R) phase. The R-phase is often called a "premartensitic" transformation because of its occurrence before the onset of the primary martensitic phase transformation. The highly symmetric austenite phase has a B2 or CsCl structure with an orthorhombic geometry where the nickel atom resides at the center of the structure and the titanium atoms at the corners as seen in Figure 2-5(b).

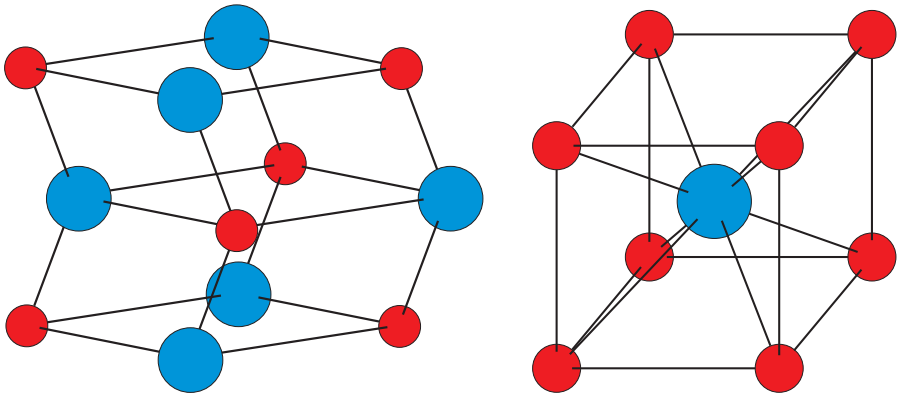

2-5(a): **2-5(b):**

Figure 2-5: Three dimensional crystalline structure of NiTi SMAs: (a) twinned martensite structure and (b) austenite structure

The phase diagram associated with a binary NiTi system can be seen in Figure 2-6. From the phase diagram, it is clear that small changes in the composition of near-equiatomic NiTi can lead to the formation of additional phases such as $NiTi_2$ and Ni_3Ti which consequently do not exhibit shape memory behavior (Bram et al., 2002). Exposure to elevated temperatures for a sufficiently long time results in the formation of a $TiNi_3$ phase which precipitates through a diffusion-based process. However, most heat treatment processes after manufacturing are done at temperatures below those mapped by the phase

diagram resulting in the formation of metastable phases. It has also been shown that prior to the formation of the $TiNi_3$ phase, metastable Ti_3Ni_4 precipitates can form from a solid solution of Ni in NiTi at moderate aging temperatures (300 °C to 600 °C) (Gall et al., 1999c,d, 1998). The size and distribution of the Ti_3Ni_4 precipitates can be used to facilitate hardening in NiTi SMAs. Impurities such as oxygen, carbon, and nitrogen can cause a shift in the M_s temperature leading to significant property changes associated with the thermoelastic nature of the material. NiTi is highly susceptible to oxidation in its molten state, so care must be taken in order to control the composition during melting to prevent introduction of impurities (Melton, 1990). The variability in properties associated with small changes in the composition and the introduction of impurities influencing the crystalline structure requires strict controls during the manufacturing process. These results suggest that the influence of composition must be considered in looking at the overall macroscopic behavior of NiTi SMAs.

2.2.2.2 Effect of Microstructure on Mechanical Properties of NiTi

Since manufacturing and processing have a large role in the ultimate behavior of NiTi SMAs, it is important to understand how different processing techniques effect the underlying microstructure of the material and the resulting mechanical properties. Typical earthquake engineering applications require that materials have a predictable and consistent behavior in order to ensure performance-based design constraints are met. Many studies of the microstructure and mechanical properties of NiTi SMAs have been conducted over the

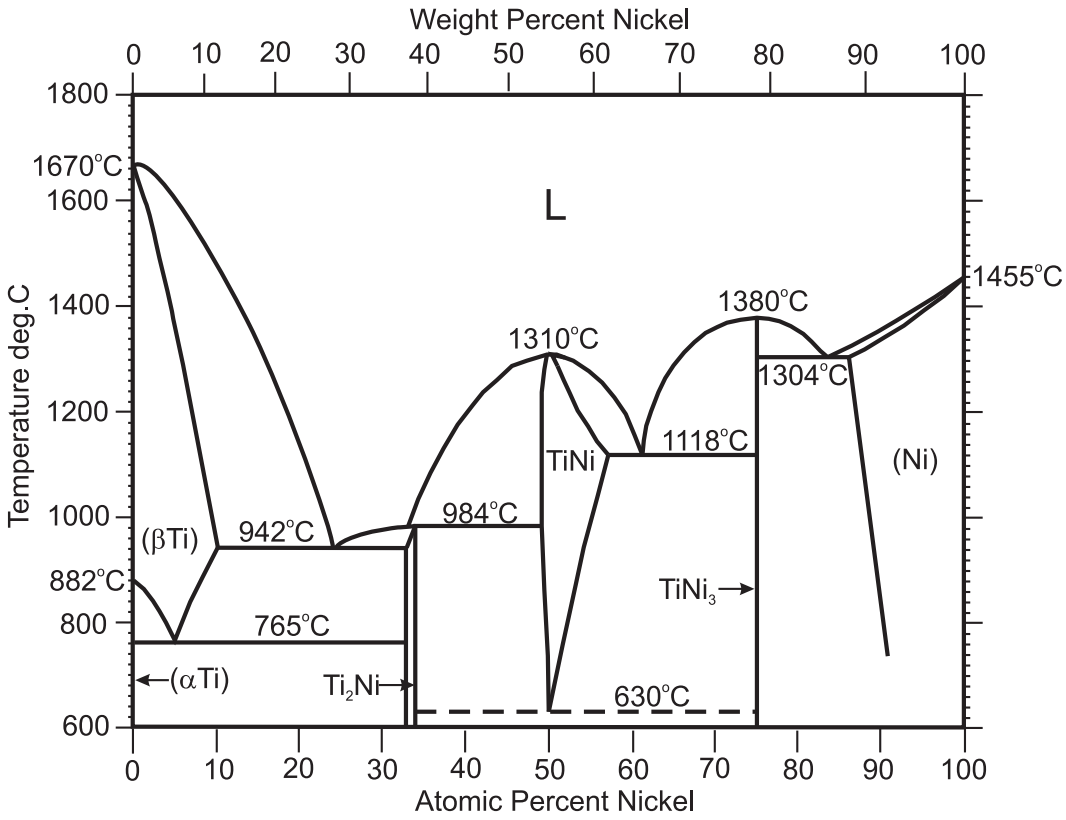

Figure 2-6: Phase diagram for binary Ni-Ti systems with NiTi SMA being near-equiatomic (Bram et al., 2002)

years, but few of these studies have examined, in detail, the relationship between processing, structure, and full-scale properties. Even fewer studies have characterized materials formed to the sizes that are typically needed for earthquake engineering applications.

A recent study by Frick et al. (2004) addresses this lack of knowledge by examining cast, cast and then hot-rolled, and cast, hot-rolled, and cold-drawn polycrystalline Ti-50.9 at%Ni bar specimens to investigate the processing, structure, and property relationship. The results found that cast specimens have a random grain orientation while the grains of the hot-rolled specimen and cold-drawn specimen have a strong <111> orientation (Frick et al., 2004). These observations are similar to early findings which found that that stress-strain response of [111] single crystals compared favorably to textured polycrystalline NiTi (Gall et al., 2001). The texture associated with both hot-rolled and cold-drawn specimens causes a asymmetric tension-compression behavior since the grains are soft under tension oriented in the [111] direction and hard under compression (Gall and Sehitoglu, 1999b). However, random texturing tends to lead to a more symmetric behavior suggesting that cast NiTi may be used for applications requiring the same tensile and compressive behavior (Frick et al., 2004).

One of the more significant findings for the use of NiTi SMAs in civil applications is that Ti_3Ni_4 precipitates tend to be the dominant factor influencing shape memory properties suggesting that deformation modes can be tailored through different thermal processing (Frick et al., 2004). This result and the correlation between thermal processing temperature and mechanical behavior of coupon specimens presented by Frick et al. (2005) suggests that the cheaper hot-rolled form of NiTi as opposed to the typical cold-work formed specimens can provide optimal shape memory properties by controlling the size and coherency

of the Ti_3Ni_4 precipitate. As a result, the cost of NiTi drops significantly removing a major obstacle in the eventual implementation of NiTi SMAs into earthquake engineering applications.

Even though these studies and others have made significant strides in determining a relationship between processing, structure, and property relationship, no study to date has concisely mapped the microstructure of a large diameter specimen across its diameter to determine changes in texturing with respect to bar size (amount of deformation processing). Further, there exist a lack of knowledge in regards to correlating the full-scale mechanical behavior of a large diameter bar used for civil engineering applications and the microstructure of the bar. These gaps in knowledge in regards to the microstructural properties need to be addressed before confidence in the behavior of large diameter NiTi SMAs can be obtained allowing their eventual implementation into practice.

2.2.3 Mechanical Properties of NiTi

As manufacturing processes for NiTi have become more refined over the last decade, uses for their unique properties have increased. With this increased interest in the use of NiTi SMAs came numerous studies to better determine the macroscopic mechanical properties of NiTi. In particular, for seismic applications, the effect on the mechanical properties of cyclic loading, strain rate, temperature, thermomechanical processing, training, and prestraining is important. The following sections review the previous studies that have been conducted with respect to these effects and elaborate on the current state of knowledge, particularly concerning those properties of superelastic NiTi SMAs important for seismic applications.

2.2.3.1 *Early Studies*

Early material testing performed on NiTi SMAs consists of experimental tensile tests using small diameter wires and thin plates in order to better understand deformation behavior associated with SMAs. These tests reveal a Lüders-like deformation resulting in a stress plateau up to strains of 7% even with continued cycling (Miyazaki et al., 1981b,a). Later tests show the formation of an intermediate phase (R-phase) consistent with a 2-stage initial yielding above the M_s temperature (Miyazaki and Otsuka, 1986b). The R-phase only develops in the first cycle of testing. Tensile tests provide the typical stress-strain curve for martensitic NiTi SMA consisting of initial elastic yielding of the twinned martensite, a stress plateau during transformation, elastic yielding of detwinned martensite, and plastic deformation to failure (Melton and Mercier, 1981). These early tests provide a basic understanding of the deformation characteristics of NiTi SMAs while exposing the complex behavior of the material and need for further testing.

2.2.3.2 *Cyclic Effect*

Due to the cyclic nature of earthquake ground motions, the effect which cycling has on the properties of SMAs is of great importance. Both mechanical and thermal cyclic tests are conducted on NiTi SMAs because of the stress, strain, and temperature interdependence. Several studies using thermal cycles have been conducted to determine the stress-strain-temperature relationship and behavior of small diameter SMA wires, but are not the focus of this dissertation (Cui et al., 2002; Hori et al., 1992; Matsumoto, 1991; Tobushi et al., 1992b,a). Hereafter, cyclic testing refers to mechanical uniaxial tests which are consistent with the typical deformation mode for SMAs in seismic applications.

An exhaustive set of tests on the cyclic properties of superelastic NiTi SMAs has been conducted. Typical tests on superelastic specimens consist of testing superelastic wire in tension up to strains between 4% to 8%. Several studies found consistent results showing major decreases in the forward transformation stress (loading plateau), slight decreases in the reverse transformation stress (unloading plateau), and increases in the residual strain with continued cycling until stabilization is reached (Dolce and Cardone, 2001; Gong et al., 2002; Miyazaki et al., 1986a; Strnadel et al., 1995a; Tobushi et al., 1998). These effects can be seen in Figure 2-7.

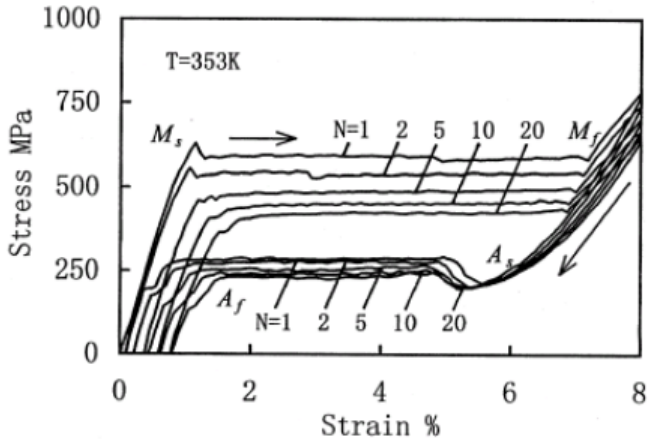

Figure 2-7: Stress-strain curve for a superelastic specimen under tension cycling (Tobushi et al., 1998)

Both Gong et al. (2002) and Miyazaki et al. (1986a) attribute the decrease in the forward transformation stress to accumulation of dislocations which assist the martensite transformation while also resulting in an increase in unrecoverable strain. This decrease in transformation stress can be avoided through the raising of the critical slip stress and there by

reducing the formation of dislocations. Strnadel et al. (1995b) performed experimental cyclic tests consisting of soft (constant maximum stress cycles of 1.1 times the forward transformation stress) and hard (constant maximum elongation cycles of 1 mm) loadings and found during low numbers of cycles stress slip dominates the deformation mode. As a result, the transformation stresses decrease. For a higher number of cycles, the effect of the transformation stress dominates, causing an increase in residual strain when cycled to a higher number of cycles. Due to the greater decrease in the forward transformation stress as compared to the reverse transformation stress, the hysteretic area decreases with cycling resulting in a decrease in the energy dissipation capacity (Dolce and Cardone, 2001).

2.2.3.3 Strain Rate Effect

Earthquake ground motions typically occur at frequencies ranging from 0.01 Hz up to 15 Hz with the dominant frequency typically falling between 0.5 Hz to 5.0 Hz. In order to be able to implement SMAs in seismic applications, the effect of strain rate on the behavior of NiTi SMAs needs to be understood. Studies on the effect which loading rate has on the tensile properties of NiTi superelastic specimens have focused mainly on small wires with differing results between investigators. Both Tobushi et al. (1998) and Leo et al. (1993) reported an increase in hysteretic area (an increase in the loading plateau and a decrease in the unloading plateau) with increased cycling rates up to 100% strain/min and 50.0 mm/min, respectively. This resulted in an increase in energy dissipated with increased strain rate. Leo et al. (1993) attributes these results to an increase in the specimens temperature with increased loading rates causing a shift in the transformation stresses, where Tobushi et al. (1998) suggests that the increase in hysteretic area is a result of the increased

loading speed not allowing for relaxation during interface movement during the transformation. Conversely, other strain rate tensile tests have reported increases in the loading plateau stress (Piedboeuf et al., 1998; Wolons et al., 1998), decreases in the loading plateau stress (Kolomytsev and Kozlov, 1998), and upward shift in the stress-strain curve (Dolce and Cardone, 2001) with increased strain rate all resulting in a decreased hysteresis and loss of energy dissipation capacity up to 50%. Further studies looking at the effect of loading rate on the cyclic behavior of superelastic NiTi SMAs need to be completed given the conflicting results.

2.2.3.4 Temperature Effect

The dependence of the mechanical behavior of NiTi SMAs on the temperature, as seen in Figure 2-4, demonstrates the importance of understanding temperature effects. As mentioned previously, the temperature of the specimen with respect to the M_s, M_f, A_s, A_f, and M_d determines whether the NiTi undergoes the shape memory effect, superelastic effect, or typical plastic deformation. Because the phase transformation is a thermoelastic process, a decrease in temperature tends to have the same effect as an increase in stress felt by the specimen and thus reduces the transformation stresses. Figure 2-8 shows the transition from the shape memory effect to the superelastic effect for a typical NiTi specimen tested at various ambient temperatures ranging from $-40\,^{\circ}\text{C}$ to $80\,^{\circ}\text{C}$. Large residual strains are seen for extremely low temperatures with complete recentering associated with the superelastic effect not occurring until temperatures above the A_f.

Further studies in the temperature range above A_f have been conducted to show the effect of temperature on the superelastic behavior. Transformation stresses (forward and

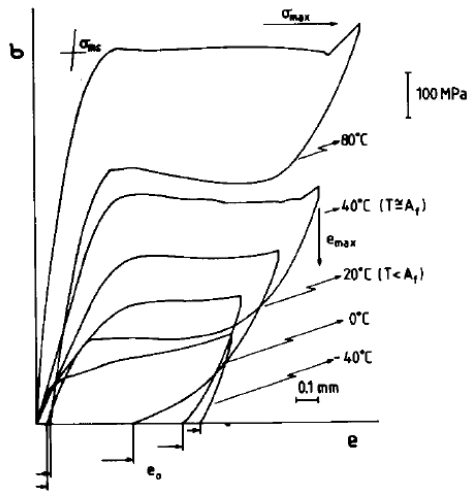

Figure 2-8: Stress-elongation curve for NiTi at different ambient temperatures (Strnadel et al., 1995a)

reverse) are temperature sensitive and are linearly related based on Equation 2.1 previously presented (Dolce and Cardone, 2001; Serneels, 1999; Strnadel et al., 1995a; Tamai and Kitagawa, 2002; Tan et al., 2002; Vokoun et al., 2003; Wolons et al., 1998). The resulting hysteresis loops are found to shift upward with an increase in temperature, but very little change occurs to the shape of the hysteresis loop. Wolons et al. (1998) determined that optimal damping is obtained at a testing temperatures of 32.20 °C with a decrease in damping capacity on either side of this temperature. Ideal superelastic behavior can be obtained when ambient temperatures are 60 °C to 80 °C above the A_f. The effect of increased ambient temperature is found to more drastically affect the cyclic properties of superelastic SMAs with increased cycling by Dolce and Cardone (2001). The high dependence of the mechanical behavior on temperature must be understood in light of the fact that many seismic applications may require the SMA to perform within a broad temperature range.

2.2.3.5 Thermomechanical Processing Effect

Preliminary research on the effect of thermomechanical processing on the cyclic behavior of NiTi SMAs has shown that changes in cold working levels, post-formation annealing temperature, and annealing time can drastically alter the tensile properties of NiTi SMAs. In particular, many studies have been conducted using a differential scanning calorimeter (DSC) to determine the change in transformation temperatures with annealing temperature and cold working (Abujudom et al., 1990; Chorbak et al., 2003; Thoma et al., 1995). Miller and Lagoudas (2001) performed thermal cycling studies on NiTi wire which revealed an increase in plastic strain accumulation with increased annealing temperature due to recrystallization. Increased cold working results in an increase in the density of dislocations which tends to inhibit the accumulation of plastic strain. VanHumbeeck and Liu (2000) report optimal damping at an annealing temperature of 550 °C, which is directly related to the martensite reorientation stress (forward transformation stress). Mechanical tests performed by Kawaguchi et al. (1991) show that a decrease in annealing temperature leads to higher transformation stresses due to remnant dislocations attributed to cold working which inhibit martensite plate movement. In using SMAs in seismic applications, annealing temperatures need to be chosen such that the optimal stresses and residual strains are obtained.

The recent study completed by Frick et al. (2004) looks at the effect of processing SMAs through casting, casting and hot-rolling, and casting, hot-rolling, and cold drawing as discussed in Section 2.2.2.2. To date, most NiTi SMA specimens are cold drawn in order to obtain good superelastic properties which results in higher expenses as compared

to hot-rolling or casting. Frick et al. (2004) found that for large diameter bars cold drawing is not necessary. Hot rolled specimens can be used while using precipitation treatment to tailor the properties of the NiTi as Ti_3Ni_4 precipitates have been shown to dominate over grain size effects and dislocation density. These findings provide promise for possible implementation of NiTi SMAs into seismic design and retrofit applications as cost is seen as one of the major obstacles.

2.2.3.6 Training Effect

During cyclic testing, many of the properties of superelastic NiTi SMAs such as forward and reverse transformation stress, residual strain, and energy dissipation capacity degrade with continued cycling as is shown in Figure 2-7. Since stabilization occurs after continued cycling, researchers have suggested first training NiTi SMA specimens before using them in applications. Some studies have used up to 100 thermal cycles in order to stabilize superelastic properties with good results (Scherngell and Kneissl, 1999; Wu et al., 1996). Fewer studies have looked at the effect of mechanical training. Tobushi et al. (1998) trained NiTi wire by applying 20 loading and unloading cycles to NiTi wire. The results found very little fluctuation in the stress-strain hysteresis with only small changes in the forward transformation stress and reverse transformation stress when subsequently cycled at various strain rates up to 2 Hz. The effect on the properties during continued cycling was not studied. It has been suggested that further research is needed in order to determine the proper number of tensile cycles at the proper strain amplitude to obtain stable mechanical behavior from NiTi SMAs. This will allow for more accurate and simplified analytical models and provide reliable behavior from SMA seismic devices.

2.2.3.7 Pre-straining Effect

Along with training, pre-straining has also been considered as a way to obtain more ideal SMA properties. By pre-straining superelastic NiTi shape memory alloys, tensile behavior can be assured over a larger strain range. Pre-straining to strain levels high enough to induce the martensitic phase transformation result in internal hysteresis loops and higher restoring forces even for small deformations. The internal hysteresis loops provide energy dissipation throughout the cycling of the NiTi, while NiTi specimens which are not pre-strained act elastically for small strain loadings. Wolons et al. (1998) has found that pre-straining affects the hysteresis shape with lower pre-straining values providing more energy dissipation. In particular, for seismic applications, Dolce and Cardone (2001) show that optimal damping and recentering capabilities can be obtained by pre-straining SMA wires to create a hysteresis about a particular point allowing different configurations of a device to apply different mechanisms. Others have also used set pre-strain levels to enhance the behavior of SMAs for seismic response reduction (Aizawa et al., 1998; Saadat et al., 2001). Although some work has been done in terms of determining the effects of pre-straining on superelastic NiTi behavior, most of these past studies have cycled only between predetermined strain levels or only pre-strained the SMAs to a single level to ensure tension-only behavior. As of yet, no study has identified significant trends in the properties of superelastic NiTi with respect to pre-straining level.

2.3 Modeling of Shape Memory Alloys

The ability of SMAs to undergo the shape memory effect and superelastic effect while providing both energy dissipation capacity and potential recentering capability are ideal

qualities for materials used in seismic design and retrofit of civil engineering structures. Due to the high cost and lack of facilities to test all full-scale structures that can potentially use SMAs to reduce their seismic response, accurate models of their behavior need to be created in order to design and implement NiTi SMA seismic devices into practice. Several studies have been devoted to such work resulting in three main types of models: phenomenological, thermomechanic, and micromechanic.

Phenomenological models reproduce the thermomechanical relationship seen during experimental testing, but do not provide an underlying explanation for the results. Models of this type tend to use a small set of parameters typically consisting of the elastic modulus, slope of the plateau, and stresses associated with the start and end of the forward and reverse transformation obtained experimentally during materials testing. Phenomenological models are the focus of this dissertation because of the ease of computation and ability to implement such a model efficiently into current nonlinear dynamic modeling platforms. Some phenomenological models that have been developed to date are those by: Tanaka (1986), Liang and Rogers (1997), Terriault et al. (1997), Auricchio and Sacco (1997),Lexcellent et al. (2000), Dobovsek (2001), Malovrh and Gandhi (2001), Zhu et al. (2002), Tamai and Kitagawa (2002), and Fugazza (2003).

Thermodynamic and micromechanic models are more complex than phenomenological models and are typically not used by practicing civil engineers. Thermodynamic models predict the behavior of an SMA element based on an energy balance between the different phases providing a good description of the physical phenomenon associated with the martensitic phase transformation. Lagoudas et al. (1996) developed a thermodynamic constitutive model to be implemented in a finite element analysis to predict the behavior of

SMAs in composites. Micromechanical models also are good at describing the physical phenomenon behind the martensitic phase transformation, but do so by looking at only a small volume of material. The average strain in each small volume is calculated and combined in order to obtain the global behavior. Reviews by Bo and Lagoudas (1994), Birman (1997), and Saadat et al. (2002) provide further information on the state-of-the-art in modeling SMA behavior.

Many of the phenomenological models mentioned above are lacking in areas such as accounting for cyclic loading effects, thermal changes, strain rate effects, and build up of residual strain. One model that accounts for cycling and inner hysteresis loop behavior is the trigger-line model shown in Figure 2-9. Müller and Huibin (1991) provide a micromechanics-based constitutive model that explains the formation of inner hysteresis loops based upon the onset of unstable phase equilibrium between the austenite and martensite phase defined as the diagonal "trigger-line" in Figures 2-9(b) and 2-9(c). The result is a model that accounts for cyclic effects by defining the start of the martensite transformation as the point at which the state variables cross the trigger-line during loading and defines the start of the reverse transformation as the point at which the state variables cross the trigger-line during unloading.

Phenomenological models can be created based on this trigger-line theory. Thomson et al. (1997) presents a phenomenological model based on both a bilinear outer hysteresis loop as well as one constructed from an experimental database. The effect of variations in the trigger-line angle are also studied with a zero degree angle corresponding to hysteresis loops that have the same forward and reverse transformation stress as the outer hysteresis loop. The results show that the phenomenological model which has an outer hysteresis

based on an experimental database provides the most accurate results, but separate trigger-lines for both the loading and unloading plateau may prove to be more accurate (Figure 2-9(c)). A similar model is implemented in a study by Masuda and Noori (2002). Although phenomenological models have been shown to provide reasonably accurate results in many applications, continued work needs to be done in terms of strain rate effects, fatigue effects, and cyclic effects.

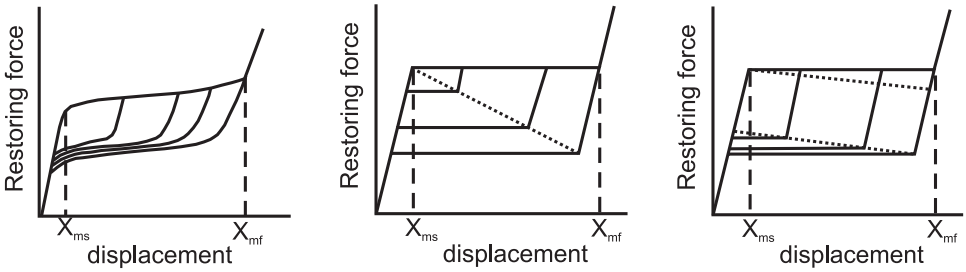

2-9(a): **2-9(b):** **2-9(c):**

Figure 2-9: (a) Typical cyclic force-displacement curve of SMA elements (b) single trigger-line models of Muller and Xu and (c) multiple trigger-line models of Thomson et al. (Masuda and Noori, 2002)

2.4 Structural and Seismic Applications of Shape Memory Alloys

As seismic design has increased focus on adopting approaches which control both the form of inelastic behavior and the location where it occurs, new and innovative devices have been developed to provide high energy dissipation within the structure while avoiding inelastic behavior in the lateral force resisting system (Martínez-Rueda, 2002). The unique properties of SMAs have led to the belief that they can be used to reliably control the response of

a structure during a seismic event. Research into the use of SMAs for structural and seismic applications began in 1991 with an initial study by Graesser and Cozzarelli (1991) who studied the behavior of NiTi SMAs to be used for seismic isolation applications due to their ability to provide supplemental damping. Since then, several other researchers have proposed the use of both NiTi and Cu-based SMA dampers for civil engineering applications based on studies of their cyclic behavior (Casciati and Faravelli, 2004; Hodgson, 2002; Tamai and Kitagawa, 2002; Torra et al., 2004; VanHumbeeck and Liu, 2000). Research into the behavior of both wire and large diameter NiTi bars undergoing cyclic loadings has been undertaken by DesRoches et al. (2004). Contrary to previous beliefs, the results suggest that good superelastic behavior can be obtained from large diameter NiTi bars which may be required for some structural applications.

One of the most significant undertakings in regards to exploiting SMAs for applications in structural systems is the MANSIDE Project (Memory Alloys for New Seismic Isolation and Energy Dissipation Devices) conducted by the European Union. As part of the MANSIDE Project, work has been completed in determining the mechanical behavior of martensite bars and austenite wires (Dolce and Cardone, 2001), developing and testing an SMA-based brace which can be configured to provide recentering, energy dissipation, or both (Dolce et al., 2000), and performing shake table tests on a scaled reinforced concrete frame with and without SMA braces (Dolce et al., 2005). A schematic of the bracing system used for the shake table tests and the behavior of the second floor brace can be seen in Figure 2-10. The results suggest that SMA braces are comparable to conventional bracing systems, but further efforts must be made to develop design criteria.

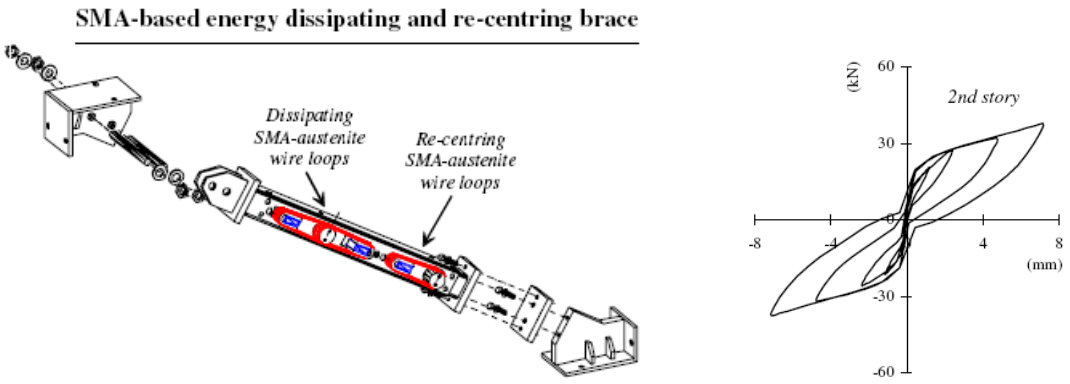

Figure 2-10: (a) SMA energy dissipating brace and (b) cyclic behavior of the SMA brace (Dolce et al., 2005)

A number of other analytical (Baratta and Corbi, 2002; Bruno and Valente, 2002; Han et al., 2003; Masuda and Noori, 2002; Sweeney and Hayes, 1995) and experimental (Clark et al., 1995; Han et al., 2005; Higashino et al., 1996) studies on SMA dampers have been conducted with typical building applications focusing on bracing systems or sacrificial damping devices at each floor level. SMA braces have been shown to increase vibration decay compared to an unbraced structure (Han et al., 2003), but have not always shown significant improvement when compared to other conventional bracing systems (Bruno and Valente, 2002). The other main applications of SMAs in building systems is as components in base isolation systems where both the recentering capability and energy dissipation can be taken advantage of to effectively decouple the building from the foundation (Corbi, 2003; Renzi et al., 2004).

As in building systems, studies have also suggested the use of SMAs in base isolation for bridges. Wilde et al. (2000) proposed a new isolation system which combined both laminated rubber bearings and SMA bars to provide both damping and isolation between the

pier and superstructure of a bridge. The analytical results show that the proposed isolation system attenuates damage energy more effectively than conventional lead-rubber systems. Alternative bridge dampers, which provide energy dissipation and create a self-repairable system, have been developed by Adachi and Unjoh (1999). Another bridge application of SMAs is as restrainers to prevent unseating of the bridge deck from the pier (Andrawes and DesRoches, 2005; DesRoches and Delemont, 2002). Analytically, the SMA restrainers are found to be more effective at preventing unseating of bridge decks during an earthquake as compared to conventional steel restrainers.

As the use of SMAs in building systems and bridge systems has gained interest, more innovative strategies taking advantage of their unique properties have been conceived. Semba et al. (2005) proposed single-stage TiNi SMA bellows for seismic isolation applications. The ability of partially restrained beam-column connections using SMA rods to limit inter-story drift angles and maximum column rotation has been considered by Ocel et al. (2004). Tamai et al. (2004) has suggested the use of SMA rods for anchoring column base plates in order to prevent deterioration of the restoring force due to large rocking displacements at the foot of building frame structures during an earthquake. Figure 2-11 provides a schematics of both the proposed partially restrained beam-column connection and the SMA column base. An innovative SMA damper system has also been investigated for stay cables in bridges (Li et al., 2004). Although considerable progress has been made in terms of developing devices to take advantage of the unique properties of SMAs in structural systems, there are only a few cases where such devices have been implemented including the Basilica of St. Francis of Assisi in Italy (Croci, 2001), the St. Feliciano Cathedral in Italy

(Castellano et al., 2001), the St. Giorgio Church bell-tower in Italy (Indirli et al., 2001), and the US-31 bridge in Michigan (Soroushian et al., 2001).

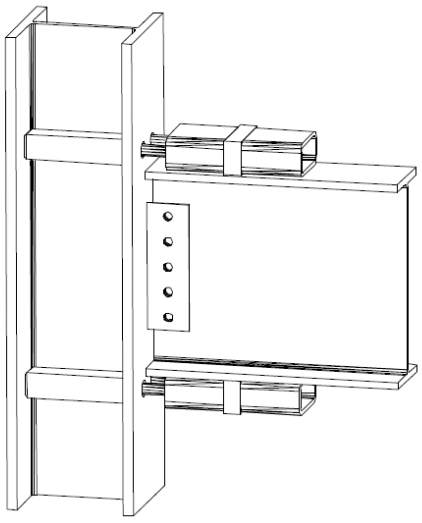

2-11(a):

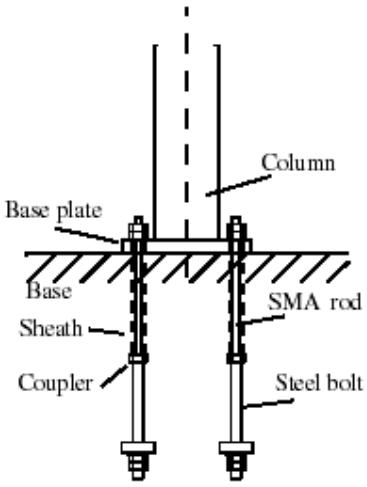

2-11(b):

Figure 2-11: Schematics of (a) SMA partially restrained beam-column connection (Leon et al., 2001) and (b) SMA exposed-type column base (Tamai et al., 2004)

2.5 Closure

Shape memory alloys are unique materials in that they can undergo large deformations while reverting back to their original shape as a result of a diffusionless martensitic phase transformation. Research into the behavior of SMAs has been conducted on several levels and promise has been shown for their use in structural seismic applications, but there remains a lack of cohesion between studies conducted by those in the materials field and those in the civil engineering field. There also exists a lack of knowledge of the properties of large diameter SMAs under typical earthquake loadings in terms of both loading rate

and strain level. This has limited the use of SMAs in actual applications. The following chapters address some of these gaps in knowledge and apply these findings to some specific seismic applications of SMAs.

CHAPTER III

MATERIAL AND MECHANICAL CHARACTERIZATION OF LARGE DIAMETER NITI

3.1 Introduction

Shape memory alloys, especially superelastic NiTi, have significant potential in structural engineering applications for structural vibration control as suggested by past research. The National Science Foundation workshop on intelligent structures and systems lauded the use of SMAs in civil structures (Rogers, 1995), while the Subcommittee on Disaster Reduction cited the continued development of smart structural systems in order to mitigate the effects of both natural and manmade disasters (NSTC, 2005). To date, the majority of the current research into structural applications of SMAs has focused on wire and thin plate specimens which have shown good behavior under seismic-like strain histories (Dolce and Cardone, 2001), but may be uneconomical due to added complexity in designing a system which requires looping of a significant number of wire strands. As a result, the actual implementation of SMA systems has been limited to the few cases described in Section 2.4. The use of larger diameter NiTi sections may prove to be economically more convenient and easier to implement because of the minimal number of bars necessary to achieve the required strength and stiffness for structural applications and the ability to resist compressive loads. An added benefit associated with larger diameter sections is the ease in which a single bar

can be replaced, as compared to looped wire strands, if necessary after an earthquake. Although the use of large diameter SMAs appears to be beneficial, there is little knowledge of the performance or property optimization of large diameter NiTi SMAs other than the study by DesRoches et al. (2004). Likewise, some efforts have been made to characterize the microstructure of large diameter specimens, but these findings have yet to be related to the macroscopic properties important for structural engineering applications.

This lack of effective knowledge transfer across materials science and structural engineering fronts has also contributed to hindering widespread exploitation of NiTi for structural applications. Materials research on NiTi SMAs typically falls into either one of two broad categories, materials and mechanics. Materials studies have been preoccupied with specifics associated with the phase transformation and microstructure, while mechanics studies have primarily focused on constitutive modeling and understanding the unique thermo-mechanical coupling in SMAs. These studies have led to considerable progress over the last 30 years in understanding NiTi SMAs. However, the resulting vast database of material science literature has made it difficult to interpret the absolutely necessary information for creating applications using SMAs, particularly for researchers and engineers unfamiliar with crystallography and electron microscopy. The mechanics models also may be impractical for use by research and design engineers in safety critical engineering structures. On the other hand, the unique requirements of materials and components for building and bridge structures in seismically active areas are unfamiliar to those researchers in material science. As a result, there exists a need to fundamentally link the work of both fields so that the behavior of NiTi SMAs can be predicted and optimized for a given application

and accurate, but viable, models developed to allow for confident use within the structural engineering community.

This chapter presents a multi-scale analysis of NiTi SMAs intended for use in structural engineering applications to address the limited knowledge with respect to the behavior of large diameter specimens and lack of knowledge transfer between material scientist and structural engineers. This work provides a fundamental and hierarchical link between the nanometer scale structure of NiTi SMAs and the mechanical behavior of full-scale large diameter specimens. The results are presented from both a material science and structural engineering point of view in order to maintain a unified vision and partially address the lack of effective knowledge transfer between the two fields enabling a means of more rapid implementation of NiTi SMAs in structural engineering applications. A basic materials characterization is first provided including nanometer sized precipitate characterization, grain size analysis, texture measurements, transformation temperature measurements, and hardness quantification. A mechanical behavior study (tension only) is then performed to connect the materials characterization results to the macroscopic behavior and explore scaling effects associated with testing coupon specimens versus full-scale NiTi bars. Finally, the full-scale bars are cycled both quasi-statically and dynamically under loadings typical of an earthquake to provide the final connection between the material science and structural engineering fields while also evaluating the performance of the NiTi SMA bars for structural applications.

3.2 Material

Three sets of hot-rolled NiTi shape memory alloy bars are used for the large bar study. In order to prevent any biasing from composition differences, all of the NiTi bars are obtained from the same stock provided by a commercial supplier with a Ni-rich composition of Ti-50.90 at%Ni (Ti-55.95wt%Ni), where at%Ni refers to the atom percentage of Nickel and wt%Ni refers to the weight percentage of Nickel. Final hot rolling by varying degrees was used to produce bars of three different diameters. The manufacturing process consisted of first casting the NiTi in a steel mold followed by Vacuum Induction Melting (VIM) and Vacuum Arc Remelting (VAR) in a graphite crucible resulting in 35.6 cm diameter cast ingots. The ingots were then hot forged at 935 °C down to a 16.8 cm rough-cut-size slab which underwent further hot rolling at 935 °C to produce a 50.8 mm rough-cut-size slab. The final bar diameters of 31.8 mm, 19.1 mm, and 12.7 mm were then obtained through precision hot rolling at 935 °C. The bars were left oversized by approximately 1 mm to allow for final grinding to remove surface material. After the final hot rolling, the bars were straightened at 600 °C, coarse centerless ground, re-straightened, and then subjected to a final centerless grind. The lengths of the 31.8 mm, 19.1 mm, and 12.7 mm bars are 26.7 cm, 16.5 cm, and 15.2 cm, respectively. "As-received" is used to refer to the bars received from the manufacturer which have undergone no further machining and heat treatment than that described above. The 19.1 mm and 12.7 mm as-received bars can be seen in Figure 3-1, which also contains the coupon specimens and machined bars used for the mechanical behavior study. Details in regards to the dimensions of the bars are given in Figures 3-2 and 3-3.

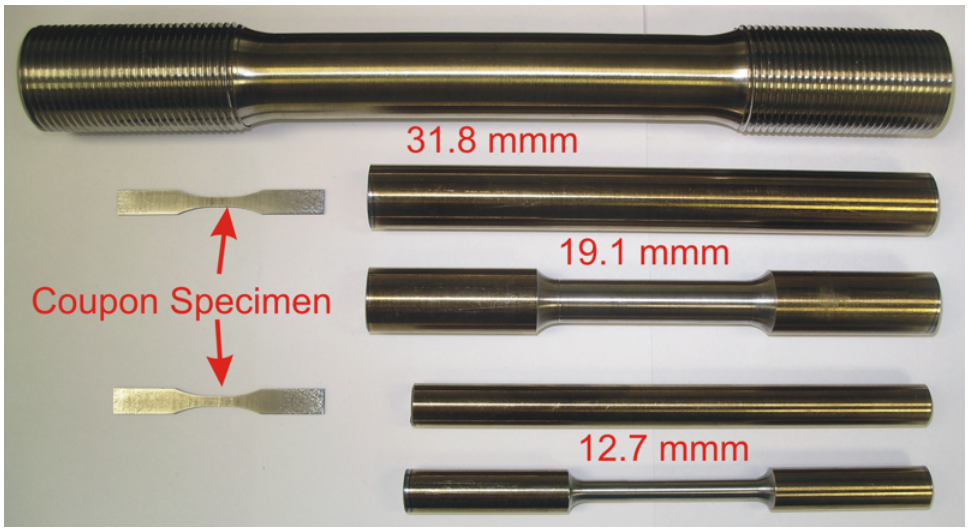

Figure 3-1: Photograph of representative as-received bars (19.1 mm and 12.7 mm), full-scale bars ((31.75 mm, 19.05 mm, 12.7 mm), and coupon specimens.

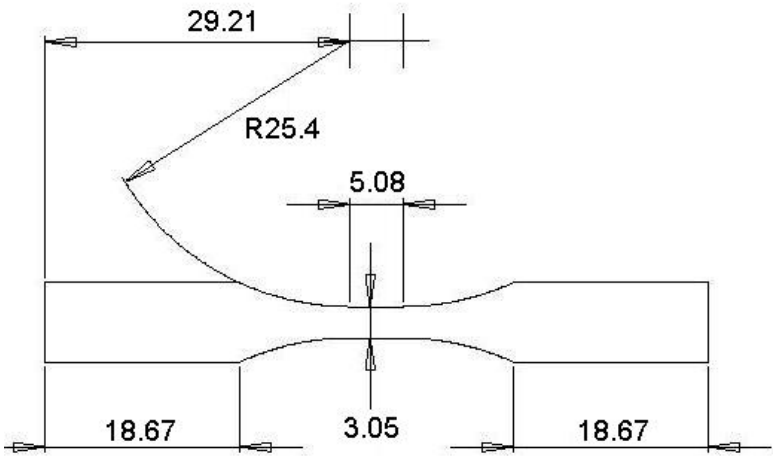

Figure 3-2: Drawing of the coupon specimen with dimensions labeled in mm.

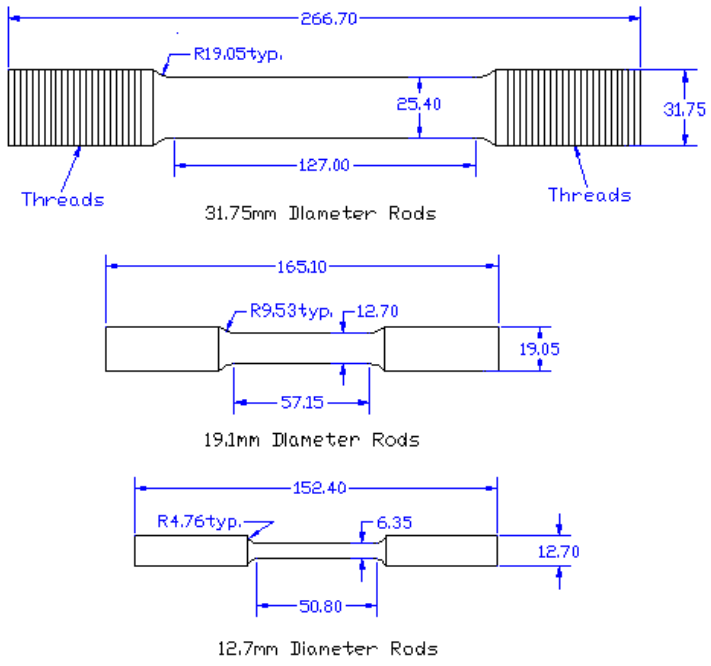

Figure 3-3: Drawings of the full-scale bar specimens with dimensions labeled in mm.

3.3 Material Characterization

To date, a significant amount of materials research on NiTi SMAs has been completed, but challenges still remain for mechanics researchers and engineers wishing to implement NiTi in new devices. In particular, many of these challenges lie with the characterization of large diameter sections. Heat treatment of NiTi SMAs has historically been used to set desired transformation temperatures. As a result, much of the literature, other than recent work by Frick et al. (2005), regarding heat treatment procedures focuses on the transformation temperature without regard for the resulting mechanical properties. It has also long been suggested that cold drawing is necessary to provide good shape recovery properties in larger diameter sections, but the work by Frick et al. (2005) and Ortega et al. (2005)

has shown good recovery in both hot rolled and as-cast NiTi, respectively. However, it is still unknown whether hot-rolled large diameter section can provide the desired properties for structural applications through precipitation hardening. This materials characterization addresses these areas by providing insight into the multi-level structure of the NiTi with respect to various heat treatments and bar sizes for NiTi whose mechanical behavior is later studied. Effects of scaling specimens to large diameters is also considered. These results provide the first step to linking the work of material scientist to the need of structural engineers

3.3.1 Methods

For the materials characterization, selected as-received bars underwent an "industry anneal" consisting of a 350 °C heat treatment for 0.5 hours followed by air cooling. The industry anneal is a standard heat treatment used to provide superelastic properties. Some of the industry annealed specimens are given a further heat treatment of 300 °C for 1.5 hours and then immediately water quenched. This added heat treatment of some of the industry annealed bars is consistent with the two part heat treatment which is used for the bars in the subsequent mechanical behavior study. In order to systematically study the effect of heat treatment on material structure, hardness, and transformation temperature and provide a reference for the industry anneal and two-stage anneal, selected as-received specimens of each size bar are heat treated at 300 °C, 325 °C, 350 °C, and 375 °C for 1.5 hours and immediately water quenched. Heat treatment temperatures are kept below 400 °C to ensure superelastic behavior (Frick et al., 2005), while the 1.5 hour time frame is chosen to

eliminate material variability associated with shorter times due to increased sensitivity to exposure time and heat treatment characteristics.

The material characterization of these NiTi bars as a function of the amount of deformation processing (bar size) and heat treatment includes nanometer sized precipitate characterization, grain size analysis, spatial crystallographic texture measurements, transformation temperature measurements, and hardness quantification. The materials characterization presented is done in collaboration with members of the Materials Science and Engineering Department at the Georgia Institute of Technology and the Material Science Department at the University of Paderborn in Paderborn, Germany.

A Philips CM200 transmission electron microscope (TEM) operated at 200 kV is utilized to characterize the microstructures. For the TEM work, 1 mm slices are cut from the bars using a slow-speed saw. The slices are mechanically ground and polished down to a 0.15 mm prior to final twin-jet electropolishing. The electrolyte employed to obtain electron transparent TEM foils consists of a 5% perchloric acid and 95% ethanol solution and electropolishing is conducted at 35 V and $-15\,^{\circ}$C. All TEM bright-field images presented in the following are recorded under two-beam conditions. Selected area diffraction patterns shown as insets with the TEM images are obtained after tilting the foil to a low-index zone axis.

Automated electron backscatter diffraction (EBSD) using a TSL system attached to a scanning electron microscope yielded spatially resolved crystallographic orientation information. For the EBSD work, the samples are electropolished using the same electrolyte used for the TEM study. It should be noted that residual martensite is sometimes present in samples after low temperature electropolishing if the difference between austenite finish

temperature and room temperature is small. Thus, all texture data presented in the following is for the B2 austenite phase only, i.e. any residual martensite present in the samples was excluded from the analysis.

The transformation temperatures for the various aging treatments on the different diameter bars are measured using a TA Instruments^{TM} Q100 Differential Scanning Calorimeter (DSC). All DSC samples are cut using a water cooled, slow speed diamond wafer blade saw and mounted in high purity aluminum sample pans. The DSC cycle is performed using the following temperature history: 1 min at 20 °C, cool to −70 °C at 10 °C/min, hold for 2 min at −70 °C, heat to 150 °C at 10 °C/min, hold for 2 min at 150 °C, and cool to −70 °C at 10 °C/min.

Hardness measurements are performed using an automated Rockwell C hardness machine calibrated using a steel standard. Thin 2.0 mm slices are extracted from each bar by electro-discharge machining, then given the appropriate heat treatment and polished to a flat finish using 600-grit sandpaper. Measurements (n=5) are performed at the bar center and four $\frac{1}{2}$ radial points for each of the hot rolled bar diameters. The as-received, systematically heat treated, industry annealed, and industrial annealed with the additional 300 °C for 1.5 hours are tested. Hardness values as a function of bar spatial location are statistically the same. Therefore, the values for the entire bar are averaged and presented as one data point with a standard deviation. The results are then plotted with respect to the various diameters and heat treatments.

3.3.2 Nanometer Scale: Effects of Precipitates

Most commercial NiTi alloys, including those studied here, contain excess Ni on the order of 0.1 to 1.0 at% making them Ni rich intermetallic alloys. As suggested by the phase diagram shown in Figure 2-6, Ni rich alloys subjected to elevated temperatures for a sufficiently long time precipitate a coarse $TiNi_3$ phase through a diffusion based process. However, prior to this precipitation process taking place, researchers have discovered the formation of metastable Ti_3Ni_4 as mentioned in Section 2.2.2.1 (Gall et al., 1999c,d, 1998). Although these precipitates do not undergo the martensitic phase transformation, they greatly enhance the thermo-mechanical properties of NiTi. Certain size precipitates assist the martensitic phase transformation and hinder dislocation movement thereby promoting the reverse phase transformation and recentering properties (Allafi et al., 2002; Gall et al., 1999c,d, 1998; Michutta et al., 2004). Since precipitation hardening is the only process dominating during low temperature heat treatment of hot rolled alloys, heat treating can be used to obtain pseudoelastic properties and hardness comparable to more expensive cold drawn alloys (Frick et al., 2005). The TEM imaging is thus used to look at the precipitate structure in the hot rolled bars as a function of both bar size and heat treatment.

The TEM images in Figure 3-4 show the material structure at nanometer scales in the as-received bars of all three diameters. The inset diffraction patterns are slightly overexposed to highlight a slight streaking between primary reflections where the streaks indicate an extremely small volume of second phase precipitates. Figure 3-4(a) and Figure 3-4(b) are both images from the as-received 12.7 mm diameter bar where Figure 3-4(a) highlights a grain triple point and Figure 3-4(b) shows a high-resolution image. In the upper two grains,

no precipitates are visible and there is only a low dislocation density. Nothing can be inferred from the bottom grain as it is out of diffraction contrast. The high resolution image does show some very tiny precipitates, but too few to influence the specimens properties. The overexposed diffraction pattern inset in Figure 3-4(b) contains streaks between primary reflections confirming the presence of these precipitates. The TEM images for the 19.1 mm and 31.8 mm bars are shown in Figure 3-4(c) and Figure 3-4(d), respectively. The images also show a low dislocation density and extremely small volume fraction of tiny precipitates evident from the streaking in the inset diffraction patterns. In summary, the as-hot rolled materials possessed very similar nanometer scale structures defined by a low dislocation density and near absence of precipitates.

The influence of aging on the material structure at nanometer scales is investigated only in the bars with a 19.1 mm diameter since the initial structure of the as-received bars with different diameters is nearly identical suggesting that the amount of deformation processing does not influence the precipitate structure. Figure 3-5 presents representative images from the 19.1 mm diameter bar given various heat treatments. Figure 3-5(a) is from the material given the industry anneal (350 °C for 1.5 hours), demonstrating a significant fraction of very fine coherent precipitates distributed in the lower grain as evident by the dark spots. The top two grains are out of diffraction contrast for imaging of the precipitates. The diffraction pattern inset in Figure 3-5(a) confirms the presence of a second phase by the secondary spots surrounding the primary diffraction spots. Figures 3-5(b) to 3-5(e) are from the as-received materials aged for 1.5 hours at 300 °C, 325 °C, 350 °C, and 375 °C, respectively. All of the images and diffraction patterns demonstrate the presence of nanometer scale, distributed second phase precipitates. However, it is impractical with small representative

1 µm

3-4(a):

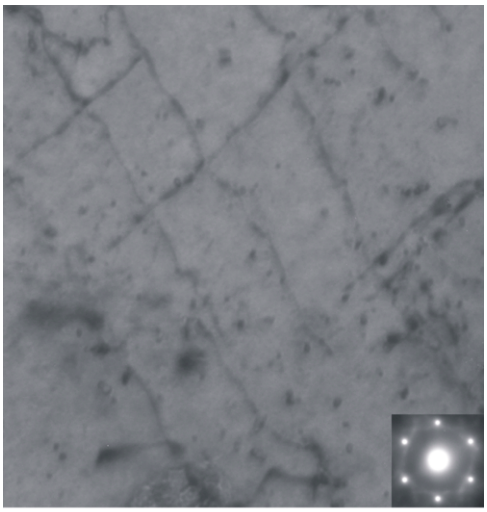

100 nm

3-4(b):

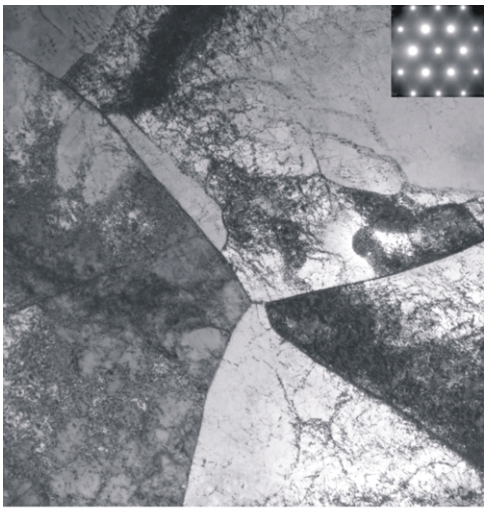

1 µm

3-4(c):

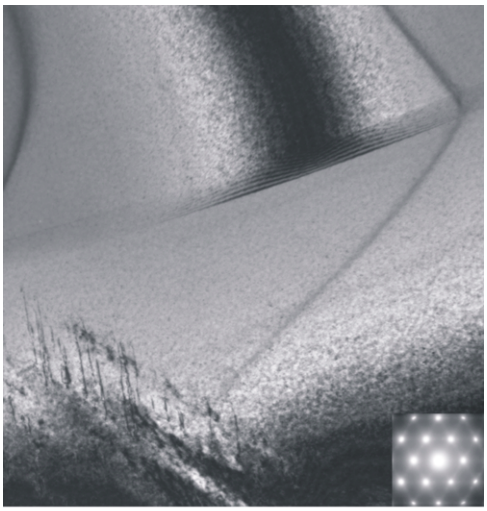

500 nm

3-4(d):

Figure 3-4: TEM images of the as-received bar structure at the nanometer scale: (a) 12.7 mm, (b) 12.7 mm high-resolution, (c) 19.1 mm, and (d) 31.8 mm.

TEM foils to detect a noticeable difference in the size of the precipitates. It is expected that the precipitates are slightly larger, on average, in the material given a higher temperature aging treatment as higher temperatures have a similar influence as increased heat treatment time promoting further growth of the precipitates. Figure 3-5(f)contains the TEM image of the material given the industry anneal plus a second heat treatment at 300 °C for 1.5 hours demonstrating a fine precipitated structure, similar to the other heat-treated materials.

The TEM analysis shows that the as-received materials contain almost no precipitates while the aged materials all contain distributed nanometer scale precipitates. The low dislocation densities in both the as-received and heat treated bars suggests that precipitation of second phase is the dominant factor in terms of aging effects in Ni-rich hot rolled NiTi alloys. It is extremely difficult to ascertain structural differences in the materials subjected to different aging treatment by TEM. However, hardness and thermal transformation measurements, presented in subsequent sections, are capable of distinguishing the influence of small changes in heat treatment on the material behavior.

3.3.3 Micrometer Scale: Grain Size and Orientation Effects

Both grain size and crystallographic orientation (texture) can influence the mechanical properties of materials. It has been recognized that a reduction in grain size results in an increase in strength due to dislocation pileup as a result of shorter grain boundaries. Likewise, the crystallographic nature of the martensitic transformation associated with superelasticity results in texture having a first order influence in NiTi. This influence of texture leads to extreme anisotropic behavior in tension and compression and stress-state dependence of

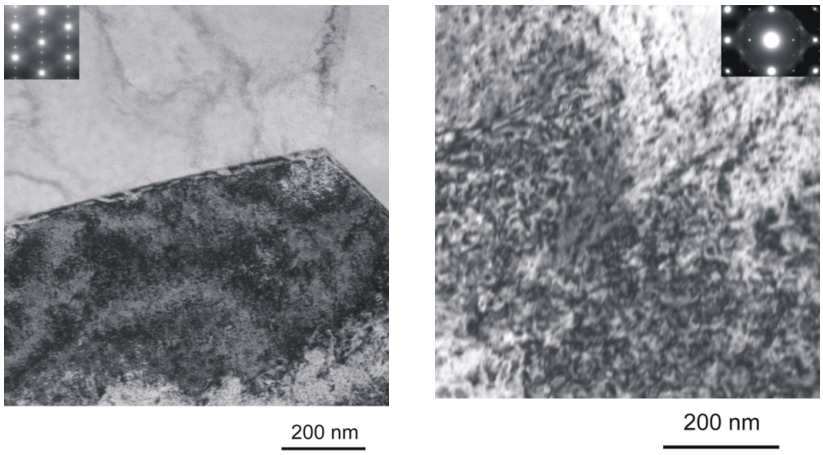

3-5(a):

3-5(b):

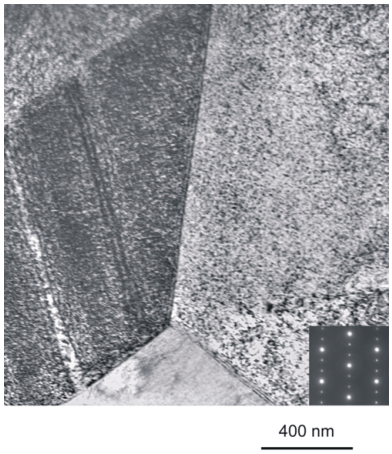

3-5(c):

3-5(d):

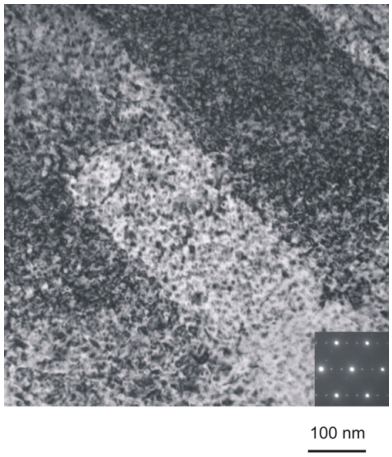

3-5(e):

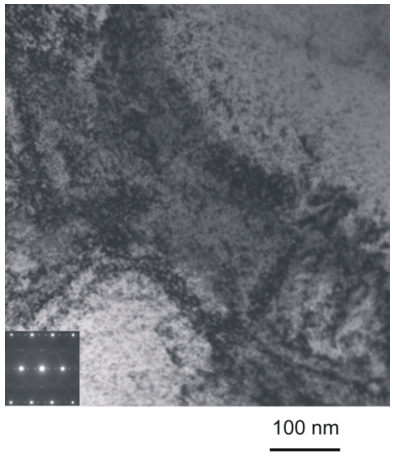

3-5(f):

Figure 3-5: TEM images of the nanometer scale structure of representative heat treated 19.1 mm bars:(a) industry anneal (350 °C for 0.5 h), (b) as-received + 300 °C for 1.5 h, (c) as-received + 325 °C for 1.5 h, (d) as-received + 350 °C for 1.5 h, (e) as-received + 375 °C for 1.5 h,and (e) industry anneal + 300 °C for 1.5h.

Table 3-1: Grain Size of the As-received Hot Rolled NiTi Bars as a Function of Bar Diameter and Location.

Average Grain Size (μm)	Bar Diameter (mm)		
	12.7	19.1	31.8
Center	38	33	52
1/2 Radius	39	39	45
Edge	32	34	58
Average	36	37	49

mechanical properties (Gall and Sehitoglu, 1999b; Gall et al., 1999a). Although, the magnitude of this influence can be diminished as a result of precipitation hardening discussed in Section 3.3.2. As mentioned, this study uses automated electron backscatter diffraction to create a spatial distribution of texture and grain size in the large diameter NiTi bars. This data is previously unavailable and is important in detecting both grain size and texture gradients across these specimens as a result of different amounts of deformation processing leading to possible scaling effects. Since crystallographic texture in NiTi is unaltered by low temperature aging, EBSD measurements are only taken of the as-received bars.

The grain size data from in Table 3-1 indicates, on average, that increased reduction via deformation processing reduces overall grain size, as expected. Specifically, the average grain size in the 12.7 mm bar is 36 μm while the average grain size in the 31.8 mm bar is 49 μm. The trends in average grain size as a function of bar location are less clear and do not follow a definitive trend. The grain sizes in large diameter cold drawn bars (Frick et al., 2004) are on the order of the sizes presented in Table 3-1 for the hot rolled bars, thus cold rolling does not produce a very significant decrease in grain size.

Figure 3-6 presents a representative map of grain orientations from a section of the 31.8 mm diameter hot rolled bar. The scale on the lower right indicates the size of the grain

orientation reconstruction while the stereographic triangle on the left indicates the orientation of various grains based on color. The map is constructed to show the orientation of the grains parallel to the rolling (long) axis of the hot rolled bar. The color of each grain in Figure 3-6 corresponds to that grains orientation based on the stereographic triangle. For example, the darkest grains (blue and dark purple in color) have a <111> orientation parallel to the rolling axis, while grains in the mid-gray range (dark red in color) have a <001> orientation parallel to the rolling axis. Intermediate colors represent crystal orientations angled away from the three standard low index poles, <111>, <001>, and <101>. Comparison of the stereographic triangle in Figure 3-6 with a more extensively labeled stereographic triangle is necessary to identify other orientations. From visual inspection, the dominant texture along the rolling axis is of the <111> type.

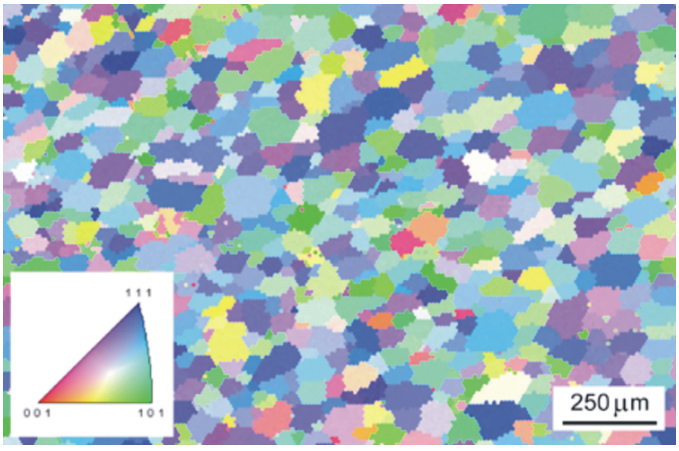

Figure 3-6: Grain orientation map from the center of the 31.8 mm diameter bar created using EBSD

The stereographic triangles shown in Figure 3-7 provide grain orientation information measured at the center, $\frac{1}{2}$ radius, and edge of each of the three as-received bar diameters. In this case, the colors shown in the stereographic triangles represent the density of a given grain orientation with darkest color (blue in color) corresponding to a low relative density of a given grain orientation and the dark grey at the top of the legend (red in color) corresponding to a high relative density. In all cases, there is a relative absence of <110> grains parallel to the rolling axis and a strong <111> texture component similar to that seen in Figure 3-6. A secondary <101> component is also present, particularly at the center of each of the bars. The presence of this secondary component increases with increased deformation processing (decreasing bar diameter) and position with the center of the 12.7 mm diameter bar being dominated by a <101> texture component. The dominant average texture is the <111> type, which is consistent with previous x-ray measurement results (Frick et al., 2005). In terms of relating strain recovery to texture, it should be noted that the grains in the <100> orientation show minimal strain recovery in tension, grains in the <111> orientation show good shape recovery in tension and poor recovery in compression, and grains in the <110> orientation also show good strain recovery in tension (Gall and Sehitoglu, 1999b; Gall et al., 1999a).

3.3.4 Thermal Transformation Behavior

Differential scanning calorimetry (DSC) is the most common method used to characterize NiTi SMAs by researchers, engineers, and commercial suppliers. Essentially, DSC measures heat flow as a function of temperature and provides an indication of the transformation temperatures of the material as it goes through endothermic and exothermic solid-state

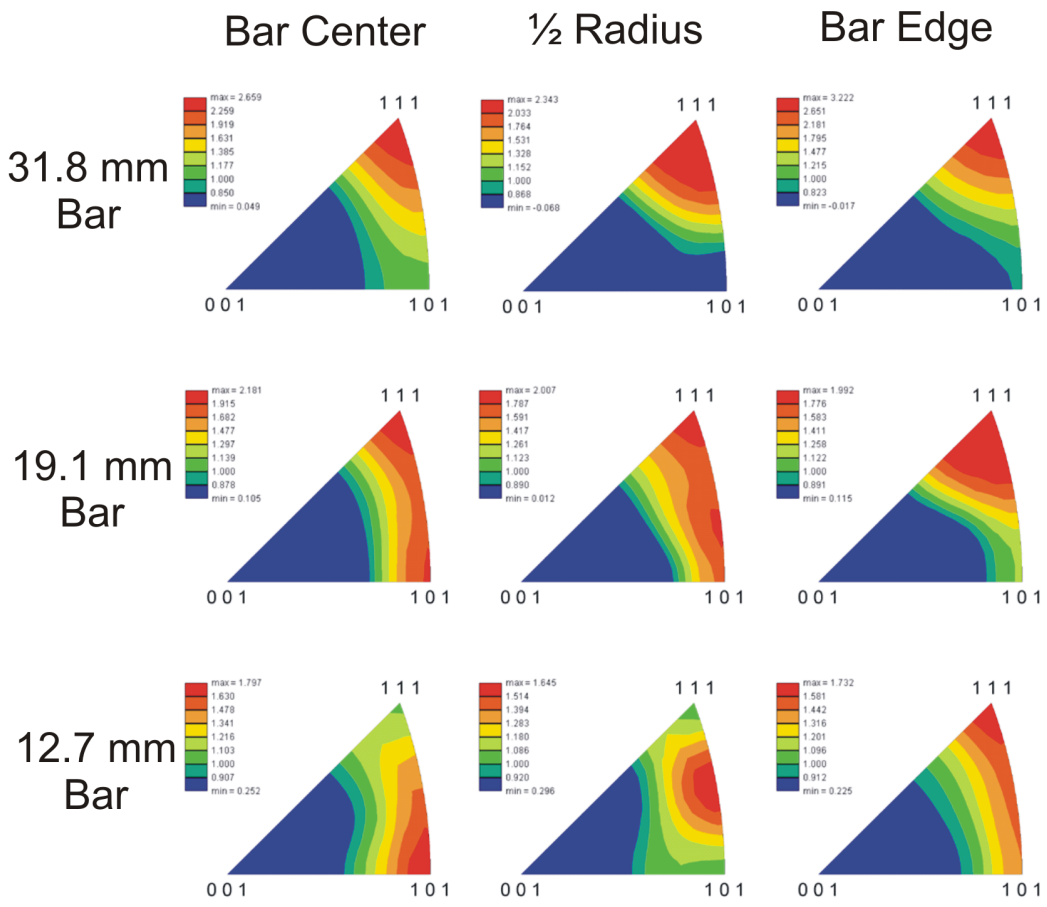

Figure 3-7: Matrix of stereographic triangles providing the crystallographic texture parallel with the drawing direction as a function of bar size and radial position.

phase transformations. Since transformation temperatures are so sensitive to alloy composition, and composition measurements at 0.1 at% levels of accuracy are difficult, most standards suggest DSC as the best method to infer the composition of NiTi SMAs. The transformation temperatures are critical because their location relative to the testing temperature determines if the material undergoes the shape memory effect or the superelastic effect. The transformation temperatures of Ni-rich NiTi alloys are particularly sensitive to heat treatment since precipitate size strongly influences the thermodynamics of the transformation (Allafi et al., 2002; Gall et al., 1999a,c,d, 1998; Michutta et al., 2004). It is possible to move the transformation temperatures in a Ni-rich material nearly 50 degrees by aging treatment alone (Frick et al., 2005). DSC measurements are used to study the effect of aging treatment on thermal transformation behavior in hot-rolled NiTi bars. Aging treatments in this study are limited to those that produce a superelastic material at room temperature (25 °C).

Figure 3-8 contains DSC results for the hot-rolled bars as a function of bar diameter and heat treatment. As labeled on Figure 3-8(a), for all graphs cooling data is presented on the bottom of the curve while heating data is presented on the top of the curve. In addition, heat flow is defined so that exothermic reactions produce a downward peak, while endothermic reactions produce an upward peak. The as-received bars all demonstrate a one-step forward (M $<-$ A) and reverse (M $->$ A) primary martensitic transformation upon cooling and heating, respectively, Figure 3-8(a). The reverse transformation temperatures are below 0 °C, so the as-received material demonstrates superelasticity at room temperature. The forward transformation temperature, or the so-called martensite start temperature, M_s, is near -50 °C for the smaller bars and slightly higher for the largest bar as shown in Figure

3-8(a). The results in Figure 3-8(a) also show a slight decrease of M_s in the as-received condition for the hot rolled bars given more deformation processing.

It should be noted that the formation of precipitates can lead to a so called multi-step transformation, which tends to complicate the DSC results due to the presence of two or three peaks during cooling and heating (Allafi et al., 2002; Michutta et al., 2004). A two-step transformation can be seen in the heat treated specimens as a result of the presence of precipitates shown in the TEM images. The formation of the R-phase between the austenite phase and primary martensite phase can be identified on the DSC curve by its relatively high temperature hysteresis, sharp peak (small transformation enthalpy), and small temperature hysteresis. Also, the primary martensitic transformation becomes difficult to measure because of its occurrence at lower temperatures and large temperature hysteresis resulting in very diffuse peaks. The DSC equipment used in this study does not have the capacity to go below $-50\,^{\circ}$C. Although as aging temperature increases, the DSC equipment is capable of measuring the primary martensitic transformation in the smaller bars (see Figures 3-8(e) and 3-8(f)).

Figure 3-8(e) contains labels for all transformations, and similar transformations occur for all materials when the primary martensite transformation temperature is in the DSC instrument range. In Figure 3-8(e), R $<-$ A indicates the forward Austenite to R-phase transformation, M $<-$ R indicates the forward R-Phase to Primary Martensite transformation, M $->$ R indicates the reverse Primary Martensite to R-phase transformation, and R $->$ A indicates the reverse R-phase to Austenite transformation. The industry anneal of $350\,^{\circ}$C for 0.5 hours results in the appearance of a R-phase transformation near $25\,^{\circ}$C and a martensitic phase transformation that occurs just under $50\,^{\circ}$C, Figure 3-8(b). The

R-phase transformation is a known signature of a precipitated structure in NiTi (Nishida and Wayman, 1988). This is confirmed by the lack of R-phase peaks in the DSC results for the as-received material which showed only minimal precipitates in the TEM images. For all heat treatments, similar R-phase peaks are observed. The location of the R-phase peak does not depend strongly on aging temperature, and thus is not a good indication of the material structure or behavior other than the general presence of precipitates.

The primary martensitic transformation occurs in all of the materials in the vicinity of $-50\,^{\circ}$C. The precise location of the M_s temperature depends primarily on heat treatment. An increase in aging temperature shifts the M_s temperature from below $-50\,^{\circ}$C (barely distinguishable in Figure 3-8(c)) to above $-50\,^{\circ}$C (clear in figure 3-8(f) for all three bar diameters). In addition, there is a slight dependence of the transformation temperatures on bar diameter inherited from the behavior of the as-received bars, which demonstrated a higher M_s for the largest (less worked) bar. The largest bars (solid line in Figures 3-8(c)-3-8(f)) usually have a slightly higher M_s temperature. However, the effect of aging temperature on transformation temperatures is more significant and reproducible than the influence of bar diameter. The industry anneal ($350\,^{\circ}$C for 0.5 hours) material demonstrates a DSC response similar to the material aged at $325\,^{\circ}$C for 1.5 hours. The material given the industry anneal ($350\,^{\circ}$C for 0.5 hours) plus a subsequent $300\,^{\circ}$C treatment for 1.5 hours demonstrated DSC behavior in between the material heat treated for $325\,^{\circ}$C for 1.5 hours and the material heat treated for $350\,^{\circ}$C for 1.5 hours. This result is inline with the fact that precipitate sizes is a key controlling feature in the DSC response.

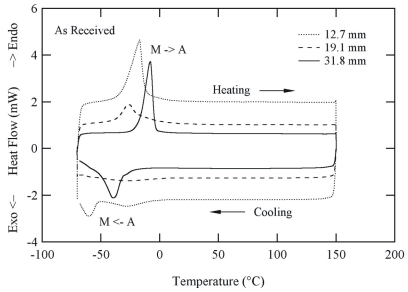

3-8(a):

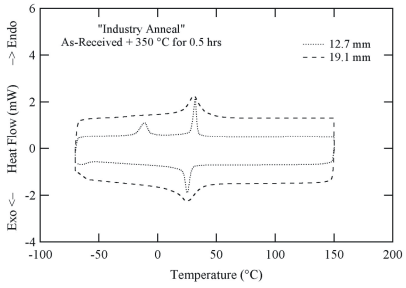

3-8(b):

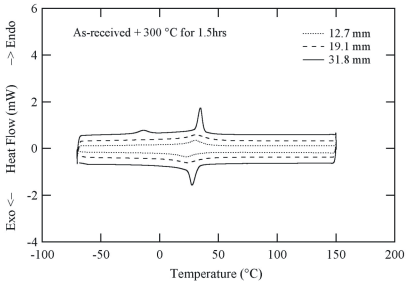

3-8(c):

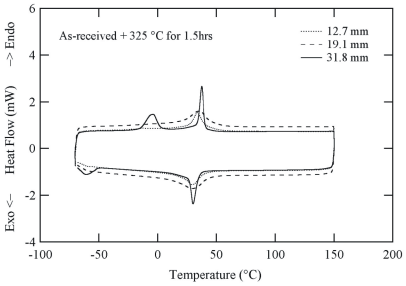

3-8(d):

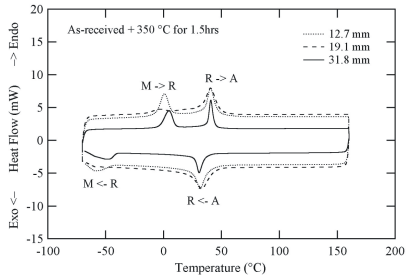

3-8(e):

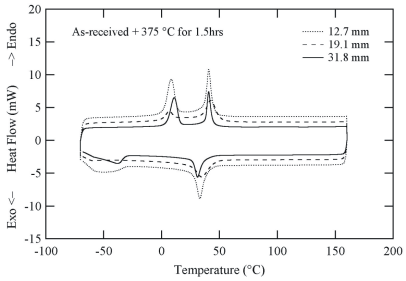

3-8(f):

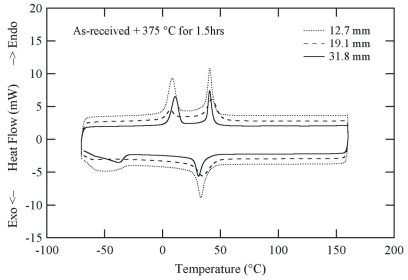

3-8(g):

Figure 3-8: DSC results showing transformation temperatures as a function of bar size and heat treatment: (a) as-received, (b) industry anneal (350 °C for 1.5 h), (c) as-received + 300 °C for 1.5 h, (d) as-received + 325 °C for 1.5 h, (e) as-received + 350 °C for 1.5 h, (f) as-received + 375 °C for 1.5 h, (g) industry anneal + 300 °C for 1.5 h.

3.3.5 Material Strength

Since the main objective is to determine the potential of using large diameter NiTi SMAs in structural applications, determining the effect of bar size and heat treatment on them is extremely important. One of the easiest ways to measure strength without actually performing uniaxial deformation tests is through hardness measurements. Hardness is an especially useful tool in age-hardenable metal alloys, such as hot-rolled NiTi, since they undergo predictable changes in hardness with respect to precipitate size and distribution allowing hardness to be related to the heat treatment parameters. As such, hardness can be used to reliably assess the effect of heat treatment in age-hardenable alloys.

The hardness results (Rockwell C) are presented in Figure 3-9 as a function of bar diameter and heat treatment. The hardness results are based on the average of 5 measurements, one taken from the bar center and four taken at the equiangular $\frac{1}{2}$ radial points. The average hardness of the as-received bars remained low, approximately 32 +/- 1 HRC due to the presence of only tiny precipitates as suggested by the TEM images of the as-received bars. Comparing the hardness results for the as-received bars which underwent heat treatments between 300 °C and 375 °C for 1.5 hours, a trend of decreasing hardness with increasing annealing temperature is seen. The mean maximum hardness values (associated with the 300 °C for 1.5 hours heat treatment) range between 39 to 41 HRC, which is a 25% increase compared to the untreated as-received bars. All of the heat-treated bars considered in this study possessed hardness values higher than the as-received bars, consistent with the TEM observations of coherent precipitates upon aging and basic theories of precipitation

strengthening. No significant trend is apparent with respect to the amount of deformation processing.

The hardness of the NiTi (averaged for all bar diameters) after a standard "Industry Anneal" performed at 350 °C for 0.5 hours is in the same range as the hardest bars heat treated for 1.5 hours at 300 °C and 325 °C, Figure 3-9. Bars with the Industry Anneal that are subsequently treated for 1.5 hours at 300 °C, demonstrated a slight drop in hardness, but remained statistically in the range of the hardest bars tested. Two-step aging treatments are sometimes used with NiTi for shape setting followed by subsequent property tailoring. The results in Figure 3-9 demonstrate that aging in the range of 300 °C to 350 °C can be used to achieve relatively hard NiTi, an advantage for high cycle fatigue resistance. Since the hardness approaches the as-received values with increased heat treatment temperature, shorter heat treatment durations are necessary to maintain high strengths. However, as suggested previously, shorter heat treatment durations can also increase variability in the material and mechanical properties.

3.3.6 Material Characterization Summary

The materials characterization study provides insight into the structural features at various scales of large diameter deformation processed NiTi bars. The results suggest a strong influence of these features on the functional properties of NiTi used in structural engineering applications. The TEM results reveal the presence of precipitates after heat treatments. The influence of these precipitates is clearly present in the DSC and hardness values where the transformation temperature and strength vary with different heat treatment temperatures. Further, smaller precipitate sizes tend to also reduce the amount of residual plasticity and

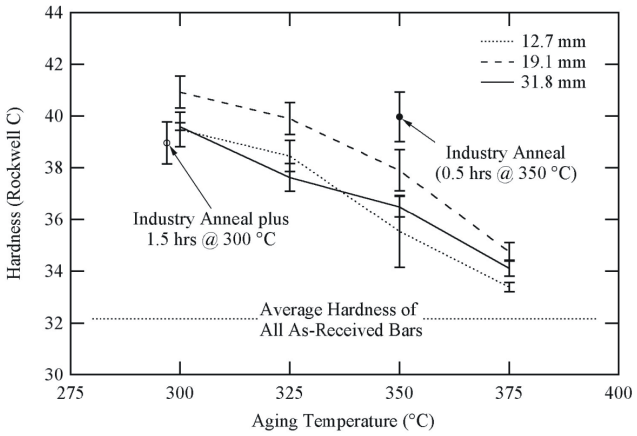

Figure 3-9: Hardness as a function of heat treatment and bar diameter with one standard deviation error bars.

thus ensure good recentering properties for structural applications. However, small precipitates do lead to smaller hysteresis loops and less energy dissipation. Thus, the results suggest that heat treatment can be used to tailor transformation temperatures (and consequently transformation stresses), strength, and recentering capability while also providing a template for determining the appropriate aging treatment for a given structural application using Ni-rich NiTi.

3.4 Monotonic Mechanical Behavior

In order to continue with the overall objective of optimizing NiTi SMA properties for structural applications and provide a link between the material characterization presented above and the macroscopic mechanical properties of large diameter SMA bars, the tensile behavior is studied until failure. These monotonic tensile tests provide some of the basic information required for structural applications in regard to the mechanical properties of large diameter NiTi, such as the initial elastic modulus, forward transformation stress, and

fracture load. These properties can then be related to the material characteristics and provide an introduction to the expected tensile cyclic behavior which must be understood for earthquake applications. Since monotonic tests are often used for the evaluation of other structural materials, the results of these tests also provide a means of comparing SMAs to other structural materials.

3.4.1 Methods

Both 19.1 mm and 12.7 mm diameter NiTi bars are used to study the monotonic tensile behavior. Because of expense and load frame requirements, the 31.8 mm NiTi bar is not tested monotonically. The 19.1 mm and 12.7 mm NiTi bars are obtained from the same batch of material used in the material characterization study (Section 3.3) and underwent the same deformation processing to their final diameters. By using specimens from the same batch, any variability in composition and during manufacturing is removed and a clear comparison between the macroscopic properties and material characterization can be made. Since NiTi suppliers usually provide specimens which are heat treated, all specimens used during both the monotonic testing and the subsequent cyclic tests underwent the standard superelastic "industry anneal" provided by the manufacture consisting of a heat treatment of 350 °C for 0.5 hours followed by air cooling. A second heat treatment of 300 °C for 1.5 hours and immediate water quenching is applied after machining in order to ensure good superelastic properties at room temperature. This two part heat treatment results in transformation temperatures equivalent to specimens undergoing a single heat treatment between 325 °C and 350 °C for 1.5 hours and immediately water quenched, but with hardness values slightly greater than specimens undergoing only this single heat treatment (see Figure 3-9).

The bar specimens used in the full-scale monotonic tests and subsequent cyclic and earthquake loading studies are tapered using conventional machining techniques in order to prevent the formation of stress concentrations at the grips during testing. The 31.8 mm, 19.1 mm, and 12.7 mm diameter NiTi specimens have reduced section diameters of 25.4 mm, 12.7 mm, and 6.35 mm at their gage and can be seen in Figure 3-1. Throughout the remainder of this dissertation, the reduced diameter specimens are referred to using their initial diameters to allow for easier comparison with the material characterization results.

The monotonic tests are performed using an MTS 250 kN hydraulic uniaxial testing apparatus fitted with MTS 647 hydraulic wedge grips. The actuator was set to run in displacement control based on the feedback to the MTS TestStar controlled with a rate of 5% strain per minute (ASTM, 2003). MTS *TestWare-SX* software is used to run the controller on a stand alone PC. The internal 245 kN load cell provided force measurements while a 25.4 mm gage Epsilon extensometer provided strain measurements up to 20% strain. Data was recorded using an Optim Electronics MEGADAC system at 20 scans per second to capture any significant behavior. The basic test set-up is shown in Figure 3-10.

3.4.2 Monotonic Tensile Test Results

The monotonic test results for the 19.1 mm and 12.7 mm diameter bars are shown in Figure 3-11. Both curves exhibit typical superelastic behavior with initial elastic straining of the austenite, formation of the loading plateau as a result of the forward phase transformation, elastic straining of the stress-induced martensite, and finally plastic deformation until failure. Comparing some of the properties of the two size bars, the initial elastic modulus associated with the straining of the austenite is 25.5 GPa for the 19.1 mm diameter NiTi

3-10(a):

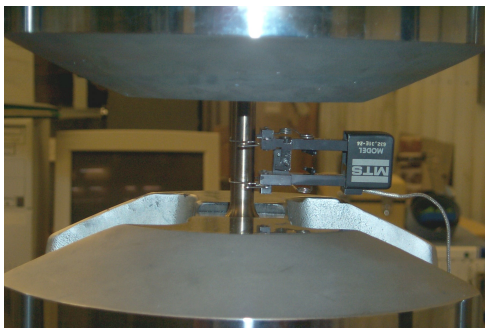

3-10(b):

Figure 3-10: Test set-up for the monotonic and subsequent large diameter bar tests showing both the full testing apparatus and a closeup of a gripped specimen.

bar. This value increases to 29.1 GPa for the 12.7 mm diameter bar. The difference may be partially attributed to the appearance of the R-phase during the loading of the 19.1 mm bar which is not fully present for the 12.7 mm bar. The forward transformation stress (stress at which the phase transformation initiates) is approximately 400 MPa for both size bars suggesting that there is no influence of deformation processing on the forward transformation stress. Analyzing the segment of the curve associated with the elastic loading of stress-induced martensite (segment after the loading plateau), the modulus for the curve is 10.6 GPa and 10.9 GPa for the 19.1 mm and 12.7 mm NiTi bars, respectively. These values represent a 58% and 63% decrease from the elastic modulus associated with the NiTi when it is in its austenite phase thus showing how much softer martensitic NiTi is compared to austenitic NiTi.

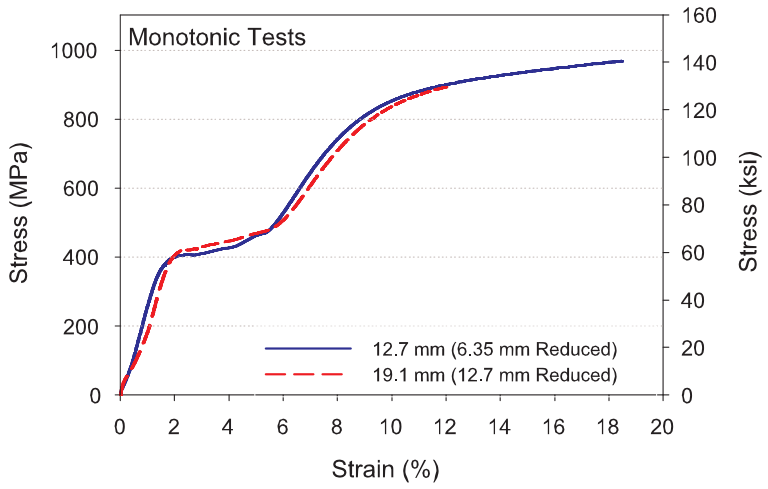

Figure 3-11: Monotonic stress-strain results for the full-scale 19.1 mm and 12.7 mm bars.

The main difference in the behavior of the two bars with respect to bar size is the failure stress and strain. The 19.1 mm bar fails at a much lower strain level as compared to the 12.7 mm diameter bar. The failure strains are approximately 12.1% and 18.5% for the 19.1 mm and 12.7 mm diameter bars, respectively, with corresponding stresses at failure of 894 MPa and 968 MPa. It should be noted that these stress levels are over twice the stress level associated with the start of the forward transformation. For both size bars, the failure of the specimen occurred in the reduced gage section, but at the point where the taper finished and not at the center of the gage length. This type of failure suggests that surface defects at these points are introduced which act as starting points for the failure. No cupping or necking typically associated with the tensile failure of steel is observed. As a result of the type of failure, it is hard to determine whether the difference in the failure strain and stress can be attributed to bar size effects. The properties obtained from the monotonic tests are presented in Table 3-2.

Table 3-2: Full-scale 19.1 mm and 12.7 mm bar Monotonic Test Properties.

	Bar size	
Property	19.1 mm	12.7 mm
Modulus (Austenite)	25.5 GPa	29.1 GPa
Modulus (Martensite)	10.6 GPa	10.9 GPa
Forward Transformation Stress	405 MPa	401 MPa
Failure Stress	895 MPa	968 MPa
Failure Strain	12.1%	18.5%

3.5 Cyclic Mechanical Behavior

Although the monotonic tests provide some key information in regard to the macroscopic properties of the large diameter NiTi SMAs, the results do not provide the full picture needed to optimize and implement NiTi into structural systems for earthquake mitigation applications. Given the cyclic nature of an earthquake, cycling effects remain a key consideration in the use of SMAs in seismic design and retrofit. As a result, the NiTi specimens are placed through tension-only cyclic loadings to evaluate their cyclic properties and any fatigue effects that may be present while also determining if there is any correlation between property trends and bar size. In order to maintain a unified vision from both a material science and structural engineering point of view, two sets of cyclic tests are run. The first set of tests uses coupon specimens taken from various points across the diameter of the bars, typical of many material science studies. The second set of tests then uses the full-scale specimens to look at the cyclic tensile behavior of large diameter NiTi SMAs which have the possibility of being used in structural applications. These two-sets of tests provide a means of disseminating the mechanical behavior of NiTi under cyclic loadings, connecting

the material characteristics to the cyclic properties, and determining the presence of any bar scaling effects.

3.5.1 Methods

The cyclic tensile tests are performed on two distinct sets of virgin specimen: (a) small coupon specimens and (b) full-scale specimens. Coupon specimens having an overall length of 63.5 mm and a thickness of approximately 1 mm were extracted from each size bar by electro discharge machining and are presented in Figure 3-1 along with the full-scale specimens. A tensile loading protocol consisting of 20 cycles to 6% strain (cyclic test) is applied using the same test setup used for the monotonic tests (see Section 3.4.1). The actuator is set to run at a constant rate of 10^{-3} mm/mm using a digital controller with the feedback from a 3 mm gage length extensometer triggering the maximum and end point of each loading cycle and providing the strain measurements.

The second set of specimens tested consisted of the 19.1 mm and 12.7 mm full-scale bars tapered to diameters of 12.7 mm, and 6.35 mm at their gage. This provides a means of connecting the monotonic results to the cyclic results. Once again, the previously mentioned 250 kN hydraulic testing apparatus is used to apply the same loading protocol and loading rate used for the coupon tests to the 19.1 mm and 12.7 mm full-scale specimens. By using the same testing apparatus, load cell, and loading protocol, a good comparison of the results can be made and biasing of results associated with different testing apparatus is eliminated. A 25.4 mm gage length extensometer provides both the strain measurements and strain feedback to the digital controller for the full-scale tests.

The cyclic loading protocols provide key information for structural engineers in regards to the cyclic properties of superelastic NiTi. The cyclic tests reveal information in regards to the degradation of specific properties with continued cycling. Figure 3-12 points out the key properties which are important for the introduction of NiTi into structural applications: forward transformation stress, σ_L, reverse transformation stress, σ_{UL}, initial elastic modulus, E_i, residual strain, ε_R, and the equivalent viscous damping, ξ_{eq}.

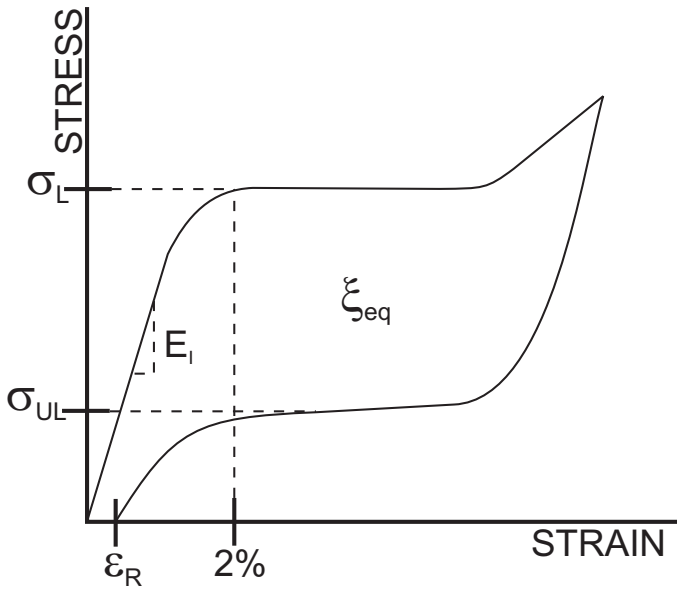

Figure 3-12: Conceptual superelastic stress-strain curve depicting those properties important for structural applications.

The forward transformation stress refers to the stress at which the martensitic phase transformation initiates. Structural engineers use this value to determine the load at which NiTi undergoes a significant stiffness change and gain an idea of the expected restoring

force obtained from a NiTi element. Past studies of NiTi in the structural engineering community have defined the forward transformation stress as the stress along the loading curve at 2% strain from the initial strain at the start of the cycle (DesRoches et al., 2004). The reverse transformation stress provides the stress at which the reverse martensitic transformation occurs and gives the structural engineer an idea of the size of the hysteresis loop which is important in the modeling of their cyclic behavior. Since the stiffness of a structure effects the magnitude of the acceleration imposed on it during an earthquake, the initial elastic modulus provides significant information in determining the expected behavior of a structure during a seismic event and is of particular importance in designing seismic protection systems. The residual strain provides a measure of the recentering capability provided by a NiTi element and refers to the plastic deformation due to the accumulation of permanent inelastic strain during cycling. Finally, the equivalent viscous damping is a measure of supplemental damping provided by the hysteretic behavior of NiTi and provides a means of comparing the energy dissipation capacity of NiTi elements to other passive energy dissipation systems. The equivalent viscous damping is calculated based on Equation 3.1:

$$\xi_{eq} = \frac{1}{4\pi}\frac{E_D}{E_{So}} \tag{3.1}$$

where E_D refers to the energy dissipated per cycle and E_{So} refers to the strain energy per cycle (Chopra, 2001). The results of the coupon and full-scale tests offer a previously non-existent connection between these properties important for structural application of NiTi and the key material characterization information presented in Section 3.4.

3.5.2 Coupon Tests

Using coupon specimens extracted from full-scale bars is one of the most common means by which material scientists study the mechanical properties of NiTi. The test coupon procedure limits the cost of testing programs and also allows use of standard load frames with reasonable load limits. By removing coupon specimens along different points across the diameter of the full-scale bar, the effects of different grain size, grain orientation, and precipitate density, which can be a function of location, on the superelastic properties of NiTi can be more clearly identified. Smaller grain sizes tend to lead to an increased strength due to the propensity of dislocation pileup attributed to the reduced distance between grain boundaries. Different grain orientations cause a larger influence on the properties with respect to loading direction (Gall and Sehitoglu, 1999b; Gall et al., 2001). In particular, the material characterization of these same NiTi bars demonstrated that texture varied spatially throughout the bar and it is critical to determine if this variation influences the mechanical properties. At specific sizes, precipitates assist both the martensitic transformation and hinder dislocation motion improving the shape recovery capability of the NiTi. Coupon specimen tests can thus provide a bridge between the basic material characterization and the mechanical behavior of full-scale specimens. As a result, coupon specimens obtained from both the center and edge of each of the three diameter full-scale bars are tested under tensile cyclic loading specified in Section 3.5.1.

Figure 3-13 contains a matrix of the tensile stress-strain plots for the six different coupon specimens tested. The stress-strain curves form a clear forward and reverse transformation plateau and show shape recovery resulting in the typical superelastic hysteresis.

For all specimens, a short plateau occurs during the first cycle at a stress level between 25 MPa and 50 MPa which can be attributed to the R-phase transformation. This is consistent with the DSC results which show the onset of a two-stage transformation which is attributed to the precipitates formed during aging. The effects of the R-phase disappear after the first cycle. A Lüders-like transformation, distinguished by the sudden drop in stress level with increased strain, is observed for all samples, regardless of bar diameter or location, during the early cycles at the onset of the forward transformation plateau. The Lüders transformation is attributed to the martensitic transformation initiating and moving as a front along the length of the specimen (Miyazaki et al., 1981b). The loss of the Lüders-like transformation with continued cycling results from a build up of dislocations which prevents a return to the austenitic phase in some areas and allows for a more random phase transformation over the length of the bar. Since both the effect of the R-phase and Lüders-like transformation can be removed through prior mechanical training, they pose no major concern to structural and earthquake applications. Some more general observations of the stress-strain curves are that they all show an accumulation of residual strain with increased cycling and a decrease in the forward transformation plateau. It should be noted that the backwards ratcheting of the stress-strain curves shown in Figure 3-13(d) and 3-13(f) is most likely attributed to slip of the extensometer implying residual strain measurements and maximum strain levels from these tests are inaccurate.

The effect of location, particularly on those properties important for seismic applications, can be determined by comparing the stress-strain curves for the coupon specimens taken at the center and edge of each size full-scale bar. The center specimens have a slightly

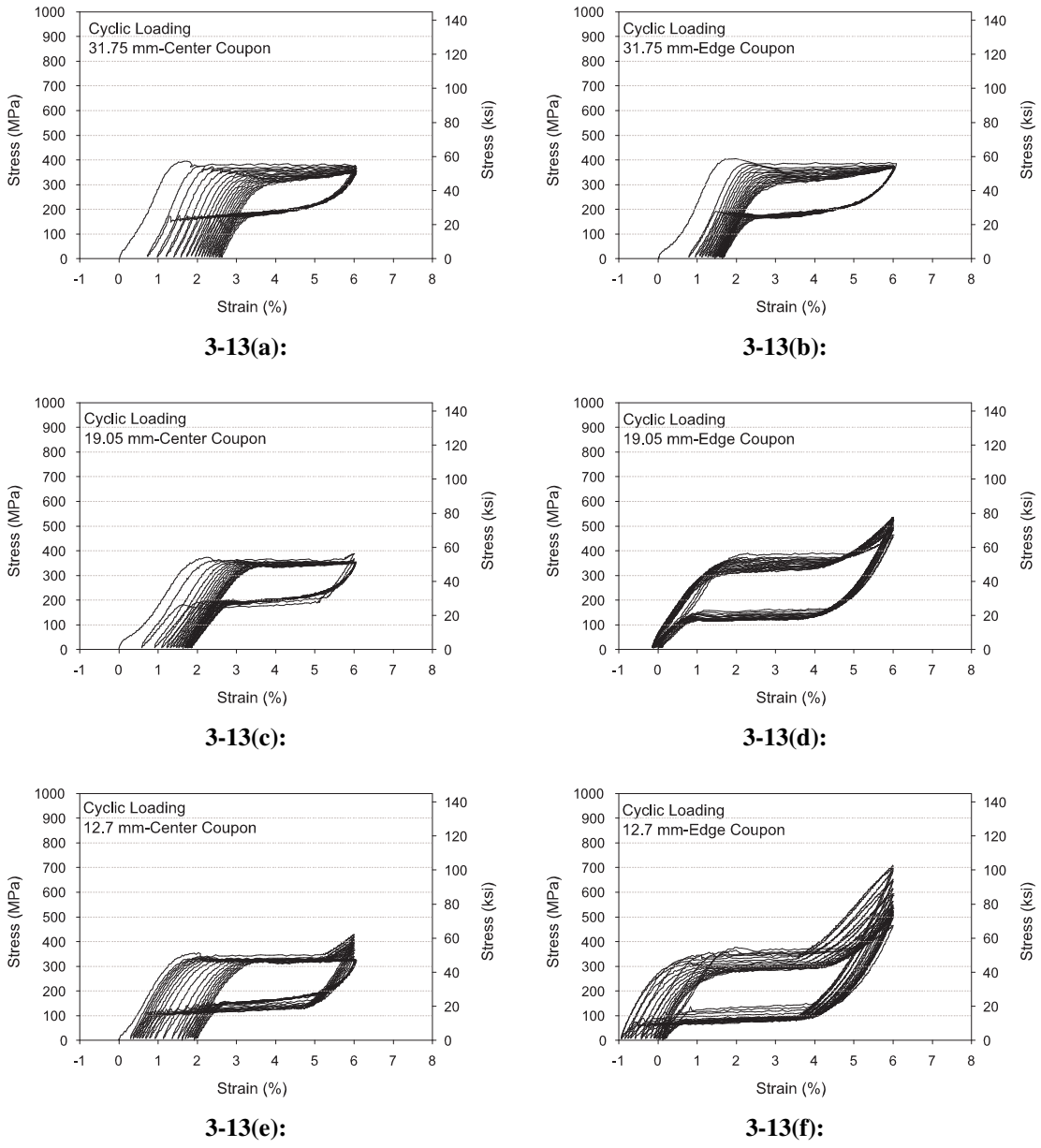

Figure 3-13: Cyclic tension coupon stress-strain results: (a) center coupon 31.75 mm bar, (b) edge coupon 31.75 mm bar, (c) center coupon 19.05 mm bar, (d) edge coupon 19.05 mm bar, (e) center coupon 12.7 mm bar, and (f) edge coupon 12.7 mm bar.

higher initial elastic modulus compared to the edge specimens with differences in their average initial elastic modulus of 2.9 GPa (8.9%), 1.9 GPa (8.6%), and 2.8 GPa (10.6%) for the 31.75 mm, 19.05 mm, and 12.7 mm specimens, respectively. The decrease in the forward transformation stress between the first and last cycle is greater for the edge specimens compared to the center specimens, but not to a significant degree. The equivalent viscous damping values and strain recovery appear to be unaffected by the coupon location. Based on the results in Figure 3-13, it can be concluded that the slight texture variation throughout the bars is not significant enough to influence cyclic degradation properties in light of typical variations seen in NiTi cyclic stress-strain properties.

Because of the need to obtain a specified strength and stiffness when using NiTi for seismic applications in structures, a wide variety of sizes may be required depending on the particular application (brace, base isolator, bridge restrainer) and the type of structure. In order to tests bars of these sizes, large capacity testing apparatus are necessary. By being able to connect the mechanical behavior of coupon tests specimens to the full-scale test results, more expensive full-scale tests can be avoided. Changes in the properties with respect to bar size can also affect the performance of a NiTi device. Past preliminary studies have shown an effect of bar size on NiTi superelastic properties, but did not conclusively define them with respect to the microstructure of the material (DesRoches et al., 2004). Of particular importance is whether reliable values of the full-scale forward transformation stress, residual strain, and equivalent viscous damping can be obtained by testing coupon specimens taken from bars of various size.

The stress-strain results for the coupon specimens taken from the center of the three different diameter full-size bars (Figure 3-13(a), 3-13(c), 3-13(c)) show a decrease in the

first cycle forward transformation stress with a decrease in bar size from 393 MPa for the 31.75 mm specimen to 353 MPa for the 12.7 mm specimen. The edge specimens provide a similar trend. Based on the material characterization, the decrease in the forward transformation stress coincides with an increase in the <110> texture component suggesting that the initial transformation stress is sensitive to this additional texture component. The effect of the grain texture and presence of precipitates dominates any potential effect of grain size as demonstrated in the hardness measurements (Section 3.3.5), which were sensitive to heat treatment but not bar diameter. The degradation of the forward transformation stress with continued cycling appears to be consistently greater for the larger diameter specimen as shown by the difference in the forward transformation stress between the first and last cycle for 31.75 mm specimen, 118 MPa, and the 12.7 mm specimen, 48 MPa.

The residual strain values decrease for the first cycle from 0.67% to 0.57% to 0.30% for the coupons taken from the center of the 31.75 mm, 19.05 mm, and 12.7 mm bars, respectively. This slight trend becomes less apparent with increased cycling as previously mentioned. As with the forward transformation stress, these results suggest a possible connection with the grain orientation and the possible presence of a higher density of precipitates in the small diameter bars assisting the strain recovery. The rate at which the residual strain accumulates does decrease with continued cycling in all specimens. For a typical recentering device used for seismic applications, the residual strain results from the coupon tests are good, providing between a 57% and 69% recovery even when cycled twenty times to 6% strain which is a larger number of high strain cycles than would typically be encountered during an earthquake.

Table 3-3: 20th Cycle Coupon Specimen Properties.

	Center Location			Edge Length		
Bar Size	31.75 mm	19.1 mm	12.7 mm	31.75 mm	19.1 mm	12.7 mm
E_i, GPa	36.3	23.3	30.9	30.3	24.1	24.2
σ_L, MPa	276.3	317.4	304.9	254.1	307.8	277.4
ε_R, %	2.58	1.82	1.91	1.63	N/A	N/A
ξ_{eq}, %	2.28	2.91	3.71	3.18	4.43	4.55

The equivalent viscous damping provides a measure of the ability of the NiTi to provide supplemental damping to a structure. For all specimens, the equivalent viscous damping decreased significantly as a result of continued cycling. This can be attributed to the decrease in the forward transformation stress and small increase in the reverse transformation stress resulting in a pinching of the hysteresis as the number of cycles increased. The overall decrease in the equivalent viscous damping between the first and last cycle is 68%, 50%, and 42% for the center coupon specimens from the 31.75 mm, 19.05 mm, and 12.7 mm bars, respectively. The equivalent viscous damping values for the first cycle showed no true bar size effect with damping values for the coupons from the large bar to the small bar being 7.11%, 5.86%, and 6.44%. The increase in the equivalent viscous damping for the smaller diameter bar is attributed to a lower initial reverse transformation for the coupon specimens taken from the smaller diameter bar. For typical damping applications, the equivalent viscous damping values remain low, even during the first cycle, suggesting larger hysteresis loops are necessary in order to use NiTi solely as a damping material. A summary of the cyclic properties as a result of the 20th cycle for the coupon specimens are shown in Table 3-4.

3.5.3 Full-scale Tests

As suggested by the literature review, a large majority of the past studies on the superelastic behavior of NiTi has focused on small diameter wires or thin plates similar to the coupon specimen results presented. Typical applications of NiTi in civil structures require larger diameter specimens because of the magnitudes of the loads, particularly those associated with a seismic event, and ease of implementation. Although the coupon tests provide details of the expected mechanical behavior of the NiTi specimens, it is not known if these results translate well into the behavior of large diameter specimens. There is also a lack in knowledge of how the thermo-mechanical and deformation processing of large diameter bars can be used to optimize their properties for structural applications. Given the life safety concerns associated with building and bridge structures, it is important that the civil engineer understand the true mechanical behavior of the bars used in design and thus the lack of synergy between the material science and structural engineering fronts has limited the actual application of NiTi in modern structures. In order to address this, the full-scale 19.1 mm and 12.7 mm bars are tested under the same cyclic tensile loading as the coupon specimens to determine the mechanical behavior of the full-scale specimens and to provide the necessary information to connect the material characterization with the full-scale macroscopic mechanical behavior.

Figure 3-14 provides representative stress-strain results for the full-scale cyclic tensile tests performed on the 19.1 mm and 12.7 mm diameter specimens. The stress-strain results for all the full-scale bars tested as part of the cyclic study can be found in Appendix A. Both size specimens show good superelastic behavior with a clear hysteresis and good

shape recovery. Although the stress-strain plots only represent one of each of the different size bars tested, the properties are found to be repeatable across the replicate tests. This consistency suggests that the necessary repeatable behavior to use large diameter specimens in structural applications can be obtained from specimens with the same composition and processing. The R-phase plateau appears in the first cycle for both size specimens. However, for the smaller diameter specimen, the R-phase is less apparent and occurs at a lower stress level compared to the 19.1 mm specimen. The R-phase is once again consistent with the DSC results which suggest a two-stage phase transformation occurs. During the initial loading cycles, no Lüders-like deformation is observed along the loading curve upon reaching the forward transformation stress suggesting that the phase transformation occurs in a random manner along the gage length of the full-scale bar. The completion of the phase transformation and subsequent hardening due to the further elongation of the NiTi in its stress-induced martensite phase is apparent in both stress-strain curves at approximately 5% strain.

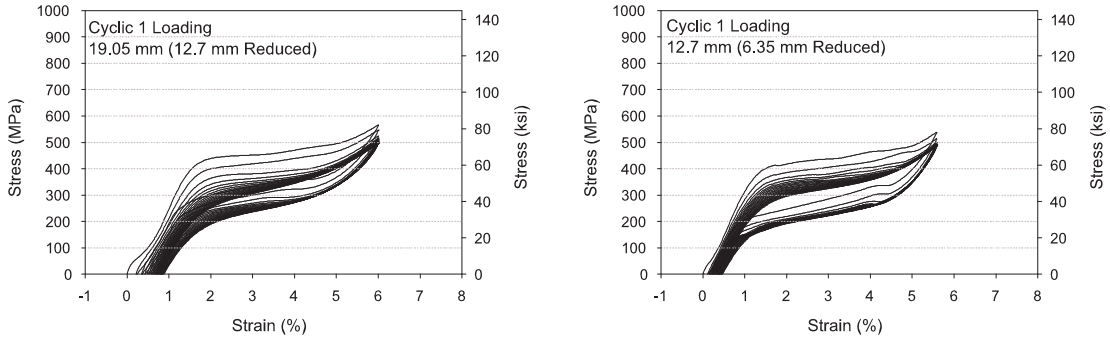

3-14(a): **3-14(b):**

Figure 3-14: Representative cyclic tensile stress-strain plots for the (a) 19.05 mm full-scale NiTi bar and (b) 12.7 mm full-scale NiTi bar.

The forward transformation stress is of particular importance for structural applications because of the significant change in stiffness that occurs at the onset of transformation. On average, the forward transformation stresses for the first cycle are 444 MPa and 421 MPa for the 19.1 mm and 12.7 mm diameter bars, respectively. The forward transformation stresses decrease by approximately 43% and 39% as a result of the 20 tensile strain cycles for the two size specimens. This degradation in the forward transformation stress can be attributed to the formation of permanent slip which tends to assist the transformation process. The proximity of the forward transformation stress values for both size bars throughout the cycling suggest that there is no discernable bar size effect on this property and that the forward transformation stress can thus be modified at the manufacturing level through composition or the processing level through heat treatment, as suggested in Section 3.3, without concern for the final specimen size.

Past cyclic tensile studies completed on large diameter bars have shown good strain recovery properties, but have not been able to distinguish any bar size effects from composition effects or microstructure effects (DesRoches et al., 2004). As a result, the use of NiTi in recentering devices has been limited due to the unpredictability of their recentering properties in different forms. Figure 3-14 shows good deformation recovery for both size bars with the residual strain for the first cycle being 0.23% and 0.19% for the 19.1 mm and 12.7 mm bars, respectively. The residual strain values increased to 0.88% and 0.75% for the last cycle. Throughout the cycling, the 19.1 mm specimen accumulated slightly higher inelastic strain values as compared to the 12.7 mm diameter specimen suggesting a slight bar size effect where a decrease in bar size also leads to an increase in the recentering capability. It should be noted that even for the larger diameter bar, over 85% of the deformation

Table 3-4: 20th Cycle Full-Scale Specimen Average Properties.

Bar Size	19.1 mm	12.7 mm
E_i, GPa	42.4	37.2
σ_L, MPa	251.3	256.6
ε_R, %	0.88	0.75
ξ_{eq}, %	1.93	2.43

is recovered during the last cycle. Although an increase in bar size leads to a decrease in the recentering capability, this decrease is not large enough to limit the use of larger diameter specimens in structural recentering applications.

The stress-strain results provide evidence that the bar size effects the damping capacity of full-scale NiTi bars. The equivalent viscous damping values associated with the first and last strain cycle for 19.1 mm diameter bars are 2.8% and 1.9%. The 12.7 mm diameter specimen provides higher damping capacity with equivalent viscous damping values of 3.6% and 2.4% for the first and last strain cycle. However, the equivalent viscous damping value decreases by approximately the same percentage, 33%, for both bar diameters over the 20 cycles. Since no apparent bar size effects are shown for the forward transformation stress and both bars reach similar maximum stress values, the change in the equivalent viscous damping with bar size must be attributed to the reverse transformation stress. Figure 3-14 clearly shows a higher reverse transformation stress for the 19.05 mm specimen resulting in a pinching of the hysteretic area to a greater extent as compared to the 12.7 mm specimen. Once again, it should be pointed out that the low equivalent viscous damping values infer that superelastic NiTi cannot provide enough energy dissipation to be used solely for damping applications in civil structural systems. A summary of the cycle properties is provided in Table 3-4.

3.5.4 Scaling Effects: Coupon versus Full-scale

The results from past tensile cyclic tests on NiTi coupon specimens completed in studies by material scientists and the few full-scale large diameter NiTi tests completed for structural engineering applications have both suggested potential for their use in both active and passive control. Until now, no comparison between the performance of coupon specimens and full-scale specimens has been undertaken resulting in a lack of connection between these studies. The mechanical behavior of the coupon specimens taken from the 19.1 mm and 12.7 mm NiTi bars and the full-scale specimens of the same size is compared in order to link the work typically performed in the material science field with the needs of structural engineers developing innovative shape memory alloy devices. Only the center coupon specimens are used for this comparison since the edge of the full-scale bar is removed in the tapering process to prevent the formation of stress-concentrations during testing as can be seen in Figure 3-1. The most significant differences observed in this work are between the coupon and full-scale tests, compared to more subtle differences attributed to bar size observed within groups of coupon or full-scale tests.

In Figures 3-15 and 3-16, the stress-strain plots for the 1st, 5th, 10th, 15th, and 20th cycles are shown for both the coupon tests and full-scale tests of the 19.1 mm bar and 12.7 mm bar, respectively. In general, both the coupon specimens and the full-scale specimens show good superelastic behavior as previously discussed, but the first cycle hysteresis loop of the full-scale specimens is shifted upward. This trend becomes less apparent in the later cycles due to the decrease in the forward transformation stress with continued cycling. The

greater variation in grain orientation across the cross-section of the full-scale bars, as suggested by the material characterization, may contribute to this occurrence with the effects being minimized with continued cycling as dislocations buildup more uniformly throughout the cross-section. Conversely, the R-phase is present in both samples during this first cycle and occurs at similar stress-levels. The Lüders-like transformation is present in the martensitic phase transformation of the first five cycles of the coupon specimens, but is not seen for the full-scale tests in both Figures 3-15 and 3-16. These results suggest specimen geometry dependence for the occurrence of a Lüders-like transformation since the martensitic phase transformation for all of the coupon specimens is Lüders-like, irregardless of location. The slope of the forward and reverse transformation plateaus increases when the bars are tested at full-scale further suggesting that phase transformation is occurring sporadically along the gage section of the bar as pockets reach the required stress level rather than as a band moving along the length of the bar. Although the use of a larger gage section in the full-scale testing may also contribute to the smearing out of the Lüders-like transformation behavior, it is, in either case, related to the volume of material being tested. As the volume of material increases, the sample shows more hardening and a departure from unstable Lüders-like transformation behavior. This finding is absolutely critical when comparing the behavior of small volume specimens of NiTi material to materials with a relatively large volume for structural applications. Another critical finding is the repeatability of the full-scale test results as compared to the randomness of the coupon tests results when replicated. The increased unpredictability of the coupon specimen properties is a direct artifact of the microstructural heterogeneity in the samples and the smaller volume of material being sampled in the coupon tests.

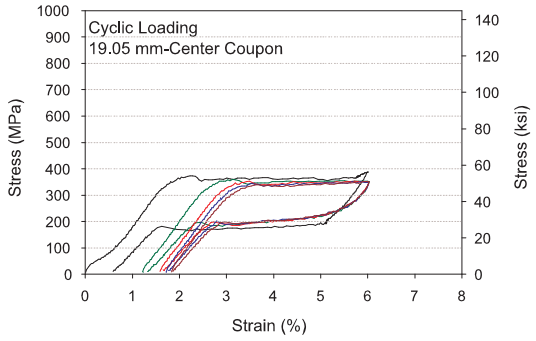

3-15(a):

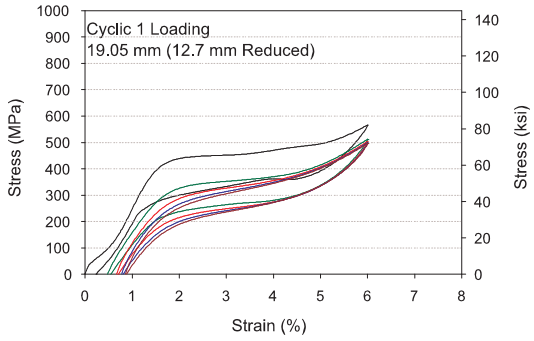

3-15(b):

Figure 3-15: Cyclic tensile stress-strain plots including the 1st, 5th, 10th, 15th, and 20th cycles for both the (a) coupon test and (b) full-scale test of the 19.05 mm bar.

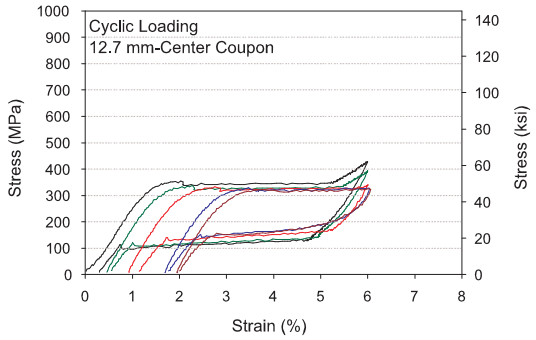

3-16(a):

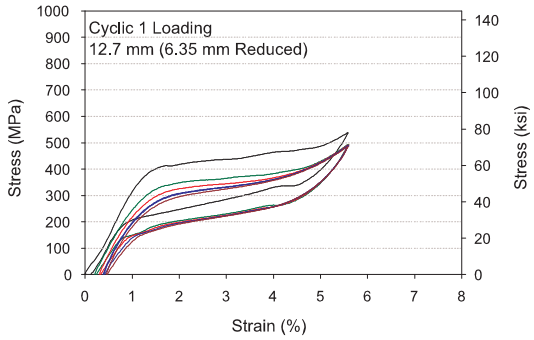

3-16(b):

Figure 3-16: Cyclic tensile stress-strain plots including the 1st, 5th, 10th, 15th, and 20th cycles for both the (a) coupon test and (b) full-scale test of the 12.7 mm bar.

Figure 3-17 shows the initial elastic modulus, forward transformation stress, residual strain, and equivalent viscous damping as a function of cycle number for the center coupon specimens and full-scale specimens. In all cases, there is a significant difference in the values associated with the center coupon specimens and full-scale specimens. The initial elastic modulus remains roughly constant during the cycling of the center coupon specimen, while both the 19.1 mm and 12.7 mm full-scale bars show an increase in the initial elastic modulus suggesting hardening with continued cycling. The full-scale bars have a higher overall initial elastic modulus with the difference between the coupon specimen and full-scale specimen being greatest for the 19.1 mm specimens. This difference for the 19.1 mm specimens is approximately 2.8 GPa (1.7%) and 19.1 GPa (45.0%) for the first and last cycles, respectively. In general, the initial elastic modulus for the first cycle can be predicted accurately from the coupon tests, but the effects of continued cycling result in an increase in the initial elastic modulus which is not predicted by the coupon tests and occurs to a greater extent in larger full-scale bars.

The forward transformation stress for both the coupon specimens and the full-scale specimens decreases with increased cycling as seen in Figure 3-17(b). Although they both decrease, the coupon tests underestimate the forward transformation stress for the first cycle by approximately 71 MPa (16.0%) and 68 MPa (16.2%) and overestimate the forward transformation stress for the last cycle by approximately 66 MPa (26.3%) and 48 MPa (18.8%). In addition, the rate of decrease and functional form for the decrease in the critical transformation stress with cycling differs for the coupon and full-scale tests. These differences are not microstructural per-se, because the same material is used for both tests. The difference is a pure scaling phenomenon, where the large bars sample a larger volume

of material than the small samples, and thus represent a more homogenized response. The differences in the critical transformation stress as a function of cycling can be attributed to the high initial forward transformation seen for the full-scale bars, which is associated with the larger variation of material structure through the cross-section. Given the same type of test sample, the coupon and the full-scale tests show no "bar size effects" and thus no effects from increased deformation processing (although there is a sample size effect as previously discussed). The rate at which the forward transformation stress drops with increased cycling decreases for both the coupon and full-scale specimens. This suggests that prior mechanical training can be used to build up dislocations and achieve more consistent values, which is particularly important for applications in civil structures.

Figure 3-17(c) provides the comparison of the residual strain for both the coupon specimens and full-scale specimens with respect to cycle number and bar size. It is evident that the coupon specimens accumulate a significantly larger amount of permanent deformation as compared to the full-scale specimens. The differences in the residual strain values between the coupon specimens and the full-scale specimens are approximately 0.94% strain and 1.2% strain for both the 19.1 mm and 12.7 mm diameter bars. The major difference, again, occurs as a function of sample size rather than bar size. The coupon samples show dramatically different accumulation of residual strain compared to the full scale bars, which is not completely surprising given the microstructural differences shown during the material characterization and the vast difference in stress-strain curves shown herein. The low residual strain values, particularly during early cycles, suggest the ability to use NiTi in recentering application for civil structures. In general, the coupon tests overestimate the

amount of permanent deformation to be expected in full-scale specimens and the residual strain is only moderately sensitive to increased deformation processing.

Both the coupon specimens and the full-scale specimens provide decreased damping with increased cycling as can be seen in Figure 3-17(d). Also for both types of tests, the 12.7 mm diameter bar specimens acquire higher equivalent viscous damping values as a result of a lower reverse transformation stress. However, the equivalent viscous damping values obtained from the coupon specimen tests are significantly higher than those found by testing the full-scale bars, particularly during the initial cycles. Comparing the stress-strain curves in Figures 3-15 and 3-16, it is obvious that the hysteresis is smaller for the full-scale specimen as a result of a higher reverse transformation stress. Overall, the equivalent viscous damping values are below those necessary to use superelastic NiTi for purely damping applications. Based on the structure of NiTi, it is possible to increase viscous damping by increasing precipitates size (reducing hardness). However, this will likely increase accumulation of permanent strain. A tradeoff exits between these two variables in structural design, and thus the material must be optimized by heat treatment to obtain the desired values.

Besides those factors which have been presented accounting for the difference in the properties of coupon specimens and full-scale specimens, residual stress may also play a role. The large amount of deformation processing needed to reduce the bar sizes results in a build up of residual stress along the surface of the full-scale bars which can affect the overall behavior of the specimen. This is evident due to the bending of the edges of the full-scale bar from which the coupon specimens are removed. Since the coupon specimens are

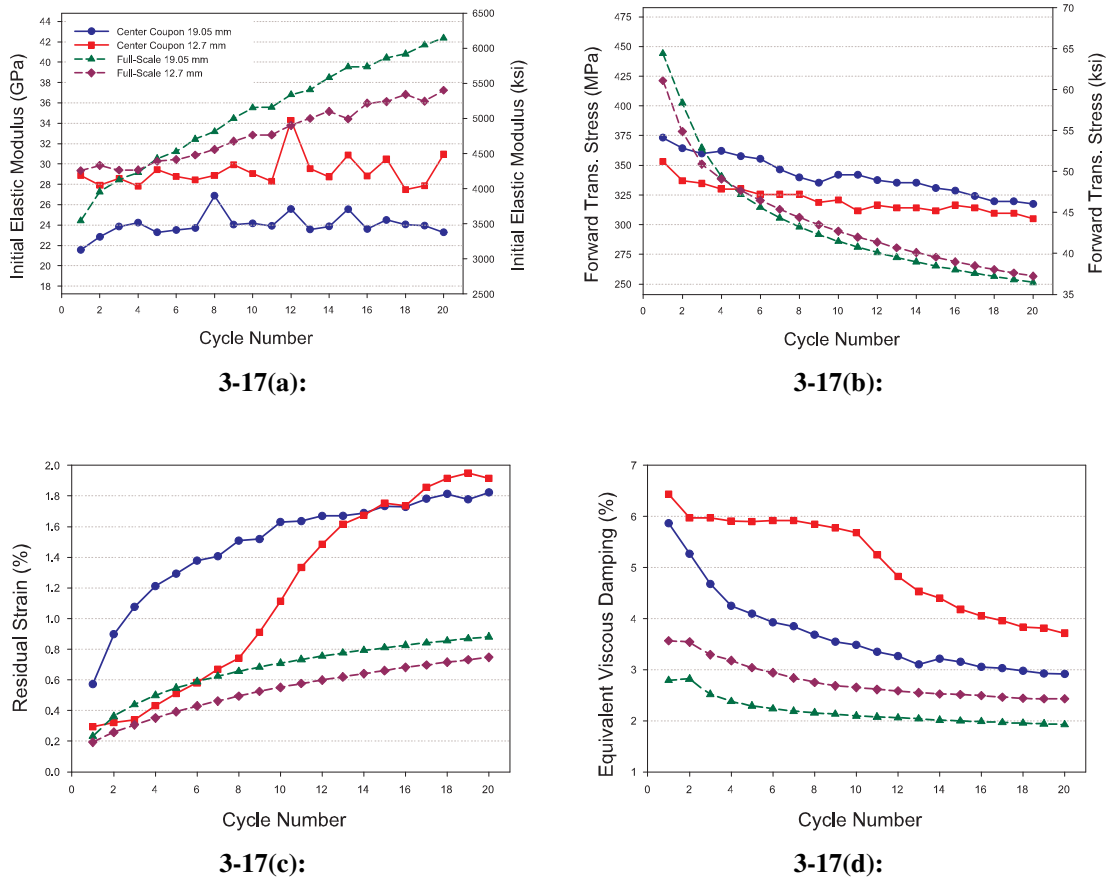

Figure 3-17: Coupon and full-scale cyclic results for the 19.05 mm and 12.7 mm bars with respect to cycle number and (a) initial elastic modulus, (b) forward transformation stress, (c) residual strain, and (d) equivalent viscous damping.

removed from the full-scale specimens, their behavior is not influenced by these residual stresses.

3.6 Earthquake Loading Mechanical Behavior

The majority of devices implementing NiTi in civil engineering applications have focused on mitigating the response of structures to extreme vibrations resulting from seismic events. These applications take advantage of the superelastic behavior of NiTi to control force transmission to essential structural members, provide recentering capabilities, and increase damping in the system. Now that a connection between the macroscopic properties based on the mechanical tests and the material characterization on a nano-scale and micro-scale level has been made and the full-scale cyclic tests results have shown adequate behavior of large diameter NiTi SMAs for use in civil structural applications, it is necessary to determine whether a typical earthquake loading with non-uniform cycles affects the superelastic properties of full-scale bar specimens. In order to do this, two sets of mechanical tensile tests are run on the three sizes of full-scale bars. The first set of tests consists of running the bars under a far-field type earthquake loading at a quasi-static rate in order to glean any effects as a result of non-uniform cycling to strain levels expected during an earthquake. The second set of tests focuses on any effect which dynamic loadings have on the properties of large diameter NiTi SMAs. For these tests, the full-scale bars are run using the same loading as the first set of tests, but with loading rates equivalent to those expected during an earthquake (0.5 Hz to 1.0 Hz).

3.6.1 Methods

The earthquake loading tests are performed with the 31.8 mm, 19.1 mm, and 12.7 mm diameter bars from the same batch of material that was used for the material characterization, monotonic tests, and cyclic tests. All specimens used for this study are previously untested. The same MTS apparatus and set-up that is used to perform the monotonic test and cyclic tests on the 19.1 mm and 12.7 mm diameter bars (see Section 3.4.1) is also used for the earthquake loading tests performed on those same size bars. An OMEGA OS554-MV infrared pyrometer is used to monitor the surface temperatures of the specimens during testing given the thermomechanical nature of NiTi SMAs. Because of the loads required to test the 31.8 mm specimens, a MTS 2.7 MN uniaxial hydraulic testing frame is used to apply the loading protocol in strain control based on the feedback from a 101.6 mm gage extensometer. An INSTRON 8500 Plus controller is used to control the actuator. As can be seen in Figure 3-1, the ends of the 31.8 mm diameter specimens are threaded in order to facilitate gripping and limiting slip during the loading.

The loading protocol used, shown in Figure 3-18, consists of increasing tensile strain cycles of 0.5%, 1.0%, 2.0%, 3.0%, 4.0%, and 5.0%, followed by six cycles to 6.0% strain. The loading protocol is chosen because the increasing strain cycles are representative of a far-field type earthquake ground motion. The first series of tests are performed at a quasi-static loading rate of 0.025 Hz, which corresponds to a maximum strain rate of 0.3% strain per second. The dynamic tests are performed at loading rates of both 0.5 Hz and 1.0 Hz, which corresponds to maximum loading rates of 6% strain per second and 12% strain per second, respectively. The dynamic loading allows for simulation of loading rates which are

expected in structural members during an earthquake. All of the stress-strain results (those reported following and the replicate tests) can be found in Appendix A.

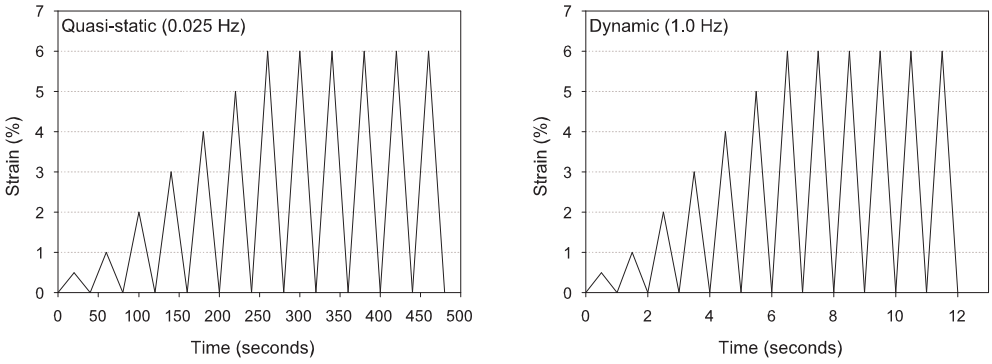

3-18(a): **3-18(b):**

Figure 3-18: Far-field type earthquake loading protocol for the (a) 0.025 Hz quasi-static case and (b) 1.0 Hz dynamic case

3.6.2 Quasi-static Tests

The quasi-static earthquake loading tests provide information in regards to the effect of unequal loading cycles. They also provide a means by which to compare how the amount of deformation processing effects the properties of superelastic NiTi large diameter specimens under earthquake type loadings. Figure 3-19 shows a representative stress-strain curve for the 31.8 mm diameter bar and individual plots of selected cycles. It should be noted that the 31.8 mm diameter bar is only cycled to 5% strain due to fracture of the specimen as a result of stress concentrations and surface defects introduced by the threading process. Failure is similar to that found during the monotonic tests. Looking at the complete stress-strain plot,

no R-phase is discernable, which is similar to the stress-strain plot of the coupon specimen taken from the center of the 31.8 mm specimen (Figure 3-13(a)) in which the R-phase transformation is only slightly discernable. No significant changes are discernable in the initial elastic modulus with the increasing strain cycles, but there is a decrease in the forward transformation stress for the 5% strain cycle. Comparing the individual stress-strain cycles, the residual strain does not show any significant increase until the 5% strain cycle where it increases by approximately 163% from the residual strain measurement at the end of the 4% strain cycle. This increase is most likely associated with a completion of the martensitic phase transformation and the formation of dislocation due to the high strain level which prohibits some of the stress-induced martensite from reverting back to its original austenite phase upon unloading. The damping capacity increased with increase strain cycles due to larger hysteresis and also the increase in the accumulation of residual strain during the 5% strain cycle. Overall, the largest diameter specimen shows good superelastic behavior. However, the premature fracture associated with threading the bar needs to be addressed.

Figure 3-20 provides a representative stress-strain curve for one of the 19.1 mm diameter NiTi specimens. Unlike the 31.8 mm diameter bar, the presence of the secondary R-phase transformation is clear even up to the first 6% strain cycle. The results suggest that large strain cycles are needed in order to remove the effect of the R-phase transformation. The overall results look similar to the full-scale cyclic test results shown in Figure 3-14(a), particularly during the six 6% strain cycles. The 2% strain cycle plot shows the initiation of the martensitic phase transformation. As with the 31.8 mm diameter bar, there is no significant decrease in the forward transformation stress until the 5% strain cycles at which point

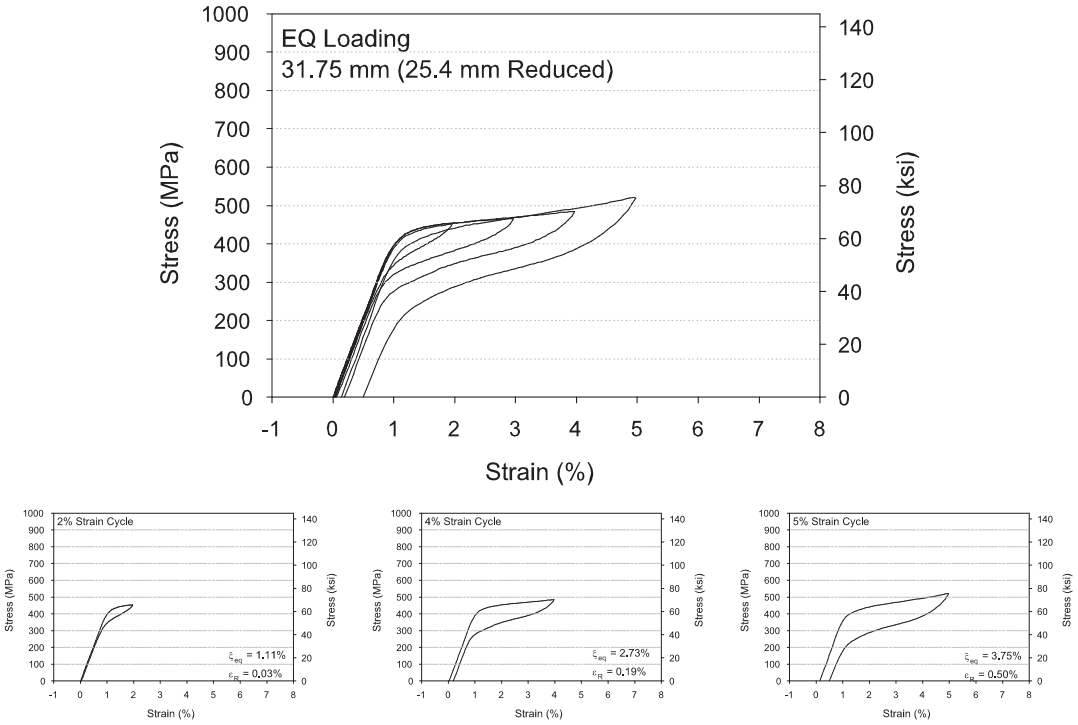

Figure 3-19: Stress-strain behavior for a representative 31.8 mm diameter bar subjected to the quasi-static earthquake loading.

a significant decrease, 27%, in the forward transformation stress occurs. The maximum residual strain remained below 0.65% suggesting good strain recovery as a result of the precipitation hardening. The final residual strain values roughly correspond to the residual strain associated with the seventh cycle of the cyclic tests for the same size bar. As a result, it can be concluded that there are no real effects associated with the early low-level strain cycles in the earthquake loading. The equivalent viscous damping values still remain low, less than 3%, and reach a maximum value at the first 6% strain cycle, but the depth of the hysteresis curve decreases with continued cycling at 6% strain.

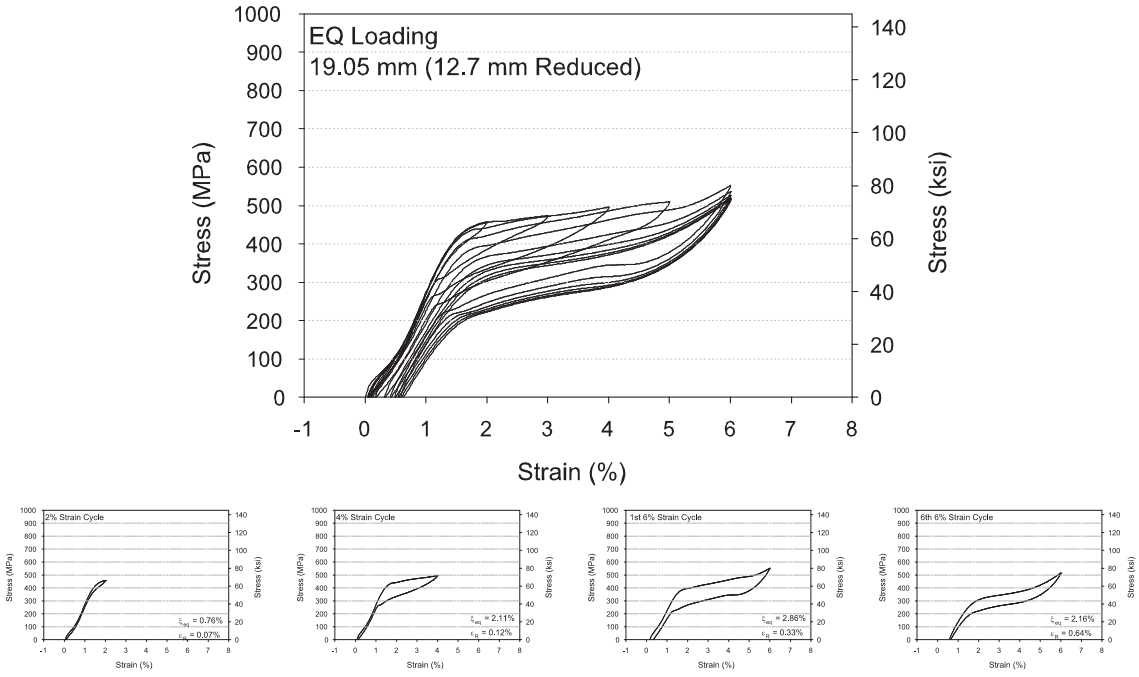

Figure 3-20: Stress-strain behavior for a representative 19.1 mm diameter bar subjected to the quasi-static earthquake loading.

Looking at the bar which underwent the largest amount of deformation processing, the stress-strain plot for a representative 12.7 mm diameter bar tested under the earthquake loading is shown in Figure 3-21. As with the 19.1 mm diameter bar, the R-phase is present. However, the R-phase is only apparent in the first two cycles as compared to all the cycles up through the first 6% strain cycle. Based on the materials characterization, it is hard to deduce the actual cause of this difference. Similar to the other two bar sizes, the low level cycling had very little effect on the forward transformation stress with no significant drop in the stress to induce the martensitic phase transformation until the 5% strain cycle. The residual strains after unloading increase after each cycle and range from 0.10% after the 2% strain cycle to 0.43% after the sixth 6% strain cycle. Once again, these increases can be attributed to the development of small levels of localized slip particularly after the onset of large strain cycles. The equivalent viscous damping values showed a similar trend to that which is seen with the 19.1 mm diameter bar with a maximum equivalent viscous damping value of 3.72% associated with the first 6% strain cycle. The stress-strain properties of the 12.7 mm diameter bar are very similar to those of the 19.1 mm diameter bar with the properties of neither bar appearing to be significantly affected by the earthquake type loading.

The representative stress-strain results for all three bars show good superelastic behavior throughout the earthquake loading with residual strain values remaining below 0.65%. Given this information, it is now important to look at how the cyclic properties are effect by the amount of deformation processing (bar size). Figure 3-22 provides a comparison of the cyclic properties (initial elastic modulus, forward transformation stress, residual strain, and equivalent viscous damping) of the three different size bars with respect to maximum cyclic

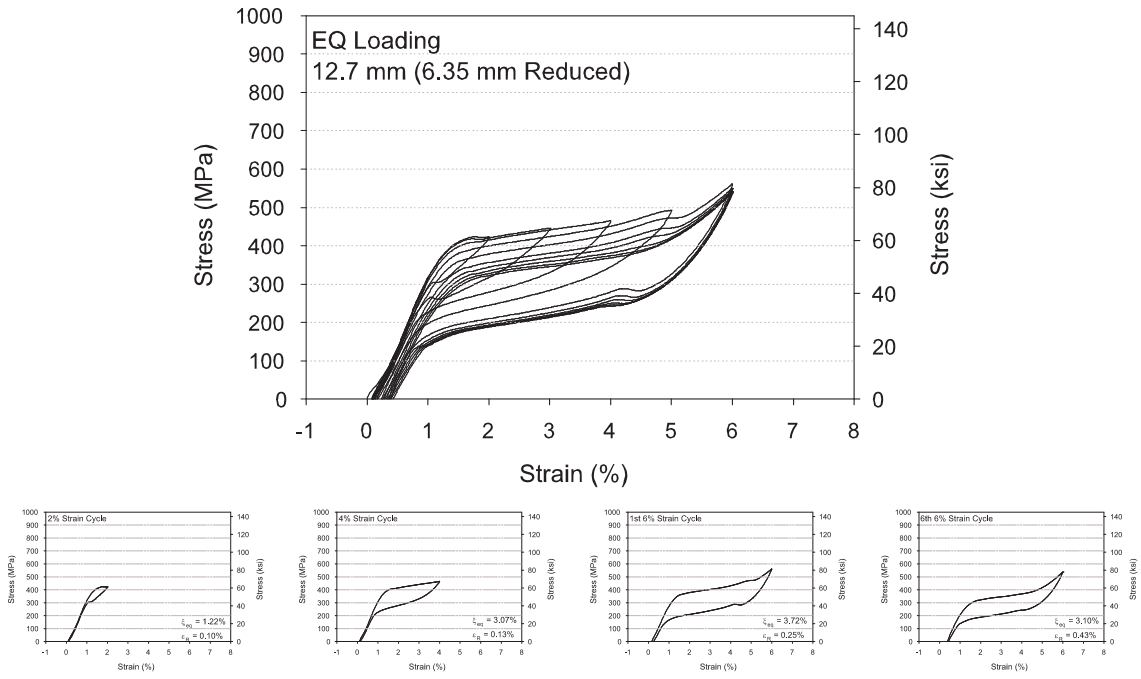

Figure 3-21: Stress-strain behavior for a representative 12.7 mm diameter bar subjected to the quasi-static earthquake loading.

strain. The reported values are the mean of the two specimens tested for each bar size. In all cases, the behavior of the two specimens at each bar size show only small differences.

Figure 3-22(a) provides the changes in the initial elastic modulus with respect to the maximum cyclic strain and bar size. The results show fairly constant initial elastic modulus values during the early cycling for all three size bars with values ranging between 40 MPa and 42.5 MPa, 28 MPa and 30 MPa, and 31 MPa and 33 MPa for the 31.8 mm, 19.1 mm, and 12.7 mm diameter bars, respectively. The large difference in the initial elastic modulus associated with the 31.8 mm diameter bar may be attributed to the fact that it is tested using a different system. Focusing on the 19.1 mm and 12.7 mm diameter bars, a similar trend is seen during the 6% strain cycles as is seen during the cyclic tests. The initial elastic

modulus increases with continued cycling with the 19.1 mm diameter bar (21%) showing a larger increase than the 12.7 mm diameter bar (5.8%).

The effect of maximum cyclic strain and bar size on the forward transformation stress is shown in Figure 3-22(b). For all three bars, the initial forward transformation stress ranges between 429 MPa and 462 MPa with no clear trend with respect to bar size. In the case of the 19.1 mm and 12.7 mm diameter bars, the forward transformation stress gradually decreases with increasing maximum cyclic strain until reaching the 6% strain cycles at which point the forward transformation stress decreases significantly with continued cycling to 307 MPa and 320 MPa, respectively. This decrease can be associated with an increase in the build up of dislocations which tend to assist the forward transformation, but also results in a decrease in the depth of the hysteresis with continued cycling.

Figure 3-22(c) provides the residual strain results with respect to maximum cyclic strain for all three amounts of deformation processing. In all cases, the residual strain increases with an increase in cycling with the largest increase occurring during the higher strain cycles. Some apparent bar size effects are present with the largest diameter bar having the lowest residual strain values and the smallest diameter bar accumulating the largest amount of residual strain up through the 3% strain cycle. After the 4% strain cycle, this trend reverses with the largest bar accruing the large amount of permanent deformation, 0.5% after the 5% strain cycle, and the smallest bar accumulating the least, 0.17% after the 5% strain cycle. In the case of the 19.1 mm and 12.7 mm diameter bars, the residual strain values remain below 0.65% suggesting good recentering capability can be provided during an earthquake.

Finally, Figure 3-22(d) shows the change in equivalent viscous damping values with respect to maximum cyclic strain and bar size. Based on the results, no clear bar size effects are present although this may be partially attributed, once again, to the fact that the large diameter specimens are tested using a different system. For all three bars the equivalent viscous damping values increase with an increase in maximum cyclic strain as is expected since the hysteresis area increases with an increase in maximum strain. For the 19.1 mm and 12.7 mm diameter specimens, the equivalent viscous damping decreases with continued cycling at 6% strain. The equivalent viscous damping for the 19.1 mm diameter bar decreases from 2.8% to 2.1% and the for the 12.7 mm diameter bar decreases from 3.6% to 3.0%. These drops in damping capacity are similar to those seen during the cyclic tests. Likewise, the equivalent viscous damping for the cyclic tests is also greater for the smaller diameter specimen (higher amount of deformation processing) as compared to the mid-size bar. Overall, the maximum equivalent viscous damping values are fairly low for seismic applications in structures.

3.6.3 Dynamic Tests

Given the dynamic nature of earthquakes, it is also important to discern any effects associated with dynamic loadings on the cyclic properties of large diameter NiTi SMAs. This is of particular importance given the fact that previous studies have led to conflicting conclusion on the effects of dynamic loadings. Tobushi et al. (1998) showed that strain rates above 0.16% strain per second resulted in an increase in the energy dissipation. However, at high frequencies above 1.0% strain per second, Wolons et al. (1998) found that the energy dissipation capacity decreased significantly. DesRoches et al. (2004) and Dolce and

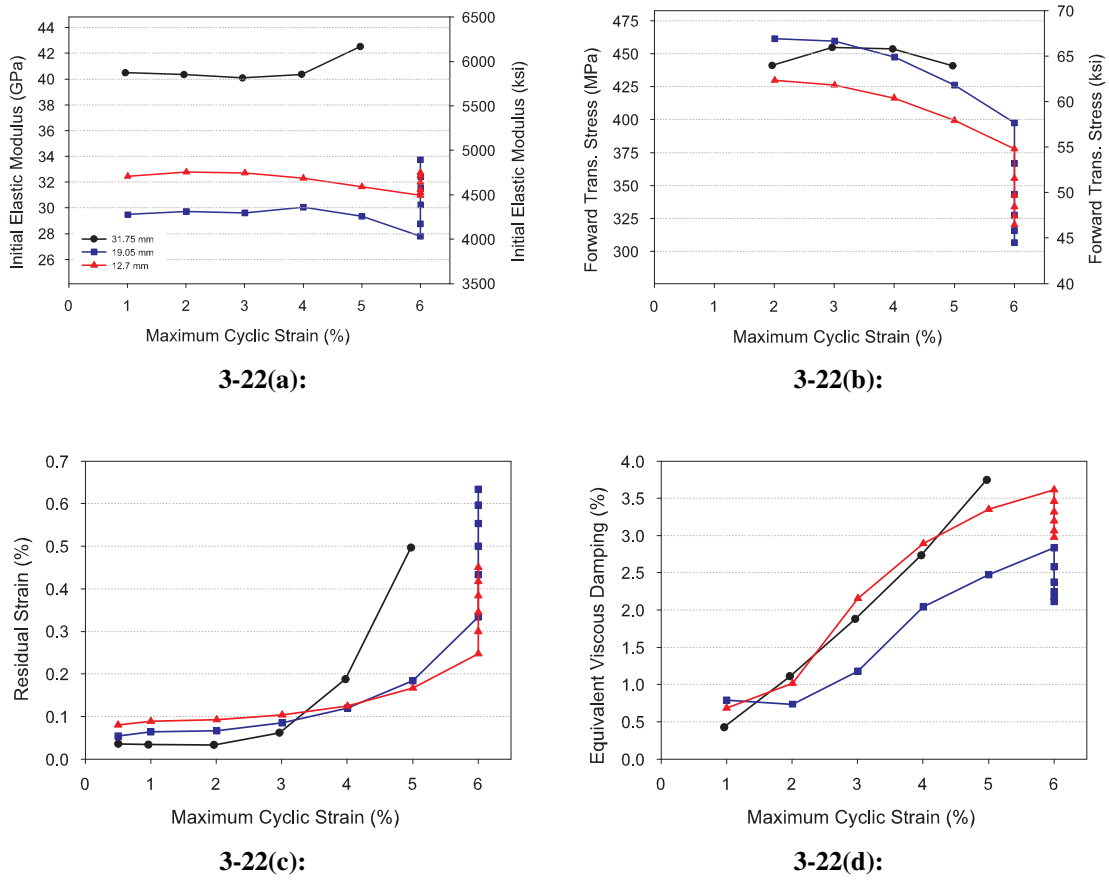

Figure 3-22: Comparison of the NiTi bars subjected to the quasi-static earthquake loading with respect to maximum cyclic strain: (a) initial elastic modulus, (b) forward transformation stress, (c) residual strain, and (d) equivalent viscous damping.

Cardone (2001) found similar results to those of Wolons in the dynamic study of NiTi bars and wires, respectively. In order to examine strain rate effects, two dynamic loading rates are considered, 0.5 Hz and 1.0 Hz. The results for the 19.1 mm diameter bar are the focus of this section, but similar observations have been made for the 31.8 mm and 12.7 mm diameter bar specimens.

Figure 3-23 contains the stress-strain plots for representative 19.1 mm diameter specimens tested under a quasi-static loading (0.025 Hz), dynamic 0.5 Hz loading, and dynamic 1.0 Hz loading. The first thing to note from these results is that all of the plots show good superelastic behavior with residual strain remaining low and a clear flag-shape hysteresis present. In all cases, the effect of the formation of the secondary R-phase is present in the early strain cycles suggesting that loading rate does not have any significant influence on its formation. The initial forward transformation stresses are similar for all three specimens with value of 457 MPa, 474 MPa, and 481 MPa at the 2% strain cycle for the quasi-static, 0.5 Hz, and 1.0 Hz loading rates, respectively. It is clear from the stress-strain curves that this is not true for the last 6% strain cycle where it is obvious that the forward transformation stress decreases by a much greater amount for the specimen cycled quasi-statically. The reverse transformation stress is also significantly influenced by the loading rate. The reverse transformation occurs at a much higher stress level for the specimens cycled under the dynamic loading rates. This results in a significant narrowing of the hysteresis with an increase in loading rate which also suggests a decrease in the hysteretic energy dissipation at higher loading rates.

The limited increase in the forward transformation stress for the dynamic specimens as compared to the quasi-static specimen and the greater increase in the reverse transformation

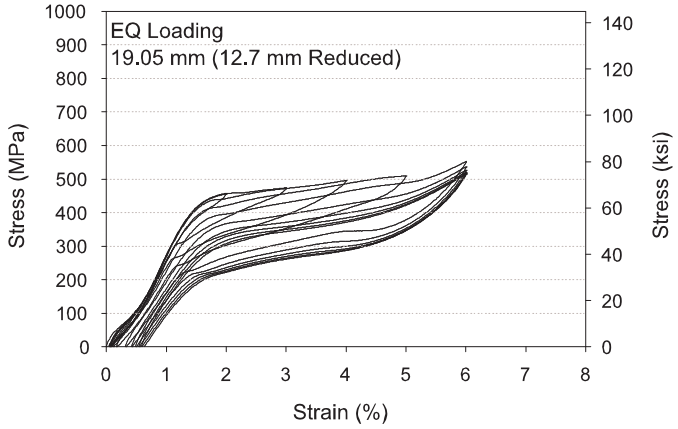

3-23(a):

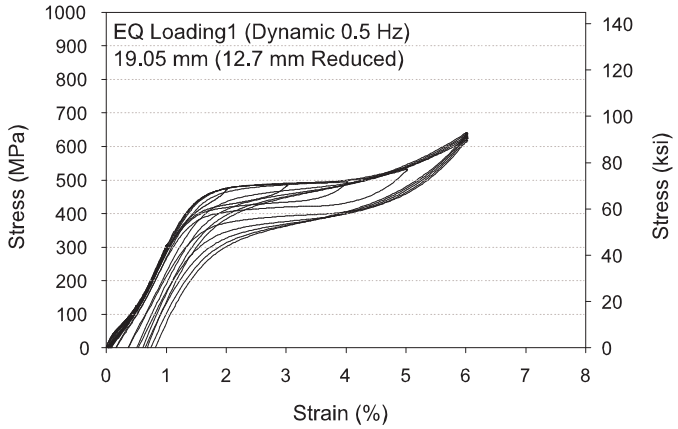

3-23(b):

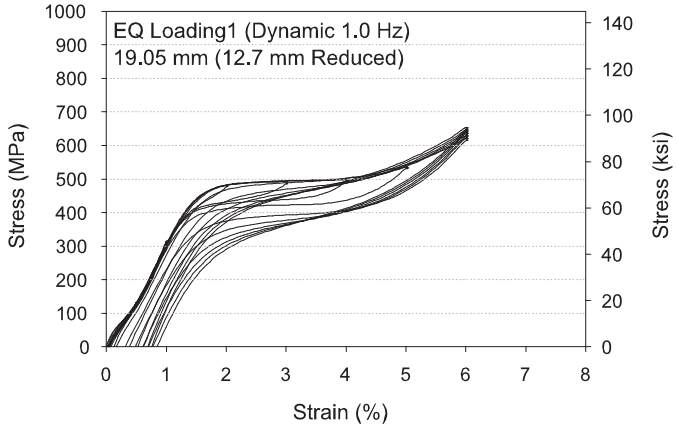

3-23(c):

Figure 3-23: Stress-strain curves for the 19.1 mm diameter specimens cycled under the earthquake type loading at various loading rates: (a) quasi-static, (b) dynamic (0.5 Hz), (c) dynamic (1.0 Hz)

stress can be attributed to a self heating of the specimen as a result of the dynamic loadings. As a result of the high loading rate not allowing the generated heat to dissipate and the fact that the martensitic phase transformation is an endothermic/exothermic process (as seen by the DSC results), the temperature of the bars increases. Combining this increase in temperature with the thermomechanical nature of NiTi, the increase in temperature acts as a decrease in stress therefore requiring large stresses to be applied to cause the phase transformation. The increase in temperature in the bars is apparent in the temperature measurements (Figure 3-24) taken at the surface of the bars using the pyrometer. In the case of the dynamic specimens, not only is there a fluctuation in the temperature as a result of the exothermic-endothermic reaction depending on whether the forward transformation is occurring or the reverse transformation, but there is also an overall increase in the average temperature of the bar with continued cycling. At a loading rate of 0.5 Hz, the temperature increases from approximately 31 °C to approximately 36 °C while for the 1.0 Hz loading the temperature increases from approximately 30 °C to 35.5 °C. For the quasi-static test, the average temperature remained fairly constant at approximately 34 °C.

Figure 3-25 provides the changes in the initial elastic modulus, forward transformation stress, residual strain, and equivalent viscous damping with respect to maximum cyclic strain and loading rate for the 19.1 mm diameter specimens. In all cases, the trends with respect to maximum cyclic strain follow those that are found for the quasi-static case discussed in detail in Section 3.6.2. In terms of strain rate effects, trends associated with each of the four properties are apparent. The initial elastic modulus increase with an increase in strain rate from 29.7 GPa for the quasi-static case to 32.8 GPa for the 1.0 Hz dynamic

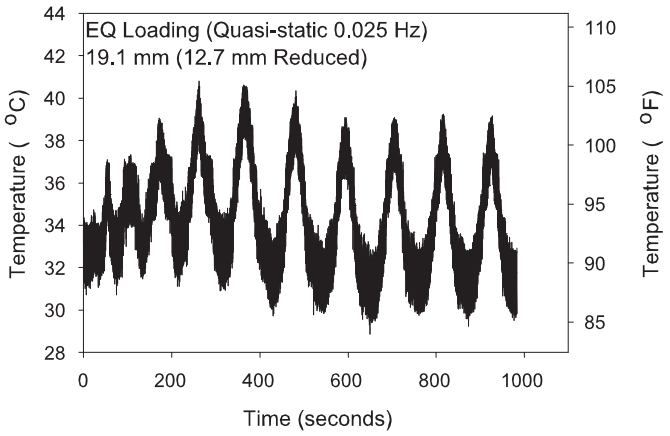

3-24(a):

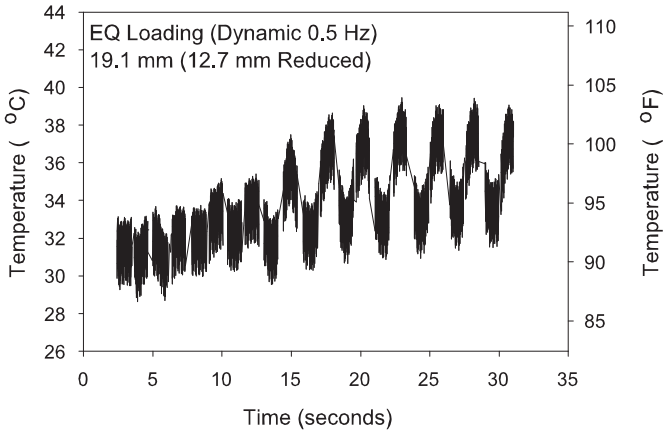

3-24(b):

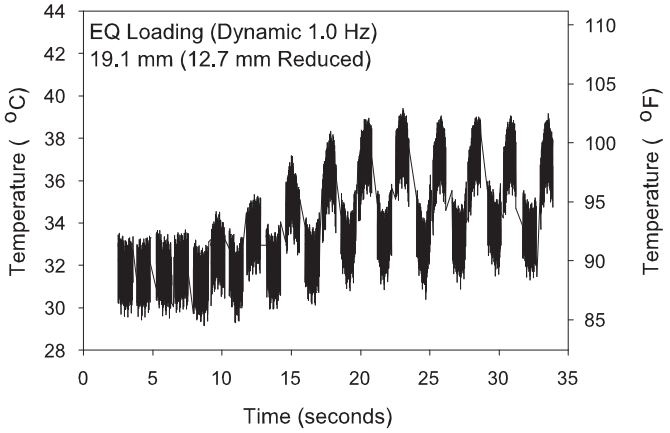

3-24(c):

Figure 3-24: Surface temperature readings taken during the earthquake loading tests of the 19.1 mm diameter specimens cycled at various loading rates (a) quasi-static, (b) dynamic (0.5 Hz), (c) dynamic (1.0 Hz)

case at the 2% strain cycle resulting in an overall increase of 10%. This is important because it suggests that a structure implementing NiTi for seismic applications will actually stiffen during dynamic loadings. The difference between the elastic modulus increases by 42% for the last 6% strain cycle. A similar trend is found with the forward transformation stress where, as was previously mentioned, the forward transformation stress increases with an increasing loading rate, but decreases with continued cycling. The overall decrease in the forward transformation stress from the 2% strain cycle to the last 6% strain cycle is approximately 33% for the quasi-static case and only 24% for the 1.0 Hz dynamic case. By cycling the specimen dynamically, the degradation of the forward transformation stress decreases as well. The residual strain measurements only show a small strain rate effect during the initial cycles where the quasi-static specimen has larger residual strains. However, this trend is reversed during the 6% strain cycles with the dynamic specimens having final residual strains of 0.88% and 0.83% (1.0 Hz and 0.5 Hz rates) while the specimen cycled quasi-statically only accumulated 0.63% residual strain. Although cycling dynamically led to higher residual strains, the values still suggest that good recentering capability can be obtained. Finally, as expected, the equivalent viscous damping decreases with an increase in strain rate as a result of the increase in the reverse transformation stress. This trend leads to maximum equivalent viscous damping values of 1.9%, 1.9%, and 2.8% for the 1.0 Hz case, 0.5 Hz case, and quasi-static case. In general, the results suggest that the dynamic properties of NiTi SMAs need to be accounted for when implementing them into structural systems.

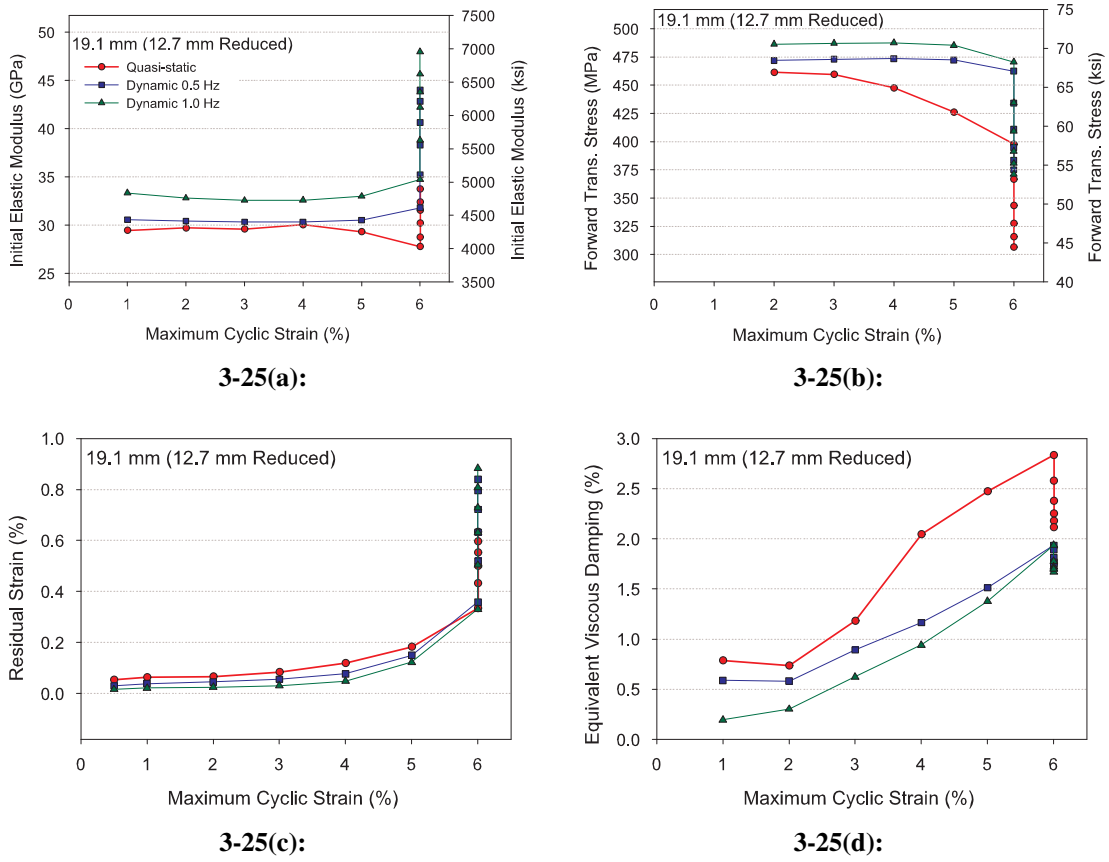

Figure 3-25: Comparison of the 19.1 mm NiTi bars subjected to the quasi-static, dynamic 0.5 Hz, and dynamic 1.0 Hz earthquake loading with respect to maximum cyclic strain: (a) initial elastic modulus, (b) forward transformation stress, (c) residual strain, and (d) equivalent viscous damping.

3.7 Closure

This chapter presents results from a multi-scale study of hot-rolled NiTi large diameter specimens for use in earthquake engineering applications. First, a material characterization of the bars is completed which includes TEM imaging, EBSD measurements, DSC testing, and hardness testing to look at the effect which various heat treatments and the amount of deformation processing have on deformation processed NiTi bars. Following the material characterization, mechanical behavior tests are completed to look at scaling effects between coupon specimens and full-scale specimens tested under cyclic tensile loadings. Given the intended use of the NiTi SMAs in structural applications, the bars are then tested in tension under an earthquake type loading at various loading rates in order determine any bar size effects, unequal loading cycle effects, and strain rate effects. The results suggest that hot-rolled NiTi specimens can provide adequate superelastic behavior to be implemented into structural engineering applications as recentering devices. The results further provide a template for obtaining the optimal behavior in terms of transformation temperature, recentering capability, and strength of hot-rolled large diameter NiTi bars.

CHAPTER IV

ADVANCED MATERIALS TESTING FOR SEISMIC APPLICATIONS

4.1 Introduction

Based on the findings in Chapter 3 and past studies (see Section 2.4), superelastic NiTi shape memory alloys have shown potential for use in civil and structural applications by aiding in controlling structural response during a seismic event. The recentering capability and added supplemental damping provide a unique means of passive control in structures. Although the cyclic properties of NiTi appear to be favorable for structural applications under the considered far-field type motion, there are other issues that need to be considered before NiTi devices can be developed for seismic resistant design. These issues include the degradation of the SMA properties with continued cycling, the low level of hysteretic damping, and the randomness associated with different earthquake types. In part, these issues have limited widespread use of NiTi SMAs in civil and structural engineering where the behavior of passive control devices needs to be predictable even under a random loading with maximum energy dissipation applied so as to limit damage in critical structural members. The problem lies in the fact that very few studies have focused on the unique civil engineering and structural engineering needs.

This chapter addresses this gap in knowledge by performing a variety of experimental studies on NiTi wire specimens in order to optimize their properties for seismic applications. The first set of tests provides information in regards to mechanically training NiTi in order to obtain stable properties. Since it has been suggested that pre-straining SMA wires can provide a more optimal behavior for seismic applications as a result of the wires remaining in tension under a larger strain range, the effect of pre-straining NiTi wires is then studied in order to determine the optimal pre-strain level to provide high damping capacity and recentering capability. Finally, the influence of different types of earthquake loadings, near-field versus far-field, is considered in order to determine how SMAs behave under large initial strain cycles as compared to gradually increasing strain cycles. All three of these studies focus on optimizing the properties of NiTi SMAs for seismic applications in civil engineering structures by studying means of improving these properties as suggested by past researchers, but have never been fully explored.

4.2 Material and Setup

Superelastic near-equiatomic NiTi wire is used throughout the advanced materials testing. Although the previous chapter focused on large diameter NiTi specimens, it is currently too expensive to test the number of previously uncycled NiTi bars needed in order to perform the training tests, pre-straining tests, and earthquake loading tests. Since the large diameter bars show good superelastic behavior and an understanding has been gained in terms of possible size effects, it is believed that many of the conclusions made while testing the wire specimens can be extrapolated to the larger diameter specimens. Also, the results from the wire tests allow for more efficient and refined advanced testing of the larger diameter

specimens in the future and thus reduce the financial burden of testing these large diameter specimens.

Two batches of 2.16 mm diameter NiTi redraw wire provided by the same manufacturer are used throughout this study. The first batch of 2.16 mm NiTi wire is used to perform the preliminary full-factorial and response surface training study and had a total length of 15.24 m. The second batch of NiTi wire is used to perform the pre-straining study and earthquake loading study and has a total length of 37.2 m. All specimens for a given test are obtained from the same batch so as to avoid biasing the results due to variability in the manufacturing and processing. Both batches of wires are as cold drawn, 40% cold worked, and have an oxide free pickled surface. As a result of variability in the manufacturing process, there is a slight difference in the A_s value between the two batches ($-20\,^{\circ}$C for the first batch and $-19\,^{\circ}$C/$-18\,^{\circ}$C for the second batch). This small difference in A_s does not have a large effect on the cyclic properties of the NiTi wire. For all of the advanced material studies, the wire specimens are cut to a length of 165.1 mm. This length allows for a nominal gage length of 63.5 mm with a gripping length of 50.8 mm on either side as can be seen in Figure 4-1. All specimens for a given test are annealed together for 30 minutes at $350\,^{\circ}$C and immediately water quenched to ensure good superelastic properties during testing. Details in regards to the selection of this annealing temperature can be found in Barbero-Bernal (2004).

All testing of the 2.16 mm diameter NiTi SMA wire is done using the same 250 kN MTS hydraulic testing frame described in Section 3.4.1 fit with hydraulic wedge grips. In order to facilitate gripping of the wires, flat specimen wedges are used due to the small diameter of the wire. All loading protocols are input using an MTS TestStar controller running

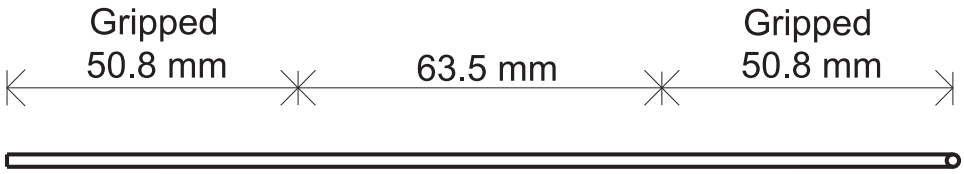

Figure 4-1: Schematic of the 2.16 mm diameter wire used for the advanced materials test.

TestWare-SX software with the actuator running in strain control based on the feedback from a 25.4 mm gage length extensometer. The load is measured by the internal 250 kN load cell. Specific loading protocols and test conditions are discussed with each test. A picture of the tests setup with a wire specimen can be seen in Figure 4-2.

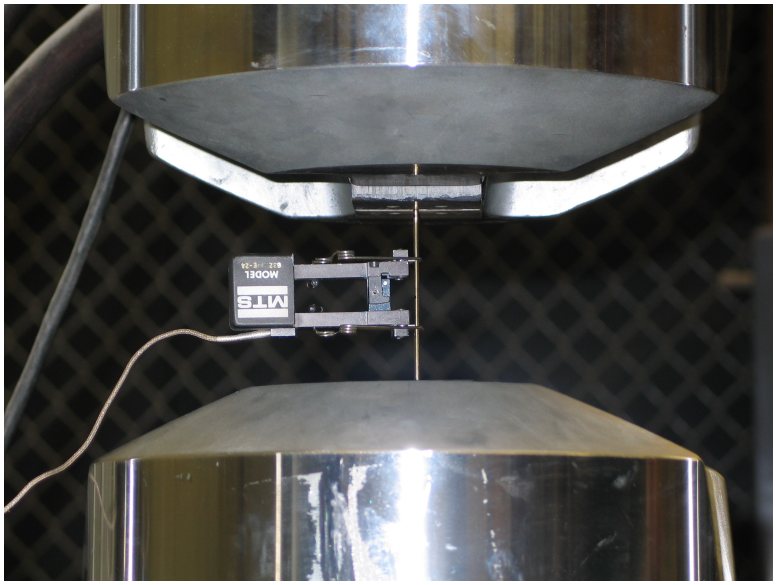

Figure 4-2: Close-up view of the wire test setup with the extensometer attached.

4.3 Mechanical Training of NiTi Wires

In order to effectively implement superelastic NiTi SMAs into civil and structural applications, stable properties are typically required in order to meet performance-based guidelines ensuring a predictable and reliable behavior of a structure during a seismic event. The results from the large diameter bar tests in Chapter 3 show degradation in the forward transformation stress, residual strain, and equivalent viscous damping with continued cycling as a result of fatigue effects. Miyazaki et al. (1986a) and Tobushi et al. (1998) have recommended "training" or preloading superelastic SMAs in order to limit fatigue effects and degradation of the properties. However, neither of these studies have looked into the optimal number of training cycles or the optimal training cycle strain level necessary to best limit fatigue effects. This study addresses this through a two-phase study consisting of an initial full-factorial study which is followed by a response surface study in order to gain an understanding of how the number of training cycles and strain level of the training cycles affect the properties themselves and the stabilization of those properties with continued cycling.

4.3.1 Method

The general approach taken for the mechanical training tests is to use design of experiment techniques to determine the important factors in stabilizing the properties of NiTi SMAs with continued cycling. In order to do this, two sets of loading protocols are used. The first set of loading protocols is the training cycles and consists of a specified number of constant strain cycles to a specified constant strain level. The training loading protocol is run at a constant strain rate of 1.5% strain per second so as to remove the training rate as a factor

from the problem. The second set of protocols consist of the earthquake loading consisting of tensile strain cycles of 0.5%, 1.0-5.0%, by increments of 1.0%, followed by six cycles up to 6% strain which can be seen in Figure 4-3. The earthquake loading protocol is run at either 0.025 Hz or 0.5 Hz for the preliminary full-factorial study and run at 0.5 Hz for the response surface study. For both studies, all specimens are first mechanically trained based on the experimental design parameters. After all of the specimens are trained for a given study, they are individually retested using the earthquake loading protocol. The cyclic properties associated with the earthquake loading are subsequently used to evaluate each training factor.

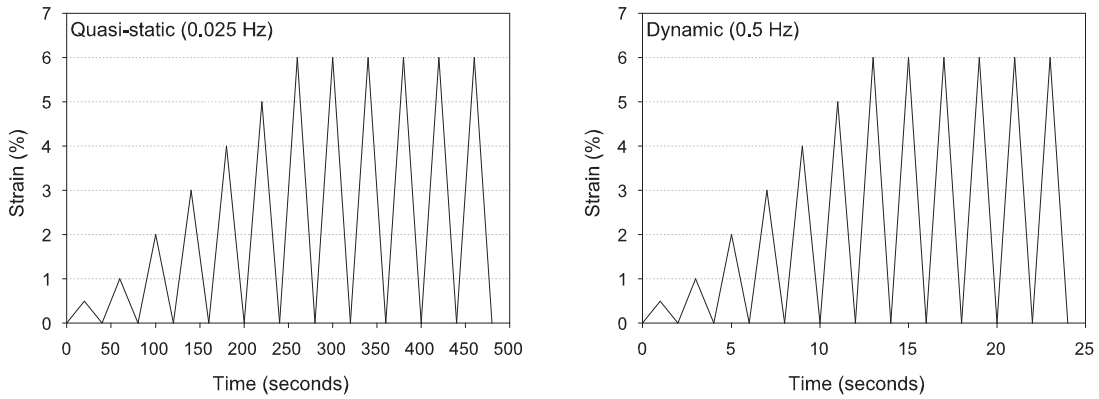

4-3(a): **4-3(b):**

Figure 4-3: Earthquake loading protocols for the (a) 0.025 Hz quasi-static case and (b) 0.5 Hz dynamic case.

4.3.2 Untrained Wire Tests

Before looking at the effects of mechanically training the 2.16 mm NiTi wire, it is important to understand the stress-strain behavior of the untrained specimens undergoing the

earthquake loading protocol. Figure 4-4 shows the stress-strain curves for two of the 2.16 mm diameter NiTi specimens undergoing the previously mentioned earthquake loading protocol (Figure 4-3) at a loading rate of either 0.025 Hz and 0.5 Hz. Both sets of stress-strain curves provide good superelastic behavior, although each shows a decrease in the forward transformation stress, a decrease in equivalent viscous damping, and an increase in the residual strain with continued cycling. Looking at the first and last 6% strain cycles for the quasi-static case, it can be seen that the forward transformation stress and equivalent viscous damping values decrease from approximately 470 MPa and 3.02% to 376 MPa and 2.36%. The residual strain increases from approximately 0.27% to approximately 0.45% from the first 6% strain cycle to the last 6% strain cycle. This results in an overall degradation of 20%, 22%, and 63% for the forward transformation stress, equivalent viscous damping, and residual strain, respectively, during the six 6% strain cycles when cycled quasi-statically. Similar changes in the forward transformation stress, equivalent viscous damping, and residual strain of the NiTi specimen cycled at a loading rate of 0.5 Hz are also found, resulting in an overall degradation of approximately 9%, 29%, and 34%, respectively. It is the purpose of this study to determine the optimal mechanical training protocol to reduce the percent change in the properties with continued cycling. Table 4-1 provides further details of the cyclic properties of the untrained wires.

4.3.3 Preliminary Full-Factorial Study

A full-factorial design is chosen as the best way to initially explore the effects that several variables associated with mechanically training NiTi SMAs can have on the mechanical

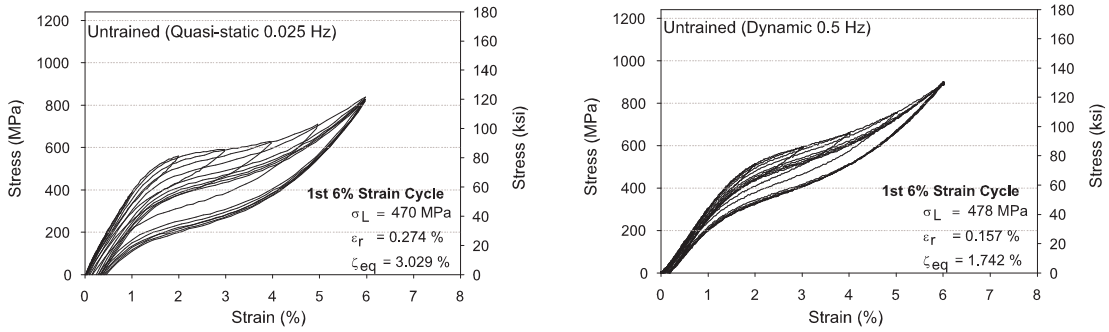

4-4(a): **4-4(b):**

Figure 4-4: Stress-strain curves for untrained NiTi wire specimens cycled at (a) 0.025 Hz (quasi-static) and (b) 0.5 Hz (dynamic).

Table 4-1: Cyclic Properties of Untrained Specimens for Selected Cycles

Cyclic Property	3% cycle	1st 6% cycle	6th 6% cycle	% difference (6% strain cycles)
Quasi-Static (0.025 Hz)				
Forward Trans. Stress	551 MPa	470 MPa	376 MPa	20%
Equiv. Visc. Damp.	1.93%	3.02%	2.36%	22%
Residual Strain	0.06%	0.27%	0.45%	63%
Dynamic (0.5 Hz)				
Forward Trans. Stress	511 MPa	478 MPa	435 MPa	9%
Equiv. Visc. Damp.	1.05%	1.74%	1.23%	29%
Residual Strain	0.06%	0.16%	0.21%	34%

behavior of the material, particularly the stability of the properties over a number of cycles. The two-level, full-factorial design which is implemented allows for a fixed number of levels, two, to be chosen for each variable or factor being studied. A low and high level is chosen for each factor based on engineering judgment in order to evaluate the setting of each factor which provides the optimal mechanical behavior of the NiTi wire for seismic applications. The direct advantage of using a full-factorial study given the relatively small number of factors being studied is that both the main effect and interaction effects of the variable can be studied simultaneously through a balanced and orthogonal design. A balanced design refers to the fact that all factor levels appear in the same number of runs and an orthogonal design refers to the fact that all level combinations appear in the same number of runs (Wu and Hamada, 2000).

Three factors are studied as part of this preliminary study. These factors include the number of mechanical training cycles, the strain level up to which these training cycles are applied, and the loading rate of the earthquake loading protocol. This last factor does not present information with regards to the actual optimal training protocol, but is rather used to see if there is a difference between trained specimens cycled quasi-statically versus those cycled dynamically. The NiTi wires are either mechanically cycled 20 or 60 times up to strain levels of either 3.0% or 5.0%. The number of cycles are arbitrarily chosen based on what has been considered a small number of cycles and a larger reasonable number of cycles in past research. The low value for the strain level is chosen such that the wire specimen has just started the detwinning process (martensitic phase transformation) from austenite to detwinned martensite placing it just into the loading plateau along the stress-strain curve. The high strain level is chosen such that the specimen has been fully

Table 4-2: Factors and Factor Levels for the Preliminary Mechanical Training Study

Level	Number of Cycles	Strain Level (%)	Post Training Loading Rate (Hz)
-	20	3	0.025
+	60	5	0.05

Table 4-3: Design Matrix for the Preliminary Mechanical Training Study

Number	Number of Cycles	Strain Level	Post Training Loading Rate
1	-	-	-
2	-	-	+
3	-	+	-
4	-	+	+
5	+	-	-
6	+	-	+
7	+	+	-
8	+	+	+

transformed to its detwinned martensite phase. After mechanically training the specimens under these factor levels, each specimen is removed from the testing apparatus and then retested either quasi-statically (0.025 Hz) or dynamically (0.5 Hz) under the earthquake loading protocol. Table 4-2 shows a summary of the factors and factor levels.

The design matrix for this experiment can be seen in Table 4-3 where the minus and plus signs represent the low and high level of each variable. One replicate is made for each factorial combination, resulting in 16 total runs, in order to provide some estimate of the error associated with the results. Randomization is also used in determining the run order so as to reduce the effects of lurking variables outside the control of the experiment. Since the recentering, force transfer, and damping capacity of NiTi SMAs are critical for seismic design and retrofit applications of the material, the average value of the replicated runs is

analyzed with respect to residual strain, equivalent viscous damping, and loading plateau stress at the 3% strain cycle, first 6% strain cycle, and sixth 6% strain cycle. The percent difference between the first 6% strain cycle and sixth 6% cycle is also studied for each of the properties in order to determine how the factors effect the stability of these properties over several cycles. The main effects of each variable for each of the properties is compared by looking at the difference between the high level <z(+)> and low level <z(-)> averages as can be seen in Equation 4.1 (Wu and Hamada, 2000).

$$ME(A) = \bar{z}(A+) - \bar{z}(A-) \tag{4.1}$$

While the interaction effects can be calculated based on Equation 4.2 (Wu and Hamada, 2000).

$$INT(A,B) = \frac{1}{2}\left\{\bar{z}(B+ \mid A+) - \bar{z}(B- \mid A+)\right\} - \frac{1}{2}\left\{\bar{z}(B+ \mid A-) - \bar{z}(B- \mid A-)\right\} \tag{4.2}$$

4.3.3.1 Stress-Strain Results

The stress-strain curves for four of the trained specimens which are cycled quasi-statically under the earthquake loading protocol are shown in Figure 4-5. The remaining stress-strain curves for the specimens cycled quasi-statically can be seen in Appendix B. Even after training, all specimens still show good hysteretic behavior and recentering capabilities suggesting that trained NiTi specimens are a viable material for seismic resistant design and retrofit of structures. The plots do show that training at any of the four levels does affect the shape of the stress-strain curve. In particular, the loading plateau is less apparent and the hysteretic area tends to shrink for all training combinations. The degradation of the

properties in each case also has decreased due to the training protocol. In particular, the wires cycled up to 5% strain during training show more consistent properties as compared to those specimens cycled to only 3% strain during training.

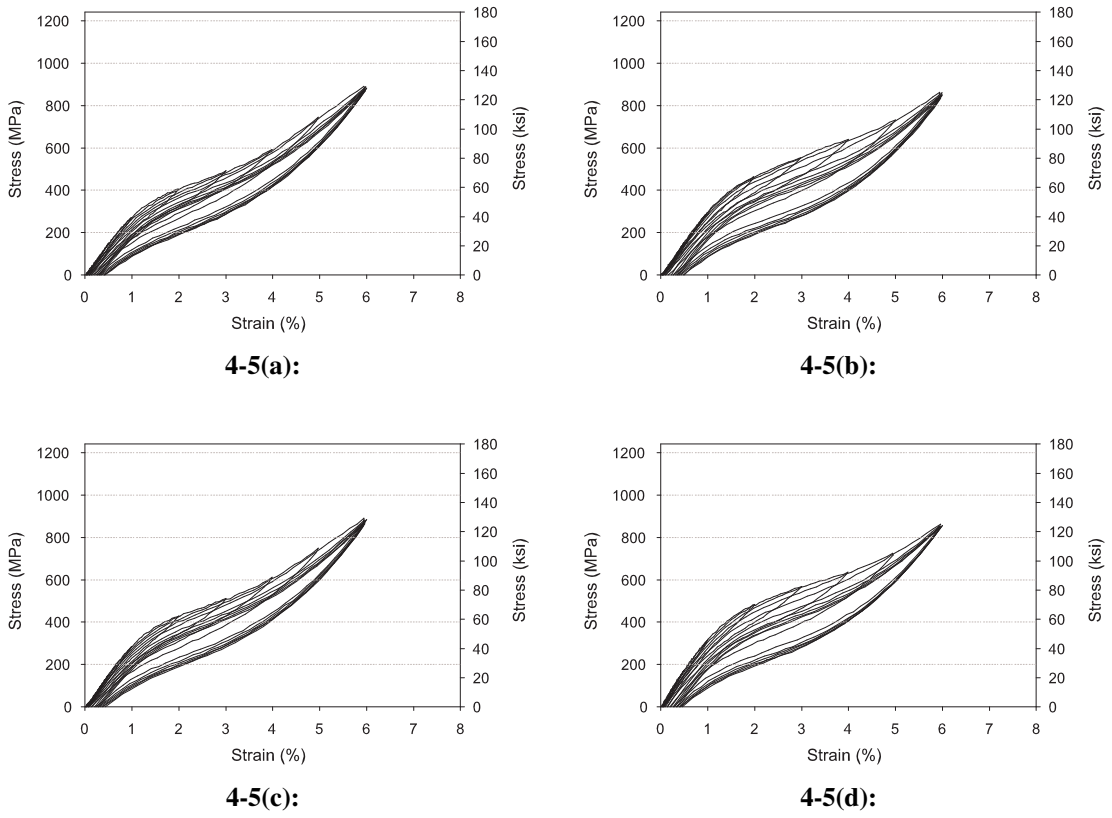

Figure 4-5: Stress-strain curves for the trained NiTi wire specimens undergoing the quasi-static earthquake loading (a) 60 cycles at 5% strain, (b) 60 cycles at 3% strain, (c) 20 cycles at 5% strain, and (d) 20 cycles at 3% strain.

Four of the stress-strain curves for the trained NiTi specimens which are cycled dynamically at 0.5 Hz under the earthquake loading protocol are shown in Figure 4-6. All of the stress-strain curves for the trained specimens cycled dynamically can be found in Appendix B. As with the stress-strain curves for the specimens cycled at 0.025 Hz, the

dynamically cycled trained specimens show good superelastic behavior. Each of the four training combinations appears to decrease the degradation of the properties with continued cycling, although those specimens which are trained using tensile cycles up to 5% strain appear to have much smaller differences in properties with continued cycling and appear to provide smaller residual strain values in general. The smaller residual strain values suggest a more consistent recentering capability from these specimens.

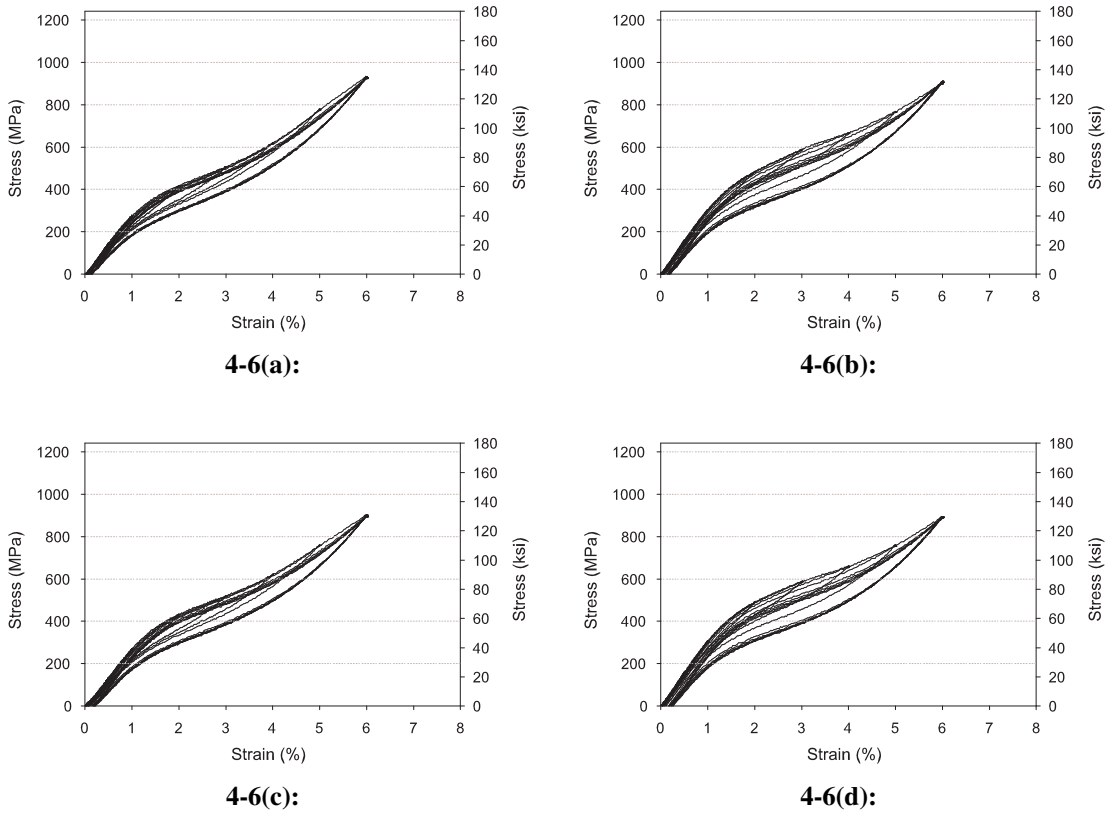

Figure 4-6: Stress-strain curves for the trained NiTi wire specimens undergoing the dynamic 0.5 Hz earthquake loading (a) 60 cycles at 5% strain, (b) 60 cycles at 3% strain, (c) 20 cycles at 5% strain, and (d) 20 cycles at 3% strain.

Comparing the quasi-static results with the dynamic results, it is obvious that the higher cycling frequencies after training cause a decrease in the hysteretic area due to an increase in the unloading plateau stress (reverse transformation plateau) which results in lower equivalent viscous damping values. These are similar to the dynamic test results found for the large diameter bars in Chapter 3. The 0.5 Hz cycled specimens do have smaller residual strains associated with them as compared to the quasi-static specimens, suggesting superior recentering capabilities. Since earthquake loadings tend to be at higher frequencies, it appears that trained NiTi SMAs are also better suited for recentering applications rather than purely damping applications.

4.3.3.2 Main Effect Results

Now that the differences in the stress-strain plots have been recognized, main effects plots can be used to determine which factors are most significant in terms of the forward transformation stress, equivalent viscous damping, residual strain, and property stabilization between the first 6% strain cycle and sixth 6% strain cycle. The greater the slope of the main effect plot, the more significant the factor. Figure 4-7 provides the forward transformation stress main effect plots for all three of the factors for the 3% strain cycle, first 6% strain cycle, and last 6% strain cycle. The number of training cycles has very little influence on the forward transformation stress, while both the strain level of training and the loading rate of the loading protocol after training have a significant effect on the value of the forward transformation stress for all three of the strain cycles given the large slopes seen in these plots. When trained to higher strain levels, the forward transformation stress tends to decrease as expected given the trend of the forward transformation stress to decrease

with increased cycling. This can be seen on each of the individual plots. This degradation of the loading plateau can be associated with the formation of permanent dislocations and small levels of localized slip during cycling to large strains which assists the forward transformation process (Miyazaki et al., 1986a). The loading rate of the loading protocol after the training cycles are completed also has a significant effect on the forward transformation stress. Higher loading rates cause larger forward transformation stresses due to the formation of heat during cycling as is seen in the dynamic tests of the large diameter bars, although to a lesser extent with the wires. The main effect plots each show a decrease in the forward transformation stress with increased cycling from the 3% strain cycle to the first 6% strain cycle to the last 6% strain cycle suggesting that complete stabilization of the forward transformation stress may not be possible by mechanically training NiTi SMAs, although at larger loading rates and training at larger strain levels the degradation in the forward transformation stress is smaller.

Figure 4-8 shows the main effect plots with respect to the equivalent viscous damping value for the 3% strain cycle, first 6% strain cycle, and the last 6% strain cycle. The number of training cycles main effect plots all have small slopes showing that this factor has very little significance on the equivalent viscous damping value. The strain level of training and the loading rate of the loading protocol after training both show significant effects for the higher strain level cycles. Training to higher strain levels tends to decrease the equivalent viscous damping value, which confirms the results shown in Figure 4-5 and 4-6. The loading rate of the loading protocol after training has the most significance effect, dropping the equivalent viscous damping value by over 0.5% by cycling the specimens dynamically as

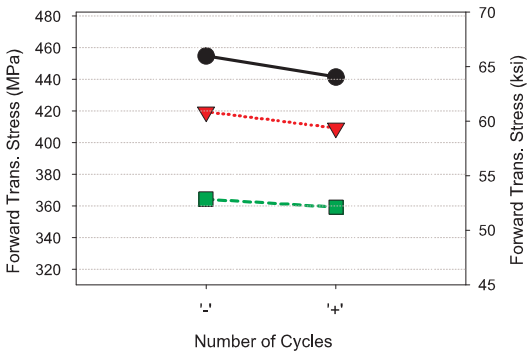

4-7(a):

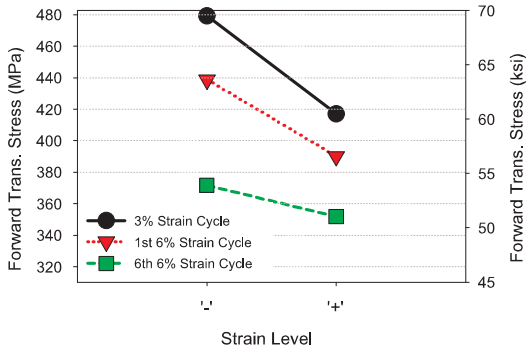

4-7(b):

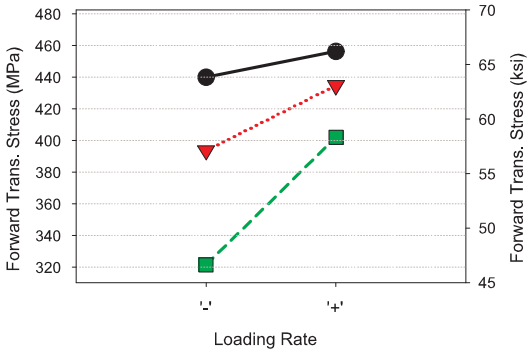

4-7(c):

Figure 4-7: Main effect plots based on the forward transformation stress (a) number of training cycles, (b) training strain level, (c) loading rate of the earthquake protocol.

compared to quasi-statically. None of the factors appear to be more significant in reducing the degradation in the equivalent viscous damping value when going from the first 6% strain cycle to the last 6% strain cycle, although training at higher strain levels does appear to reduce the degradation by a small amount.

The main effect plots (Figure 4-9) for the residual strain at the 3% strain cycle, first 6% strain cycle, and last 6% strain cycle show that both the number of training cycles and the strain level at which the training is conducted have minor significance on the residual strain value after undergoing a typical earthquake loading protocol. The results do show that by training for a larger number of cycles and larger cyclic strains, small decreases in the residual strain values can be obtained. The loading rate factor clearly has a significant effect on the amount of residual strain that is accumulated, particularly at the larger strain cycles. The reduction in residual strain for the 0.5 Hz cycled specimen versus the 0.025 Hz cycled specimen is approximately 0.25% for the sixth 6% strain cycle. This shows promise for the use of trained NiTi SMAs for seismic applications given that earthquake loadings occur at dynamic strain rates. There is also a small reduction in the residual strain values as compared to the untrained specimens shown in Figure 4-4. The main effect plots also show a trend of increasing residual strain with increased cycling which can be attributed to the formation of permanent dislocations.

As has been previously mentioned, the degradation of superelastic NiTi SMA properties has been one of the reasons for their slow acceptance as a viable earthquake mitigation material in structural engineering. It has been suggested that by mechanically training NiTi shape memory alloys more stable properties can be obtained. In order to evaluate whether mechanical training can help stabilize SMA properties, the difference in values between

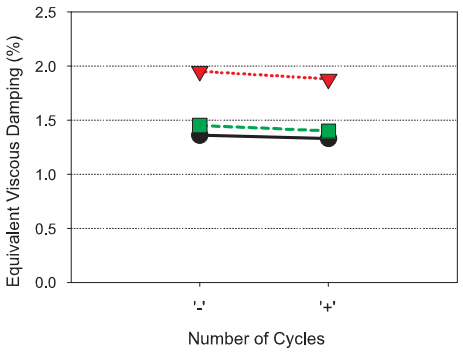

4-8(a):

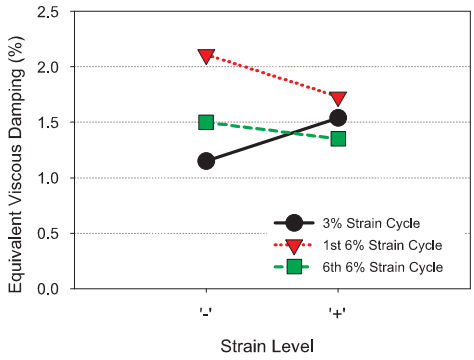

4-8(b):

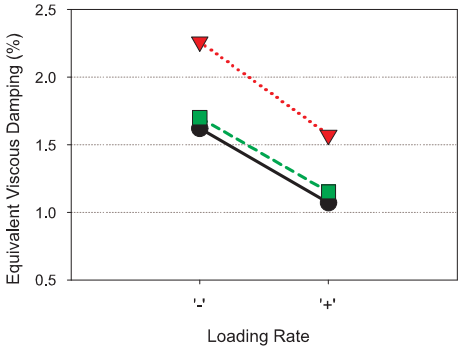

4-8(c):

Figure 4-8: Main effect plots based on the equivalent viscous damping (a) number of training cycles, (b) training strain level, (c) loading rate of the earthquake protocol.

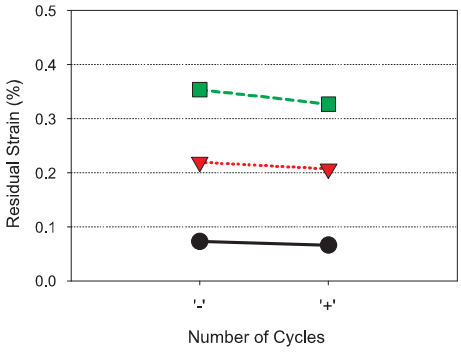

4-9(a):

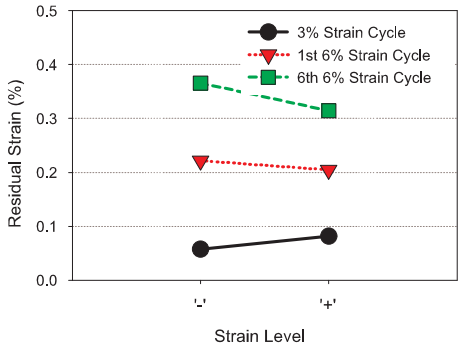

4-9(b):

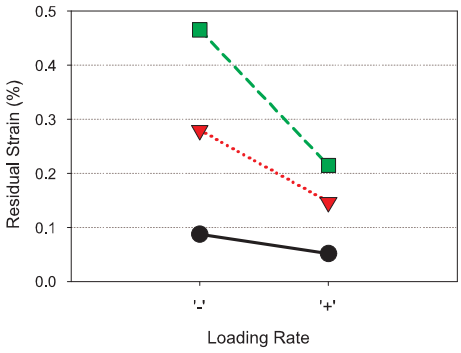

4-9(c):

Figure 4-9: Main effect plots based on the residual strain value (a) number of training cycles, (b) training strain level, (c) loading rate of the earthquake protocol.

the first 6% strain cycle and sixth 6% strain cycle for the forward transformation stress, equivalent viscous damping values, and residual strain values are compared with respect to the number of training cycles, strain level of training, and earthquake loading rate factors. The results of this comparison can be seen in the main effect plots shown in Figure 4-10. The first plot shows how each of the factors effects the percent change in the forward transformation stress. The loading rate of the loading protocol applied after training has the largest significance in stabilizing the forward transformation stress, but the high level of all three factors provides some stabilization. The strain level at which a specimen is trained has the largest effect in stabilizing the equivalent viscous damping properties, although a larger number of training cycles and lower strain rates after training can also provide more stable damping values. Both the strain level during training and the loading rate that the specimen undergoes during an earthquake have a significant effect on the stabilization of the residual strain value and the recentering capability of the material. The high values of all three of the factors acts to stabilize the residual strain capacity of NiTi SMA wires.

Comparing all three plots, it is clear that the number of training cycles has the least significance in stabilizing the mechanical properties of NiTi SMAs. Choosing a higher strain level for the training cycles works to stabilize all of the properties where a trade off between stabilizing the forward transformation stress and the residual strain versus stabilizing the equivalent viscous damping value must be made with respect to the loading rate undergone by the fully trained material. The results suggest that mechanically training NiTi shape memory alloys wires can help stabilize the properties of the material, but the loading rate on the trained or untrained material has the most significant effect on the degradation of its properties.

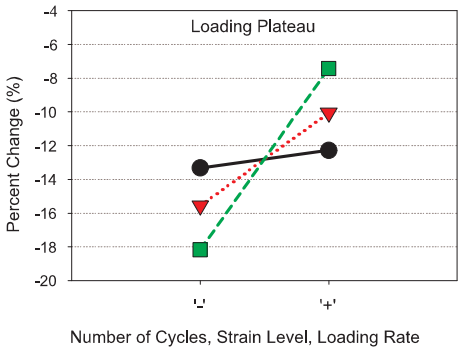

4-10(a):

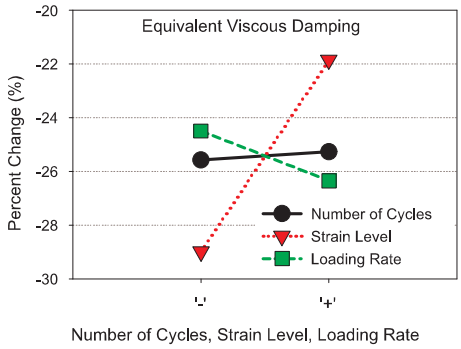

4-10(b):

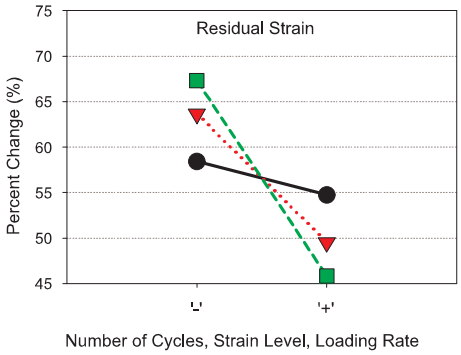

4-10(c):

Figure 4-10: Main effect plots comparing the ability of each factor to reduce change in the (a) forward transformation stress, (b) equivalent viscous damping , (c) residual strain between the first 6% strain cycle and sixth 6% strain cycle.

The ability of trained wires to stabilize the forward transformation stress, equivalent viscous damping, and residual strain can now be compared to the degradation of these same properties for the untrained wires shown in Figure 4-4. Since in all cases the high level for the number of cycles trained and strain level of training acts to reduce the degradation of the properties, the percent change results for the 60 cycles at 5% strain trained specimens can be compared to the untrained specimens cycled both quasi-statically and dynamically (0.5 Hz). For the quasi-static earthquake loading protocol, the trained specimens show percent changes of approximately 14%, 22%, and 54% for the forward transformation stress, equivalent viscous damping, and residual strain, respectively (see Table 4-4). The untrained specimen, as previously mentioned, has percent changes of 20%, 22%, and 63% for the same properties. The results show a clear stabilization in the forward transformation stress and the residual strain by training and no real change in the stabilization of the equivalent viscous damping value. Comparing the stabilization of the trained and untrained specimens cycled under dynamic loadings at a rate typical of an earthquake, it can be seen that the trained specimens have percent changes of 4%, 21%, and 35% (Table 4-4) and the untrained specimens show percent changes of 9%, 29%, and 34% for the forward transformation stress, equivalent viscous damping, and residual strain, respectively. Even at the higher loading rates, training of the specimens provides more stable properties, particularly with the forward transformation stress and equivalent viscous damping values.

Although this preliminary study shows promise for the use of SMAs in earthquake engineering by first mechanically training the material, more work needs to be done in order to better quantify the results. A closer look at larger numbers of training cycles and training to larger strain levels needs to occur. This is particularly important given that the results

Table 4-4: Cyclic Properties of Trained Specimens for Selected Cycles

Cyclic Property	1st 6% cycle	6th 6% cycle	% difference	
			Trained	Untrained
Quasi-Static (0.025 Hz)				
Forward Trans. Stress	361 MPa	310 MPa	14%	20%
Equiv. Visc. Damp.	2.01%	1.57%	22%	22%
Residual Strain	0.29%	0.44%	54%	63%
Dynamic (0.5 Hz)				
Forward Trans. Stress	402 MPa	386 MPa	4%	9%
Equiv. Visc. Damp.	1.31%	1.03%	21%	29%
Residual Strain	0.12%	0.15%	35%	34%

show that both factors are significant depending on the property that is being considered. One of the major outcomes of this preliminary full-factorial study is the knowledge that a simple mechanical training procedure can be used to reduce the degradation of those properties important for seismic applications when NiTi SMAs are trained for approximately 60 cycles to strain levels of approximately 5%.

4.3.4 Follow-up Response Surface Study

The preliminary full-factorial training study provides an initial understanding of the effect which mechanical training has on the cyclic properties of the NiTi wire and shows that both the number of training cycles and strain level of training are significant factors. The results suggest that training to a high strain level for a high number of cycles provides the most stable properties. In order to expand upon this work and gain a better understanding of the relationship between the response and the input factors (number of training cycles and strain level of training), a response surface study is used where a second order regression model is considered. Specific details on response surface methodology can be found in Wu and Hamada (2000). This response surface study looks at the effect of the different factor

levels on the stabilization of the properties important for seismic applications and provides an understanding of how the value of those properties change with different factor levels. Since the results from the preliminary study show that the loading rate of the earthquake loading protocol also effects the cyclic properties of the NiTi wire, a constant earthquake loading rate of 0.5 Hz is chosen given the dynamic nature of an earthquake.

The response surface study focuses on only two factors given the results from the preliminary study, the number of training cycles and the strain level of the training cycles. Since the preliminary study suggests that higher values for these factors provides better subsequent property stabilization, the high levels are increased to 80 cycles and 7% strain. The factor levels chosen can be seen in Table 4-5. A central composite design is used with an alpha value equal to 1 resulting in a face center cube design with 8 runs. This design is replicated once and four center point runs are added resulting in a total of 20 wires being tested. The response surface design matrix can be seen in Table 4-6 where "0" represents the center point between the high and low level, "-" represents the low level, and "+" represents the high level of a given factor. The testing procedure is similar to that used for the preliminary full-factorial study with all training being performed at a rate of 1.5% strain per second. The dynamic 0.5 Hz earthquake loading protocol used to study these trained specimens is shown in Figure 4-3(b). The stress-strain curves for all of the response surface specimens undergoing this loading protocol can be found in Appendix B. All subsequent analysis of the results is performed using MINITAB software (MINITAB, 2004).

Table 4-5: Factors and Factor Levels for the Follow-up Response Surface Mechanical Training Study

Factors	Low Level	High Level
Number of training cycles	40	80
Strain level of training cycles	3%	7%

Table 4-6: Design Matrix for the Follow-up Response Surface Mechanical Training Study

Number	Number of Cycles	Strain Level
1	-	-
2	-	0
3	-	+
4	+	-
5	+	0
6	+	+
7	0	-
8	0	+
9	0	0
10	0	0
11	-	-
12	-	0
13	-	+
14	+	-
15	+	0
16	+	+
17	0	-
18	0	+
19	0	0
20	0	0

4.3.4.1 Training Effects with Respect to the Cyclic Properties

The response surface study is first used to determine the effect which the different training protocols have on the forward transformation stress, equivalent viscous damping, and residual strain measured at the first 6% strain cycle. The first 6% strain cycle is chosen because it provides the typical values expected during the first large earthquake pulse. In order to look at these effects, a second-order regression analysis is used where the t-statistic or p-value provides information on the significance of a given coefficient. A coefficient is deemed significant based on a 95% confidence (α=0.05). Thus, a p-value less than 0.05 means the null hypothesis is rejected and the coefficient is significant. Further detail in regards to the regression analysis can be found in the work by Neter et al. (1996). For the forward transformation stress and equivalent viscous damping properties, the full regression equation is provided (including non-significant coefficients) for the purpose of completeness with the significant coefficients pointed out based on the regression results. The regression results provide a quantitative understanding of the effects which training to a specific number of cycles at a specific strain level have on the properties.

The regression results for the forward transformation stress measured during the first 6% strain cycle of the earthquake loading suggest that the strain level of the mechanical training cycles has the most significant effect on its value. The regression data shown in Table 4-7 provides the p-values for each of the terms. The p-value associated with the training strain level is the only one less than 0.05. In particular, the forward transformation stress decreases with an increase in the strain level at which the training cycles are run from greater than 480 MPa for training to 3% strain to below 345 MPa for training to 7%

Table 4-7: Regression Results for the Forward Transformation Stress

Term	Coef.	SE Coef.	T	P
Constant	63.42	1.88	33.69	0.000
Num. Cyc.	1.37	1.29	1.06	0.305
Strain	-12.49	1.29	-9.71	0.000
Num. Cyc.* Num. Cyc	0.43	2.06	0.21	0.838
Strain * Strain	-2.75	2.06	-1.34	0.203
Nu,. Cyc.* Strain	0.58	1.58	0.37	0.720

strain. This decrease can be associated with the formation of localized slip which tends to assist the forward transformation and is more prevalent as a result of cycling to large strain levels (Miyazaki, 1990; Miyazaki et al., 1986a; Tobushi et al., 1992b). This decrease in the forward transformation stress as a result of training needs to be taken into account in order to use trained NiTi SMAs in structural systems. In order to quantify the expected forward transformation stress over the factor range selected for this study, Equation 4.3 provides the second order regression equation where FTS refers to the forward transformation stress in ksi, NC refers to the number of training cycles (40 to 80), and SL refers to the training strain level (3% to 7%). The adjusted R-squared value is 82.9% suggesting an adequate fit to the response surface experimental data.

$$FTS(ksi) = 81.50 - 0.132(NC) - 0.221(SL) + 0.0011(NC)^2 - 0.69(SL)^2 + 0.014(NC)(SL) \tag{4.3}$$

Unlike the forward transformation stress results, both the number of training cycles and strain level of those cycles have a significant effect on the value of the equivalent viscous damping for the first 6% strain cycle with p-values of 0.003 and 0.000, respectively. The regression data can be seen in Table 4-8. Although both factors are significant, they do not show any significant second order effects based on the analysis of variance work. For a low number of training cycles and low strain level the equivalent viscous damping values are largest (>6%) while increasing the number of training cycles or increasing the strain level of training leads to a decrease in the equivalent viscous damping. This is consistent with the forward transformation stress results as a decrease in the forward transformation with increased strain levels typically leads to a decrease in the hysteretic area. This response surface study thus further confirms the findings of the preliminary study which show that any level of training leads to a decrease in the energy dissipation capacity of the NiTi wire. Equation 4.4 provides the regression equation with respect to the equivalent viscous damping for the first 6% strain cycle with an adjusted R-squared value of 85.6% suggesting a good fit with the measured results.

$$EQV(\%) = 1.80 - 0.010(NC) + 0.164(SL) + 0.0001(NC)^2 - 0.024(SL)^2 - 0.002(NC)(SL) \tag{4.4}$$

The first 6% strain cycle residual strain response surface study results show the number of training cycles to be the only significant factor. However, the model does not provide a good fit with an adjusted R-squared value of only 24.9% suggesting that the regression results do not provide an accurate idea of the expected residual strain values for trained

Table 4-8: Regression Results for Equivalent Viscous Damping

Term	Coef.	SE Coef.	T	P
Constant	1.21	0.06	21.49	0.000
Num. Cyc.	-0.14	0.039	-3.55	0.003
Strain	-0.39	0.039	-9.99	0.000
Num. Cyc.* Num. Cyc	0.04	0.06	0.71	0.489
Strain * Strain	-0.10	0.06	-1.56	0.142
Nu,. Cyc.* Strain	-0.08	0.05	-1.64	0.123

Table 4-9: Regression Results for Residual Strain

Term	Coef.	SE Coef.	T	P
Constant	0.15	0.17	8.64	0.000
Num. Cyc.	-0.03	0.011	-2.32	0.036
Strain	-0.02	0.011	-1.88	0.081
Num. Cyc.* Num. Cyc	-0.01	0.018	-0.35	0.733
Strain * Strain	0.004	0.018	0.19	0.849
Nu,. Cyc.* Strain	0.02	0.014	1.51	0.154

specimens. The lack of fit can be traced to the high variability in the experimental residual strain data which may be attributed to small amounts of slip in the extensometer. The regression results are shown in Table 4-9. As a result the regression equation is not reported here for the residual strain. However, some general trends with respect to the residual strain can be pointed out. In general, the residual strain remained low for the first 6% strain cycle with all trained specimens having residual strains between approximately 0.12% and 0.20%. Also, the residual strain tends to decrease for specimens that are trained for a larger number of cycles and at higher strain levels.

Comparing the values of the forward transformation stress, equivalent viscous damping, and residual strain for the first 6% strain cycle of the trained specimens to those of

the untrained specimens shown in Table 4-1 allows for the training effects to be distinguished. The untrained specimen cycled dynamically has a forward transformation stress of 478 MPa which is equivalent to those specimens trained to only 3-4% strain. As the training strain level increases, the difference in the forward transformation stress between the untrained and trained specimens increases. A similar result is found with the equivalent viscous damping, where a low number of training cycles and low strain level results in similar equivalent viscous damping values to an untrained specimen, approximately 1.7%. Because of the variation in the residual strain, it is difficult to discern any trend, but it is obvious that higher numbers of training cycles at higher strain levels reduces the residual strain below the values found for the untrained specimen, 0.16%.

4.3.4.2 Stabilization of Cyclic Properties

Besides the actual effect on the value of the forward transformation stress, equivalent viscous damping, and residual strain, the ability of mechanical training to stabilize these properties during the six 6% strain cycles is important. For all three properties, the training strain level is shown to be significant. Also, the training strain level appears to have a quadratic effect on the stabilization of the forward transformation stress. The number of training cycles is only significant in stabilizing the residual strain values meaning that both the number of training cycles and strain level of training need to be considered for recentering-type devices. For all three properties, the adjusted R-square values remained between 72% and 77% suggesting a reasonable fit of the regression equation to the experimental data. The regression chart and regression equation are not presented in this section as the specific percent difference between the first 6% strain cycle and sixth 6% strain cycle

for each of the properties has little value, but it is rather the trend that is of interest. As a result, contour plots are provided showing the regression results from the response surface study.

Figure 4-11 provides contour plots showing the regression results from the response surface study for the stabilization of the forward transformation stress, residual strain, and equivalent viscous damping during the six 6% strain cycles. The forward transformation stress contour plot suggests that the number of training cycles does not effect property stabilization which is confirmed by the analysis of variance results. When the specimen is trained at above approximately 5% strain for at least 40 cycles the decrease in the forward transformation stress is less than 2%. This result suggests that the formation of localized slip, which tends to assist the forward transformation, slows at a more rapid rate when the SMA is cycled to levels at which the martensitic transformation is completed causing a stabilization of the forward transformation stress (Miyazaki et al., 1986a). The residual strain results suggest that a stable recentering device can be obtained if the NiTi is first mechanically trained above 6% strain for at least 40 cycles. Prior training at lower cycles to higher strain levels tends to reduce the accumulation of residual strain with continued cycling, although the training strain level appears to have a much larger effect on stabilizing the accumulation of residual strain over the six 6% strain cycles than does the number of training cycles. The equivalent viscous damping results shown in Figure 4-11(c) also suggest that training at a higher strain level reduces degradation of the damping capacity of NiTi. However, the equivalent viscous damping does not stabilize to the extent of the other two properties as the damping capacity still decreases by 15% during the six 6% strain cycles. The results suggest that mechanically training superelastic NiTi for 40 cycles

to a strain level of 6-7% can drastically reduce the fatigue affects associated with all three properties. However, the effect of training on the actual value of each of the properties (discussed in Section 4.3.4.1) also needs to be considered.

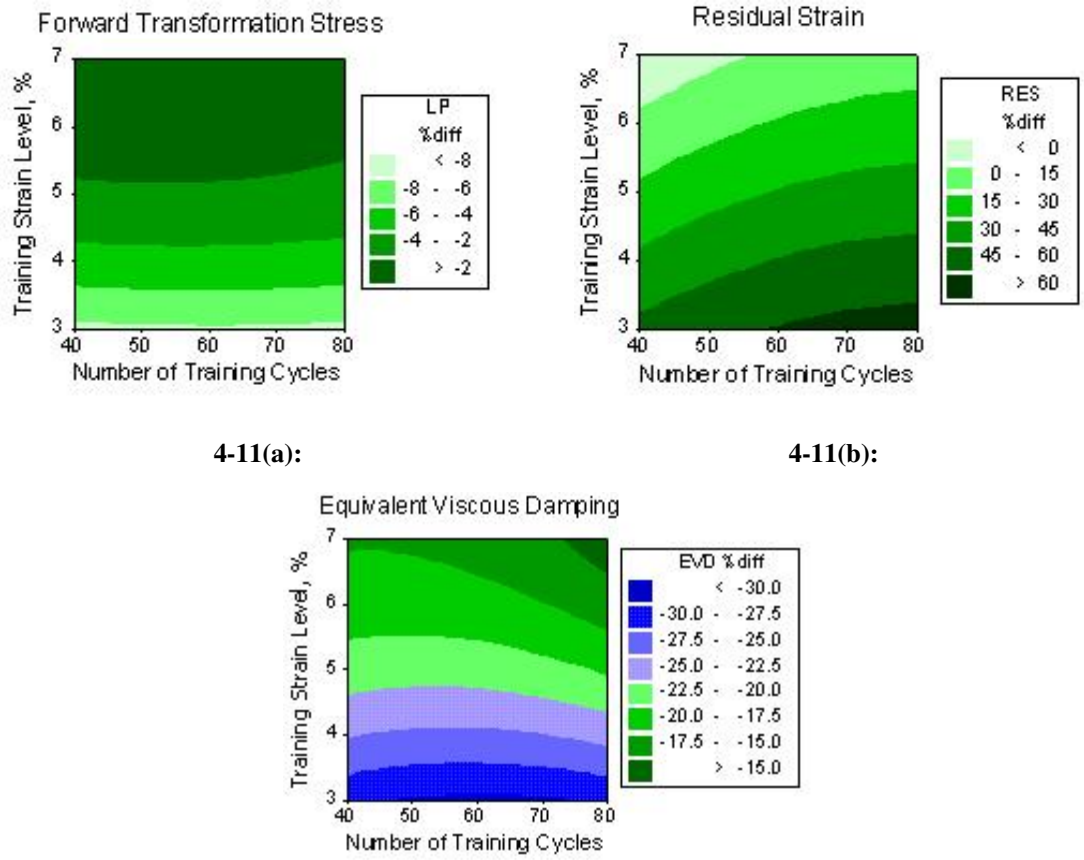

4-11(a): **4-11(b):**

4-11(c):

Figure 4-11: Response surface results showing the percent change in the (a) forward transformation stress, (b) residual strain, and (c) equivalent viscous damping values between the first and last 6% strain cycle of the earthquake loading with respect to the mechanical training factors.

4.4 Pre-straining Effects on NiTi Wires

Beyond mechanical training, it has also been suggested that pre-straining SMA wire can provide a more optimal behavior for seismic applications in civil engineering structures. This has been shown in recent studies which have implemented pre-strained SMA wires in a variety of experimental structural systems. Dolce and Cardone (2001) and Dolce et al. (2000) proposed pre-straining the SMAs to approximately 3.5% strain for their bracing system consisting of looped SMA wires to provide recentering, damping, or a combination of recentering and damping. As a result of this pre-strain level, the wires are always stressed in tension causing a wide hysteresis loop. Others have also found that the energy dissipation associated with SMA wires can be maximized by pre-straining the SMA wires resulting in a noticeable impact on the response of a structure (Aizawa et al., 1998; Saadat et al., 2001).

In general, pre-straining the NiTi ensures that the device engages even during small motions and can be designed so as to always act in tension. Thus, the device provides more control over the structural response. Pre-straining above the forward transformation stress (above 2% strain) can also be used to try to improve the energy dissipation as a result of early sub-looping. Although pre-strained SMA wires have been shown to work well in experimental devices, few studies have experimentally looked at the cyclic behavior of a single pre-strained NiTi wire to try to determine an optimal pre-straining level for structural applications. Many of the past studies have cycled the SMA wires only between predetermined strain levels or pre-strained the SMAs to only a single strain level to ensure tension-only superelastic behavior. This study to the knowledge base in regards to the tensile cyclic behavior of pre-strained SMA wire by experimentally studying the behavior

of NiTi wires pre-strained to a variety of levels and either cycled at a constant strain level or undergoing strain cycles of increasing width.

4.4.1 Method

A two-phase approach is taken in order to study the effect of pre-straining on the NiTi wires. The first phase of the study focuses on the energy dissipated by pre-strained NiTi wire by cycling under constant strain cycles. Pre-straining levels of 1.0%, 1.5%, 2.0%, 2.5%, 3.0%, 3.5%, and 4.0% are used to provide pre-strain levels half-way along the elastic curve up to just before the completion of the martensitic phase transformation along the loading plateau. Once pre-strained, the NiTi wire specimen is cycled about the pre-strain level ten times to each level: ±0.5% strain, ±1% strain, and ±2% strain. Since cycling the 1.0% and 1.5% pre-strained specimens to ±2% strain causes the wire to undergo compression, this set of ten cycles is dropped for these specimens. For each pre-strain level, two NiTi wires are tested resulting in a total of 14 constant cycle pre-strain tests with all of these tests being run at a quasi-static loading rate (0.025 Hz) in strain control. A representative loading protocol for the 3.0% pre-strain case is shown in Figure 4-12.

Since the focus is on the use of NiTi for earthquake applications in structures, the second phase is used to look at the tensile behavior of pre-strained NiTi wire undergoing a loading more similar to that undergone by structural members during an earthquake. For this phase, only four pre-strain levels are used: 1.0%, 2.0%, 3.0%, and 4.0%. After pre-straining, the wires are either cycled at a quasi-static loading rate (0.025 Hz) or dynamic loading rate (0.5 Hz) under strain cycles of increasing width where a strain cycle with a width of 1% refers to one cycle of ±0.5% strain about the pre-strain level. The width of the

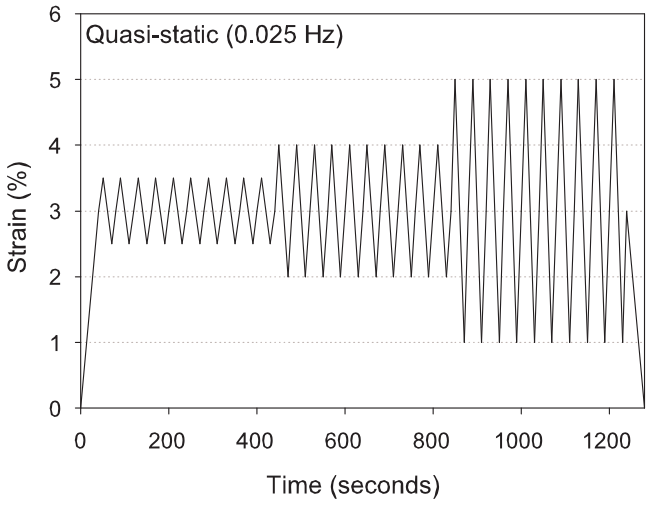

Figure 4-12: Cyclic loading protocol for the 3.0% pre-strain case (phase one).

strain cycles increases with each cycle to 6% at which point the wire is cycled five times. This is followed by a last cycle to 6% and a return to the zero stress point. Each of these cycles is centered about the pre-strain level until the cycles are large enough where either 0% strain is reached during unloading or 6% strain is reached during loading at which point the loading and unloading strain levels are uneven to maintain all cycling within the bounds of 0% strain and 6% strain. This loading protocol ensures tension-only behavior and limits maximum deformations to 6% strain. A representative loading protocol for the 2.0% pre-strain level is shown in Figure 4-13(a) and for the 4.0% pre-strain case in Figure 4-13(b). For each pre-strain level and each loading rate, two tests are run resulting in a total of 16 wires being tested.

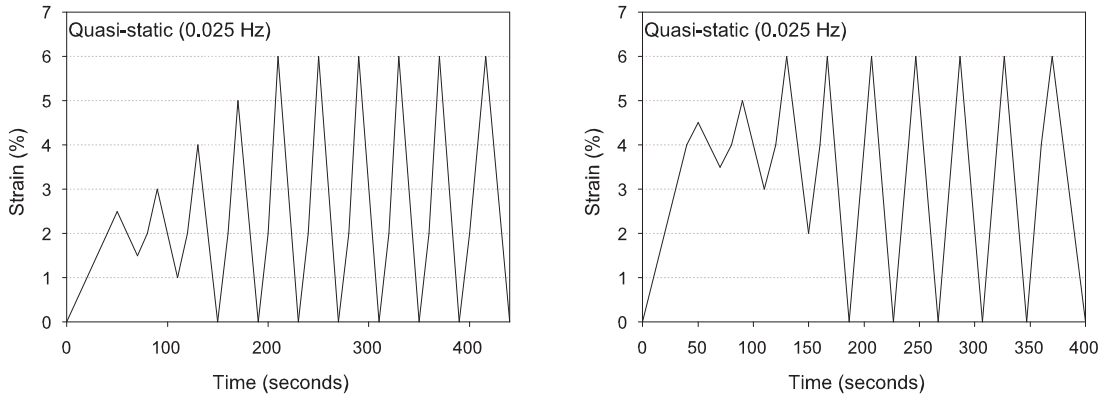

4-13(a): **4-13(b):**

Figure 4-13: Earthquake pre-straining loading protocol for the (a) 2.0% pre-strain case and (b) 4.0% pre-strain case (phase two).

4.4.2 Phase One: Cyclic Loading Results

Phase one (constant strain cycle experimental testing) provides a means of distinguishing the behavior of a superelastic NiTi wire pre-strained at various levels. Representative stress-strain curves for the NiTi wires pre-strained to 1.0%, 1.5%, 2.0%, 2.5%, 3.0%, 3.5% and 4.0% strain are shown in Figure 4-14. All 14 of the stress-strain curves are also provided in Appendix C. Similar results are also found for the replicate of each of these tests. In general, all of the curves show good superelastic behavior and the formation of typical sub-cycles associated with superelastic wire specimens (Dolce and Cardone, 2001). The results suggest that a trigger-line or instability line which runs diagonal from the start of the forward transformation (A $->$ M) to the start of the reverse transformation (M $->$ A) depending on whether the specimen is loading or unloading can be used to account for sub-cycling. However, as the number of cycles increases, the appearance of the stress plateaus becomes less distinguished, particularly for the smaller strain cycles (±0.5% and ±1.0%).

The effect of the different pre-strain levels is also apparent as the curves for the specimens pre-strained to lower values appear similar to those of specimens which are not pre-strained. As the pre-strain level increases, the loading plateaus and unloading plateaus become less distinguished as neither the forward transformation nor the reverse transformation are ever fully completed.

The change in some of the cyclic properties with respect to pre-strain level can also be evaluated based on the constant strain cycle results. Figure 4-15 provides the stress at the start of a given strain cycle with respect to the cycle number. These stress values provide details on how the stress in the NiTi wire changes when pre-strained to different levels. As expected, the stress at the pre-stain level for the 1.0% and 1.5% pre-strain cases are lowest with initial stresses due to pre-straining being measured at 214 MPa and 352 MPa, respectively. Since pre-straining between 2.0% to 4.0% strain places the pre-strained specimen along the loading plateau, the initial stresses for all these specimens are similar and range between 474 MPa and 568 MPa. For all pre-straining cases, the stress at the beginning of each cycle decreases significantly during the first few cycles. This is more prevalent in specimens pre-strained to higher strain levels as a result of the formation of permanent localized slip due to the larger amounts of deformation. All of the specimens show a slight increase in the stress at the pre-strain level when the strain cycle is increased from ±0.5% strain to ±1.0% strain and from ±1.0% strain to ±2.0% strain. In general, the initial cycles cause the largest drop in the stress at the pre-strain level while later cycles show fairly stable properties.

One of the most highly cited reasons for using pre-strained NiTi wires is for added damping capacity. Figure 4-16 shows the change in energy dissipated (area inside the

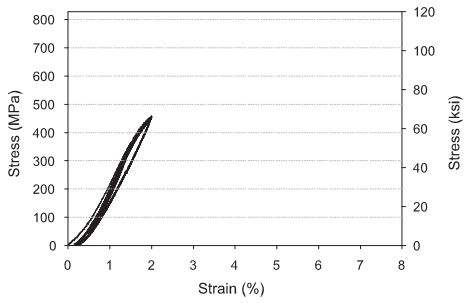

4-14(a):

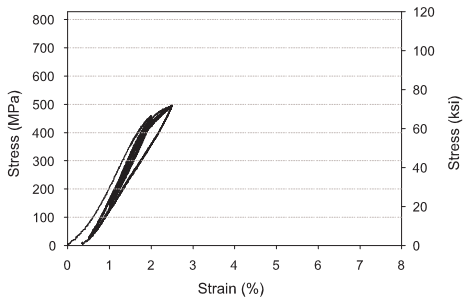

4-14(b):

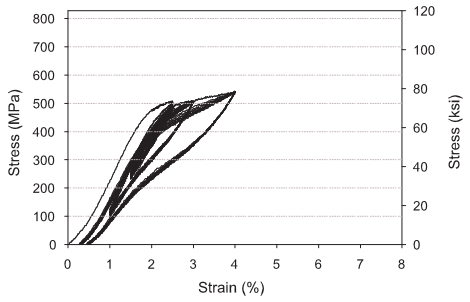

4-14(c):

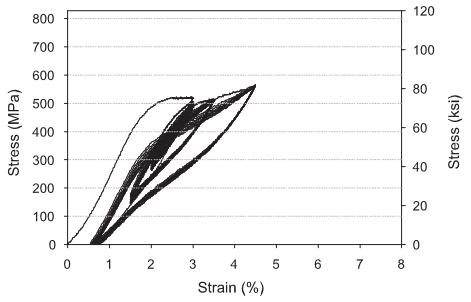

4-14(d):

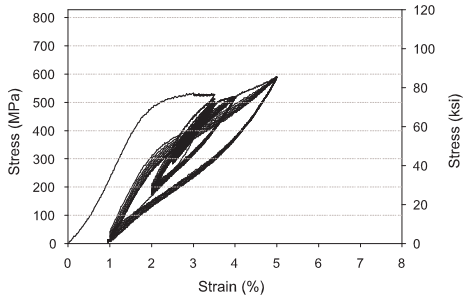

4-14(e):

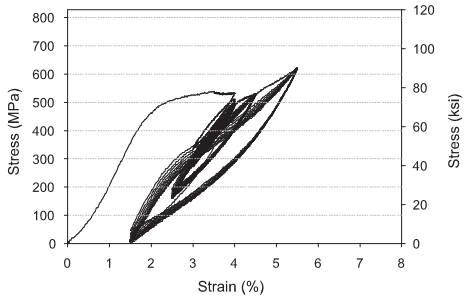

4-14(f):

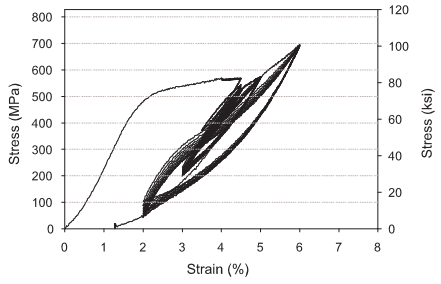

4-14(g):

Figure 4-14: Representative constant strain cycle stress-strain curves of NiTi wires pre-strained to (a) 1.0%, (b) 1.5%, (c) 2.0%, (d) 2.5%, (e) 3.0%, (f) 3.5%, and (g) 4.0%.

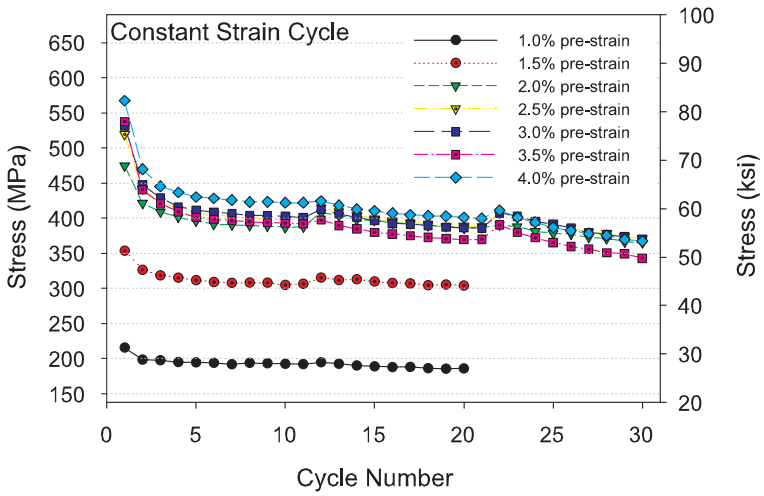

Figure 4-15: Stress measured at the beginning of each cycle (at the pre-strain level) with respect to cycle number.

hysteresis curve) with respect to cycle number for the constant strain cycle tests. The results suggest that even through pre-straining, only small amounts of energy dissipation are provided by the SMA wire for the small strain cycles. This is not the case for the larger strain cycles (±1.0% and ±2.0% strain) where the 2.5%, 3.0%, and 3.5% pre-strained wires have the largest energy dissipation. The results suggest that damping capacity can be maximized by pre-straining NiTi SMAs to between 2.5% and 3.5% strain. The decrease in the energy dissipated with an increase in pre-strain level above 3.5% can be attributed mainly to the completion of the forward transformation causing a stiffening of the SMA and a smaller hysteretic curve in this area. The maximum energy dissipation for the ±2.0% strain cycles is 0.45 N-m and is a result of pre-straining to 3.0% strain. There is a decrease in the energy dissipation with continued cycling which is similar to that seen for the large bar tests. This is attributed to the decrease in the forward transformation stress discussed

previously. As a result, the energy dissipated per a cycle decreases on average by 22% during the ten ±2.0% strain cycles. The other important property for SMA applications in structures is the recentering capability. This is only measured at the end of the loading protocol when the specimen is brought back to its zero stress state since all other cycles are sub-loops. The results show an increase in residual strain with an increase in pre-strain level from 0.27% for the 1.0% pre-strained wire to 1.28% for the 4.0% pre-strained wire as can be seen in Figure 4-14. This is mainly attributed to the large strains which the specimens pre-strained at the higher levels experience. Overall, pre-straining has been shown as one way to obtain more damping from moderate level strain cycles.

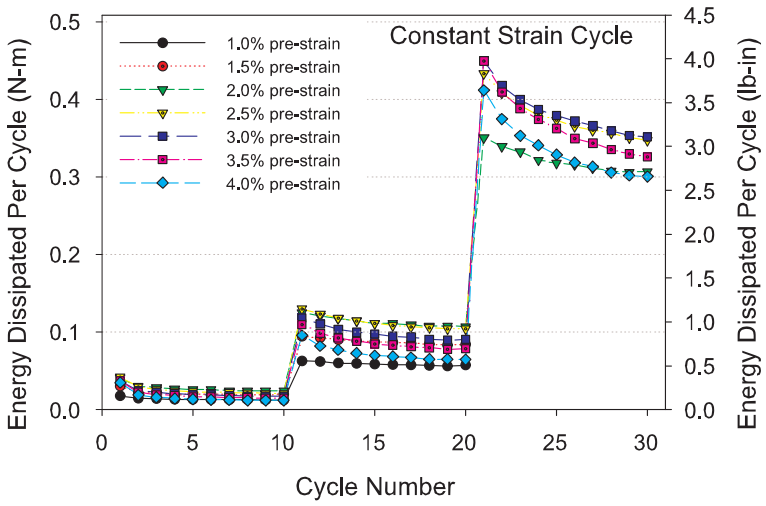

Figure 4-16: Energy dissipated per cycle for each of the pre-strain cases with respect to the cycle number.

4.4.3 Phase Two: Earthquake Loading Results

Phase two of this pre-straining study focuses on the increasing strain cycle loading protocol discussed in Section 4.4.1 and shown in Figure 4-13. This loading protocol is closer to that expected as a result of an earthquake and provides information on how a pre-strained NiTi wire behaves under increasing strain cycles. Since earthquakes are dynamic in nature, the tests are run both at a quasi-static loading rate and dynamic loading rate. For both cases, the cyclic properties are compared with respect to the pre-strain level.

4.4.3.1 Quasi-static Tests

Figure 4-17 contains the stress-strain plots for the NiTi wire specimens trained at each of the four pre-strain levels and cycled under the quasi-static increasing strain cycle loading. The replicate tests (see Appendix C) at each pre-strain level show similar behavior. Thus, the results reported in this section are based on the properties obtained from only one of the specimens tested at each pre-strain level. As with the constant strain cycle tests, there is a clear difference between the behavior of the specimen pre-strained to 1.0% as compared to the behavior of the specimen pre-strained at 4.0%. The 1.0% pre-strain case shows very similar behavior to a non-prestrained specimen which can be associated with the fact that the pre-straining level is small enough that the wire specimen initially remains on the initial elastic curve. Conversely, the 4.0% pre-strained NiTi wire specimen undergoes several sub-cycles before reaching the zero stress level during the last 6% strain cycles.

Comparing some of the cyclic properties of the NiTi wires pre-strained to different strain levels, the initial forward transformation stress (as a result of pre-straining or the actual cycling) remains constant for all cases between 462 MPa and 475 MPa. Although, the

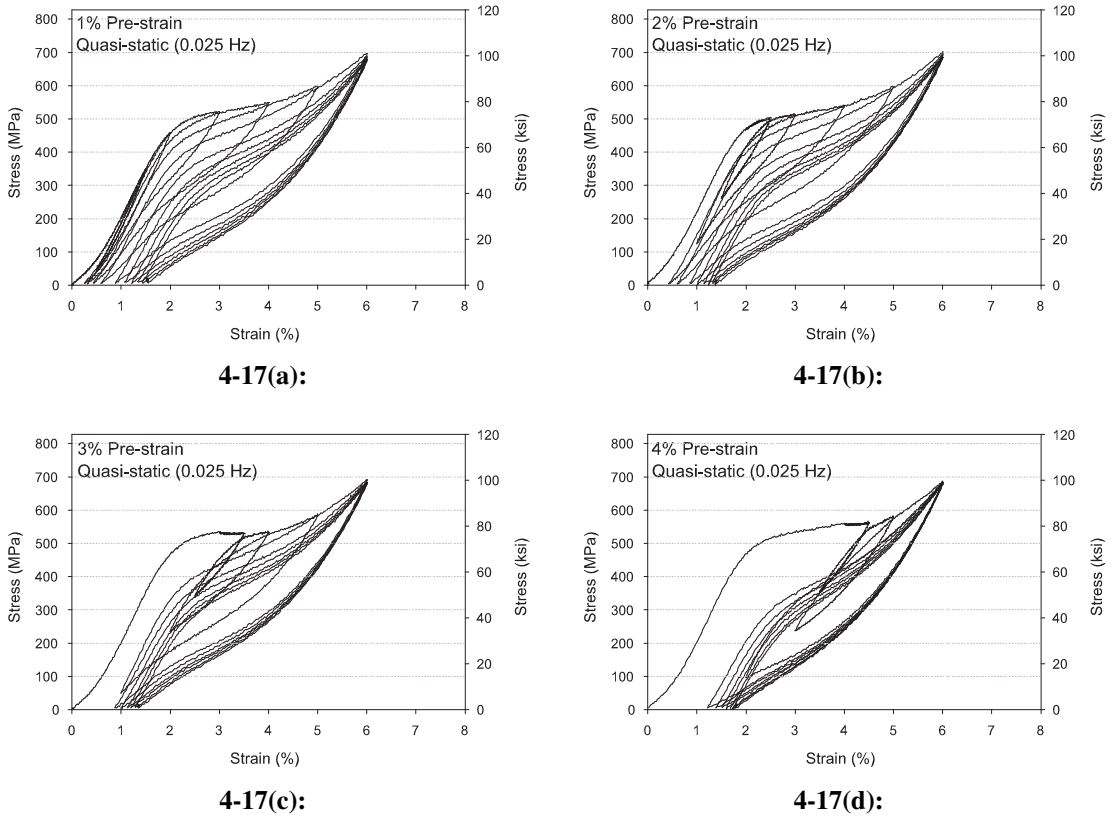

Figure 4-17: Representative stress-strain curves for the NiTi wires pre-strained to (a) 1.0%, (b) 2.0%, (c) 3.0%, and (d) 4.0% undergoing increasing cyclic strain cycles at a quasi-static loading rate (0.025 Hz).

forward transformation stress drops with continued cycling. The decrease in the forward transformation stress is dependent mainly on the maximum cyclic strain. In this regards, pre-straining to higher strain levels causes a more rapid decrease in the forward transformation stress as higher strain levels are reached more quickly during cycling. This is most apparent in Figure 4-17(d).

Since superelastic SMAs are typically used for recentering applications, it is also important to see if pre-straining has any effects on the accumulation of residual strain. The residual strain shows the largest variation between replicates and no general trend with respect to pre-strain level. However, for all of the tests conducted, the residual strain values at the end of cycling remain between 1.26% and 1.78% strain. These values are larger than those seen during the constant strain cycle tests of phase one, but can be attributed to the larger width of the strain cycles associated with the phase two loading causing the formation of permanent dislocations. These residual strains have a significant effect on the 1.0% pre-strain case. By the second 6.0% strain cycle, the residual strain has accumulated beyond the pre-strain level basically negating any of the benefits of pre-straining.

As with the constant strain cycle tests, it is important to understand the effect which the different pre-straining levels have on the damping capacity of the NiTi wire. Figure 4-18 contains the energy dissipated per cycle versus the strain cycle for the four pre-strain levels. As expected, the energy dissipated during the 1% strain cycle is similar for the 2.0%, 3.0%, and 4.0% pre-strain cases because of the onset of minor sub-looping and almost zero for the 1.0% pre-strain case since it remains along the initial elastic curve. Both the 3.0% and 4.0% pre-strained NiTi wires follow a similar trend and have the highest energy dissipation up to the 5% strain cycle. The 1.0% and 2.0% pre-strain cases follow a similar trend to each other

after the 4% strain cycle as both are basically cycling between 0% strain and the maximum strain for the given cycle. The energy dissipated increases by approximately 28% at the 4% strain cycle by pre-straining to either 3.0% or 4.0% as compared to pre-straining to only 1.0% or 2.0%. This behavior is then reversed during the 6% strain cycles where the energy dissipation associated with the 4.0% pre-strain specimen is the least, approximately 25% less than that associated with the other three pre-strain levels. As a result, the quasi-static increasing strain cycle tests suggest that an optimal pre-strain level is around 3.0% in order to provide the largest amount of damping. This result is similar to the findings during phase one of this study.

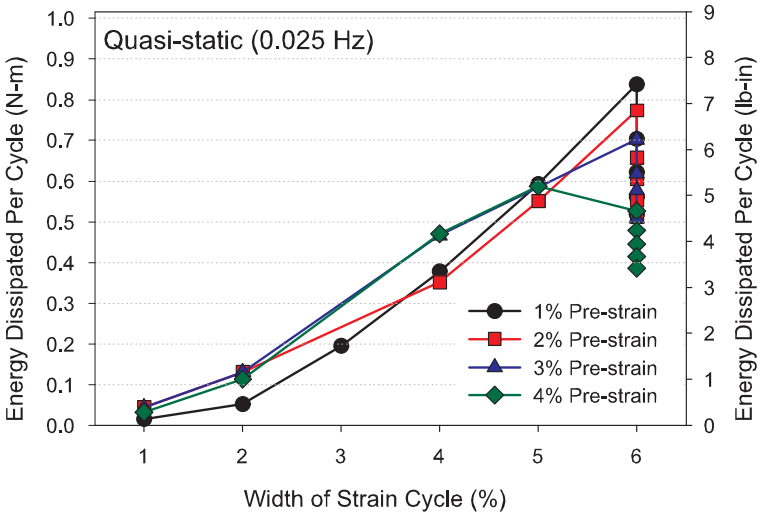

Figure 4-18: Energy dissipated per cycle for each of the pre-strain cases with respect to the width of the strain cycle for the quasi-static increasing strain cyclic loading.

4.4.3.2 Dynamic Tests

The 0.5 Hz increasing strain cycle tests provide information in regards to whether dynamic loadings have a significant effect on the behavior of pre-strained NiTi wires. The stress-strain plots from a representative test at each of the four pre-strain levels are shown in Figure 4-19. All of the stress-strain curves for the dynamic tests are also contained in Appendix C. A clear difference in the behavior can be seen with each increasing strain cycle for each pre-strain case. As with the quasi-static specimens, pre-straining to 1.0% strain results in a stress-strain plot similar to a non-prestrained specimen. Conversely, the 4.0% pre-strain specimen undergoes several internal hysteresis loops even during the small initial strain cycles.

The decrease which the forward transformation stress undergoes in the quasi-static tests is also prevalent during the dynamic tests. For the 1.0% and 2.0% pre-strain cases, the forward transformation stress decreases gradually with the increasing strain cycles. For the 3.0% pre-strain case, the forward transformation stress significantly decreases by 17% between the 3% strain cycle and 4% strain cycle suggesting that even small sub-cycles can cause a significant accumulation of localized slip. This decrease is even more apparent in the 4.0% pre-strain case where the decrease between the 4% strain cycle and the 5% strain cycle is approximately 27% from 466 MPa to 342 MPa. The forward transformation stresses in comparison with the quasi-static tests tend to be higher with a smaller decrease in the loading plateau with continued cycling at the dynamic loading rate. The plateaus are more defined for the dynamic specimens, as well, with the reverse transformation occurring at a higher stress level.

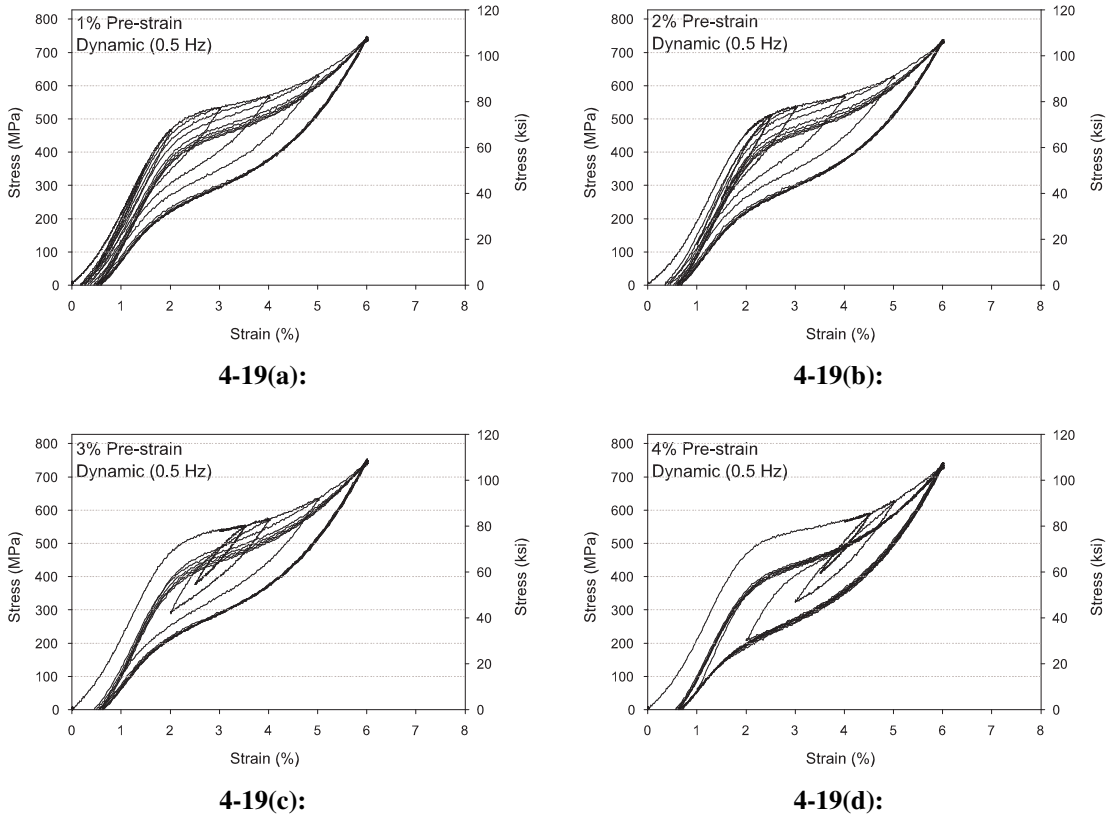

Figure 4-19: Representative stress-strain curves for the NiTi wires pre-strained to (a) 1.0%, (b) 2.0%, (c) 3.0%, and (d) 4.0% undergoing increasing cyclic strain cycles at a dynamic loading rate (0.5 Hz).

Similar to the quasi-static tests, pre-straining appears to have little effect on the residual strain (recentering capability). The residual strain at the end of the loading protocol only differed between 0.57% strain and 0.66% strain with no real trend associated with the pre-strain level. These values are approximately half those found when the specimens are cycled quasi-statically suggesting good recentering capability during a dynamic event such as an earthquake. Since the accumulation of residual strain is not significantly affected by pre-straining, devices for structural control systems can be developed using pre-strained superelastic NiTi in order to ensure that they act in tension and provide energy dissipation even during small strain cycles.

Many of the similar trends seen during the quasi-static testing with respect to the damping capacity are also apparent with the pre-strained specimens cycled dynamically. The energy dissipated per cycle is shown with respect to the width of the strain cycle for the four pre-straining cases in Figure 4-20. The energy dissipated increases by approximately 31% at the 4% strain cycle by pre-straining to either 3.0% or 4.0% as compared to pre-straining to only 1.0% or 2.0%. This increase is basically the same as that found for the quasi-static specimens. Although the dynamic tests and quasi-static tests show similar trends, they differ in the value of the energy dissipated per cycle with the maximum energy dissipated being 0.84 N-m and 0.68 N-m for the quasi-static and dynamic tests, respectively. The decrease is a direct result of the increase in the reverse transformation stress during dynamic cycling which can be attributed to a self-heating of the specimen. In general, the results suggest that higher small cycle energy dissipation can be obtained by pre-straining, but care must be taken in choosing a pre-strain level so as not to induce rupture when large strain levels are required and to account for the decrease in energy dissipation during dynamic

loading. When pre-straining SMAs for structural devices for seismic response reduction, the change in stiffness of the SMA element as a result of pre-straining needs to be taken into account as well to ensure proper performance of the structure.

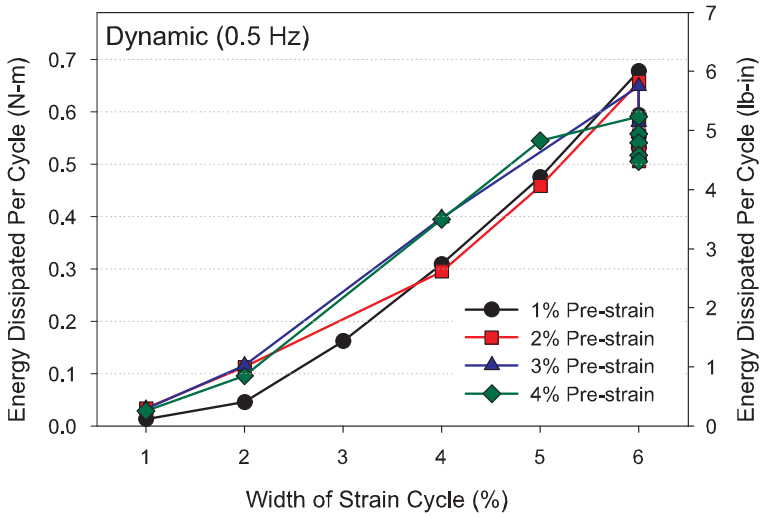

Figure 4-20: Energy dissipated per cycle for each of the pre-strain cases with respect to the width of the strain cycle for the 0.5 Hz dynamic increasing strain cyclic loading.

4.5 Earthquake Type Effects on NiTi Wires

The mechanical training study and the pre-straining study suggest that NiTi SMA wires perform well under earthquake loadings with prior mechanical training and pre-straining improving the stability of the cyclic properties and damping capacity, respectively. However, both these studies and the large bar study completed in Chapter 3 only look at the effects of earthquake type motions which gradually increase in magnitude similar to a far-field type earthquake. In order to consider the use of NiTi SMAs for seismic applications

in buildings, the effect of near-field type earthquake motions on the cyclic behavior of superelastic NiTi must also be considered. As compared to the more gradual increase in the magnitude of far-field type motions, near-field motions experience large early cycles which can have a significant effect on the cyclic properties. To date, no study has experimentally looked at near-field type loadings on superelastic NiTi wires. This study preliminarily addresses this gap in knowledge by cycling previously untested NiTi wires under both types of loading protocols at quasi-static and dynamic loading rates.

4.5.1 Loading Protocol

The loading protocols which are used for this earthquake type study are based on those developed for the SAC Steel Project to test steel moment resisting frame components and assemblies (Krawinkler et al., 2000). The SAC earthquake loading protocols are given based on an applied inter-story drift angle which can then be converted into a brace elongation (or SMA strain) for a single-bay braced frame. This procedure is followed since braced frames are the application of superelastic SMAs being explored in this dissertation. The conversion is based on Equation 4.5 shown below.

$$\varepsilon_{SMA} = \frac{H \cdot W \cdot \theta}{L \cdot L_{SMA}} \tag{4.5}$$

ε_{SMA}, H, W, θ, L, and L_{SMA} represent the strain in the SMA element, height of the frame, span of the frame, inter-story drift angle, length of the brace, and length of the SMA element used with the brace, respectively. The actual strain levels can then be changed based on the dimensions of the frame and the length of SMA considered. Although these loading protocols are meant for the testing of steel moment resisting frames, they provide

a good means of evaluating the cyclic properties of NiTi under the two different loading types. The loading protocols are also adapted so as to only apply tension loadings since tension-only applications of NiTi SMAs are being studied and the wire specimens have only a small compressive capacity before buckling occurs. These adapted loading protocols can be seen in Figure 4-21 for the quasi-static loading rate (0.025 Hz). The maximum strain level for the far-field loading protocol is 6% strain where for the near-field loading protocol it is 7.2% strain. Tests are also run for both types of loadings at dynamic loading rates of 0.25 Hz and 0.5 Hz in order to glean any dynamic loading effects. For each loading protocol and each loading rate, two wire specimens are tested resulting in a total of 12 tests being run. All replicates showed similar results (see Appendix D.

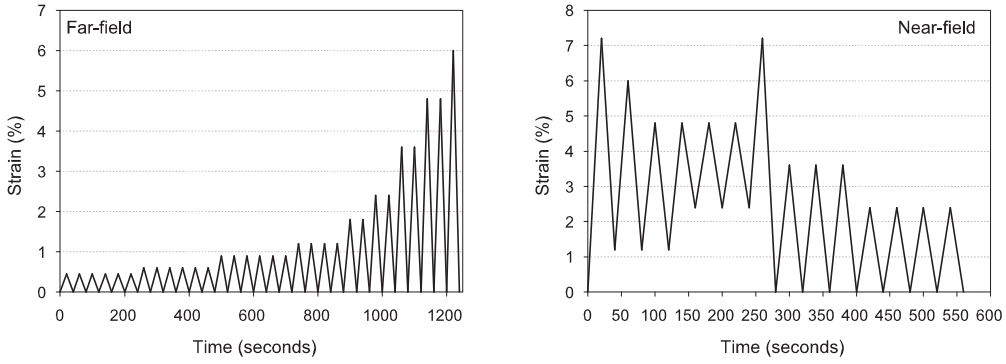

4-21(a): **4-21(b):**

Figure 4-21: (a) Far-field and (b) near-field type earthquake loading protocols for the quasi-static (0.025 Hz) loading rate.

4.5.2 Evaluation of Loading Type Effects

Representative stress-strain plots for the NiTi wire specimens undergoing either the far-field or near-field earthquake loadings at the quasi-static, 0.25 Hz dynamic, and 0.5 Hz dynamic loadings rates are shown in Figure 4-22. As expected, the stress-strain curves for the specimens undergoing the far-field loading look similar to those in Section 4.3.2 showing the behavior of untrained NiTi wire. Likewise, the specimens undergoing the near-field loading appear to behave in a similar manner to the pre-strained specimens as a result of the early large strain cycles and sub-cycling. The difference between the behavior of the specimens undergoing the far-field earthquake loading and near-field earthquake loading can be associated with the sub-cycling apparent in Figures 4-22(b), 4-22(d), and 4-22(f). The cyclic properties of the NiTi wire undergoing the near-field loading also appear to be more stable than those associated with the wire specimens undergoing the far-field loading after the initial large strain cycles. The dynamic loading rates have a clear effect on the cyclic behavior of the NiTi wire specimens loaded under both types of earthquake protocols. For both cases, the loading plateau and unloading plateau (to a greater extent) appear to shift upward to larger stress levels. This is similar to the dynamic loading effects seen for both the large bar testing and pre-straining studies. In general, the stress-strain behavior under both types of loadings shows good superelastic behavior with deformation recovery and the formation of the typical flag-shape hysteresis.

A closer look at the behavior of the NiTi wires cycled under the far-field loading protocol (Figures 4-22(a), 4-22(c), and 4-22(e)) can now be undertaken. The behavior of the NiTi wires is similar to other specimens tested using increasing strain cycles. For the first

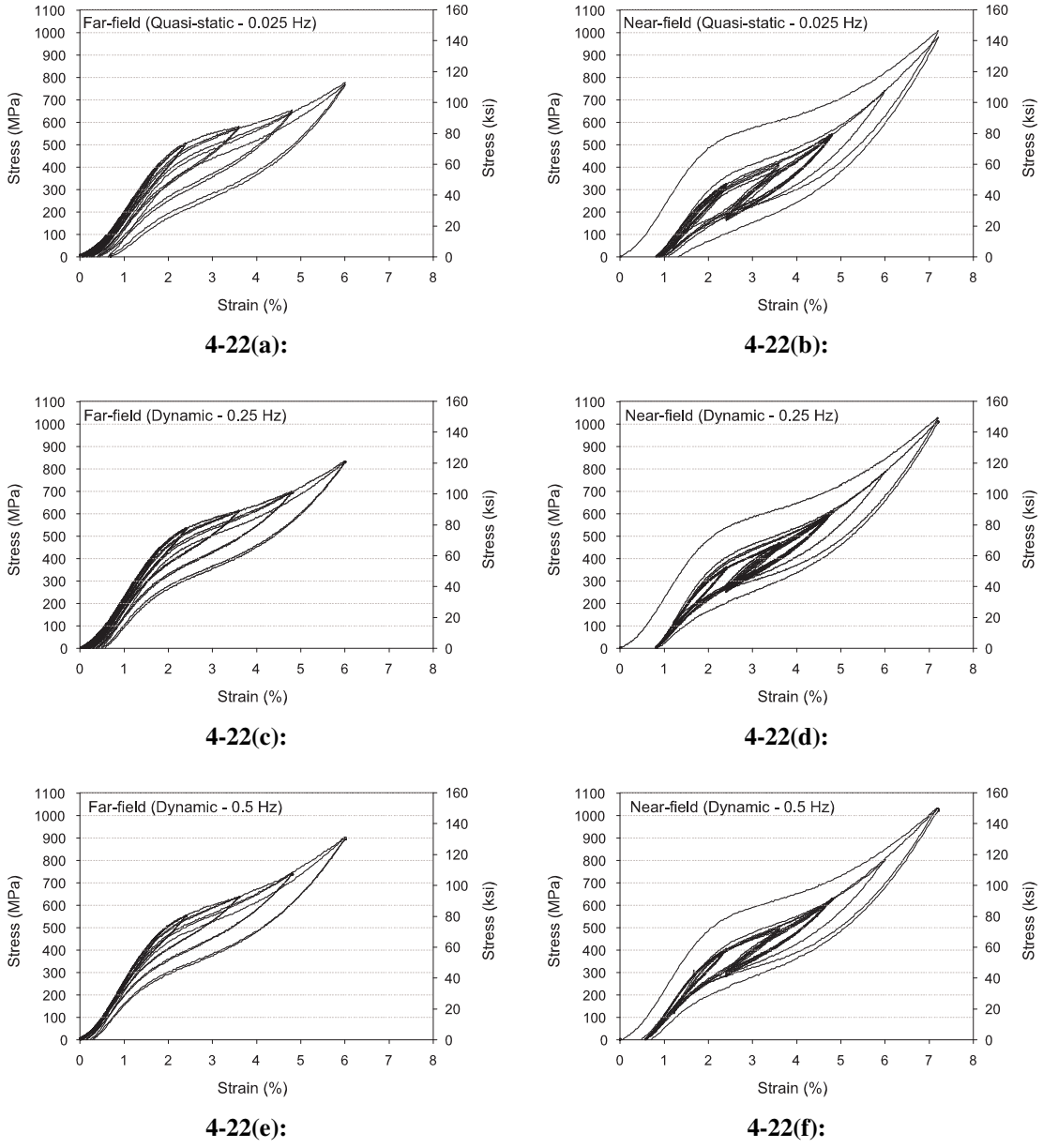

4-22(a): **4-22(b):**

4-22(c): **4-22(d):**

4-22(e): **4-22(f):**

Figure 4-22: Representative stress-strain curves for the NiTi wires cycled under the far-field or near-field earthquake loading protocols at either a 0.025 Hz, 0.25 Hz, or 0.5 Hz: (a) 0.025 Hz far-field, (b) 0.025 Hz near-field, (c) 0.25 Hz far-field, (d) 0.25 Hz near-field, (e) 0.5 Hz far-field, and (g) 0.5 Hz near-field.

18 strain cycles (maximum strain of 0.9%), the NiTi wire remains along the initial elastic curve and as a result shows no real accumulation of residual strain and no initiation of the phase transformation. The formation of the stress plateau starts with the 2.4% strain cycles and results in a forward transformation stress of approximately 454 MPa which decreases by 28% to 327 MPa during the last 6% strain cycle for the specimen tested quasi-statically. The dynamic loadings result in an increase in the initial forward transformation to 485 MPa and 510 MPa for the 0.25 Hz and 0.5 Hz dynamic cases, respectively. The fatigue effects also decrease with an increase in loading rate as the forward transformation stresses only decrease by 18% and 15% between the initial forward transformation stress and the forward transformation stress measured during the last cycle. This result is similar to the findings in both the pre-straining and mechanical training studies. The reduction in the fatigue effects with an increase in loading rate is also seen with respect to the residual strain. The total accumulated residual strain for the quasi-static, 0.25 Hz dynamic, and 0.5 Hz dynamic loading rates is approximately 0.70%, 0.55%, and 0.27%, respectively. Once again, the dynamic specimens are shown to have good recentering capabilities suggesting that NiTi can be used for recentering applications in structures to control their response due to an earthquake. The damping capacity reduces with an increase in the loading rate as a result of thermal effects associated with the martensitic phase transformation. Unlike with the large diameter bars, this decrease is not significant since the surface area percentage is greater for the wires allowing the heat generated to be dissipated at a faster rate. In general, the damping capacity remained below 2.5% equivalent viscous damping.

Since very few studies have looked at the effect of large early strain cycles on the properties of superelastic NiTi, it is also important to understand how the near-field earthquake

protocol affects the cyclic behavior of the NiTi wires (Figures 4-22(b), 4-22(d), and 4-22(f)). The effect of the large initial strain cycle is apparent from the stress-strain curves shown in Figure 4-22. The initial forward transformation stress associated with this first cycle for all three loading rates is approximately 482 MPa. At this point, the wire has not accumulated significant heat and thus does not show any dynamic loading effects. The forward transformation stress does decrease significantly between this first cycle and the last 2.4% strain cycle of the loading protocol. The decreases in this value with respect to the loading rate are 45%, 38%, and 28% for the quasi-static, 0.25 Hz dynamic, and 0.5 Hz dynamic cases. This trend is similar to that seen for the far-field specimens with the decreases being slightly larger which can be associated with the higher maximum strain value of cycling. One other major effect associated with the near-field motion is the large accumulation of residual strain during the first strain cycle. Since this accumulation occurs at the beginning of the loading, it means that an SMA based recentering device is less effective during the later loading cycles which needs to be accounted for in the design for areas susceptible to near-field events. The overall accumulation of residual strain decreased with an increase in the loading rate as has been seen with the other wire specimens with a maximum of value of 1.32% for the quasi-static case and a minimum of 0.64% for the 0.5 Hz dynamic case. The maximum energy dissipation occurs during the first cycle (since this is the largest of the strain cycles), but remains below 4% equivalent viscous damping. The energy dissipation also decreases with an increase in loading rate as a result of an increase in the reverse transformation stress due to a self-heating of the specimens when cycled dynamically.

Table 4-10 contains a summary of some of the mean cyclic properties of the two replicated tests at each loading type and loading rate. A comparison of the NiTi wire properties for each of the loading protocols shows that the initial forward transformation stress is similar for all specimens with only a minor difference coming from the quasi-static specimen cycled under the far-field loading protocol. However, the different loading protocols cause a difference in the forward transformation stress of the final cycle. The forward transformation stress is on average 23% smaller for the NiTi wires undergoing the near-field protocol as compared to those undergoing the far-field protocol. This difference can be attributed to the larger maximum strain reached during the near-field loading allowing the formation of more localized slip which assists the forward transformation stress (Miyazaki, 1990; Miyazaki et al., 1986a; Tobushi et al., 1992b). Because of these larger strain cycles, the residual strain is also larger for the near-field loading case, although it is apparent that cycling at higher loading rates can limit these residual strains below 1% suggesting that NiTi wires under both types of loadings can provide good recentering capability. Although as mentioned, the fact that the residual strains increase greatly early on when cycling under a near-field type ground motion does need to be accounted for in the design. The damping capacity for both types of loadings is small compared to other damping devices suggesting the best use for superelastic NiTi is as a recentering type device. In general, the near-field loading protocol results in large initial changes in the properties, but the NiTi SMA wires still maintain the benefits associated with superelastic SMAs.

Table 4-10: Mean Properties Based on the Earthquake Type Loading Stress-Strain Results

Property (Mean)	Far-field Loading			Near-field Loading		
	QS	0.25 Hz	0.5 Hz	QS	0.25 Hz	0.5 Hz
Initial Forward Trans. Stress (MPa)	468	490	496	486	482	482
Final Forward Trans. Stress (MPa)	337	402	419	256	298	337
Max Residual Strain (%)	0.66	0.52	0.37	1.41	0.85	0.68
Max Equiv. Visc. Damp. (%)	2.54	2.17	2.01	3.85	3.16	2.97

4.6 Closure

This chapter analyzes a variety of experimental studies in order to try to understand and optimize the behavior of superelastic NiTi SMA wire to be used for seismic applications in civil structures. A two-phase mechanical training study is completed to determine the optimal training protocol in terms of strain level and number of cycles in order to stabilize and optimize the NiTi properties. The results show that training for greater than 40 cycles at 6% to 7% strain can reduce the fatigue effects. Equations are provided based on the response surface analysis which allow for the optimization of the forward transformation stress and equivalent viscous damping. Pre-straining tests are conducted at various pre-strain levels to determine the most appropriate level for seismic applications. Pre-straining between 3.0% and 3.5% strain provides the largest amount of energy dissipation because of the onset of sub-cycling during the initial loading stages. Finally, the properties of the superelastic NiTi wires are evaluated under both far-field and near-field type loadings to determine if there is any change in the cyclic behavior as a result of a large magnitude initial loading cycle. This initial loading cycle causes a large decrease in the forward transformation stress and a significant accumulation of residual strain, but the NiTi wires still maintain good superelastic behavior. The results from these three sets of tests provide a means of optimizing the

properties of SMAs for seismic applications through methods which up to this point have never been concisely studied.

CHAPTER V

STATISTICAL ANALYSIS OF NITI WIRE PROPERTIES

5.1 Introduction

Chapters 3 and 4 show significant potential for the use of SMAs in civil and structural application in terms of their properties and the ability to optimize these properties. However, each of these experiments only looks at a small number of specimens for a given set of parameters, limiting any knowledge of the consistency of these properties. Although nominal properties are typically used in structural engineering, it is well known that variability in material properties can effect the reliability of a structure resulting in a random behavior during loading. Given that performance-based seismic design demands reliable behavior of structures so that performance goals are met, it is becoming increasingly important to account for this variability in the material properties through proper reliability-type studies. In particular, for earthquake engineering applications, this is especially true for those materials acting as the main means of providing lateral load resistance or seismic response mitigation in a structure. In general, a good understanding of the variability of typical structural materials (steel and concrete) has been gained. However, as new and innovative materials are being introduced, there is little knowledge in regards to the consistency of

these properties which tends to limit the speed in which new materials are implemented into practice even though they have been proven effective.

This chapter address this problem with respect to superelastic NiTi SMAs through a preliminary statistical analysis of the properties of NiTi wires from the same manufacturer. A number of experimental tensile tests are run on NiTi wires taken from the same batch of material so that statistical distributions for the initial elastic modulus, forward transformation stress, loading plateau slope, stress at which point stress-induced martensite is fully formed, stress at which point the reverse transformation begins, and the residual strain can be determined. These properties are the basic properties necessary to be able to accurately model the uniaxial tensile behavior of SMAs. With probabilistic distributions for these properties, future analytical studies can begin to make more accurate assessments of the reliability of structures implementing SMA systems and determine representative fragility curves in order to compare them to other seismic mitigation systems. Before these goals can be approached, a deterministic understanding of the behavior of NiTi systems needs to also be gained and is presented in the following chapter. However, quantification of the variability of various SMA properties at this time provides a means to more quickly and reliably introduce SMA systems into practice.

5.2 Material, Setup, and Method

In order to determine probability distributions associated with various SMA properties, 2.16 mm diameter NiTi redraw wire taken from the same batch of material used to conduct the pre-straining and earthquake type loading tests is used. Details in regards to the manufacturing, processing, and physical properties of these wires can be found in Section

4.2. Wire specimens are chosen because of the high cost associated with testing numerous large diameter bars. As with the training, pre-straining, and earthquake type loading study, all specimens are annealed at 350 °C for 30 minutes and immediately water quenched to ensure good superelastic properties. The specimens themselves each have a length of 165.1 mm with a nominal gage length of 63.5 mm based on a grip length of 50.8 mm at each end. The same 250 kN MTS hydraulic testing frame used throughout the previous experimental studies is used here to perform the experimental aspects of this statistical study with all tests being run in strain control based on the feedback from a 25.4 mm gage length extensometer. A dynamic loading protocol run at 0.5 Hz is chosen for this study consisting of tensile strain cycles of 0.5%, 1.0%, 2.0%, 3.0%, 4.0%, 5.0%, and six cycles to 6.0%. This loading protocol has been previously presented in Figure 4-3(b). Care is taken to ensure that the same procedure is followed in the testing of each individual wire so as not to bias the study or add any further error.

The NiTi SMA properties which are the focus of this study are chosen based on those typically needed to accurately model SMA behavior so that the distributions can be used for future reliability-type studies. The initial elastic modulus, E_i; forward transformation stress, σ_L; and residual strain, ε_R have already been defined as the slope of the initial elastic curve, stress at 2% strain from the start of the cycle on the loading curve, and strain at zero stress at the end of a cycle. The other properties considered are the slope of the loading plateau, E_{PL}; the stress at which stress-induced martensite is fully formed (strain hardening begins), σ_M; and the stress at which the reverse transformation begins, σ_{UL}. σ_M and σ_{UL} are defined as the stress at 4.5% strain on the loading and unloading curve, respectively, based on previous stress-strain results of the NiTi wire being studied. These properties are

labeled on the schematic shown in Figure 5-1. For the purpose of this study, the properties from the first 6% strain cycle are used to obtain the distributions since this is the first full-cycle where the stress-induced martensite is ensured to have completely formed and substantial deformation of the stress-induced martensite has occured.

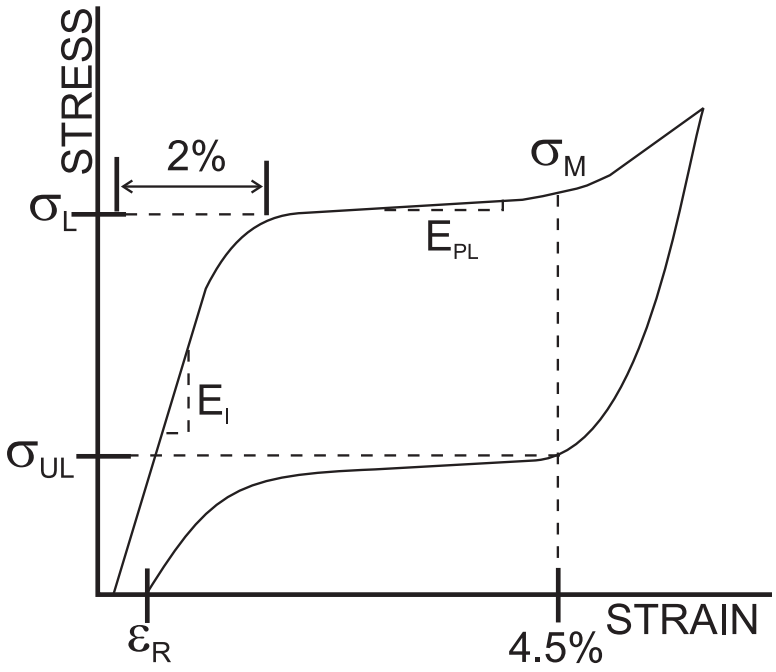

Figure 5-1: Schematic of idealized stress-strain curve for NiTi SMAs with the parameters from the statistics study labeled.

A two-phase approach is taken to determine probability distributions for these SMA properties. The first phase consists of roughly determining the number of experimental tests needed to obtain an accurate probability distribution model and the subsequent mechanical testing of the NiTi SMA wires. The second phase of this statistics study consists of the fitting of probability distributions to the data and determining the accuracy or significance

associated with each of these fits. The following sections outline the results of these two phase.

5.3 Phase I: Experimental Testing of NiTi Wires

Before running the tensile tests with each of the NiTi wires, a rough estimate of the number of wires which need to be tested in order to obtain accurate results is obtained. This number is chosen based on the desire to obtain a 95% confidence interval on the mean of the initial elastic modulus, forward transformation stress, and residual strain. For this purpose, it is assumed that the confidence interval on the mean is of a normal distribution in which the variance is unknown. The assumption of a normal distribution has been shown to hold in a variety of different practices and provides a good starting point given limited data on the properties of the wires (Ang and Tang, 1975). Because of the limited data, the variance is also assumed unknown. Given these assumptions, the confidence interval based on the t-distribution, shown in Equation 5.1, is used to back out the required number of tests.

$$< \mu >_{1-\alpha} = [\bar{x} - t_{\alpha/2,n-1}\frac{s}{\sqrt{n}}; \bar{x} + t_{\alpha/2,n-1}\frac{s}{\sqrt{n}}] \tag{5.1}$$

$t_{\alpha/2,n-1}$, $\bar{x}$, μ, s, n, and $(1-\alpha)$ represent the percentile value of the t-distribution, known sample mean, mean of the Gaussian population, sample standard deviation, number of samples, and confidence level, respectively. Because the sample size term affects the percentile value term, an iterative process is needed to determine the required sample size. Further details can be found in Ang and Tang (1975) and Hines et al. (2003).

For the initial elastic modulus, forward transformation stress, and residual strain, past results are used to obtain an estimate of the sample mean and sample variance. Confidence intervals of ±70 MPa, ±3.5 MPa, and ±0.005% are chosen for a confidence level of 95%. The forward transformation results dictate requiring 25 samples to provide this confidence for the given interval. Although the sample mean and sample standard deviation are obtained from relatively few results and a normal distribution is assumed, this result is still valid because only a rough estimate is required. Also, the accuracy and significance of the distributions are ensured in the testing of the fit of the distributions. To account for any discrepancies, an extra five tests are performed, bringing the total number of specimens tested as part of this statistics study to 30.

Two representative stress-strain curves of the 30 specimens tested are shown in Figure 5-2. The remainder of the stress-strain curves are provided in Appendix E. The stress-strain curves both depict typical superelastic behavior with a clear flag-shape hysteresis and good recentering capabilities. The results are very similar to those found for the untrained specimens shown in Figure 4-4(b). The similarity between the two curves also suggests consistency in the properties.

For each of the 30 specimens, the initial elastic modulus, forward transformation stress, slope of the loading plateau, stress at which point martensite is fully formed, and the stress at which point the reverse transformation begins is determined for the first 6% strain cycle. Based on these results, the sample mean, unbiased sample variance, and median values are computed (Ang and Tang, 1975). These values are listed in Table 5-1. The sample statistics show that the median values and the mean values are similar for all cases suggesting that the distribution is both symmetric and of a single mode. Given that the standard deviations

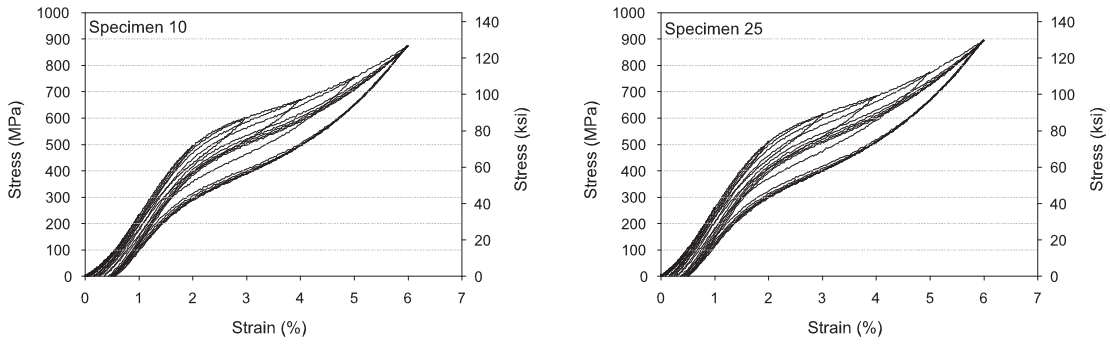

5-2(a): **5-2(b):**

Figure 5-2: Representative stress-strain curves of the 2.16 mm diameter NiTi wire tested for the statistics study: (a) Specimen 10 and (b) Specimen 25.

Table 5-1: Sample Statistics Based on the 30 NiTi Wires Tested

	E_i (Gpa)	σ_L (Mpa)	E_{PL} (Gpa)	σ_M (Mpa)	σ_{UL} (Mpa)	ε_R (%)
Sample Mean	24.30	467.24	10.34	716.80	588.77	0.41
Sample St. Dev.	1.26	6.56	0.49	15.51	17.08	0.04
Median	24.20	467.12	10.18	713.71	586.71	0.41

are fairly small for most of the statistics, it is assumed that the dispersion or variability between the properties of the 30 specimens is minimal. However, the dispersion appears to be the greatest in both the stress at which martensite is completely formed and the stress at which point the reverse transformation initiates. In general, the sample statistics suggest consistent properties between the 30 specimens tested.

5.4 Phase II: Probability Distributions for NiTi Wire Properties

Now that the sample statistics for the NiTi wire properties have been obtained, the probability distributions for these properties can be determined. Three probability distributions are considered as part of this study, the normal distribution, the lognormal distribution, and

the Weibull distribution. The normal distribution is chosen based on the fact that the small variance in the sample statistics suggests that the data is of a single mode and symmetric. Often, the variability of material properties has been found to be distributed lognormally providing justification for checking the lognormal distribution. The Weibull distribution (Type III asymptotic smallest value) is also selected because of its connection with fatigue and fracture studies of various materials (Ang and Tang, 1984). From these three distributions, the one which provides the best fit is determined and that distribution is assigned to the given property for use in future work.

The distributions are fit to each property using the method of moments to determine the parameters for each corresponding distribution. The method of moments is based on the relationship between the moments of a random variable and the parameters of the corresponding distribution. In this manner, the parameters are estimated by replacing the mean and variance of the random variable with the sample mean and sample variance obtained from the experimental testing of the NiTi wire. The equations for the mean and variance are listed below for the normal distributions (Equations 5.2 and 5.3), the lognormal distribution (Equations 5.4 and 5.5), and the Weibull distribution (Equations 5.6 and 5.7)

$$E(X) = \mu \tag{5.2}$$

$$Var(X) = \sigma^2 \tag{5.3}$$

$$E(X) = e^{\lambda + \frac{1}{2}\zeta^2} \tag{5.4}$$

$$Var(X) = E^2(X)[e^{\zeta^2} - 1] \tag{5.5}$$

$$E(Y) = u\Gamma(1 + \frac{1}{\alpha}) \tag{5.6}$$

$$Var(Y) = E^2(Y)\left[\frac{\Gamma(1 + \frac{2}{\alpha})}{\Gamma^2(1 + \frac{1}{\alpha})} - 1\right] \tag{5.7}$$

The parameters for the normal distribution are μ and σ, while λ and ζ are the parameters for the lognormal distribution. The Weibull distribution uses the parameters α and u, although it should be noted that the parameter α is estimated based on $\alpha \approx (\mathrm{V}_Y)^{-1.08}$ where V_Y is the coefficient of variation. By substituting the sample mean and sample variance into these equations, the parameters for each distribution are obtained. Further details in regards to the method of moments and the respective cumulative distribution functions can be found in Ang and Tang (1975, 1984).

The goodness of the distribution fit is estimated using the Kolmogorov-Smirnov (K-S) test which compares the difference (K-statistic) between the cumulative frequency based on the experimental data to the assumed distribution function using the parameters obtained from the method of moments. If the difference is less than the critical value, D_n^α, for a given significance level, then the distribution is accepted at that specified significance level. The 20% significance is used to compare the distributions because it provides the smallest critical value. Thus, all significance values below 20% are satisfied as well. The K-S test is chosen over various other tests because it eliminates the need to place the data into bins allowing for it to be more easily implemented into an animated process. The K-S test also has the advantage of not having to make any assumptions about the distribution of the data. Specific details in regards to the K-S test are found in Ang and Tang (1975).

The procedure for determining the probability distributions is followed for the initial elastic modulus, forward transformation stress, loading plateau slope, martensite stress, reverse transformation stress, and residual strain properties obtained based on the first 6% strain cycle. For each property, the results for all three distributions are presented with the most significant pointed out in bold in the Tables. A histogram depicting the experimental results and the theoretical best fit probability distribution is also shown to provide a visual reference of the fit.

5.4.1 Initial Elastic Modulus

The initial elastic modulus provides the initial slope of the stress-strain curve which corresponds to the elastic modulus of NiTi SMA in its austenite phase. The results from the distribution fitting and K-S test are shown in Table 5-2. For all three types of distributions, the fit of the distribution is accepted at a 20% significant level (the highest level evaluated for this study). Since all three are accepted at this level, the K-statistic can be used to compare the three models. The K-statistic is 0.114, 0.122, and 0.145 for the normal distribution, lognormal distribution, and Weibull distribution. Since the normal distribution fit provides the smallest difference between the experimental data and the theoretical distribution, it is chosen as the distribution to represent the initial elastic modulus.

Figure 5-3 provides the histogram of the experimental data for the first 6% strain cycle initial elastic modulus obtained from the 30 specimens along with the probability density function (PDF) for the fitted normal distribution. The result show that the PDF for the normal distribution catches the general trend of the experimental data with a mean value of 24.3 GPa and a standard deviation of 1.26. The resulting 95% confidence interval for this

Table 5-2: Summary of Distribution Fit Results for the Initial Elastic Modulus

	Distributions		
	Normal	Lognormal	Weibull
Parameters			
μ, λ, α	**24.3**	3.189	24.509
σ, ζ, u	**1.257**	0.052	24.845
K-S Test Results			
K statistic	**0.1139**	0.1219	0.1448
Critical Value	**0.1904**	0.1904	0.1904
Significance Level	**20%**	20%	20%

distribution thus lies between 21.8 GPa and 26.8 GPa. Although there is some variability in the initial elastic modulus, the low standard deviation and fairly small confidence interval suggests that consistent stiffness can be obtained from NiTi wire which is important for implementation of SMAs into structural engineering applications. Based on the figure, the results do suggest that the normal distribution overestimates the lower elastic modulus values and underestimates the higher values.

5.4.2 Forward Transformation Stress

The forward transformation stress is an important property for modeling SMA behavior because it is the equivalent to the yield stress in other materials which undergo plastic deformation. It basically provides the stress at which the loading plateau forms and the stress required to initiate the martensitic transformation. Table 5-3 provides the distribution parameters and goodness of fit results. Once again, all three distributions show an acceptable fit at the 20% significance level. However, the lognormal distribution provides the smallest K statistic, 0.121, as compared to the normal and Weibull distributions, 0.124 and 0.190, respectively. As a result, the lognormal distribution is chosen to represent the variability

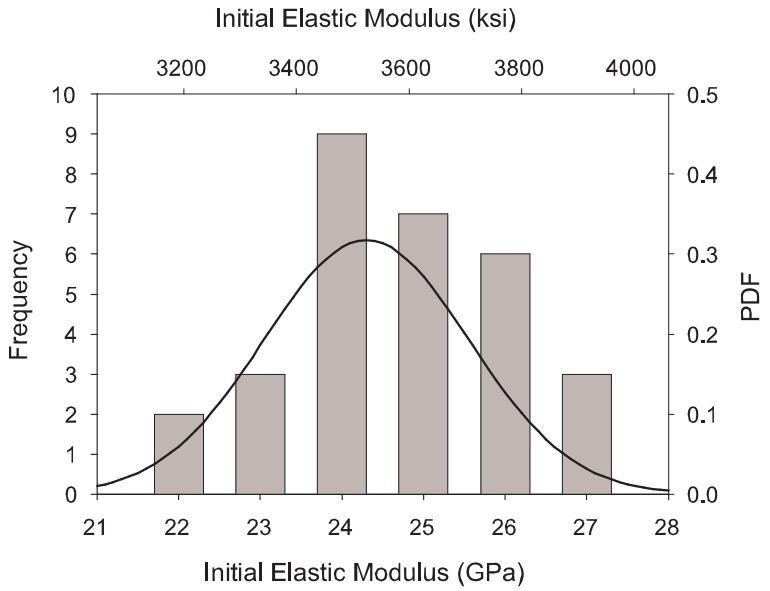

Figure 5-3: Histogram and overlayed fitted PDF for the first 6% strain cycle initial elastic modulus.

in the forward transformation stress. This is not surprising given that material strength is often taken as being lognormally distributed.

The resulting mean and standard deviation which is obtained from the lognormal distribution is 467.36 MPa and 6.54 MPa, respectively. The mean value is similar to the results

Table 5-3: Summary of Distribution Fit Results for the Forward Transformation Stress

	Distributions		
	Normal	**Lognormal**	Weibull
Parameters			
μ, λ, α	467.239	**6.147**	100.237
σ, ζ, u	6.557	**0.014**	469.899
K-S Test Results			
K statistic	0.1238	**0.1210**	0.1902
Critical Value	0.1904	**0.1904**	0.1904
Significance Level	20%	**20%**	20%

found for the untrained specimens tested dynamically as part of the training study. A histogram of the experimental data for the first 6% strain cycle forward transformation stress obtained from the 30 specimens is shown in Figure 5-4 along with the PDF of the lognormal distribution. The PDF follows a similar trend as the histogram further suggesting a good fit of the distribution. The bounds of the 95% confidence interval are 454.7 MPa and 480.3 MPa. In general, consistent behavior in terms of the forward transformation stress is obtained for NiTi wires based on the small 95% confidence window.

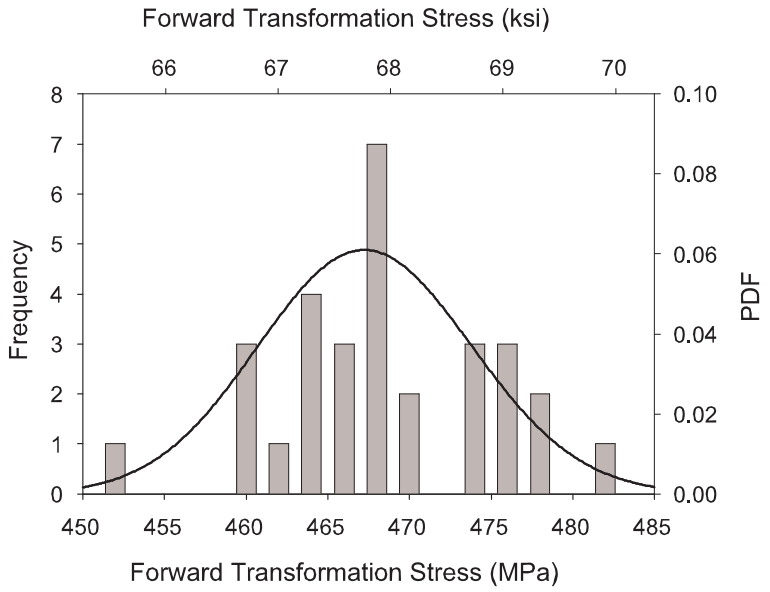

Figure 5-4: Histogram and overlayed fitted PDF for the first 6% strain cycle forward transformation stress values.

5.4.3 Loading Plateau Slope

Many past studies have considered the slope of the loading plateau to be either flat or fixed to some arbitrary percentage of the initial elastic modulus. The slope of the loading

Table 5-4: Summary of Distribution Fit Results for the Loading Plateau Slope

	Distributions		
	Normal	**Lognormal**	Weibull
Parameters			
μ, λ, α	10.341	**2.335**	27.063
σ, ζ, u	0.488	**0.047**	10.552
K-S Test Results			
K statistic	0.1604	**0.1518**	0.2194
Critical Value	0.1904	**0.1904**	0.2417
Significance Level	20%	**20%**	5%

plateau can be highly dependent on the means in which the phase transformation occurs (randomly or Lüders-like) and on the presence of residual martensite. For this reason, it is important to gain some understanding of the distribution of this property for typical NiTi wires. In terms of structural applications, the loading plateau slope is important because it determines the stiffness of the structure during intermediate strain levels. The distribution parameters and the results from the K-S tests are shown in Table 5-4. Both the normal and lognormal distributions pass the K-S test with an associated 20% significance level, but for the case of the Weibull distribution only a 5% significance level is reached. Comparing the K-statistic for the normal and lognormal distributions, it is clear that the lognormal distribution provides the best fit out of the two.

The PDF for the lognormal distribution overlayed on top of the histogram of the experimental data of the loading plateau slope for the first 6% strain cycles is shown in Figure 5-5. As with the past results, the PDF from the lognormal distribution shows a good fit with the experimental results. The mean and standard deviation associated with this distribution are 10.34 GPa and 0.49 GPa. The small value of the standard deviation suggests that the variation in the slope of the loading plateau is minimal provided the material has the same

composition and underwent the same processing. This is also shown by the 95% confidence interval which ranges between 9.42 GPa and 11.33 GPa. Comparing the mean value of the loading plateau slope to that of initial elastic modulus, the loading plateau slope is approximately half that of the initial elastic modulus resulting in a large decrease in the stiffness of the structure. However, it should be noted that the large diameter bars tested in Chapter 3 have much flatter loading plateaus. Further work may be necessary to correlate this value with either bar size or composition.

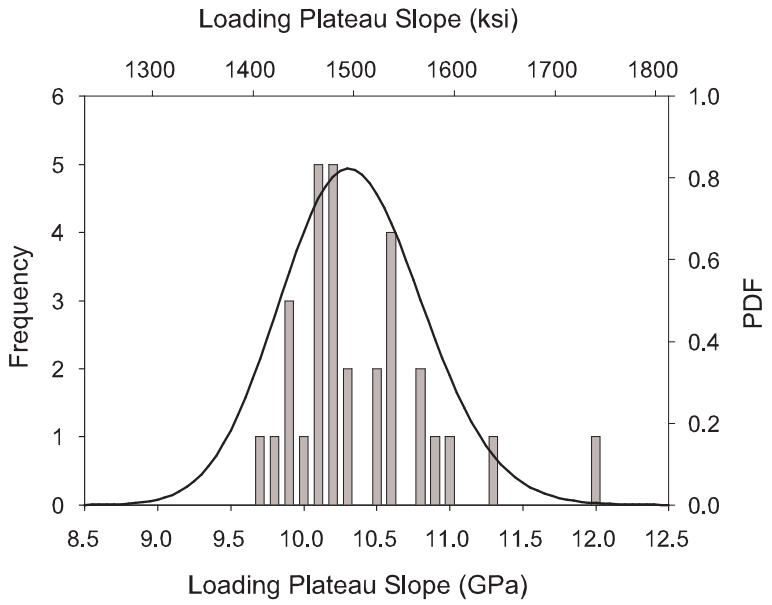

Figure 5-5: Histogram and overlayed fitted PDF for the first 6% strain cycle loading plateau slope values.

Table 5-5: Summary of Distribution Fit Results for the Martensite Stress

	Distributions		
	Normal	**Lognormal**	Weibull
Parameters			
μ, λ, α	716.801	**6.575**	62.822
σ, ζ, u	15.505	**0.022**	723.268
K-S Test Results			
K statistic	0.1447	**0.1422**	0.2002
Critical Value	0.1904	**0.1904**	0.2002
Significance Level	20%	**20%**	15%

5.4.4 Martensite Stress

The martensite stress provides a general idea of the stress values when stress-induced martensite is fully formed resulting in a significant increase in the stiffness of the material to some value between the initial elastic modulus and slope of the loading plateau. Based on experimental results (see Figure 5-6), the martensite stress values is taken as 4.5% strain along the loading curve. Table 5-5 summarizes the parameters obtained for each of the distributions and the results for the goodness of fit testing. As with the loading plateau slope, the Wiebull distribution does not reach a 20% significance level. However, both the normal distribution and the lognormal distribution do with the lognormal distribution just barely providing a better fit based on the K-statistic. As a result, the lognormal distribution is chosen to represent the martensite stress measured for the first 6% strain cycle.

The PDF based on the lognormal distribution for the martensite stress provides a fairly accurate fit of the experimental data (Figure 5-6). The resulting mean and standard deviation associated with this distribution are 717.1 MPa and 15.78 MPa, respectively. This distribution has a larger variance than that associated with the forward transformation stress

given that the standard deviation is almost double that found for the forward transformation stress. The 95% confidence interval spans 61.8 MPa with end values of 686.7 MPa and 748.5 MPa. The variability in the martensite stress may be due to a variety of reasons such as the locations of dislocations within the material and the build up of residual martensite. The high variability of this property makes it even more important to account for the uncertainty in the material behavior when modeling SMAs for seismic applications in structures.

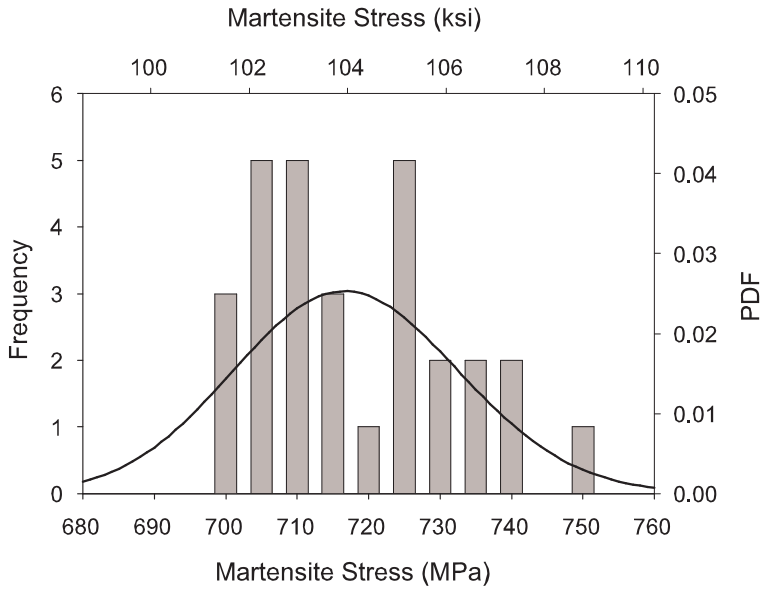

Figure 5-6: Histogram and overlayed fitted PDF for the first 6% strain cycle martensite stress values.

5.4.5 Reverse Transformation Stress

The reverse transformation stress assumed for this study is a rough estimate of the start of the reverse transformation. For this purpose, the stress at 4.5% strain along the unloading

Table 5-6: Summary of Distribution Fit Results for the Reverse Transformation Stress

	Distributions		
	Normal	**Lognormal**	Weibull
Parameters			
μ, λ, α	588.773	**6.378**	45.759
σ, ζ, u	17.079	**0.029**	596.016
K-S Test Results			
K statistic	0.1310	**0.1289**	0.1837
Critical Value	0.1904	**0.1904**	0.1904
Significance Level	20%	**20%**	20%

curve is chosen to represent this value based on the stress-strain curves and typical phenomenological modeling practice. The parameters for each distribution and results from the subsequent K-S testing are shown in Table 5-6. For the reverse transformation stress, all three distributions provide a 20% significance level. A comparison of the K-statistic shows that the lognormal distribution provides the smallest difference between the CDF established based on the experimental data and that based on the theoretical fit distribution. As a result, the lognormal distribution is chosen to represent the reverse transformation stress for the first 6% strain cycle with parameters of 6.38 and 0.03 for λ and ζ, respectively.

The mean and standard deviation for the lognormal distribution representing the reverse transformation stress are 589 MPa and 17.1 MPa. The PDF for the lognormal distribution with these mean and standard deviation values is shown in Figure 5-7 with a histogram of the experimental results. One obvious point to note from Figure 5-7 is the lack of ability for this distribution to capture the high frequency of reverse transformation stresses with a value of approximately 575 MPa. However, the PDF does capture the general trend besides this one peak in the histogram. The general importance of the reverse transformation stress

lies in how the SMA material model accounts for cycling. If the material model uses a trigger-line approach (as is seen in the following chapter) the reverse transformation stress value is not needed. The 95% confidence interval for this property ranges between 556 MPa and 623 MPa.

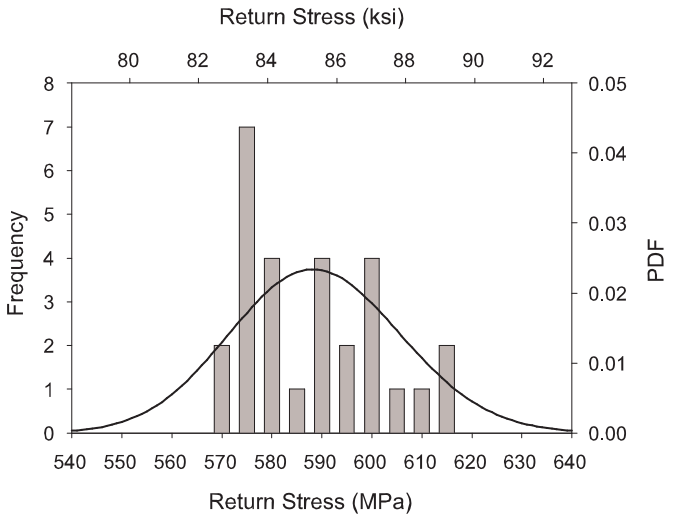

Figure 5-7: Histogram and overlayed fitted PDF for the first 6% strain cycle return stress values.

5.4.6 Residual Strain

The residual strain is one of the most important properties to understand for structural applications, since it provides a measure of the recentering capability of the material. The first 6% strain cycle residual strain values provide a general idea of the loss of recentering capability and provide a means of being able to model the uncertainty associated with the residual strains. The parameters for each distribution and the goodness of fit results are provided in Table 5-7. As with many of the other properties, all three distributions provide

Table 5-7: Summary of Distribution Fit Results for the Residual Strain

	Distributions		
	Normal	**Lognormal**	Weibull
Parameters			
μ, λ, α	0.412	**-0.892**	11.630
σ, ζ, u	0.042	**0.103**	0.430
K-S Test Results			
K statistic	0.1112	**0.0933**	0.1531
Critical Value	0.1904	**0.1904**	0.1904
Significance Level	20%	**20%**	20%

a good fit with a 20% significance level, but the lognormal distribution has the lowest K-statistic suggesting that it is the most appropriate distribution for modeling the residual strain.

Figure 5-8 provides a histogram of the experimental data with respect to the residual strain measured after the first 6% strain cycle along with the corresponding PDF for the lognormal distribution. The PDF provides a good representation of the experimental data capturing the general trend seen in the histogram. The mean and standard deviation associated with the lognormal distribution are 0.41% and 0.043%, respectively. The low mean value suggests that good recentering capability can be obtained from the NiTi wires even after being cycled to 6% strain. The low standard deviation also suggests that the variation in the residual strain values is small. This is further confirmed by the 95% confidence interval which lies between 0.33% and 0.50%.

5.5 Closure

This chapter performs a statistical study based on the results of 30 cyclic tensile tests performed on 2.16 mm diameter NiTi wires. From these stress-strain curves, the initial elastic

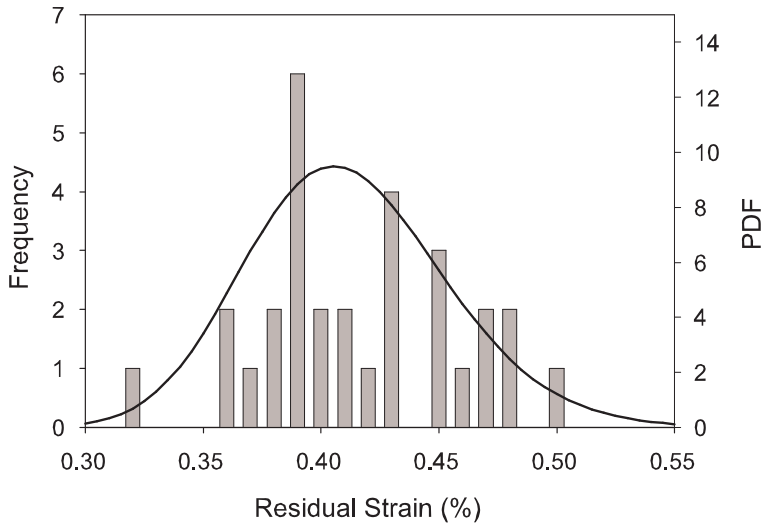

Figure 5-8: Histogram and overlayed fitted PDF for the first 6% strain cycle residual strain values.

modulus, forward transformation stress, slope of the loading plateau, martensite stress, reverse transformation stress, and residual strain values are obtained for the first 6% strain cycle. Normal distributions, lognormal distributions, and Weibull distributions are then fit to each of these properties using the method of moments. The goodness of the fit is then tested for each type of distribution with the K-S test providing the determining factor on which distribution is selected. For all of the properties, a 20% significance level is obtained for the fit of the chosen distribution with the lognormal distribution being selected for all properties except the initial elastic modulus. The normal distribution provides the best fit for this property. The determination of distributions to account for variability in these material properties is important given the focus on performance-based and consequence-based seismic design. These distributions provide a means of performing future reliability studies

on structures implementing NiTi SMAs and increase the likelihood of seeing NiTi used in practice. A next step in looking at the distribution of SMA properties is to include wires from a variety of manufactures, which claim to have the same composition and properties. It is expected that the SMA properties from such a study would show larger variances, but more general distributions would also be obtained. These studies can then be extended to various compositions to determine if the distributions are consistent with respect to composition. Also, future work is still necessary to develop distributions for large diameter sections such as those studied as part of this dissertation.

CHAPTER VI

ANALYTICAL STUDY OF SEISMIC APPLICATIONS OF SHAPE MEMORY ALLOYS

6.1 Introduction

The occurrence of recent earthquakes in urban areas has exposed the vulnerability of structures to moderate and strong ground motions. The 1989 Loma Prieta, 1994 Northridge, and 2001 Nisqually earthquakes in the United States; the 1995 Hyogoken-Nanbu (Kobe) earthquake in Japan; and the 1999 Kocaeli earthquake in Turkey have resulted in major damage to the building and bridge infrastructures and subsequent large monetary losses being sustained. Critical building and bridge components experienced large permanent deformations as a result of conventional design techniques which rely on the inelastic response of beams, columns, and connections in buildings and piers in bridges to dissipate energy during a seismic event. Increased population in these areas of moderate and high seismicity has led to unusually high economic losses with estimates in excess of $50 billion (U.S.) to $100 billion (U.S.) each being attributed to both the Northridge and Kobe earthquakes (Comartin et al., 1995; Eguchi et al., 1998). As a result, the structural engineering community in the United States has focused on a more performance-based design approach to earthquake mitigation in structures in order to prevent such damage, loss of life, and economic losses in the future.

Performance-based design provides engineers with a means to design and analyze buildings such that they have a more predictable and reliable performance in the event of an earthquake (Hamburger et al., 2003). Much of the focus of performance-based design is the characterization of acceptable inter-story drift values for a structural engineering system given a seismic hazard where increased maximum inter-story drift can be associated with increased damage levels. As a result, the SAC steel project funded by the Federal Emergency Management Agency (FEMA) developed guidelines defining performance levels based on drift limits for steel moment frames which accounted for the uncertainties associated with seismic events (FEMA, 2000). Performance-based design guidelines have led to the development of devices to limit the inelastic behavior of critical structural members based on three main concepts: pure energy dissipation (damping), decoupling of the structure from the foundation (base isolation), and limiting force transmission to critical load bearing members (VanHumbeeck and Liu, 2000).

Passive energy dissipation devices have been introduced and proven as a means to meet performance-based design guidelines, but often fail to significantly reduce residual drifts affecting the final state of the structure. Since excessive residual drifts can lead to increased repair costs and economic losses, an alternative to traditional passive energy dissipation systems is the development of seismic mitigation systems for civil structures which implement non-traditional civil engineering materials to reduce both inter-story and residual drifts. However, in order to implement such a device into practice, a good understanding of its ability to improve the performance of different building systems under a performance-based design approach needs to be confirmed. Shape memory alloys are one particular smart material which has shown significant potential for exploitation as a cost effective

means to control the response of civil engineering structures in both retrofit and new building applications.

In particular, steel frame structural systems have been widely used in the United States for mid- to high-rise structures and may benefit from the use of SMA-based devices. A large majority of the steel frame systems built before 1994 consist of steel moment-resisting frames to provide lateral resistance during an earthquake. The 1994 Northridge earthquake and 1995 Kobe earthquake caused damage to many of the steel moment-resisting frames due to unanticipated fracture of welded beam-to-column connections resulting in unacceptably large displacements and permanent deformation (Nakashima et al., 1998). In order to address these problems, a considerable amount of research, both in Japan and the United States, has focused on steel moment frames. Researchers in Japan emphasized the development of new, more reliable, materials while researchers in the United States focused on the development of different connection geometries and configurations (Nakashima et al., 2000).

The problems associated with steel moment frame systems also led to a search for alternative economical lateral load resisting systems. As a result, the popularity of concentrically braced frames and more recently special concentrically braced frames has risen over the past decade (Sabol, 2004). Although there has been an increase in the use of braced frame systems, damage during past earthquakes suggests that braced frame systems, too, may perform poorly due to limited ductility and energy dissipation of the bracing system, failure of the connection between the brace and frame, and asymmetric behavior of the brace in tension and compression (Sabelli et al., 2003). As a result of these possibilities and the focus on performance-based design, there exists a need to investigate means of

improving both design and retrofit measures for current concentrically and special concentrically braced frame systems to ensure desired limit states are met.

Based on the results from the experimental materials testing of the NiTi SMAs, one means of improving the performance of concentrically braced frame systems in terms of limiting inter-story drift levels is through the use of innovative materials in the bracing element. In particular, the flag-shape hysteresis under cyclic axial loading which can provide recentering and supplemental energy dissipation to a structural system may act to limit inter-story drifts and decrease the onset of permanent deformation within the structural frame. In order to assesses these bracing systems through analytical means, models of the SMA material must be developed which can accurately capture the cyclic behavior of the SMA while also not incurring large increases in computation time. With these models, an SMA bracing system can be compared to current systems to determine the benefits.

This chapter evaluates the performance of an SMA bracing systems in special concentrically braced steel frames and compares their behavior to the same system using conventional steel braces. Two experimental phenomenological models of the SMA behavior are first developed, the simplified model and the trigger-line model. The difference between how each of the models account for sub-cycling is evaluated through a simple single degree of freedom (SDOF) system study. Second, the performance of concentrically braced systems implementing either conventional buckling-allowed steel braces or superelastic SMA braces are studied through a series of nonlinear time history analyses to determine the potential of using SMAs in earthquake engineering applications in order to control the dynamic response of building structures.

6.2 Analytical Models

Before structural systems implementing SMAs for earthquake engineering applications can be studied through analytical techniques, models of their cyclic behavior need to be developed. Modeling of SMAs has attracted a large amount of attention over the past two decades with models of varying complexities and capabilities for capturing the exact behavior of the SMAs being developed. The requirements for SMA models to be used in structural engineering are unique in the fact that they need to be able to be manipulated by professionals who may not have a background in SMA behavior or materials science. As a result, the model should only consider a minimal number of variables to explain the SMA uniaxial behavior. These models also must not significantly increase the processing time needed to perform nonlinear time history analyses as the SMA component represents only a small (albeit significant) portion of the overall structure. With these points in mind, two experimental phenomenological models are developed which use minimal parameters to predict the force-displacement relationship of an SMA component undergoing uniaxial loading. The models that are developed consist of two different approaches for accounting for sub-cycling or incomplete cycle behavior. These models are discussed and evaluated in detail in this section before actual applications of SMAs in structural systems can be considered.

6.2.1 Simplified Model

The simplified model is similar to piecewise phenomenological models used in early studies on damping applications of SMAs in structures (Thomson et al., 1995). The phenomenological force-displacement relationship has constant loading and unloading stress

plateaus where the forward and reverse martensitic phase transformations occur and elastic loading and unloading when the material is not undergoing a phase transformation as is seen in Figure 6-1. Only a few parameters are needed to construct the simplified model which captures the hysteretic behavior and strain hardening at large tensile strains. These parameters include the initial stiffness, k_i; the stiffness during phase transformation, k_{PL}; the stiffness during strain hardening as a result of the formation of stress-induced martensite, k_M; the forward transformation force, F_L; the force at which strain hardening begins, F_M; and the force at which the reverse transformation is completed, F_{UL}. These parameters are labeled in Figure 6-1. The simplified model assumes both the forward and reverse transformation stress plateaus occur with the same stiffness or slope. Incomplete cycling or internal cycling is accounted for by loading or unloading in an elastic manner until either the loading or unloading plateau is reached. This simplified model cannot capture degradation of the loading and unloading plateaus or the accumulation of residual strain with continued cyclic loading. However, the training results from Chapter 4 suggest that stable behavior can be obtained through proper mechanical training. As a result, this model should provide the appropriate behavior for trained specimens.

6.2.2 Trigger-line Model

Similar to the simplified model for SMA behavior, the trigger-line model provides a phenomenological model of the force-displacement relationship of a superelastic SMA, as seen in Figure 6-2. The trigger-line model is based on the proposed model by Müller and Huibin (1991) and Thomson et al. (1997) where a trigger-line is used to account for the formation of inner hysteresis loops and to account for incomplete cycling. The model requires only

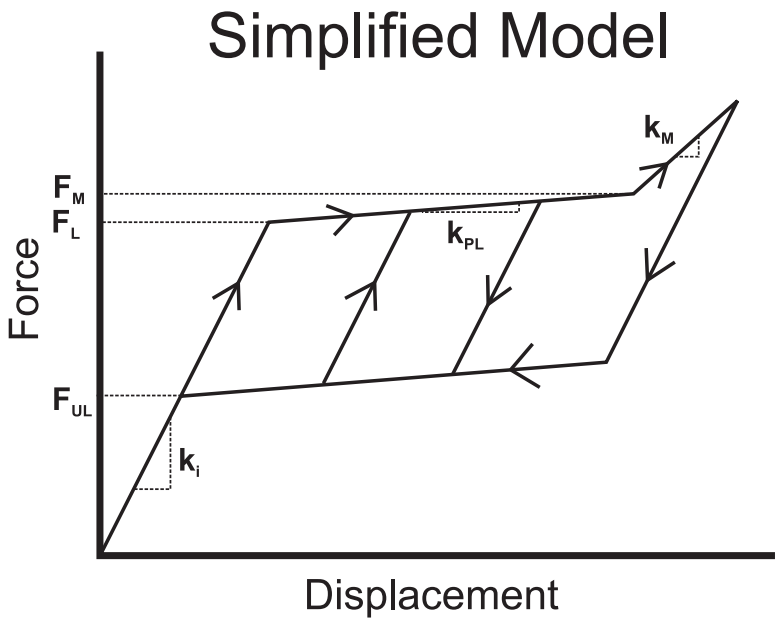

Figure 6-1: Schematic of the simplified uniaxial material model for NiTi SMAs with the required parameters labeled.

a few parameters which are obtained from previous experimental materials tests and is capable of accounting for strain hardening at large strain values. The parameters which are needed for the trigger-line model include the initial stiffness, k_i; the stiffness during phase transformation, k_{PL}; the stiffness during strain hardening as a result of the formation of stress induced martensite, k_M; the forward transformation force, F_L; the force at which strain hardening begins, F_M; and the slope of the trigger-line, kk. Use of a trigger-line results in a changing forward and reverse transformation plateau stress for inner hysteresis loops. The value depends on the force level where the loading and unloading occurs with respect to the trigger-line which runs diagonally across the hysteresis loop from the onset of initial yielding (forward transformation stress). The trigger-line defines the formation of the inner hysteresis loops by defining the point at which the material starts its

forward transformation (upon crossing the trigger-line while loading the SMA) and starts the reverse transformation (upon crossing the trigger-line while unloading the SMA). By implementing a trigger-line model, the force at which the unloading plateau occurs decreases with larger elongations of the SMA element, which has been shown to be more consistent with experimental results (see Chapter 3 and 4). As with the simplified model, the trigger-line model cannot account for loading plateau degradation or the accumulation of residual strain due to cycling.

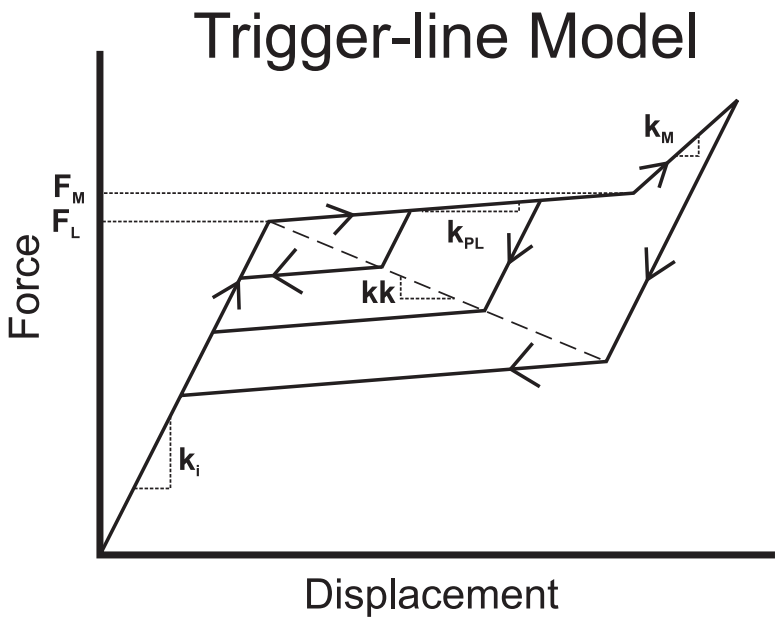

Figure 6-2: Schematic of the trigger-line uniaxial material model for NiTi SMAs with the required parameters labeled.

6.2.3 SDOF of Freedom Comparison Study

In order to compare the behavior of the two models and gain an understanding of how the different sub-cycling approaches affect the overall response of a system, a simple SDOF

system implementing SMAs is evaluated. A single case study ground motion is used to compare the force-displacement behavior for the two different SMA models and the resulting displacement time histories for the system. The maximum displacements of the system resulting from the suite of ground motions are then compared to see the effect of the two different models. The differences in the result provide an idea of which model is most appropriate in terms of balancing simplicity and accuracy.

A one-bay, one-story frame fitted with tension-only SMA cross-braces is chosen to evaluate the most appropriate method of modeling the SMA behavior with respect to accuracy of results and ease of implementation. The frame structure has a height of 3.05 m and a span of 6.10 m. The columns are designed and modeled so as to remain linear elastic while undergoing a seismic event in order to provide a better comparison of the two SMA constitutive models. The beam spanning the bay is assumed to be rigid and acts to transfer the same displacement to each of the column members. These assumptions allow the frame to be modeled as a basic single degree of freedom system with a stiffness of approximately 76.4 MN/m based on the stiffness of the column members and the initial elastic stiffness of the SMA cross-braces as seen in Figure 6-3. A weight of 961 kN is chosen for the system in order to ensure that the SMA components undergo the martensitic phase transformation. The resulting natural period of the SDOF system is 0.24 seconds.

The parameters of the SMA constitutive models are based on the 19.1 mm diameter NiTi bar stress-strain curve when cycled through the earthquake type loading at 0.5 Hz (Figure 3-23(b)). This stress-strain behavior is chosen because the 19.1 mm bars are tapered down to 12.7 mm in diameter which is a convenient size for structural applications and this stress-strain behavior accounts for dynamic loading effects. The model parameters for both

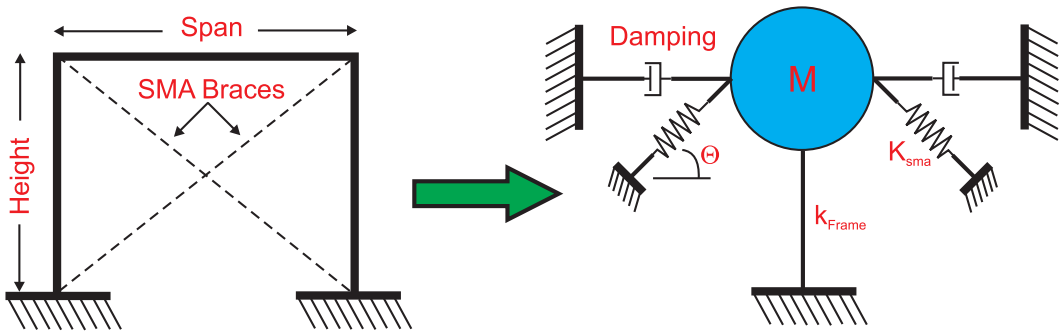

Figure 6-3: Schematic of the one bay, one-story frame fitted with SMA cross-braces and the subsequent SDOF model used to represent it for the analysis.

the simplified model and trigger-line model are given in Table 6-1. The parameters are assigned assuming that the SMA component is only 45.72 cm long and the total cross-sectional area of SMA material is 7.6 cm^2 (six 12.7 mm reduced diameter bars). In order to provide the required stiffness, the SMA does not span the total length of the cross-brace. Instead, the braces are assumed to consist of two stiff members that connect the required length of SMA to the frames, forcing all deformation into the SMA segment rather than in the connecting members. Converting the resulting force-displacement behavior to stress and strain based on the SMA dimensions, Figure 6-4 shows the behavior of the models overlaid on top of the actual stress-strain behavior of the 19.1 mm diameter bar. The results clearly show that the trigger-line model is more accurate in accounting for the change in the unloading plateau with increasing strain level.

A suite of ground motion records is used to analyze the difference between the simplified model and the trigger-line model. This suite consists of 20 ground motions corresponding to a seismic hazard level of 10% probability of exceedance in 50 years. The ground motions are developed from historical records for the Los Angeles, CA area as part

Table 6-1: Model Parameters for SDOF Study Based on the 19.05 mm Diameter NiTi Bar Results

	Model	
Property	Simplified	Trigger-Line
k_i (MN/m)	52.0	52.0
k_{PL} (MN/m)	1.72	1.72
k_M (MN/m)	15.3	15.3
F_L (kN)	356	356
F_M (kN)	380	380
F_{UL} (kN)	283	-
kk (MN/m)	-	-2.41

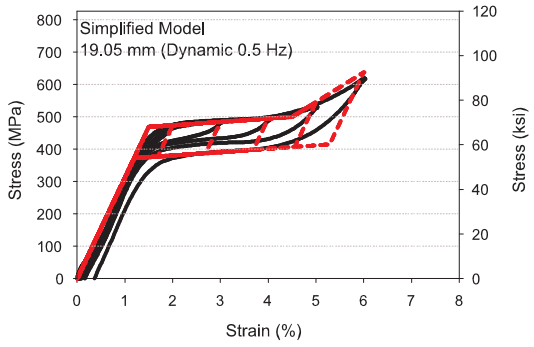

6-4(a):

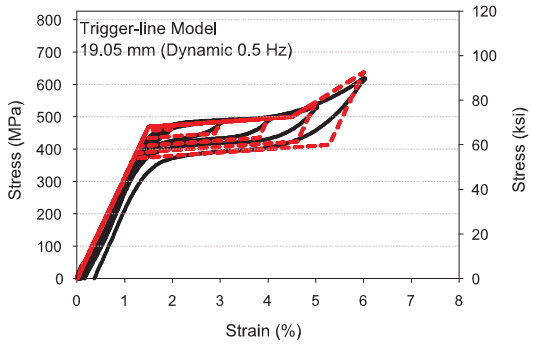

6-4(b):

Figure 6-4: SMA constitutive models used for the SDOF study overlaid on top of the experimental stress-strain behavior of the 19.05 mm NiTi bar tested at 0.5 Hz from which the parameters are based: (a) simplified model and (b) trigger-line model.

of the FEMA/SAC study on steel moment-resisting frames (Somerville et al., 1997). More details in regards to the ground motions can be found in Appendix F. No further scaling of the ground motions is conducted for this analysis in order to better gauge the behavior of the two models under different spectral accelerations at the fundamental period of the frame.

In order to evaluate the behavior of both of the SMA models, the LA19 ground motion (1986 North Palm Springs fault normal motion) is used for a case study focusing on the displacement time history of the systems and force-elongation plots for one of the braces. The displacement time history for the SDOF system using either the simplified model or the trigger-line model to predict the behavior of the SMA element is shown in Figure 6-5. The results suggest that both models predict a very similar behavior, particularly over the time range where large motions are expected. The system implementing the simplified model predicts a maximum displacement of 35.75 mm and the system using the trigger-line model predicts a maximum displacement of 36.18 mm. The difference between the two models is just over 1% suggesting very little change with respect to which model, the simplified model or trigger-line model, is used to predict the SMA behavior.

Figure 6-6 compares the force-elongation plots for one of the braces (SMA springs) in the SDOF model undergoing the LA19 ground motion. Both types of SMA models result in similar maximum elongation and maximum brace force values. The difference in the reverse transformation stress is also evident as the trigger-line model shows a decrease in the reverse transformation stress with an increase in strain magnitude which more closely mimics the real behavior of an SMA bar under tension. Since both models reached the same force level, the reverse transformation plateau for the trigger-line model is slightly

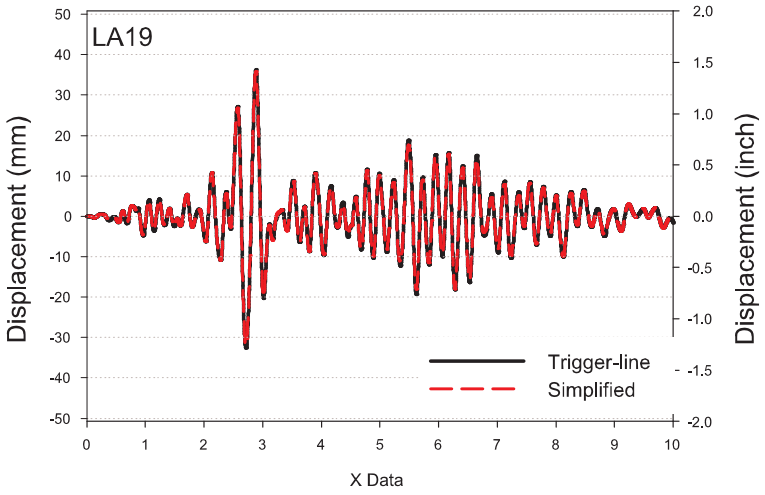

Figure 6-5: Displacement time-histories for the SDOF system undergoing the LA19 ground motion and using either the simplified SMA model or the trigger-line SMA model for the SMA element.

lower than that associated with the simplified model for the maximum elongation cycle. One important point to note is that even though both models produce a similar behavior, the simplified model overestimates the energy dissipated per cycle as the hysteretic area (particularly for low strain level cycles) is greater than that found experimentally as a result of the constant forward and reverse transformation plateaus. The trigger-line model provides a more accurate estimate of the actual hysteretic area. In general, both models capture the same general trends without much difference in computational effort.

The maximum drift for all twenty ground motions is shown in Figure 6-7 for the cases where either the simplified SMA model or trigger-line SMA model is used. For all of the ground motions, both models predict similar maximum drift values for the system with the largest difference in the maximum drift being only 0.04% as a result of the LA10 ground

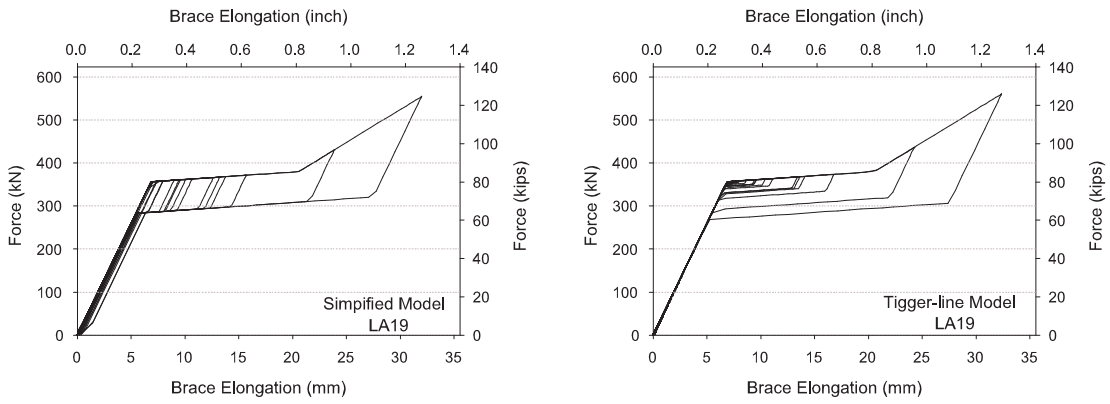

6-6(a): **6-6(b):**

Figure 6-6: Force-displacement plots for one of the braces in the SDOF system undergoing the LA19 ground motion using either the (a) simplified SMA model or (b) trigger-line SMA model.

motion. These results suggest that either model can accurately capture the maximum expected inter-story drifts for a system implementing SMAs. The similarity of the two SMA models may be a direct result of using the stress-strain curve of a dynamically tested bar in order to obtain the model parameters. The difference between the forward transformation plateau and reverse transformation plateau for a specimen tested dynamically remains small. The fact that the reverse transformation plateau does not change in the simplified model has only a minor effect compared to a case where the difference in the plateaus is greater. The similarity between the two models may not be as close for cases in which the system undergoes large amounts of sub-cycling, as is the case when the SMAs are previously pre-strained. Also, the stiffness ratio between the frame itself and the braces may affect the choice of the most appropriate SMA model, which needs to be explored in the future. In general, it appears that either model can be used to accurately predict the response

of a system implementing SMAs, but the trigger-line model more accurately predicts the true behavior of the SMA under tensile loads.

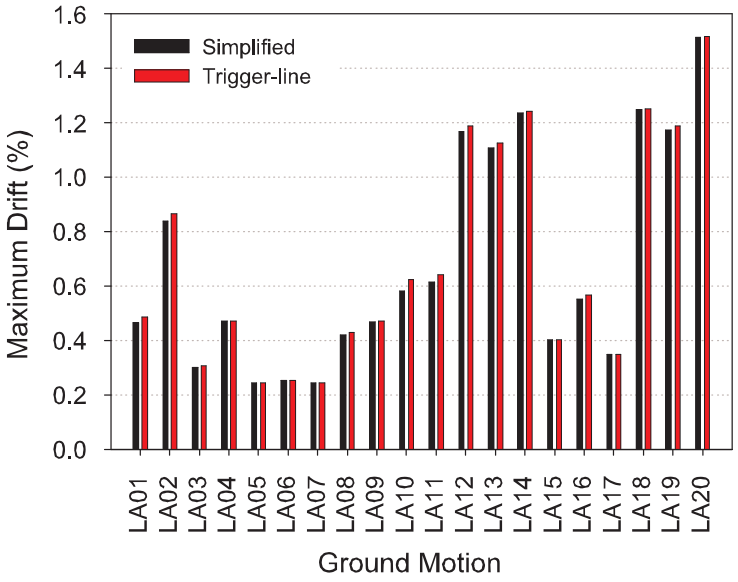

Figure 6-7: Maximum drift values of the SDOF system for all twenty ground motions where either the simplified SMA model or the trigger-line SMA model is implemented.

6.3 Evaluation of Braced Frames

With the development of capable models to predict the behavior of NiTi SMAs, specific applications can be analyzed to determine whether the use of SMAs is suitable under current seismic performance-based guidelines. One specific application which has been suggested is the implementation of superelastic SMAs in steel braced frame systems to provide both recentering and energy dissipation capabilities. The fact that the stress-strain behavior always passes through the origin limits the accumulation of permanent deformation in SMA

braces ensuring that the brace itself is always fully engaged. The stress plateaus limit the force transfer to other structural members at intermediate strain levels while strain hardening as a result of the formation of stress-induced martensite at large strain levels results in a stiffer structure and better control over subsequent floor displacements. These reasons, coupled with increased interest in special concentrically braced frames as an alternative to steel moment frames, provide an opportunity to understand in better detail whether there exists benefits in using SMA braces in terms of improving the structures performance. The following section outlines a preliminary analytical study designed to compare innovative SMA bracing systems to current steel bracing systems.

Four frames are selected from several presented by Sabelli (2001) in order to evaluate the performance of a superelastic SMA bracing systems as compared to conventional steel bracing systems. Two chevron (inverted-V) braced frames consisting of either three or six stories are first used to perform a detailed study evaluating the effects of using SMA braces as compared to conventional steel braces in which buckling is allowed. A case study using the 3-story inverted-V braced frame provides considerable detail between the difference in the behavior of the conventional steel braced frame versus the SMA braced frame. All subsequent frames are then compared based on the ability of a given bracing system to limit inter-story drifts and residual drifts as a result of the differences in their respective behaviors. The performance of the SMA braced system is then compared to more recently developed steel buckling-restrained braces implemented into the two chevron braced frames. Following the study of the chevron braced frames, a 3- and 6-story cross-braced frame is evaluated to determine if similar behavior can be obtained with alternative bracing configurations. The cross-braced systems also allow for evaluation of SMA tension-only systems.

These four frame configurations provide a good means of evaluating SMA bracing systems as compared to conventional systems.

6.3.1 Frame Characteristics

All four of the frames chosen for this study have been designed based on the 1994 Uniform Building and the 1997 NEHRP Recommended Provisions for Seismic Regulations for New Buildings and Other Structures assuming the structure is constructed in the Los Angeles, CA area with soil characteristics based on Site Class D. Both of the 3-story frames (inverted-V and cross-braced) are designed for the same building layout and both the 6-story frames (inverted-V and 2-story cross-braced system) are designed for an alternative building layout. The plan view for both of these buildings can be seen in Figure 6-8. Both buildings are designed with the braced bays along the perimeter to provide lateral load resistance during a seismic event. A total of four braced bays in each direction for the 3-story building and six braced bays in each direction for the 6-story building are incorporated into the design of the lateral load resisting system in order to prevent an increase in the brace design forces due to the Reliability Factor. Further details corresponding to the building design can be found in the work by Sabelli (2001) and Sabelli et al. (2003).

All of the braced frames have spans of 9.14 m with story heights of 3.96 m, except for the first story of the 6-story frames which has a story height of 5.49 m. The members of the framed system are designed consistent with the AISC Load and Resistance Factor Design Code and Seismic Provisions for Structural Steel Buildings. Member sizes for the various steel braced systems are shown in Table 6-2 and 6-3 for the 3-story frames and Table 6-4 and 6-5 for the 6-story frames. Because of the unbalanced load placed on the

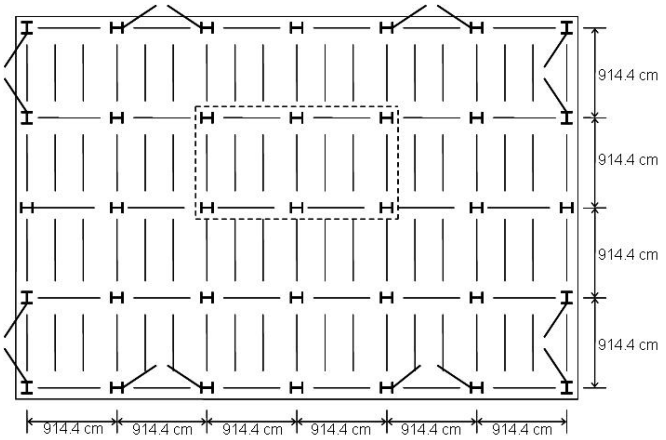

6-8(a):

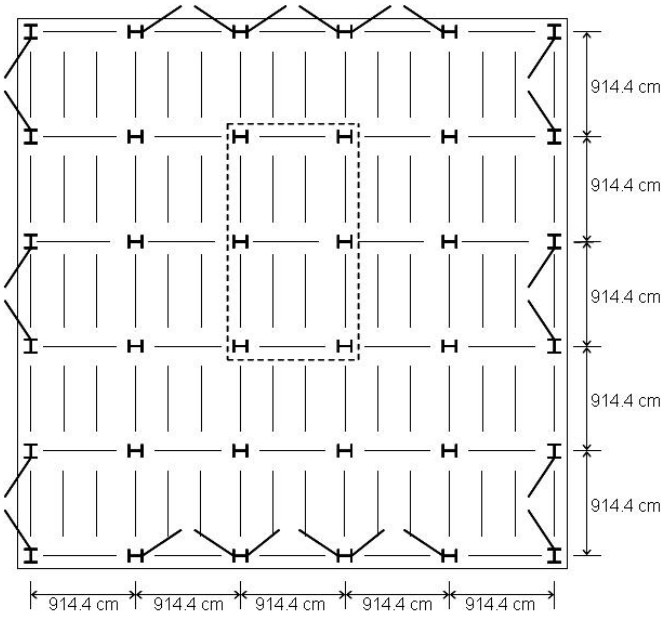

6-8(b):

Figure 6-8: Plan view of the (a) 3-story and (b) 6-story building used for the analysis of different concentrically braced frames .

Table 6-2: 3-Story Element Sizes for the Inverted-V Braced Frame

	Conventional			Buckling-Restrained		
Story	Column	Beam	Brace	Column	Beam	Brace
1	W12x96	W30x90	HSS 8x8x1/2	W12x96	W14x48	P_y 1441 kN
2	W12x96	W27x84	HSS 8x8x1/2	W12x96	W14x48	P_y 1152 kN
3	W12x96	W18x46	HSS 6x6x3/8	W12x96	W14x48	P_y 698 kN

Table 6-3: 3-Story Element Sizes for the Cross-Braced Frame

	Conventional		
Story	Column	Beam	Brace
1	W12x106	W18x46	HSS 8x8x1/2
2	W12x106	W18x46	HSS 6x6x1/2
3	W12x106	W18x46	HSS 5x5x3/8

beams when the steel braces buckle in compression, all beams of the inverted-V braced system, excluding the roof beam, are designed to account for the post-elastic behavior mode. Standard hollow-tube sections are used for the conventional buckling-allowed steel braces. The buckling-restrained braces, used as an alternative to the conventional steel braces in the inverted-V braced frames, are assumed to be constructed using a steel mortar filled tube with an unbonded yielding steel core. Details on the design of the buckling-restrained braces and future design recommendations can be found in Sabelli (2001). A general elevation view of the four types of braced frames can be seen in Figure 6-9 with the member sizes labeled for the conventional buckling-allowed steel braces. It should be noted that the cross-braces for the 6-story structure do not span two stories, but are actually alternating inverted-V and V-braces spanning only a single story. The system is labeled as cross-braced because of the visual appearance.

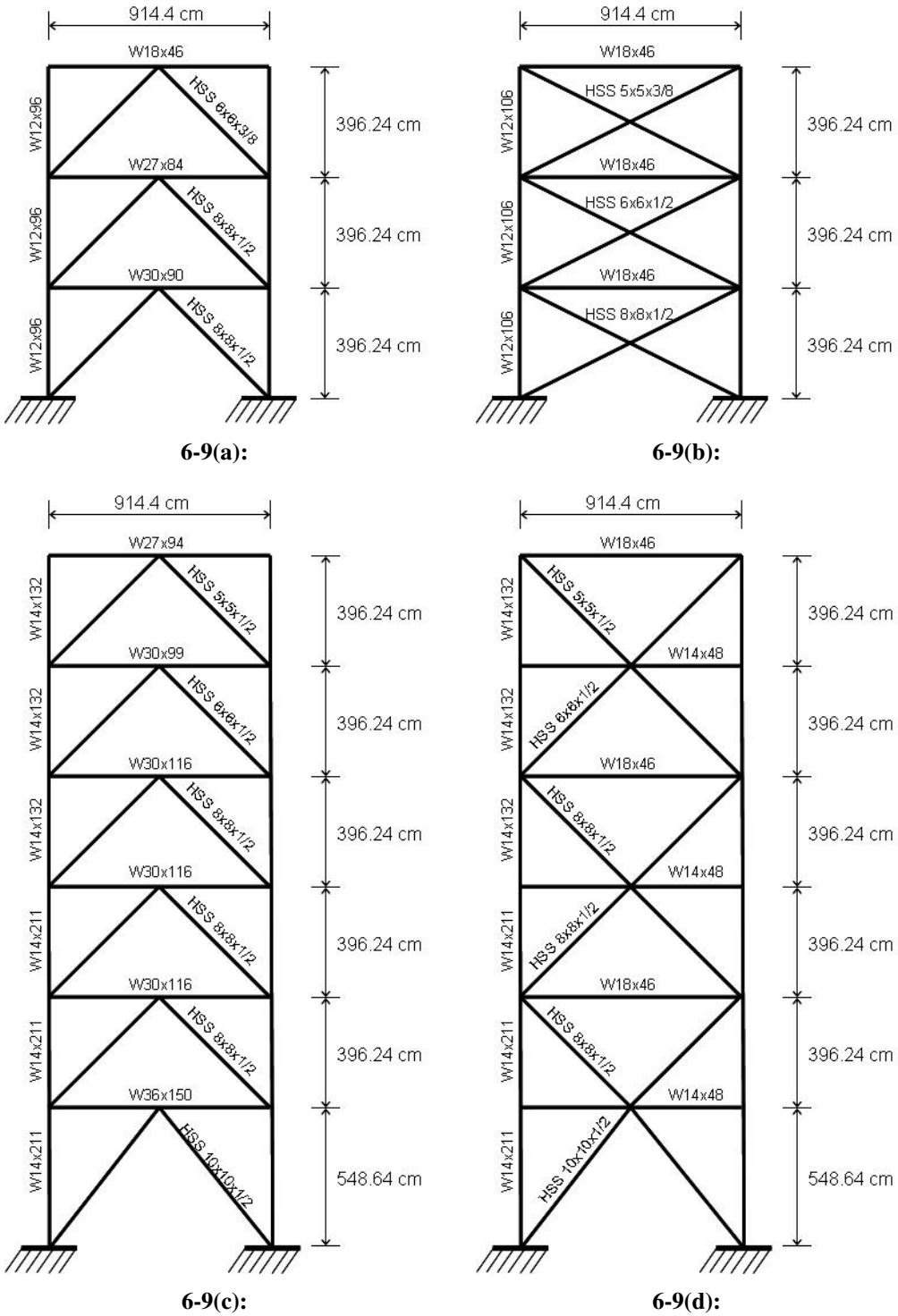

Figure 6-9: Elevation of the (a) 3-story inverted-V braced frame, (b) 3-story cross-braced frame, (c) 6-story inverted-V braced frame, and (d) 6-story cross-braced frame with the member sizes labeled for the conventional steel braced frame.

Table 6-4: 6-Story Element Sizes for the Inverted-V Braced Frame

	Conventional			Buckling-Restrained		
Story	Column	Beam	Brace	Column	Beam	Brace
1	W14x211	W36x150	HSS 10x10x1/2	W14x211	W14x48	Py 2273 kN
2	W14x211	W30x116	HSS 8x8x1/2	W14x211	W14x48	Py 1730 kN
3	W14x211	W30x116	HSS 8x8x1/2	W14x211	W14x48	Py 1552 kN
4	W14x211	W30x116	HSS 8x8x1/2	W14x132	W14x48	Py 1410 kN
5	W14x211	W30x99	HSS 6x6x3/8	W14x132	W14x48	Py 1281 kN
6	W14x211	W27x94	HSS 5x5x1/2	W14x132	W14x48	Py 770 kN

Table 6-5: 6-Story Element Sizes for the Cross-Braced Frame

	Conventional		
Story	Column	Beam	Brace
1	W14x211	W14x48	HSS 10x10x1/2
2	W14x211	W18x46	HSS 8x8x1/2
3	W14x211	W14x48	HSS 8x8x1/2
4	W14x132	W18x46	HSS 8x8x1/2
5	W14x132	W14x48	HSS 6x6x3/8
6	W14x132	W18x46	HSS 5x5x1/2

Along with the conventional steel braces and buckling-restrained steel brace, a superelastic SMA bracing system is considered. The frames which implement the SMA braces have the same beam and column design as the respective steel braced systems to which they are being compared (conventional steel braced or buckling-restrained steel braced). For each type of frame, all braces are replaced with the superelastic SMA braces. The SMA braces are conceptually designed such that the SMA does not span the whole length of the brace. Rather, the SMA is connected to an extremely rigid member which runs almost the length of the brace or the brace can be conceptualized as two steel tube members in which one tube slides within the other tube with the SMAs providing the connection between the tubes and all of the subsequent axial resistance. In either case, the SMA braces

can thus be modeled using an extremely rigid member in series with the appropriate length of SMA which is much softer. This forces all of the deformation into the SMA segment. This assumption assumes that the connecting section will be designed to resist buckling in compression and excessive yielding in tension. It is acknowledged that the actual system will not be completely rigid, but given the stiffness difference between the SMA and steel segment, displacements are expected to be minimal. Future work to account for deformation in this segment will be needed upon the actual development of these bracing systems when a more accurate assessment of the behavior of the connecting segment can be made. A simple schematic of how the SMA braces are models for the inverted-V braced and cross-braced frames is shown in Figure 6-10. In all cases, SMA braces are assumed to be able to take both tensile and compressive loads without undergoing buckling. This is accomplished by assuming that the SMA bars are encased in a grouted tube to prevent the onset of buckling during compression, but remain unbonded to still provide recentering capability. Given the corrosion resistance of NiTi SMAs, encasing the SMAs in grout poses no significant problems in terms of fatigue life or deterioration of the material. For the cross-braced systems, a tension-only SMA bracing system is also compared to the conventional steel bracing system in which the braces are assumed to engage only when undergoing tension, which eliminates the need to encase the SMAs in a grouted tube.

The SMA bars which are used in these systems consist of a number of bars of a single diameter in the range of 12.7 mm to 31.75 mm and are connected to the bracing system so as to act in parallel with each other. A sufficient number of bars are used to provide the required cross-sectional area with the length of all bars being equal. Since much of the analytical work has been performed in parallel with the materials characterization, the SMA

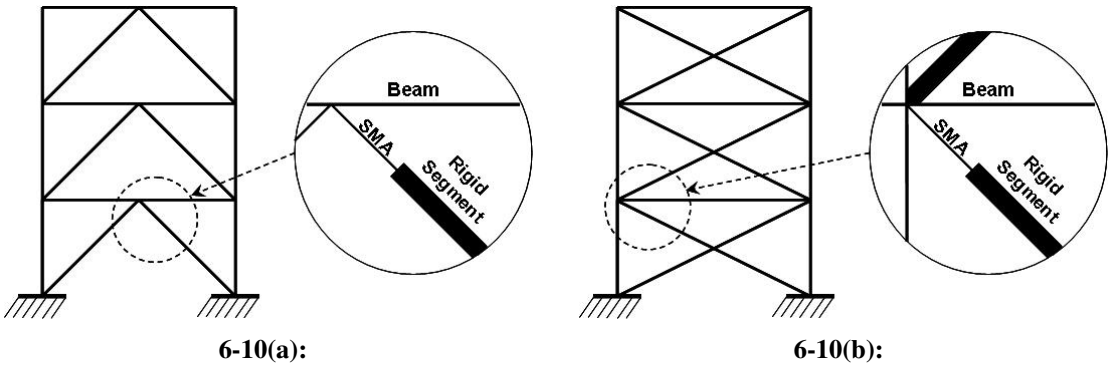

Figure 6-10: Idealized model for the SMA bracing system implemented into (a) the inverted-V braced frame and (b) the cross-braced frame.

behavior is modeled based on uniaxial tests presented in the work by DesRoches et al. (2004), which provides the cyclic properties of large diameter superelastic cold drawn SMA bars. These are similar to the hot rolled results shown in during the mechanical testing of the large diameter bars. The material properties selected for the numerical simulations are those obtained from the dynamic tests of the 12.7 mm diameter NiTi bar in order to correctly consider the reduced energy dissipation capability of such materials at high frequency loads. These properties are labeled in Figure 6-11(a) and are based on the stress-strain curve shown in Figure 6-11(b). The SMA braces are designed to provide the same initial axial stiffness and yield strength as either the conventional steel or buckling-restrained steel braces. As a result, the SMA braced frames have the same initial natural period as the corresponding steel braced frame to which they are being compared. The natural period of each of the frames is provide in Table 6-6 with the label in parenthesis following SMA referring to the frame to which that SMA braced frame is being compared. Moreover, both the steel and SMA braces yield at the same force levels. Table 6-7 and 6-8

provides the length and cross-sectional area of the SMA elements for each of the frame systems.

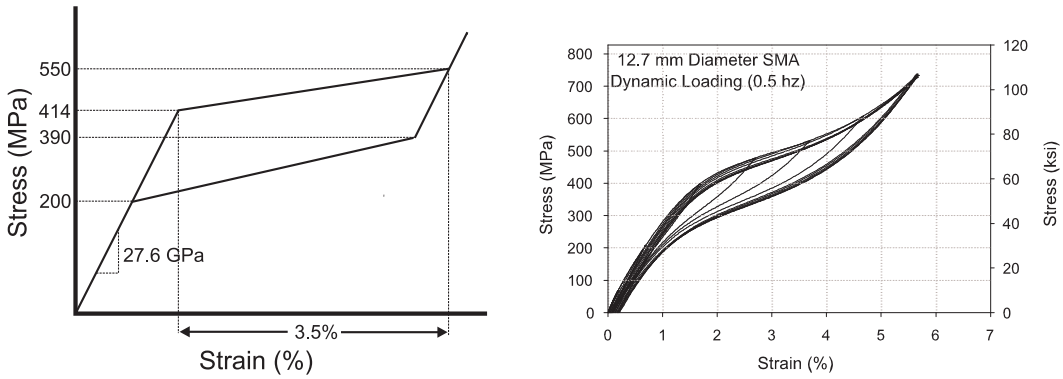

6-11(a): **6-11(b):**

Figure 6-11: (a) Idealized stress-strain curve for the SMA model with the properties used for the analytical analysis labeled and (b) the experimental stress-strain curve from DesRoches et al. (2004) used to determine the analytical SMA property values.

6.3.2 Analytical Model

In order to evaluate the dynamic performance of the braced frames, non-linear dynamic time history analyses are carried out using the OpenSEES (McKenna and Fenves, 2004) analysis platform. As suggested by the symmetry of the 3- and 6-story structures, only one braced bay is modeled. The floor masses used in the analysis to account for horizontally acting inertial forces are taken as the total mass of each floor divided by the number of braced bays in the lateral load resisting frame for each principal direction. Each floor mass is then distributed along the beam.

Beams and columns are modeled using the *nonlinearBeamColumn* element with fiber sections. Apart from the hinge connections between the beams and columns at the roof

Table 6-6: Natural Periods for all Analytical Frames

Frame	Brace	Natural Period (seconds)
	Inverted-V Braces	
3-story	conventional steel	0.46
3-story	SMA (conventional)	0.46
3-story	buckling-restrained steel	0.51
3-story	SMA (buckling-restrained)	0.51
6-story	conventional steel	0.74
6-story	SMA (conventional)	0.74
6-story	buckling-restrained steel	0.79
6-story	SMA (buckling-restrained)	0.79
	Cross-Braces	
3-story	conventional steel	0.52
3-story	SMA (conventional)	0.52
3-story	SMA tension only (conventional)	0.52
6-story	conventional steel	0.75
6-story	SMA (conventional)	0.75
6-story	SMA tension only (conventional)	0.75

Table 6-7: Geometric Characteristics of the SMA Elements for the Inverted-V Braced Frames.

	3-Story SMA (Conventional)		6-Story SMA (Conventional)		3-Story SMA (No Buckling)		6-Story SMA (No Buckling)	
Story	Length (mm)	Area (mm^2)	Length (mm)	Area (mm^2)	Length (mm)	Area (mm^2)	Length (mm)	Area (mm^2)
1	504	5259	595	6701	378	3481	153	5490
2	504	5259	504	5259	351	2783	349	4180
3	504	5259	504	5259	336	1687	346	3750
4	-	-	504	5259	-	-	343	3406
5	-	-	504	3795	-	-	340	3095
6	-	-	504	3795	-	-	330	1859

Table 6-8: Geometric Characteristics of the SMA Elements for the Cross-braced Frames.

	3-Story SMA (Conventional)		3-Story SMA Tension Only		6-Story SMA (Conventional)		6-Story SMA Tension Only	
Story	Length (mm)	Area (mm2)	Length (mm)	Area (mm2)	Length (mm)	Area (mm2)	Length (mm)	Area (mm2)
1	830	5258	830	5259	595	6701	595	6701
2	830	3793	830	3795	504	5259	504	5259
3	830	2406	830	2408	504	5259	504	5259
4	-	-	-	-	504	5259	504	5259
5	-	-	-	-	504	3795	504	3795
6	-	-	-	-	504	3070	504	3070

level, fixed connections are assumed between elements due to the use of gusset plates to form the connection between the brace and the frame, even though the frames themselves are not designed to be moment resisting (Sabelli et al., 2003). Braces are pinned at both ends so as to impose axial loads only. Global P-Δ effects are taken into consideration, but for the purpose of this analysis any added lateral stiffness from the gravity load framing is not considered. Collapse of the frame is not considered, as well, during this analysis. As commonly used for code-designed steel structures, a damping coefficient of 5% is assumed (Sabelli, 2001; Sabelli et al., 2003).

In order to model the material properties of the columns and beams, a typical uniaxial bilinear force-deformation relationship is considered based on typical structural steel properties (*Steel01* material model). A modified version of the *hysteretic* material model provides the axial deformation behavior of the conventional steel braces. This model has been implemented into OpenSEES to account for strength and stiffness degradation, negative post-buckling tangent stiffness, and pinching of the hysteresis associated with buckling-allowed steel braces. Figure 6-12(a) provides a schematic of the force-deformation curve

for this model. However, it should be noted that the steel brace behavior does not account for any stiffening in the buckled brace which would tend to reduce the displacements in the structure. As more accurate steel bracing models are developed, further comparisons between the systems should be completed. For the purpose of this preliminary study, the presented steel model is considered appropriate. The buckling-restrained steel braces are modeled using the *Steel01* material model (Figure 6-12(b)) since they are able to sustain compressive loads without buckling. This model provides a similar behavior to the idealized buckling-restrain brace behavior presented by Sabelli (2001).

The superelastic behavior of the SMA braces is simulated using a modified (Fugazza, 2003) one-dimensional constitutive model proposed by Auricchio and Sacco (1997). This model is selected since it provides a similar behavior to the previously presented trigger-line model and has previously been implemented into OpenSEES. The force-deformation behavior of the SMA model can be seen in Figure 6-12(c). Its formulation, developed in the small deformation regime, relies upon the assumption that the relationship between stresses and strains is represented by a series of straight lines whose extension depends on the transformation properties. As with previous studies, the austenite branch and stress-induced martensite branches are assumed to have the same Young's modulus (Bruno and Valente, 2002). A few shortcomings of this model is the inability to accurately account for tension-compression asymmetry and degradation of the cyclic properties, which is one area where continued efforts are needed to more accurately model SMA behavior. Further details in regards to the model formulation and integration techniques can be found in the work by Fugazza (2003).

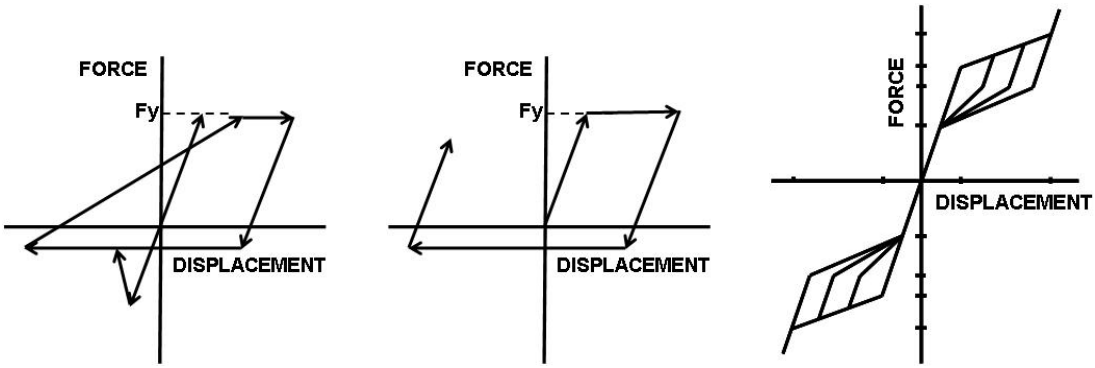

Figure 6-12: Force-displacement models for the (a) conventional steel braces, (b) buckling-restrained steel braces, and (c) SMA tension-compression braces.

6.3.3 Earthquake Ground Motions

The same suite of ground motions which are used for the SDOF study (Section 6.2.3) are used here to analyze the behavior of the 3- and 6-story braced frames. Along with the twenty 10% probability of exceedance in 50 years ground motions, a suite of twenty 2% probability of exceedance in 50 year ground motions are used. Appendix F provides further detail on these ground motions. All of the ground motions are developed from either historical records or from simulations for the Los Angeles, CA area as part of the FEMA/SAC study on steel moment-resisting frames (Somerville et al., 1997). No further scaling of the ground motions is conducted as part of this analysis in order to better gauge the response of the different bracing systems under different spectral accelerations and in order to maintain the integrity of the suites of motions.

6.3.4 Inverted V-braced Frames

The inverted-V braced frame systems is chosen to study in detail the behavior of both a conventional steel braced system where brace buckling is allowed and an SMA braced system which acts in both tension and compression. This is accomplished through a detailed case study of the 3-story frame followed by a comparison of the behavior of both the 3- and 6-story frames implementing each type of brace. The SMA bracing system is then compared to a more recently developed steel buckling-restrained system in order to determine how beneficial the recentering capability of the SMA braces is when both systems are able to sustain large compressive loads without buckling.

6.3.4.1 Case Study - 3-Story Braced Frame

The detailed comparative study of the 3-story inverted-V braced frame with either conventional steel braces or SMA braces which act in both tension and compression is conducted for a single ground motion. This case study uses the 6.7 magnitude Rinaldi RS Northridge ground motion (LA16) taken from the suite of ground motions having a seismic hazard level of 10% probability of exceedance in 50 years. The spectral acceleration associated with the first deformation mode for both types of braced 3-story frames is approximately 1.11g, which is approximately the average spectral acceleration (1.20g) imposed by the twenty ground motions making up the 10% probability of exceedance ground motion suite.

The inelastic behavior of both braced frames is shown in Figure 6-13, where column and beam members which have undergone yielding during the ground motion are depicted as solid circles with the size of the circle representing the extent of the yielding based on the recorded curvature. Buckling of the conventional steel braces along with the onset of

the martensitic phase transformation in the superelastic SMA braces are also labeled in the figure. The conventional steel braced frame shows yield points at every floor level along the continuous columns and buckling in the first and third floor braces suggesting large permanent displacements at these levels. The center of the first floor and third floor beams also experienced yielding with the second floor experiencing only a relatively small amount of damage. For the case of the SMA braced frame, only the first floor columns show the onset of yielding with all other large deformation being concentrated in the SMA braces. The ability of more members in the SMA braced frame to remain elastic can be attributed to the increased stiffness of the SMA braces at large strain levels due to the formation of stress-induced martensite resulting in smaller rotational demands in the column members. The loss of brace capacity due to buckling of the steel braces can result in large demands placed on the other members of the frame system, which are not present in the SMA system as a result of the SMAs ability to resist compressive loadings and provide recentering with no degradation of the properties.

The inelastic response of the two frame systems can be further assessed by looking at the moment-curvature relationship for the top of one of the first floor columns shown in Figure 6-14. The results show a considerably smaller maximum curvature for the column of the SMA braced frame as compared to the column of the conventional steel braced frame. The maximum curvature for the SMA braced frame is 0.014 m^{-1} compared with 0.061 m^{-1} for the conventional steel braced frame. More significant is the large permanent residual curvature for the column in the steel braced frame, 0.045 m^{-1} as compared to the SMA braced frame, $8x10^{-4}$ m^{-1}. The results suggest that the SMA bracing system can limit the amount of inelastic behavior in the other frame members and that the onset of

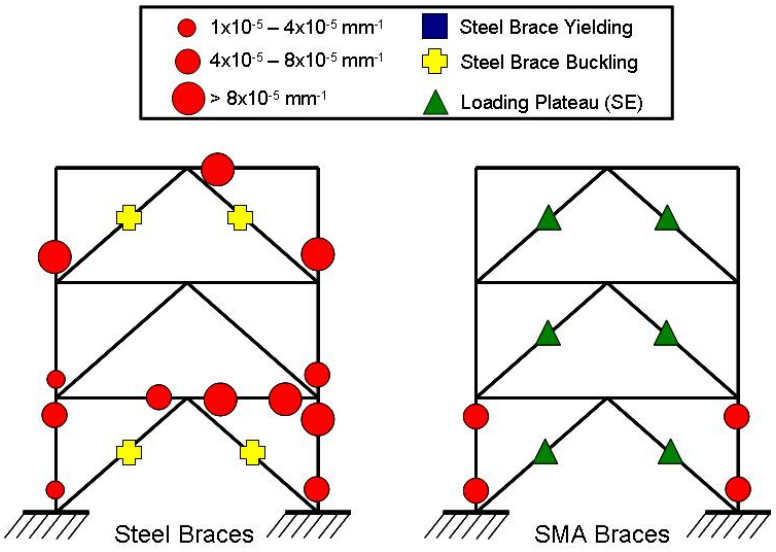

Figure 6-13: Member yielding as a result of the LA16 ground motion for the conventional steel and SMA inverted-V braced frames.

the loading and unloading plateaus and stiffening at large strain levels do not significantly increase member forces throughout the frame during a seismic event.

Now that the effects on the beam and column elements have been presented, the differences in the behavior of the two braces can be studied. Since the beam and column members are the same in both of the frames and the yield force and initial stiffness of both types of bracing systems are constant, the difference in the response must be attributed to the different behavior of the conventional steel braces, which undergo buckling, as compared to the superelastic SMA braces, which can sustain both tensile and compressive loads. The force-displacement plots for one of the first floor braces in each braced system are shown in Figure 6-15. Large deformations occur in the steel braces after buckling, 60 mm, while the SMA members have much lower displacements, 30 mm, due to the recentering capability guaranteed by the superelastic effect. The plots clearly show the ability of the superelastic

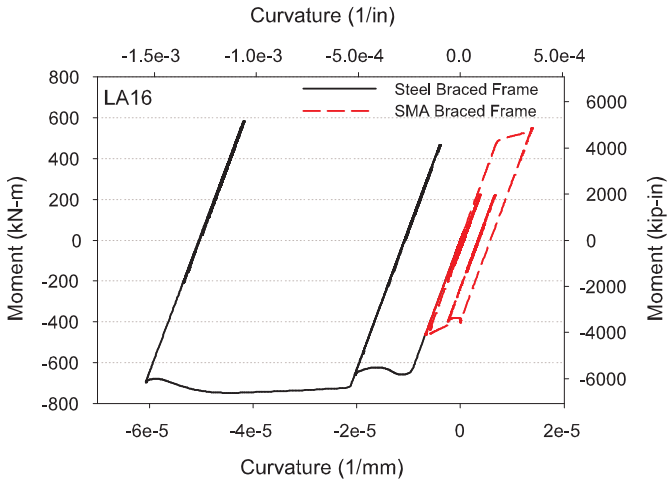

Figure 6-14: Moment-curvature for the top of the bottom, left column of both the conventional steel braced frame and SMA braced frame undergoing the LA16 ground motion.

SMA bracing system to provide recentering, undergo compressive loadings, and stiffen at large strains as compared to the conventional steel braces. Further, a comparison of the hysteretic loops of the two types of braces suggests that the supplemental damping provided by the SMAs is comparable to the post-buckling energy dissipation provided by the steel braces as a result of the reduced load capacity of the steel braces after buckling.

In order to examine the response of the overall structure for the two bracing systems, the story drifts and residual drifts are compared. This approach is similar to approaches used in the past to compare the performance of new systems. Figure 6-16 provides the time history for the top floor displacement of both frames. The peak roof displacements for the conventional steel braced and SMA braced system are approximately 299 mm and 106 mm, respectively, representing roof drifts of 2.5% and 0.89%. The large drifts associated with the steel structure can be attributed to the buckling of the steel braces and the onset of permanent deformation in the columns as has been discussed. The stiffening of the SMA

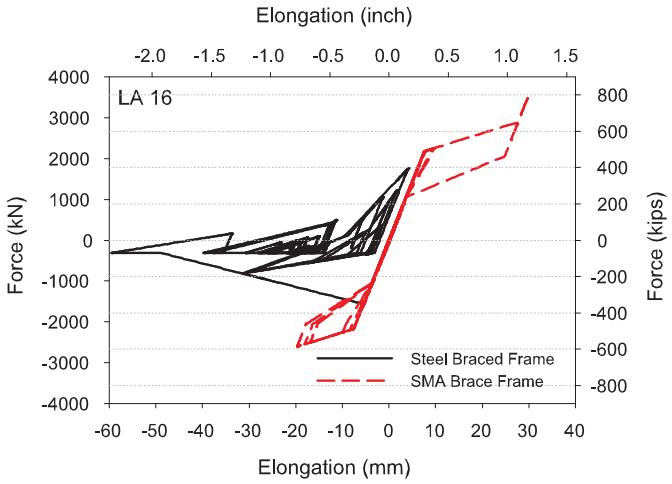

Figure 6-15: Force-displacement relationship exhibited by the left brace implemented into the first floor as a result of the LA16 ground motion.

braces and recentering capability decreases the peak roof displacement by approximately 65%. The roof displacement time history supports the residual curvature results shown in Figure 6-14. The use of conventional steel braces results in a residual roof displacement of approximately 16 mm while the SMA braced system only undergoes 0.10 mm of residual displacement. However, given the large maximum roof displacement associated with the steel braced frame, the actual steel braced system may have undergone collapse as a result of P-Delta effects. As a result, the residual roof displacement would be considerably higher than that reported for the conventional steel braced frame. Conversely, the behavior of the superelastic SMA elements strongly reduce the permanent deformation in other steel members. Even in cases where yielding still occurs, the amount of deformation is reduced by implementing SMA braces.

As suggested by Sabelli et al. (2003), a further measure of the potential for concentrated damage in a given floor can be obtained from the column drift ratio. The column drift

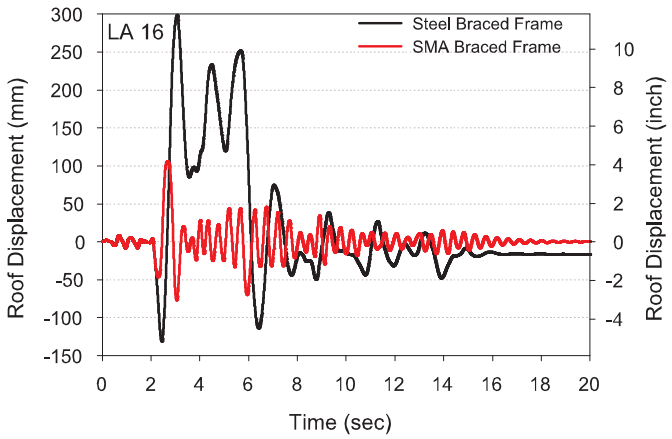

Figure 6-16: Displacement time histories for the top floor of the 3-story conventional steel and SMA braced frames undergoing the LA16 ground motion.

ratio refers to the difference in drift values for adjacent floors where larger values result in higher flexural demands and larger column rotations. The 3-story conventional steel braced structure has a larger column drift ratio of 6.68% as compared to the SMA braced structure which has a column drift ratio of only 0.58% as a result of the LA16 ground motion. The large drift ratio for the steel braced structure suggests a significant amount of rotation at the floor level and the possibility of higher mode responses. The column drift ratio for the SMA braced structure implies that flexural demands on the columns are reduced through the use of this innovative system. In general, this case study has shown that the use of SMA braces does not detrimentally effect the behavior of the other members in the frame in terms of inelastic behavior and demands.

6.3.4.2 Conventional Steel Braces vs. SMA Braces

A more comprehensive study of both the 3-story and 6-story inverted-V braced frames is conducted to verify that the findings of the case study are consistent over the two suites of

ground motions. It is necessary to understand the response of the conventional steel bracing system and the SMA bracing system relative to each other and the effect that the different seismic hazard levels have on the bracing systems performance in order to have confidence in the predicted behavior of these systems in real world structures. Attention is focused both on the maximum inter-story drift and the residual roof displacement, two quantities traditionally considered to judge the seismic performance of structures undergoing dynamic loads (Hamburger et al., 2003). The average maximum inter-story and residual drifts for each floor level are also considered to gain an understanding of which floor levels are placed under the highest demands for the given bracing systems.

The maximum inter-story drift and residual roof displacement provide good measures of the performance of a structure during an earthquake and the resulting damage to both structural and non-structural components. These responses are used to compare the behavior of the subsequent frames studied, as well. It should be kept in mind that the residual drift values for the conventional steel braced frames may be underestimated since collapse of the frame due to P-Delta effects is not considered. Figure 6-17 shows the maximum inter-story drift and residual drifts for the 3- and 6-story frames with either conventional steel braces or the superelastic SMA braces for the 10% and 2% probability of exceedance in 50 years suites of ground motions. In all cases, the maximum inter-story drift is lower for the SMA braced structure compared with the steel braced structure. The average peak inter-story drifts for the steel braced structures based upon the 10% probability of exceedance motions is 3.6% and 1.97% (3- and 6-story structure, respectively) and based upon the 2% probability of exceedance motions is 8.1% and 4.7% (3- and 6-story structure, respectively).

However, the average maximum inter-story drifts for the 3- and 6-story SMA braced structures are considerably less, 0.99% and 0.91% for the 10% probability of exceedance motions and 1.8% and 1.9% for the 2% probability of exceedance motions. On average, use of SMA braces reduced the maximum inter-story drift as compared to use of conventional steel braces by approximately 76% and 56% for the 3- and 6-story frames, respectively, undergoing the 2% probability of exceedance ground motion suite. The results suggest that the ability of the SMA brace hysteresis to pass through the origin during cycling while undergoing large deformations reduces the demand on the beam and column members.

The use of SMA braces also reduces the residual roof displacement in almost all case as shown in Figure 6-17. Focusing on the 2% probability of exceedance motions since these provide the larger demands, on average, the reduction in residual roof displacement as a result of using the SMA braces is approximately 91% for both the 3- and 6-story structures. As a result, it can be assumed that the recentering capability of the SMAs is effective in reducing permanent deformation in the frames. For both the 3- and 6-story structure, it is important to note that the LA32 ground motion results in larger residual roof displacements in the SMA braced system as compared to the steel braced system suggesting that certain ground motion parameters may have an effect on the performance of the SMA bracing system (see Section 4.5). Although the steel braced system does show lower residual roof drifts for a small number of ground motions, the average residual roof drift for the steel braced structures is 1.8% and 0.57% while the SMA braced structures have residual roof drifts of only 0.15% and 0.2% for the 3-story and 6-story frames, respectively, when undergoing the 2% probability of exceedance ground motion suite.

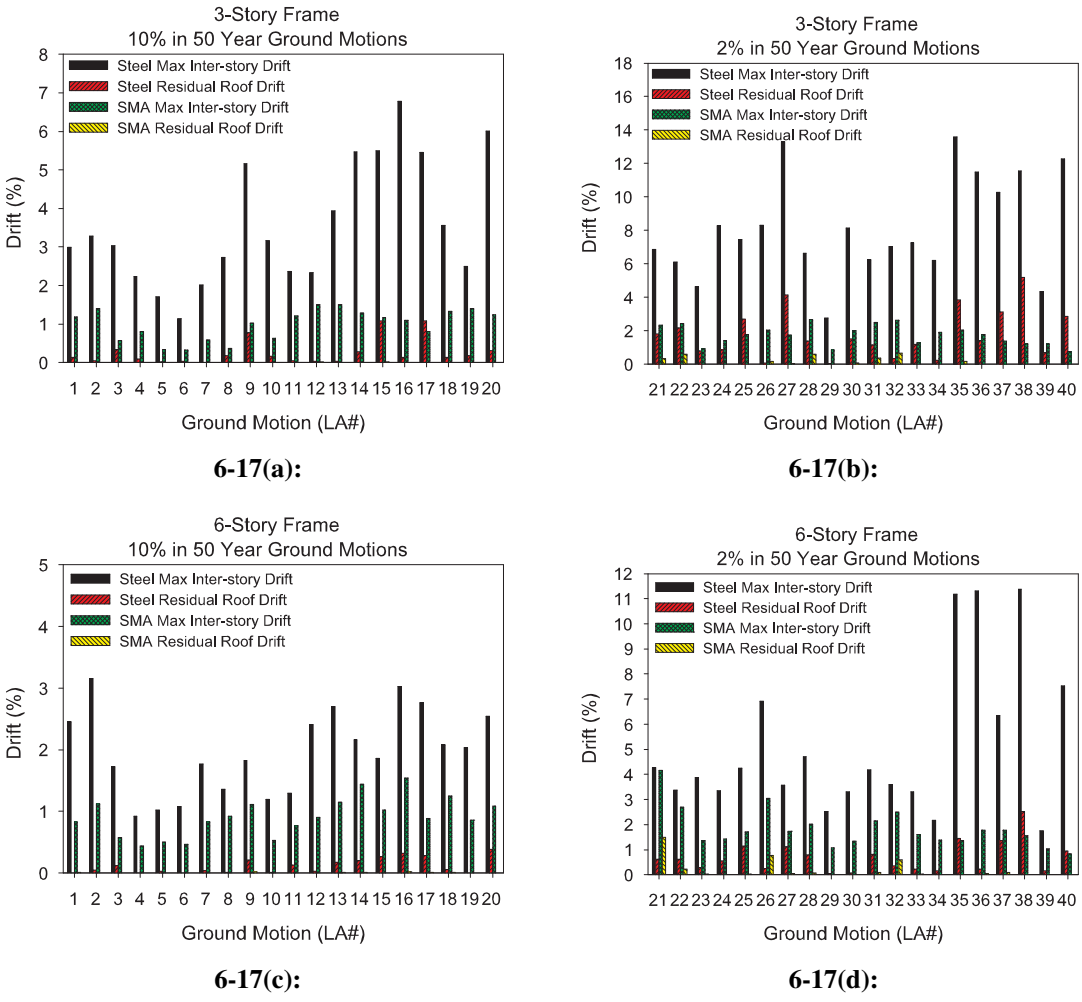

Figure 6-17: Maximum inter-story drift and residual roof drift of the 3-story and 6-story frame as a result of the 10% and 2% probability of exceedance ground motion suites: (a) 3-story 10%, (b) 3-story 2%, (c) 6-story 10%, (d) 6-story 2%.

Table 6-9 provides the mean and standard deviation values of the maximum inter-story drift and residual roof drift for the four structures studied with respect to the seismic hazard level. The results show a consistent behavior of the SMA braces with respect to the seismic hazard and structure height. The mean value and standard deviation of the maximum inter-story drift and residual roof drift increase slightly between the 10% in 50 year and 2% in 50 year ground motions as is expected with the increased seismic hazard. In all instances, the mean maximum inter-story drift and residual roof drift decrease with the use of the SMA braces. Based on the results, conventional steel braces perform better in the 6-story building as compared with the 3-story building with both the maximum inter-story drifts and residual roof drifts being smaller for the 6-story structure. This occurrence can most likely be attributed to the smaller demands placed on each brace due to the inherent flexibility of taller buildings resulting in a smaller percentage of the conventional steel braces undergoing buckling. The difference in the performance of the SMA braces and conventional steel braces also tends to decrease with the increase in building height suggesting that the benefit of using SMA braces in taller buildings may be limited. The decrease in the maximum inter-story drift and residual strain obtained by using SMA braces in the 6-story structure does not appear to be large enough to economically justify SMA braces along the whole height of a tall building.

As a final means of evaluating the two bracing sytems, a comparison of the average maximum and residual inter-story drifts with respect to story level can be seen in Figure 6-18 for the 6-story steel and SMA braced frames undergoing the 2% probability of exceedance in 50 year ground motions. The conventional steel braced frame shows large

Table 6-9: Mean and Standard Deviation (in brackets) of the Maximum Inter-story Drift and Residual Roof Drift for the Conventional Frame Comparison with Respect to Seismic Hazard Level.

	Max Inter-story Drift				Residual Roof Drift			
	2% in 50 years		10% in 50 years		2% in 50 years		10% in 50 years	
	3-story (%)	6-story (%)	3-story (%)	6-story (%)	3-story (%)	6-story (%)	3-story (%)	6-story (%)
SMA	1.75	1.9	0.99	0.91	0.15	0.2	0.004	0.006
	[0.60]	[0.78]	[0.40]	[0.31]	[0.23]	[0.39]	[0.005]	[0.006]
Steel	8.13	4.67	3.57	1.97	1.78	0.57	0.25	0.12
	[3.03]	[2.70]	[1.61]	[0.68]	[1.45]	[0.45]	[0.33]	[0.12]

structural demands placed on the first and sixth story of the structure due to local bending action in the columns as a result of large inter-story drifts. The demand on the SMA braced structure remains almost constant over the frames height. Most of the residual drift for the conventional steel braced frame can be attributed to deformation in the first story while the SMA braced structure shows almost equal permanent displacement at each story level. These findings suggest that the most economical bracing system may be one which takes advantage of the recentering behavior of SMA braces for the first and second floors and uses conventional braces for each subsequent floor. However, the large inter-story drift at the first floor level may also be a function of the larger story height. A combination of conventional steel and SMA braces may be particularly effective for taller buildings given the limited difference in performance between the conventional steel bracing systems for the 6-story structure.

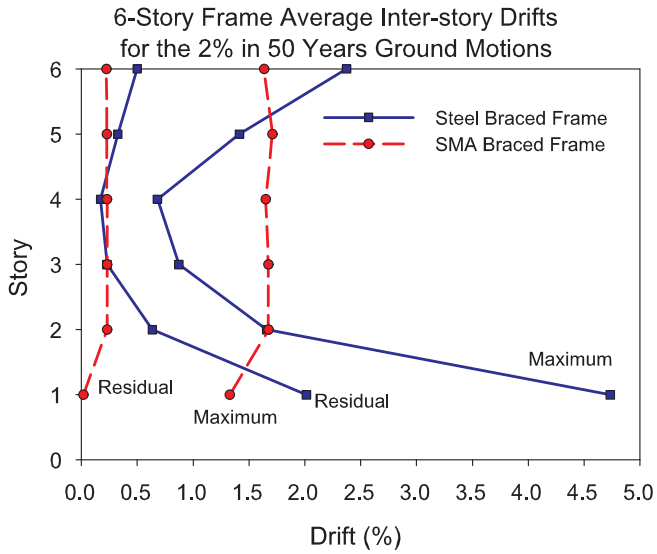

Figure 6-18: Maximum and residual inter-story drifts with respect to each floor level for the 6-story frame undergoing the 2% probability of exceedance ground motions.

6.3.4.3 Buckling-Restrained Steel Braces vs. SMA Braces

The results from the comparison of the conventional steel braced frames versus the tension-compression SMA braces show that the SMA braces work well at reducing both inter-story drifts and residual drifts. However, it is important to determine whether the large decreases obtained using the SMA braces is a direct result of their ability to carry compressive loads or whether the reductions can be attributed mainly to the SMA recentering properties. Given the growth in the development of buckling-restrained steel braces, they provide an opportunity to compare the SMA tension-compression braces to steel braces which can undergo compressive loads. The details of the 3-story and 6-story buckling-restrained frames are given in Section 6.3.1. A full detailed comparison of the two systems is not considered in this section. Only a general comparison of the buckling-restrained steel

braces with the SMA braces is being made as a result of the large difference found between the inter-story drifts for the conventional steel braced frame and subsequent SMA braced frame in the previous section. It should be noted that the buckling-restrained frame results cannot be compared directly to those presented in the previous section as the frame itself has a different design to account for the buckling-restrained steel braces.

The 1986 North Palm Spring (LA20) ground motion is used to evaluate the roof displacement time history and the brace behavior of the 3-story braced frame. Given that the natural period of both the steel buckling-restrained braced frame and the SMA braced frame is 0.51 seconds, the spectral acceleration associated with this motion is 1.4g. This spectral acceleration is slightly higher than the average spectral acceleration from all twenty 10% probability of exceedance in 50 years ground motions. This record is also chosen since the residual drifts and maximum inter-story drifts for the two frames follow a similar pattern to the average for all twenty ground motions in the suite.

Figure 6-19 provides the roof displacement and force-elongation curve for the 3-story frame with both types of bracing systems as a result of the LA20 ground motion. Comparing the roof displacement results, it can be seen that the SMA braced frame actually has a slightly larger maximum roof displacement of 149 mm as compared to 145 mm for the buckling-restrained steel braces. This fact suggests that the added energy dissipation capacity associated with the buckling-restrained steel braces along with the ability to sustain compressive loads provides similar benefits as the stiffening of the SMA specimens at large strains and ability of the encased SMA bars to take compressive loads. However, the residual roof displacement associated with the steel buckling-restrained braced frame is larger than that of the SMA braced frame by 134%. The residual roof displacement of

the SMA braced frame is only 33 mm as compared to 76 mm for the buckling-restrained steel braced frame suggesting that the recentering capability and stiffening at large strains associated with the SMAs has a major influence in reducing the permanent deformation in the structure.

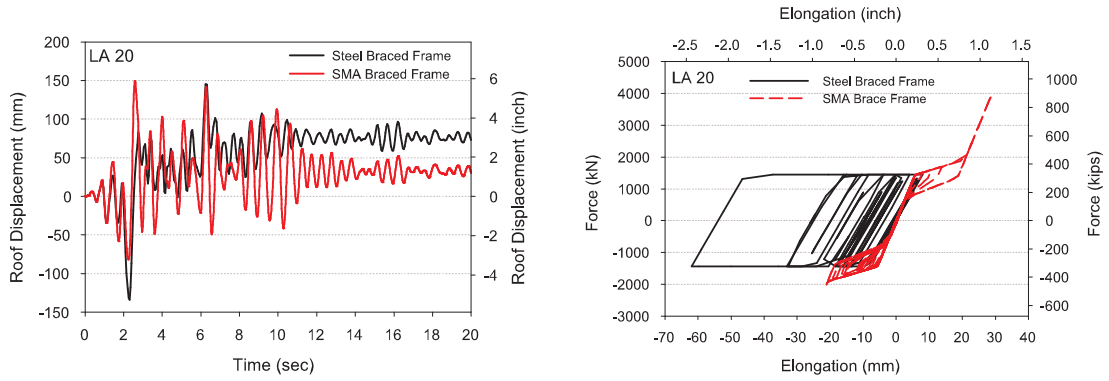

6-19(a): **6-19(b):**

Figure 6-19: (a) Roof displacement time history and (b) force-elongation curve as a result of the LA20 ground motion for the 3-story frame fitted with either buckling-restrained steel braces or SMA braces.

Comparing the force-elongation plots for one of the first floor braces in each of the 3-story frames, the accumulation of permanent elongation in the steel braces due to yielding is apparent. It is also apparent that as a result of this yielding, the buckling-restrained steel braces provide a significantly larger amount of energy dissipation as compared to the SMA braces (particularly at high strain levels). The recentering capability limits the overall elongation of the first floor SMA brace to just under 30 mm while the elongation of the steel braces reaches over 60 mm. Although, the corresponding strain in the SMA brace is approximately 8% (still within the full recovery range) compared to approximately 1%

for the steel braces given that the deformation in the SMA is confined to a much smaller segment. Part of the difference in the elongation of the braces, along with the accumulation of residual strain in the steel brace, is the stiffening of the SMA brace at the higher strain levels.

Table 6-10 provides the mean and standard deviation values of the maximum inter-story drift and residual roof drift for both the 3- and 6-story buckling-restrained frames with respect to the seismic hazard level. The average maximum inter-story drift for all cases is larger for the SMA braced frames as compared to the steel braced frame. The difference in the average maximum inter-story drift increases with an increase in the seismic hazard with the largest difference occurring in the 3-story frames undergoing the 2% probability of exceedance in 50 year ground motion suite. The average inter-story drifts for the 10% probability of exceedance ground motions remains between 1.34% and 1.22% for the four different frame configurations. Comparing the residual drift values, it is clear that the SMA braces reduce permanent deformation in all cases to a greater extent than the buckling-restrained steel braces. The percent reduction in average residual roof displacement between the SMA and steel braces is approximately 77% and 57% for the 3-story frame and 75% and 40% for the 6-story frame with respect to the 10% and 2% probability of exceedance ground motions. The ability of the SMA braces to undergo strain hardening and provide recentering capability significantly reduces the residual drift values even when compared to high damping systems such as buckling-restrained steel braces. The results do suggest that part of the large difference in the response of the conventional steel braced frames can be attributed to the ability of the SMAs to sustain compressive loads,

Table 6-10: Mean and Standard Deviation (in brackets) of the Maximum Inter-story Drift and Residual Roof Drift for the Buckling-restrained Frame Comparison with Respect to Seismic Hazard Level.

	Max Inter-story Drift				Residual Roof Drift			
	2% in 50 years		10% in 50 years		2% in 50 years		10% in 50 years	
	3-story (%)	6-story (%)	3-story (%)	6-story (%)	3-story (%)	6-story (%)	3-story (%)	6-story (%)
SMA	5.17	3.69	1.34	1.29	0.66	0.49	0.11	0.07
	[4.40]	[2.25]	[0.76]	[0.99]	[0.59]	[0.55]	[0.17]	[0.13]
Steel	3.28	2.78	1.26	1.22	1.53	0.81	0.47	0.28
	[1.48]	[1.12]	[0.56]	[0.43]	[1.45]	[0.79]	[0.35]	[0.26]

but the benefits in terms of recentering capability still compare favorably to other tension-compression systems.

6.3.5 Cross-braced Frames

The improvement in the performance of the inverted-V braced frame when superelastic SMA braces are implemented suggests that the use of SMAs in other bracing configurations may be beneficial. In order to determine the plausibility of this, a brief study is completed using the 3- and 6-story cross-braced frames presented in Section 6.3.1. Along with comparing a buckling-allowed steel bracing system in a cross-brace configuration to an SMA bracing system that can withstand both tensile and compressive loads, the 3-story conventional steel braced systems is also compared to a tension-only SMA bracing system to see if the same benefits can be obtained when the SMAs act only in tension. Thus, the need to encase them in grout to prevent buckling is removed. The comparison of all five of the frames analyzed as part of the cross-bracing study is made using the maximum inter-story drift and residual roof displacement in order to gain a general idea of the response of a cross-braced SMA frame in comparison to typical steel cross-braced frames. Throughout

this study, the 1986 North Palm Springs (LA19) ground motions is used as a case study to look at the behavior of the braces and the behavior of the structure during an earthquake. Both the 2% and 10% probability of exceedance in 50 years ground motions are used to account for different seismic hazard levels as is done for the inverted-V braced frame study.

6.3.5.1 Conventional Steel Braces vs. SMA Braces

First, the response of the 3- and 6-story systems using conventional steel braces which are allowed to buckle (Figure 6-12(a)) is compared to a superelastic SMA braced system in which the SMAs can act in both tension and compression as a result of being confined. Figure 6-20 provides the roof displacement time history and the force-displacement behavior for one of the first-floor braces in the 3-story frame as a result of the LA19 ground motion. The roof displacement time history shows that the superelastic SMA braces significantly reduce the maximum roof displacement from approximately 176 mm to 88 mm as compared with the frame using conventional steel braces. These displacements correspond to maximum roof drifts of 1.48% and 0.74%, respectively. The residual roof displacement also decreases when SMA braces are used. There is almost no residual roof displacement associated with the SMA braced frame while the conventional steel braced frame shows a permanent roof displacement of approximately 70 mm which corresponds to a residual roof drift of 0.59%. Although the conventional steel braces do limit the response of the frame, the SMA braces with the same initial stiffness and "yield" force provide a means to further limit displacements in the frame. The results are similar to those found during the inverted-V braced frame study and suggest that SMA braces used in alternative bracing configurations can still provide a positive influence on the behavior of the structure as

a result of their unique properties. However, the fact that failure of the steel braces and collapse of the structure is not considered may lead to even larger differences.

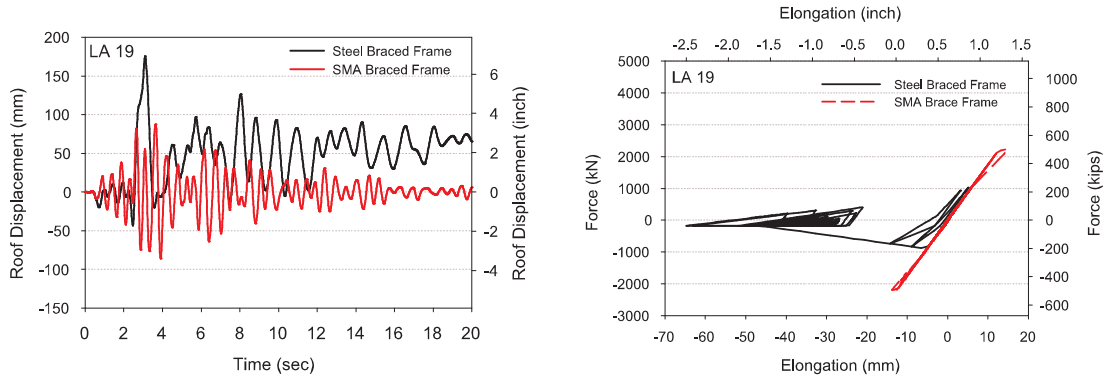

6-20(a): **6-20(b):**

Figure 6-20: (a) Roof displacement time history and (b) force-elongation curve as a result of the LA19 ground motion for the 3-story cross-braced frame fitted with either conventional steel braces or SMA braces.

The force-displacement curves shown in Figure 6-20(b) suggest that the recentering capability and ability of the SMAs to provide resistance in both tension and compression limits the response of the frame. For the case of the LA19 ground motion, this particular SMA brace only undergos limited deformation with the phase transformation never being completed and no onset of stiffening as a result of the formation of stress-induced martensite. The maximum strain sustained by the SMA braces is only approximately 2%. On the other hand, the conventional steel brace undergoes a significant amount of deformation in compression, approximately 65 mm with buckling occurring early on during the ground motion. As a result of this buckling behavior, permanent deformation occurs limiting the effectiveness of the conventional steel brace to control the response of the structure. Since

the conventional steel brace buckles and does not undergo a large number of tension cycles, the difference in the energy dissipated by the steel brace as compared to the SMA brace is not as large as was seen when comparing the SMA braces to buckling restrained steel braces. Thus, the force-displacement plot further suggests that the ability of the superelastic SMAs to always pass through the origin while also acting in both tension and compression is the main reason for the better performance of the frame. Based on the performance of the frame under the LA19 ground motion, it appears that SMA braces work well at reducing the roof displacement in a cross-bracing configuration.

In order to verify that the findings for the 3-story frame undergoing the LA19 ground motion are true for other ground motions and building heights, Figure 6-21 provides the maximum inter-story drift and residual roof drift for the 6-story frame undergoing the suite of 10% probability of exceedance in 50 years ground motions. The results for the LA01 ground motion are not shown due to convergence problems during the nonlinear time history analysis. For all ground motions except LA07, the maximum inter-story drift is reduced through the use of the SMA braces. However, the difference in inter-story drifts for this case are minimal, but further suggest possible effects associated with ground motion parameters. Further, the residual roof drifts are minimal for the SMA braced frame and are on average 0.16% for the steel braced frame. These may be higher if collapse of the frame is modeled. The results suggest that even in taller cross-braced buildings, the benefits of using an SMA bracing system as compared to a conventional steel bracing system are measurable.

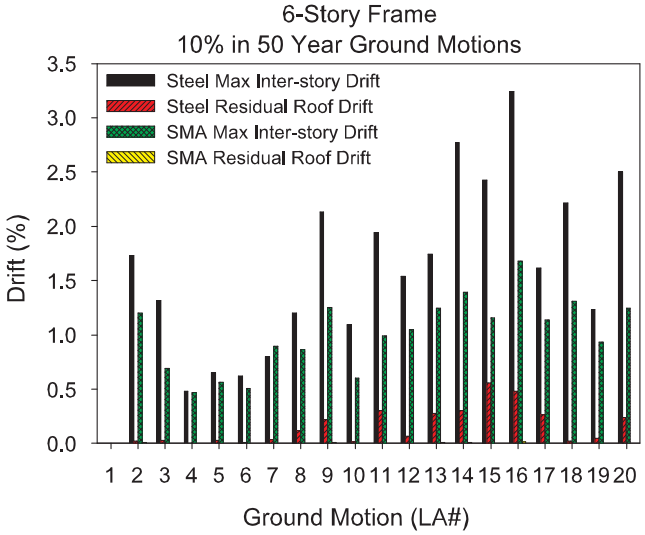

6-21(a):

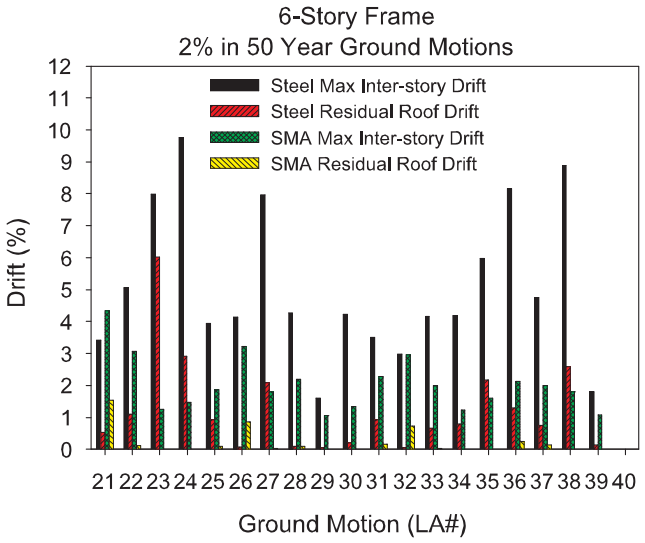

6-21(b):

Figure 6-21: Maximum inter-story drift and residual roof drift for the 6-story cross-braced structure with either conventional steel braces or SMA braces with respect to seismic hazard: (a) 10% probability of exceedance in 50 years and (b) 2% probability of exceedance in 50 years.

Table 6-11 provides the mean and standard deviation of the maximum inter-story drift and residual roof displacement for all brace-types and frame height combinations with respect to the seismic hazard level. In general, the decrease in the maximum inter-story drift and residual roof drift when using the superelastic SMA braces is the largest for the 3-story frame at both seismic hazard levels. For the 10% probability of exceedance suite of ground motions, the mean maximum inter-story drift decreases from 3.29% to 1.19% for the 3-story frame and from 1.64% to 1.01% for the 6-story frame. For both frame heights, the 10% probability of exceedance ground motions cause little to no permanent deformation in the SMA braced frame. The mean maximum inter-story drift and residual roof drifts increase with an increase in the seismic hazard level as is expected. However, the increase appears to have no trend associated with the building configuration or the type of bracing system. One result of the 2% probability of exceedance ground motions is higher standard deviation values suggesting that there is more variability in the response of structures with respect to the ground motion when the ground motions are more intense. In general, the results show a similar behavior to the inverted-V braced frame in which SMA braces consistently reduced both maximum inter-story drifts and residual roof displacements as compared to conventional steel braces. As a result, SMA braces may provide a means of minimizing losses associated with damage to the structural system during an earthquake irregardless of the brace configuration .

6.3.5.2 Effect of Using Tension-only SMA Braces

As a final segment of the study using cross-braced steel frames, tension-only SMA braces are considered for the 3-story frame to see if the benefits shown in the previous studies

Table 6-11: Mean and Standard Deviation (in brackets) of the Maximum Inter-story Drift and Residual Roof Drift for the Conventional Cross-braced Frame Comparison with Respect to Seismic Hazard Level.

	Max Inter-story Drift				Residual Roof Drift			
	2% in 50 years		10% in 50 years		2% in 50 years		10% in 50 years	
	3-story (%)	6-story (%)	3-story (%)	6-story (%)	3-story (%)	6-story (%)	3-story (%)	6-story (%)
SMA	1.66	1.99	1.19	1.01	0.12	0.20	0.02	0.00
	[1.83]	[0.85]	[0.51]	[0.33]	[0.32]	[0.39]	[0.04]	[0.01]
Steel	7.01	4.84	3.29	1.64	1.37	1.17	0.32	0.16
	[2.59]	[2.57]	[1.04]	[0.77]	[1.26]	[1.44]	[0.27]	[0.17]

stem from the ability of the SMA to sustain compressive loadings or from the properties of the superelastic SMA. There is no difference between the cross-braced frames used in this segment of the study and the previously discussed cross-braced frames besides the fact that the SMA is modeled as tension-only. Since the behavior of the conventional steel brace (buckling-allowed) lies somewhere between a buckling-restrained brace and a tension-only brace, it is important to see how the frames response with a tension-only SMA brace compares to a frame using conventional steel braces.

Figure 6-22(a) provides the displacement time history for the top floor of the 3-story frame as a result of the LA19 ground motion when tension-only SMA braces are implemented. The plot also provides the conventional steel braced frame results from the previous section. The displacement time history shows a reduction in the maximum roof displacement of 20.5% when the tension-only SMA braces are used as compared to the conventional steel braces. This reduction is less than that found when tension-compression SMA braces are used, but shows the ability of the SMA behavior to control the response

of the frame. The residual roof displacements are also reduced through the use of tension-only braces. The conventional steel braced frame has residual roof displacements of 70.5 mm while the residual roof displacement of the tension-only SMA braced frame is 20.8 mm representing a 70.5% reduction in the residual roof displacement. The results suggest that the properties of the superelastic SMAs have a significant effect on the response of the frame, although the ability to carry compression loads does lead to further reductions in the maximum roof displacements and residual roof displacements.

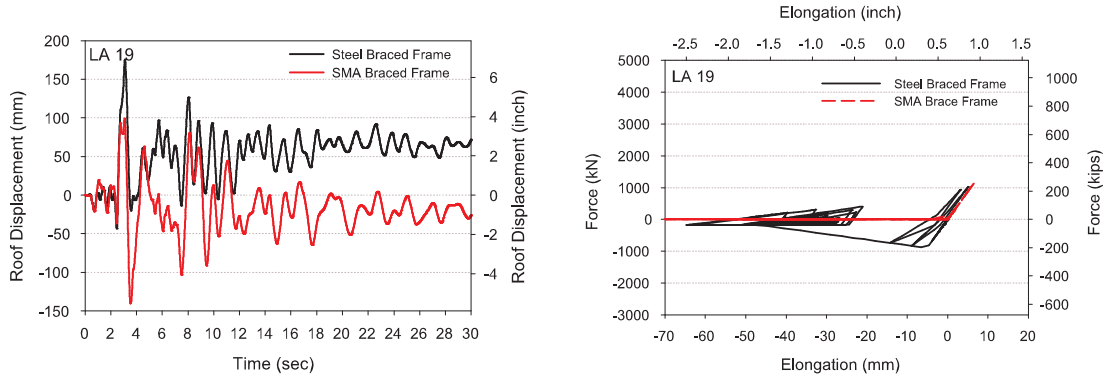

6-22(a): **6-22(b):**

Figure 6-22: (a) Roof displacement time history and (b) force-elongation curve as a result of the LA19 ground motion for the 3-story cross-braced frame fitted with either conventional steel braces or SMA tension-only braces.

The force-displacement curves shown in Figure 6-22(b) represent the behavior of one of the first floor braces of the 3-story frame as a result of the LA19 ground motion. The force-displacement plot for the tension-only SMA braces shows that brace remains in its initial elastic range and never undergoes an initiation of the phase transformation. This further suggest that the other first story SMA tension-only brace takes a significant amount

of the load attributed to deformation at the first floor, but provides little detail in terms of the comparison between the tension-only SMA bracing system and the conventional steel bracing system beyond the fact that the maximum force reached in both bracing systems is similar.

Figure 6-23 provides the maximum inter-story drifts and residual roof displacements for the tension-only SMA braced frame and the conventional steel braced frame for both suites of ground motions. For almost all cases, the maximum inter-story drift is reduced with the use of the SMA tension-only braces as compared to the conventional steel braces. This finding suggests that even in their tension-only form, the use of SMA braces reduces the demand on other structural members as a direct result of their ability to not accumulate permanent deformation and to undergo apparent stiffening as a result of the formation of stress-induced martensite. One of the pitfalls of using tension-only SMA braces appears to be the partial loss of the recentering capability since only one brace at a given instance is ever engaged. This lack of recentering needs to be addressed before tension-only SMA braces can be implemented into actual structures. However, it should be noted that the SMA braces are designed so as to provide the same initial stiffness and yield force as the conventional steel braces which do provide some resistance in compression. Thus, the results suggest that specific design procedures need to be developed for tension-only SMA braces. Further statistics with respect to the mean and standard deviation values for the average maximum inter-story drift and residual roof drift of the 3-story tension-only SMA braced frame are given in Table 6-12 with respect to the seismic hazard level.

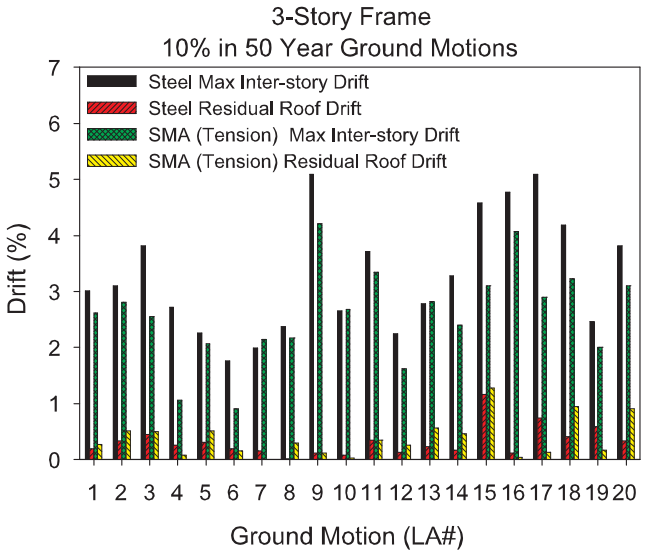

6-23(a):

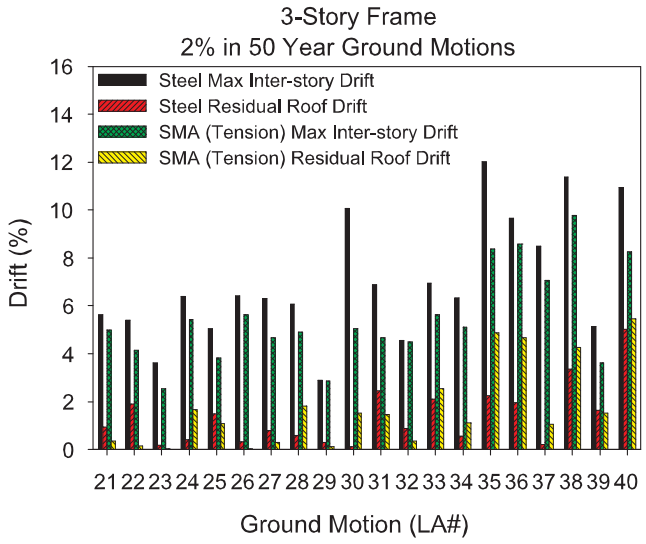

6-23(b):

Figure 6-23: Maximum inter-story drift and residual roof drift for the 3-story cross-braced structure with either conventional steel braces or SMA tension-only braces with respect to seismic hazard: (a) 10% probability of exceedance in 50 years and (b) 2% probability of exceedance in 50 years.

Table 6-12: Mean and Standard Deviation (in brackets) of the Maximum Inter-story Drift and Residual Roof Drift for the 3-story Tension-only SMA Braced Frame Comparison with Respect to Seismic Hazard Level.

	Max Inter-story Drift		Residual Roof Drift	
	2% in 50 years (%)	10% in 50 years (%)	2% in 50 years (%)	10% in 50 years (%)
SMA	5.48	2.59	1.73	0.38
	[1.97]	[0.85]	[1.74]	[0.34]
Steel	7.01	3.29	1.37	0.32
	[2.59]	[1.04]	[1.26]	[0.27]

6.4 Closure

This chapter focuses on applications of superelastic SMAs for controlling the response of building systems undergoing seismic events. Initially, two experimental phenomenological models are developed to predict the behavior of the superelastic SMAs. A simplified model which maintains constant forward transformation and reverse transformation stress plateaus and a trigger-line model which accounts for sub-cycling through an instability (trigger) line are studied with parameters based on the previous materials tests presented. A SDOF study using the two models shows that both models can capture the superelastic SMA behavior, although the force-deformation curve for the trigger-line model more accurately mimics the experimental results in terms of sub-looping and low strain level cycles. However, neither of these models accurately accounts for the degradation of the superelastic SMA properties with continued cycling as a result of fatigue effects.

A similar uniaxial constitutive model which has been implemented into OpenSEES is then used to evaluate the behavior of concentrically braced steel frames using conventional steel braces, buckling-restrained steel braces, SMA tension-compression braces, and SMA

tension-only braces. Both inverted-V braced frames and cross-braced frames of 3- and 6-stories are used. The results show a significant decrease in the inelastic demand placed on the structural members when SMA braces are used as compared to conventional steel braces and a decrease in the maximum inter-story drift and residual drift for both configurations of bracing systems. The comparison between the buckling-restrained steel braces and the SMA tension-compression braces shows that both systems result in similar maximum inter-story drift values, but the SMA braces limit residual deformations. However, the limiting of residual deformations can be compromised if tension-only SMA braces are used. In general, the results show promise for the use of SMA braces as they compare favorably to the conventional steel braces for all cases and provide considerable reduction in the permanent deformation sustained by the frame when used either in an inverted-V configuration or cross-bracing configuration. However, further analytical work needs to be completed in order to study alternative configurations, ways of optimizing the use of SMAs in the frame structures, and more accurate models of both the steel and SMA braces.

CHAPTER VII

SUMMARY, CONCLUSIONS, AND RECOMMENDATIONS

7.1 Summary and Conclusions

Shape memory alloys are unique metallic materials which have applications in the biomedical, aerospace, and commercial industries because of their ability to undergo large deformations while reverting back to their original undeformed shape through either the applications of heat (shape memory effect) or the removal of the load (superelastic effect). The repeatable recentering capability, formation of loading and unloading plateaus, hysteretic damping, stiffening at large strains, and excellent low- and high-cycle fatigue properties which are taken advantage of in these past and current applications are also advantageous for earthquake engineering applications. In particular, these properties fit the needs of performance-based design criteria currently used in the seismic design of building and bridge systems. However, there is a lack of past knowledge in regards to the material properties of large diameter NiTi SMA sections and a disconnect between the material science and structural engineering communities which has limited the development of NiTi SMA based systems for seismic applications. The main objective of this study has been to characterize the behavior of large diameter superelastic NiTi SMAs and determine means of optimizing their properties for seismic applications. The approach taken

is multi-disciplinary and multi-scale in nature providing a connection between the nano-scale properties up through the macroscopic mechanical behavior of large diameter NiTi specimens. These results are then further used to analytically evaluate a superelastic SMA bracing system for use in steel braced frame systems.

7.1.1 Large Diameter NiTi Bars

The first task undertaken was to gain an understanding of the material properties and mechanical behavior of large diameter NiTi SMAs so that the properties can be optimized for future seismic applications. This task is accomplished through an extensive multi-disciplinary, multi-scale experimental study developed to provide a link between current material science approaches and the needs of structural engineers. A basic material characterization study including the evaluation of nanometer-size precipitates through transmission electron microscopy (TEM), grain size and texture measurements through electron backscatter diffraction (EBSD), transformation temperatures through differential scanning calorimetry (DSC), and strength through hardness measurements has been conducted. The results show that hot-rolled Ni-rich NiTi SMAs can provide good superelastic properties through precipitation hardening and aging. These results are then used to help characterize the mechanical behavior of both coupon and large diameter bar specimens under cyclic loadings.

Coupon specimens are typical of past studies conducted in the material science field and provide much of the information in regards to the properties of NiTi SMAs. However, the heterogeneous nature of the NiTi bars shown in the material characterization suggests

that the mechanical behavior of the coupon specimens may not provide an accurate measure of the properties of full-scale large diameter NiTi bars. This possible scaling effect, the difference in behavior between specimens tested full-size and reduced coupon specimens taken from the full-scale bars, is explored through cyclic uniaxial tensile testing of both coupon specimens taken from various locations across the diameter of the full-scale NiTi bars and the full-scale bars themselves. Throughout the mechanical behavior study, the materials characterization results are used to explain the macroscopic properties. The results show a definitive scaling effect in terms of different properties being obtained from the coupon specimens as compared to the full-scale specimens. This result suggests that full-scale specimen properties cannot be predicted from coupon specimen test results.

Since the intention is to use the large diameter specimens for earthquake engineering applications, the full-scale specimens are also cycled through a far-field earthquake-type loading at various strain rates. The observed results suggest that NiTi SMAs maintain their typical superelastic behavior even when cycled through uneven strain cycles. Dynamic loading rate effects are observed as a result of a self-heating of the specimen with the most significant effect being a decrease in the hysteretic area. In general, the earthquake loading tests suggest that large diameter NiTi SMA cyclic properties are suitable for seismic applications. The compilation of this task provides a previously non-existent connection between the nano-scale structure up through the full-scale mechanical properties allowing for past material studies to be linked with the current needs of structural engineers.

Conclusion based on the large diameter bar study are summarized below:

- As-received large diameter hot rolled NiTi bars are relatively precipitate free given a final thermal exposure near 600 °C, but with heat treatment at temperatures below 400 °C for 0.5 to 1.5 hours, nanometer-scale metastable phase precipitates can be formed which promote shape recovery.

- Hot-rolled bars have a significant <111> texture along the rolling axis. However, this depends on the amount of deformation processing and location across the bar diameter. An increase in deformation processing and locations closer to the center of the bar bring out a <101> type texture suggesting heterogeneity in large diameter hot rolled NiTi bars

- The hardness of superelastic NiTi bars can be modified through heat treatment temperature and time with the hardest bars resulting from heat treatments in the vicinity of 300 °C to 325 °C for 1.5 hours.

- Coupon specimens taken from full-scale large diameter bars only provide limited information in terms of the true full-scale cyclic properties when compared to the full-scale specimen test results. This scaling effect can be attributed to a relatively small volume of material being sampled in the highly heterogeneous full-scale specimen when these small coupon specimens are used.

- The forward transformation stress is independent of bar size. This lack of a bar size effect confirms that precipitates have a larger influence on the stress to induce the phase transformation in hot-rolled NiTi as compared to grain size.

- Both the recentering capability and equivalent viscous damping values increase with a decrease in bar size suggesting an influence from deformation processing. Residual strains tend to remain in the range needed for the development of recentering devices for seismic applications, but damping values tend to remain too low to suggest the use of superelastic NiTi SMAs in purely damping applications.

- Typical earthquake loadings result in no significant change in the cyclic properties. However, dynamic loading rates cause a decrease in the hysteretic area and a general shift upward of the hysteresis due to a self-heating of the specimen

- Full-scale large diameter hot rolled NiTi specimens show good superelastic properties providing a more cost effective alternative to cold drawn bars previously deemed necessary to obtain good superelastic behavior.

7.1.2 Optimization of NiTi Wires for Seismic Applications

Since NiTi SMAs have been shown to maintain suitable properties for seismic applications, the second task sought to optimize these properties. A variety of experimental studies were performed using NiTi wires in order to complete this task. Previous cyclic tests showed a significant degradation of the superelastic properties of the SMAs. It has been suggested that prior mechanical training can be used to stabilize these properties, but no research, to date, presents an optimal training protocol in terms of number of training cycles and strain level of training. A basic full-factorial study and response surface study have been conducted to address this lack of knowledge with the results showing more stable superelastic behavior after mechanical training to any strain level. The full-factorial study shows the significance of both the number of training cycles and strain level of training, but also

suggests that the loading rate to which the SMAs are cycled after training has a significant influence on their properties as well. The response surface study provides regression equations to determine the expected forward transformation stress, equivalent viscous damping, and residual strain values given a specimen trained for a specific number of cycles to a specific strain level. An optimal training scheme in terms of stabilizing these properties is also determined.

The second part of this task consists of experimentally testing pre-strained NiTi wires. It has been suggested that pre-straining can provide better energy dissipation during cycling due to the onset of sub-cycling for low level strain cycles. However, the effect of different strain cycles had yet to be systematically characterized. In order to address this, experimental tests have been performed on NiTi wires pre-strained to various strain levels with the loading protocols either consisting of constant strain cycles or increasing strain cycles. By pre-straining the NiTi wires, sub-cycling or sub-looping occurs even for small strain cycles resulting in an increase in the hysteretic energy dissipation and further suggesting that the energy dissipation capacity can be modified through pre-straining.

The last part of this task evaluated the performance of NiTi wire specimens under both far-field and near-field loading protocols in order to determine the effect of early large strain cycles. Past studies of SMAs have mainly focused on gradually increasing strain cycles and given the possibility of a near-field event, it is important to ensure that NiTi SMAs maintain good superelastic behavior for cases where there is a large early strain cycle. The effect of dynamic loadings is also studied with respect to the earthquake loading type. The far-field motion results in similar behavior to untrained wires, while the early large strain cycle associated with the near-field motion causes a significant increase in the residual strain

value. The forward transformation stress also drops significantly with continued cycling. In general, the near-field protocol causes large initial changes in the cyclic properties, but the NiTi SMA still maintains the benefits associated with superelastic behavior.

The key conclusions from the optimization study of NiTi wire are summarized below:

- The number of training cycles and strain level of the cycles used for the mechanical training of NiTi can be used to control the forward transformation stress, residual strain, and equivalent viscous damping values providing a further means of obtaining desired properties for use in seismic applications.

- The full-factorial results and response surface results suggest that mechanical training of NiTi specimens for greater than 40 cycles to strain levels of 6-7% can drastically reduce fatigue effects and provide more stable properties.

- Pre-straining provides a means of obtaining sub-cycling even for small strain level loadings as well as maintaining tension in the specimen for a much wider strain range.

- Damping capacity of NiTi SMAs can be maximized by pre-straining to between 2.5% and 3.5% (along the midpoint of the loading plateau).

- Near-field loadings cause a much larger decrease in the forward transformation stress between the first and last cycle and result in much larger residual strain values with respect to those incurred as a result of a far-field type loading. However, the near-field specimens still maintained good superelastic properties suggesting that NiTi can be used in areas susceptible to near-field type motions.

7.1.3 Variability in Shape Memory Alloy Cyclic Properties

A third task undertaken is the evaluation of the variability of SMA cyclic properties by fitting specific properties to probability distributions. These probability distribution allow for the variability of these properties to be accounted for in future studies of SMA systems in structures. This is particularly important given the current performance-based and consequence-based frame work used in seismic design and provides a means of performing fragility assessments of systems using SMAs and compare the benefits of such a system to other systems in a more rapid manner. The probability distributions are fit through a two phase study. The first phase of the study involves preliminarily determining the number of samples needed to provide accurate results. This value is estimated to be approximately 25, but is increased to 30 to provide more accuracy. NiTi wires are chosen for this study since they are readily available at a cost significantly below that of large diameter bars. The thirty wires are then run through a tensile cyclic loading with the properties as a result of the first 6% strain cycle being evaluated. The properties chosen include the initial elastic modulus, forward transformation stress, slope of the loading plateau, martensite stress, reverse transformation stress, and residual strain. Each of these properties is particularly important in modeling the behavior of SMAs with phenomenological models providing justification for their selection. The second phase then consists of fitting these properties to normal distributions, lognormal distributions, and Weibull distributions using the method of moments based on the sample statistics. The Kolmogorov-Smirnov test is then used to evaluate which distribution provides the best fit. As a result, a previously non-existent understanding of the variability of NiTi wire properties is gained.

The key outcomes from this statistics study on NiTi wire properties are summarized below:

- The sample statistics from the 30 NiTi wires specimens tested show low standard deviation values for most properties. The martensite stress and reverse transformation stress provide the largest amount of variability.

- For all of the properties except the initial elastic modulus, the lognormal distribution provides the best fit. Alternatively, the distribution which provides the best fit for the initial elastic modulus is the normal distribution. These results are typical of those found for past material property studies of steel and concrete.

- A 20% significance level is obtained for the chosen distributions fit for each property suggesting good accuracy of the results and providing confidence in the parameters obtained for the distributions.

7.1.4 Seismic Applications of Shape Memory Alloys

The final task of this study on SMAs focuses on the evaluation of SMA bracing systems implemented in concentrically braced steel frames. Before this could be undertaken, models representing SMA cyclic behavior needed to be developed. A significant amount of attention has been given to the modeling of SMA behavior in the past, but few of these models have focused on the requirements needed for structural applications in terms of limited variables and minimal processing time. Two phenomenological models (simplified and trigger-line) with different approaches to account for sub-cycling have been developed to address these concerns. The behavior of these models is then compared through a simple

SDOF study which shows both types of models capturing approximately the same maximum displacements. However, the trigger-line model more accurately predicts the expected stress-strain behavior.

Given the ability to model SMA cyclic behavior, four concentrically braced steel frames are then used to analytically evaluate superelastic SMA bracing systems. The frames consist of both chevron (inverted-V) braces and cross-braces. Past studies have suggested that SMAs can be used to control the response of structures, but very few of these studies have compared an SMA bracing system to currently used bracing systems. In order to provide this comparison, this analytical study compares conventional buckling-allowed steel bracing systems and buckling-restrained steel bracing systems to both tension-compression superelastic SMA braces and tension-only superelastic SMA braces by designing the SMA braces such that they provide the same stiffness and yield force as the steel bracing system to which they are being compared. The results show, in general, that the SMA braces provide a significant reduction in the response of the frame when compared to conventional steel braces. The recentering capability of the SMA braces reduces the permanent deformation sustained by the frame when compared to buckling-restrained steel braces. The SMA bracing system shows potential for use under performance-based design guidelines given the limited maximum inter-story drifts and residual drifts obtained in frames implementing them.

The following conclusion result from the analytical study of SMA applications for earthquake engineering:

- Shape memory alloy constitutive models implementing a trigger-line to account for sub-cycling more accurately predict the tensile behavior seen experimentally. However, both the simplified model and trigger-line models capture similar maximum displacements when implemented in a SDOF system undergoing a suite of ground motions.

- Little difference is obtained when comparing the behavior of a superelastic SMA bracing system in an inverted-V configuration to a cross-brace configuration suggesting that SMAs can be used in a wide variety of bracing configurations.

- The use of the SMA bracing system reduces column drift ratios as compared to those obtained when using a conventional steel bracing system providing a decrease in the flexural demand on the column members.

- As compared to conventional steel braces, use of tension-compression SMA braces results in significantly smaller maximum inter-story drift values and residual roof drift values for both seismic hazard levels. However, when compared to buckling-restrained steel braces, only the residual roof drift is decreased with the use of the SMA braces.

- The tension-only SMA braces reduce both the average maximum inter-story drift and residual roof drift as compared to conventional steel braces for the 10% probability of exceedance ground motions, but not necessarily when considering higher seismic hazard levels.

- The study of the mean inter-story drifts of the 6-story inverted-V braced frame shows that a large percentage of the overall residual drift in the conventional steel braced frame occurs in the first and second stories. The result for the upper stories are equivalent to those experienced by the tension-compression SMA braced frame suggesting that SMA braces may be most beneficial in the lower levels of tall buildings, while conventional steel braces can still be used in the upper stories.

7.2 Impact

A multi-scale process consisting of both experimental and analytical techniques has been incorporated to evaluate the use of SMAs for seismic applications. The significant contributions resulting from this include the following:

- The most significant contribution of this study is the development of a previously non-existent link between material science research on NiTi shape memory alloys and the needs of structural engineers. This connection will allow for easier implementation of SMAs into structural systems by providing a connection between nano-scale properties up through the macroscopic behavior. With this information, heat treatment and processing techniques leading to precipitation hardening can be used to tailor the properties of NiTi SMAs for specific structural engineering needs.

- The results showed that less expensive large diameter hot-rolled NiTi bars can provide good superelastic properties and provide a more economical option to cold

drawn specimens. This is particularly significant given the budget for most structural engineering projects and the fact that others have suggested that large diameter specimens cannot provide typical superelastic behavior.

- An understanding of how the properties of NiTi SMAs can be optimized through both mechanical training and pre-straining is gained in order to provide both stable properties and higher energy dissipation capacities.

- Previously unknown distributions accounting for the variability of specific NiTi properties have been obtained which can aid in more accurately modeling NiTi behavior. This will also allow for more rapid implementation of NiTi systems in the future.

- Proof of concept studies illustrate that SMA bracing systems can be used to reduce the response of concentrically braced steel frames when compared to currently used systems. The decrease in both permanent deformation and the demands on other structural members when SMA braces are used suggests a means of limiting both economic losses and the possible loss of life during an earthquake. These results provide several areas for future research.

- The multi-scale, multi-disciplinary approach taken for this study can provide a road map for future studies of new and innovative materials for structural engineering applications. Such an approach would limit the disconnect between material scientist and structural engineers and thus promote the use of new materials in a more rapid manner.

7.3 Future Recommendations

Areas in which this work can be extended through additional research are cited below:

- Since only tension material testing was conducted, there still exists a need to study the compressive, torsional, and bending properties of large diameter NiTi shape memory alloys. These properties may prove to be advantageous for future applications in structural systems.

- Given the vast amount of material data collected, specific guidelines for controlling the properties of NiTi SMAs should be developed with specific attention placed on those properties important for civil and structural engineering applications. In the process of compiling these guidelines, further testing in regards to ambient temperature effects and composition effects should be conducted.

- Training and pre-straining studies need to be conducted on large diameter specimens to determine if the large bar behavior can truly be extrapolated from the tests conducted on the NiTi wire. Given the results of the wire testing, this future study can be conducted in a concise and economical manner.

- More realistic materials models need to be developed which account for the degradation of many of the SMA cyclic properties with continued cycling as a result of fatigue effects. These models need to be developed within the confines of the needs and understanding of structural engineers. Along these same lines, more accurate models accounting for pre-straining effects and tension-compression asymmetry are needed as well.

- The results from the analytical study suggest that it may be more economical and advantageous to only use SMA braces in specific areas of a structure. Analytical studies should be run in order to try to optimize the use of SMAs in terms of both amount and placement through out the structure with respect to both cost and control of the response of the structure.

- Although the analytical results suggest that SMA bracing systems using large diameter bars reduce inter-story drifts and residual drifts, the results need to be explored experimentally to determine the accuracy of these findings through both component testing of the bracing system and full-scale testing of frame systems implementing SMA braces.

- In the wake of recent man-made and natural disasters, the use of SMAs in other areas beyond seismic applications should be considered. The unique properties of NiTi SMAs may prove useful in the areas of hurricane mitigation, impact load mitigation, and blast load mitigation.

- Finally, only SMA bracing systems are considered in this dissertation, but there are many other structural applications where SMAs can be applied. These area include partially-restrained connections, ductile cladding connections, post-tensioning applications, and innovative column base plate connections. The use of large diameter bars needs to be further studied in these areas.

APPENDIX A

LARGE DIAMETER NITI TENSILE TEST RESULTS

In order to ensure the accuracy of the material properties of the large diameter NiTi bars used for the material and mechanical characterization study in Chapter 3, replicates of the cyclic and earthquake loading tensile tests of the large diameter bars are conducted whenever possible. Only a single replicate for a given tests is performed. Due to a minimal number of 31.8 mm specimens, no replicates are performed for bars of this size. All of the tensile stress-strain curves are presented in this appendix.

A.1 Full-scale Cyclic Tensile Tests

Figures A-1 and A-2 provide the stress-strain curves from the cyclic tensile tests of the 19.1 mm diameter and 12.7 mm diameter NiTi bars, respectively.

A.2 Earthquake Loading Tensile Tests

Figure A-3 through Figure A-5 provide the stress-strain curves for the 19.1 mm diameter specimens tested under the far-field type earthquake loading protocol at various loading rates. The stress-strain curves for the 12.7 mm diameter specimens tested under the same loading protocols are presented in Figure A-6 through Figure A-8. It should be noted that a 7% strain cycle is added to the end of the loading protocol of the 2nd specimen tested quasi-statically for each of the bar sizes.

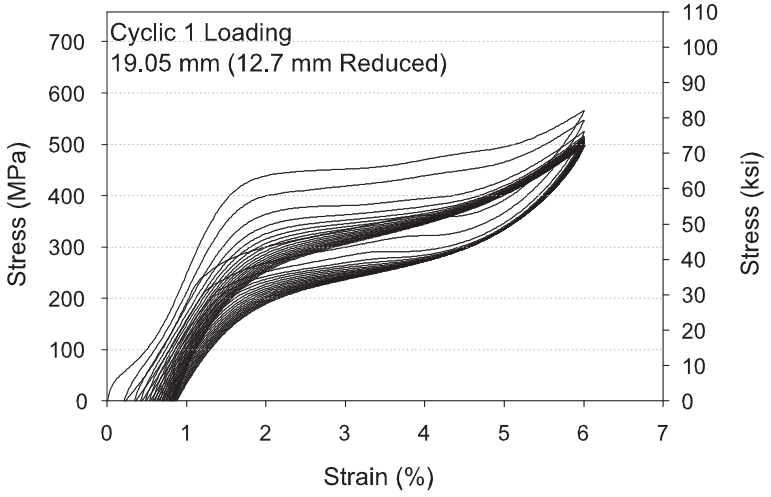

A-1(a):

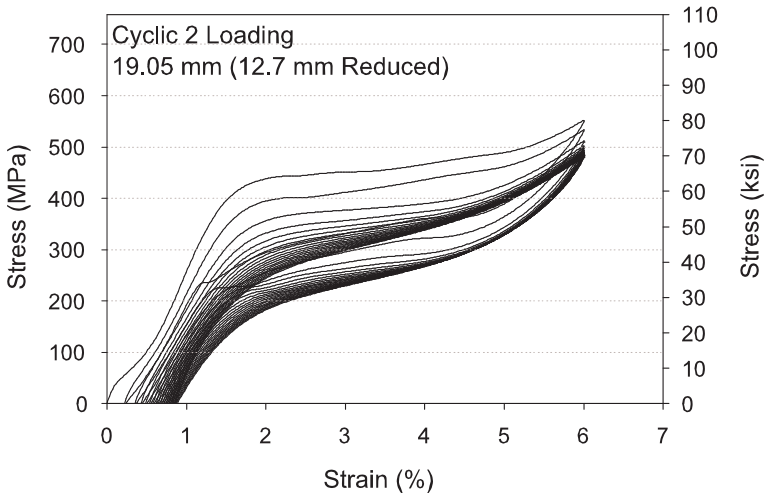

A-1(b):

Figure A-1: Cyclic tensile stress-strain plots for the 19.1 mm full-scale specimen: (a) test 1 and (b) test 2.

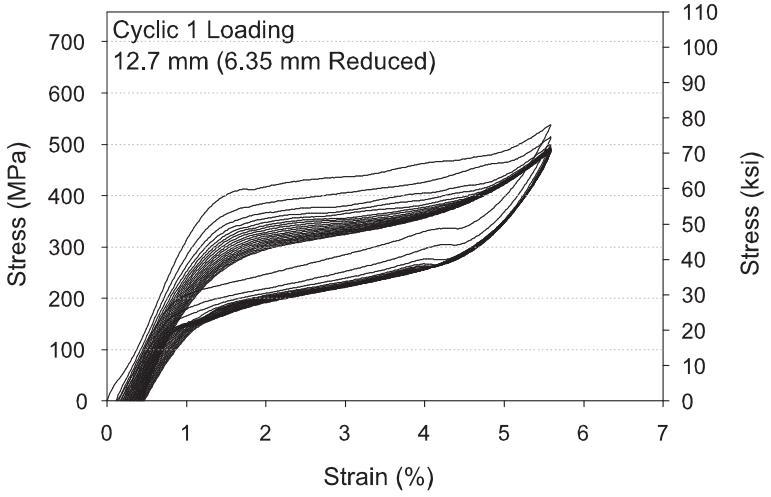

A-2(a):

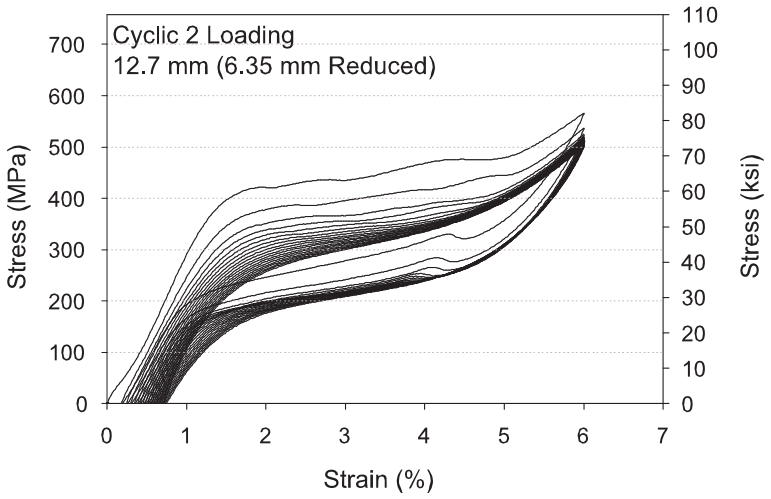

A-2(b):

Figure A-2: Cyclic tensile stress-strain plots for the 12.7 mm full-scale specimen: (a) test 1 and (b) test 2.

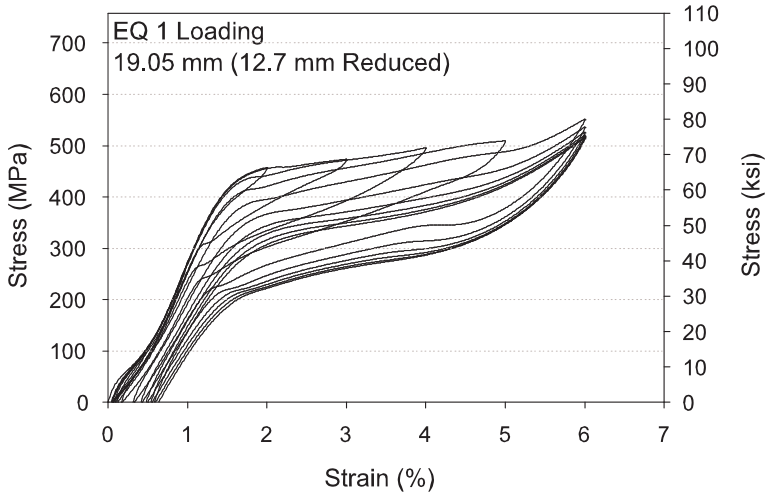

A-3(a):

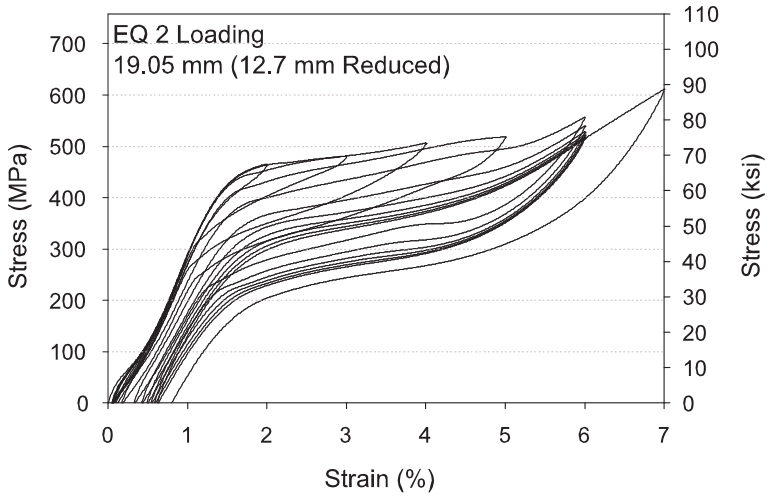

A-3(b):

Figure A-3: Quasi-static tensile earthquake loading protocol stress-strain plots for the 19.1 mm full-scale specimen: (a) test 1 and (b) test 2.

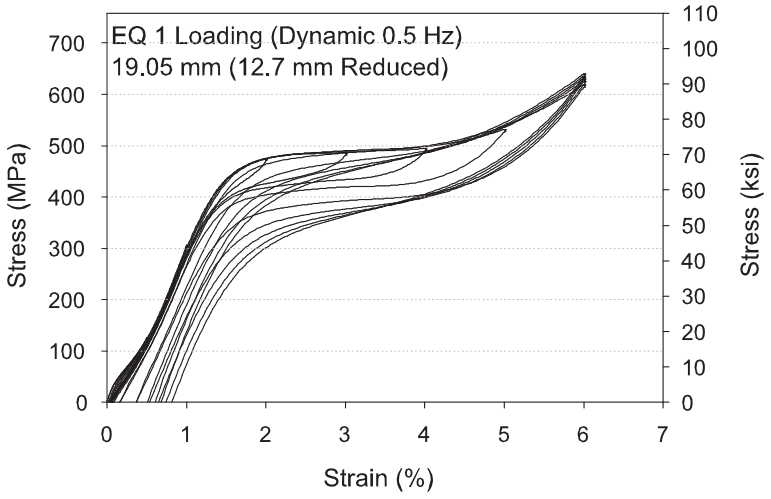

A-4(a):

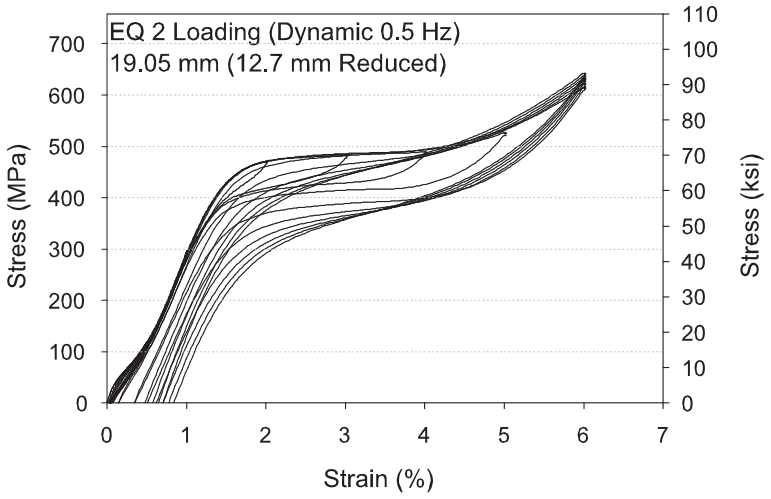

A-4(b):

Figure A-4: Dynamic 0.5 Hz tensile earthquake loading protocol stress-strain plots for the 19.1 mm full-scale specimen: (a) test 1 and (b) test 2.

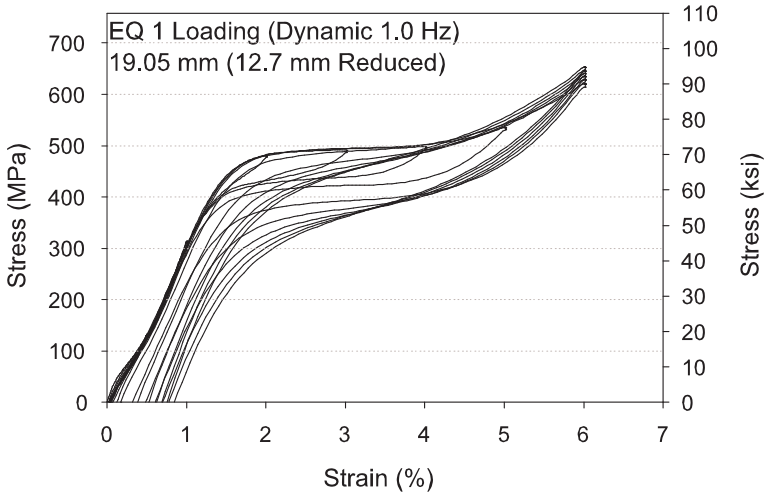

A-5(a):

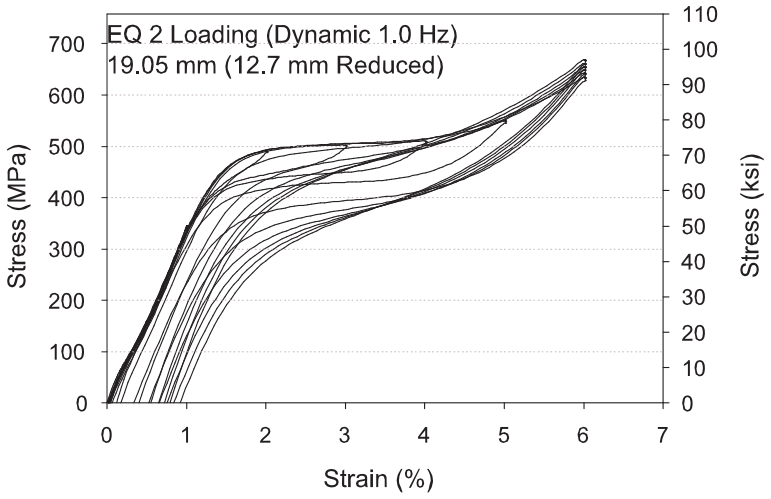

A-5(b):

Figure A-5: Dynamic 1.0 Hz tensile earthquake loading protocol stress-strain plots for the 19.1 mm full-scale specimen: (a) test 1 and (b) test 2.

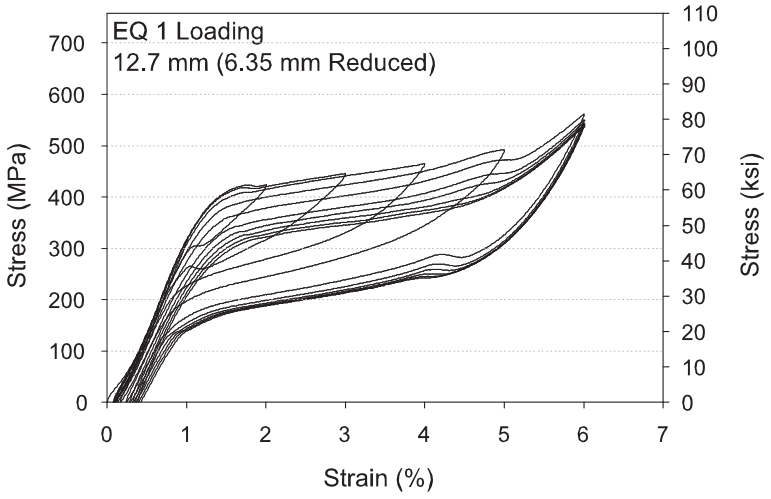

A-6(a):

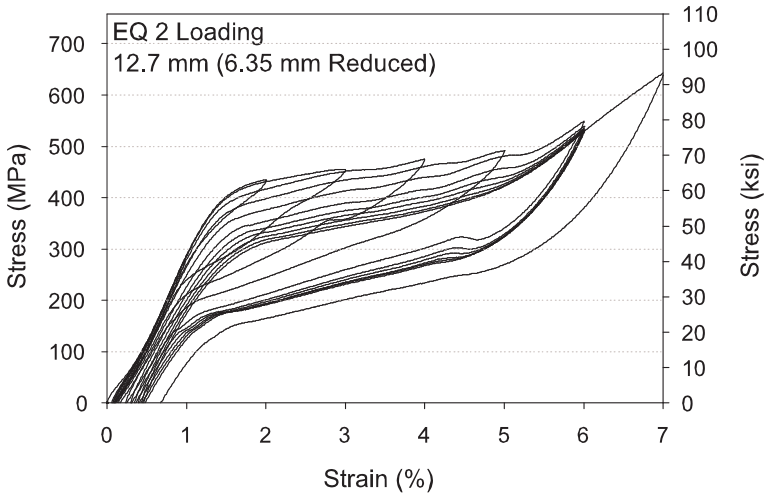

A-6(b):

Figure A-6: Quasi-static tensile earthquake loading protocol stress-strain plots for the 12.7 mm full-scale specimen: (a) test 1 and (b) test 2.

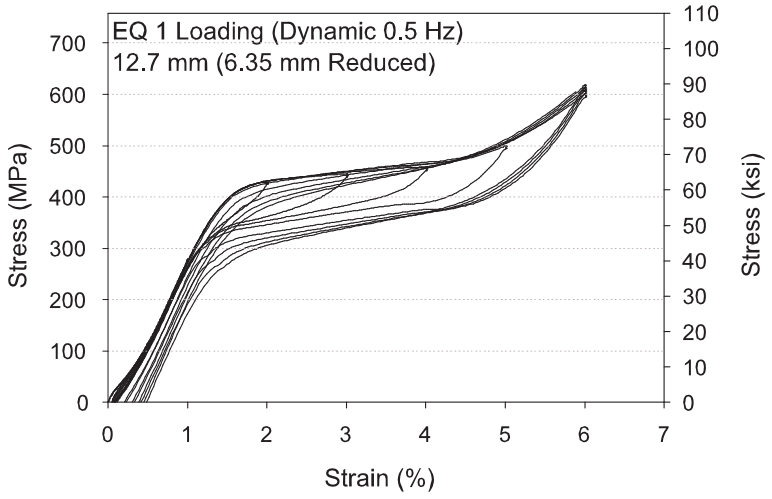

A-7(a):

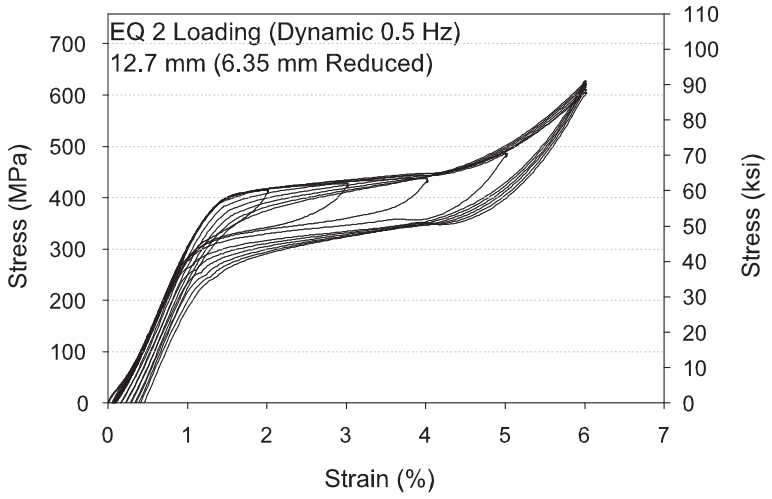

A-7(b):

Figure A-7: Dynamic 0.5 Hz tensile earthquake loading protocol stress-strain plots for the 12.7 mm full-scale specimen: (a) test 1 and (b) test 2.

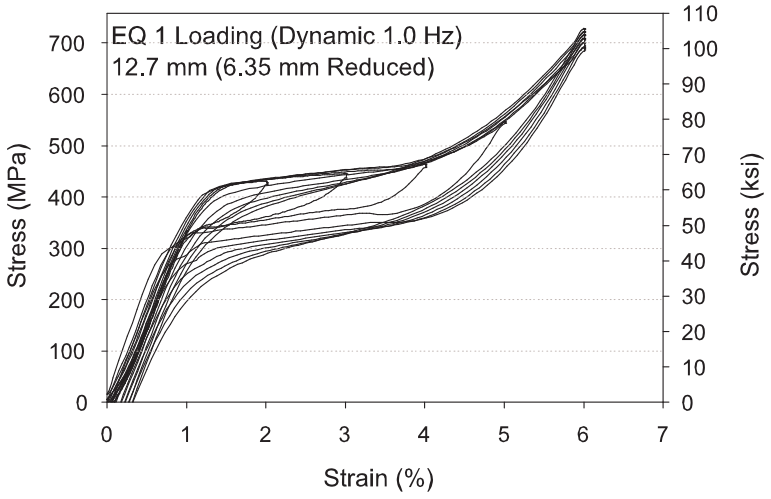

A-8(a):

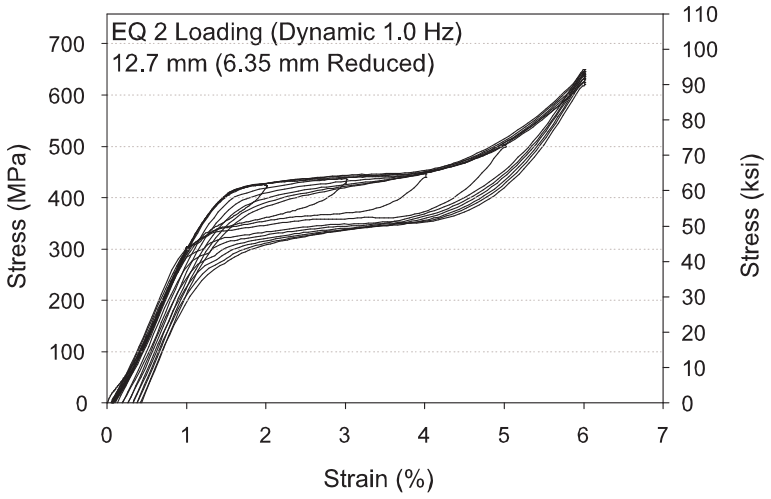

A-8(b):

Figure A-8: Dynamic 1.0 Hz tensile earthquake loading protocol stress-strain plots for the 12.7 mm full-scale specimen: (a) test 1 and (b) test 2.

APPENDIX B

NITI WIRE MECHANICAL TRAINING RESULTS

The mechanical training study (Chapter 4) provides information on which factors are most significant in changing and stabilizing the cyclic mechanical properties of the NiTi wire. Two sets of tests are run as part of the mechanical training study. The first set of tests is based on a full-factorial design and the second set of tests is a more in depth response surface design in order to better provide the relationship between the response and input factors. This appendix provides all of the tensile stress-strain curves of the NiTi wires undergoing the earthquake loading protocol after initial mechanical training. For each training study, the randomly generated planning matrix is provided in order to be able to match the factor levels to each corresponding specimen.

B.1 Full-factorial Training Study

Table B-1 provides the planning matrix for the full-factorial mechanical training study. Figures B-1 to B-4 show the corresponding stress-strain curves for each specimen grouped into sets of four.

B.2 Response Surface Training Study

Table B-2 provides the planning matrix for the response surface mechanical training study. Figures B-5 to B-9 show the stress-strain curves for each specimen grouped into sets of four.

Table B-1: Planning Matrix for the Preliminary Full-Factorial Mechanical Training Study

Specimen Number	Number of Cycles	Strain Level	Post Training Loading Rate
1	-	-	-
2	-	-	+
3	+	-	+
4	+	+	-
5	+	+	+
6	-	-	+
7	+	-	-
8	+	+	+
9	-	+	-
10	+	-	+
11	+	-	-
12	-	-	-
13	+	+	-
14	-	+	+
15	-	+	-
16	-	+	+

Table B-2: Planning Matrix for the Follow-up Response Surface Mechanical Training Study

Specimen Number	Number of Cycles	Strain Level
1	-	0
2	-	-
3	+	+
4	-	0
5	+	+
6	-	-
7	0	+
8	0	0
9	0	-
10	+	-
11	0	-
12	0	+
13	+	-
14	-	+
15	+	+
16	+	0
17	-	+
18	0	0
19	0	0
20	0	0

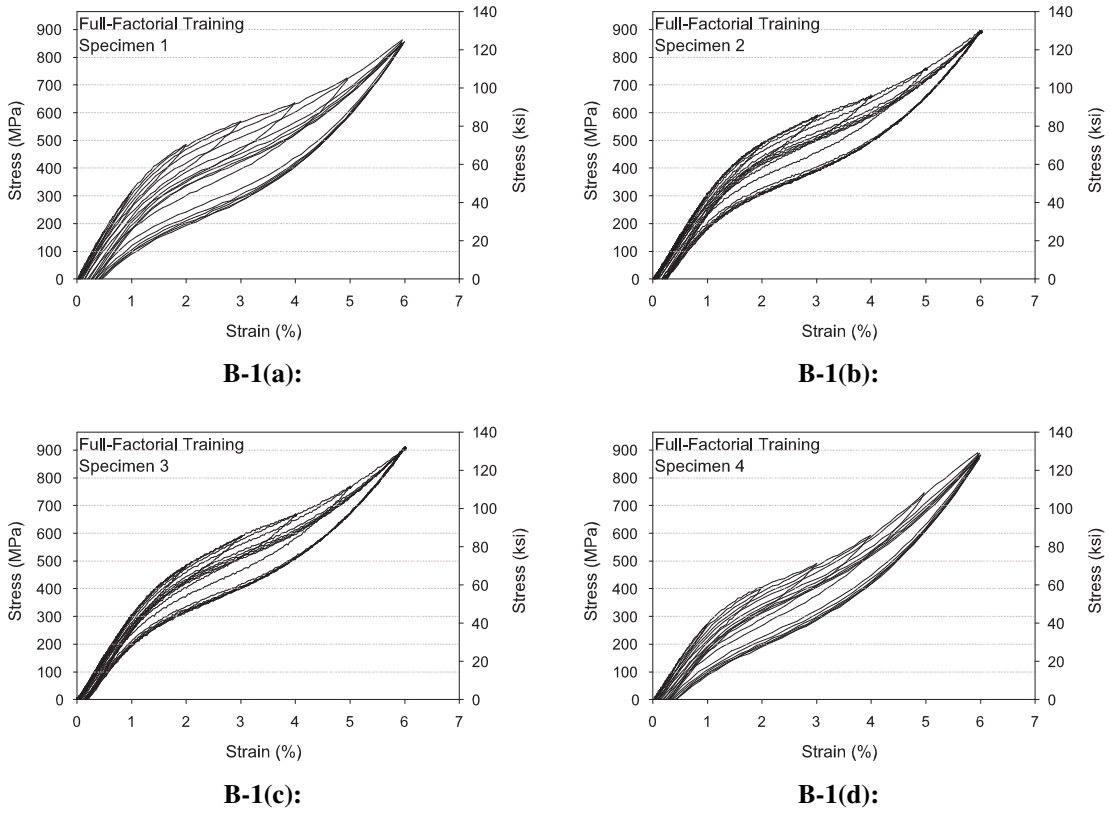

Figure B-1: Stress-strain curves for previously trained specimens from the full-factorial mechanical training study undergoing the earthquake loading protocol: (a) Specimen 1, (b) Specimen 2, (c) Specimen 3, and (d) Specimen 4.

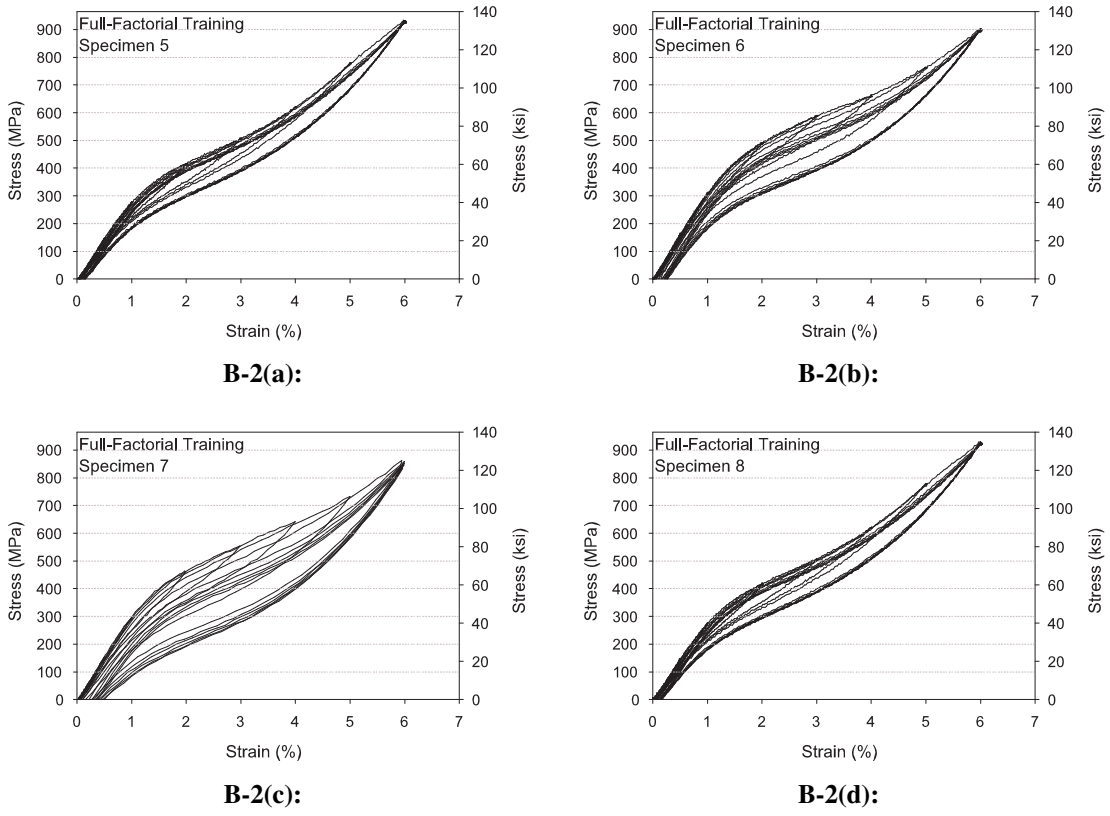

Figure B-2: Stress-strain curves for previously trained specimens from the full-factorial mechanical training study undergoing the earthquake loading protocol: (a) Specimen 5, (b) Specimen 6, (c) Specimen 7, and (d) Specimen 8.

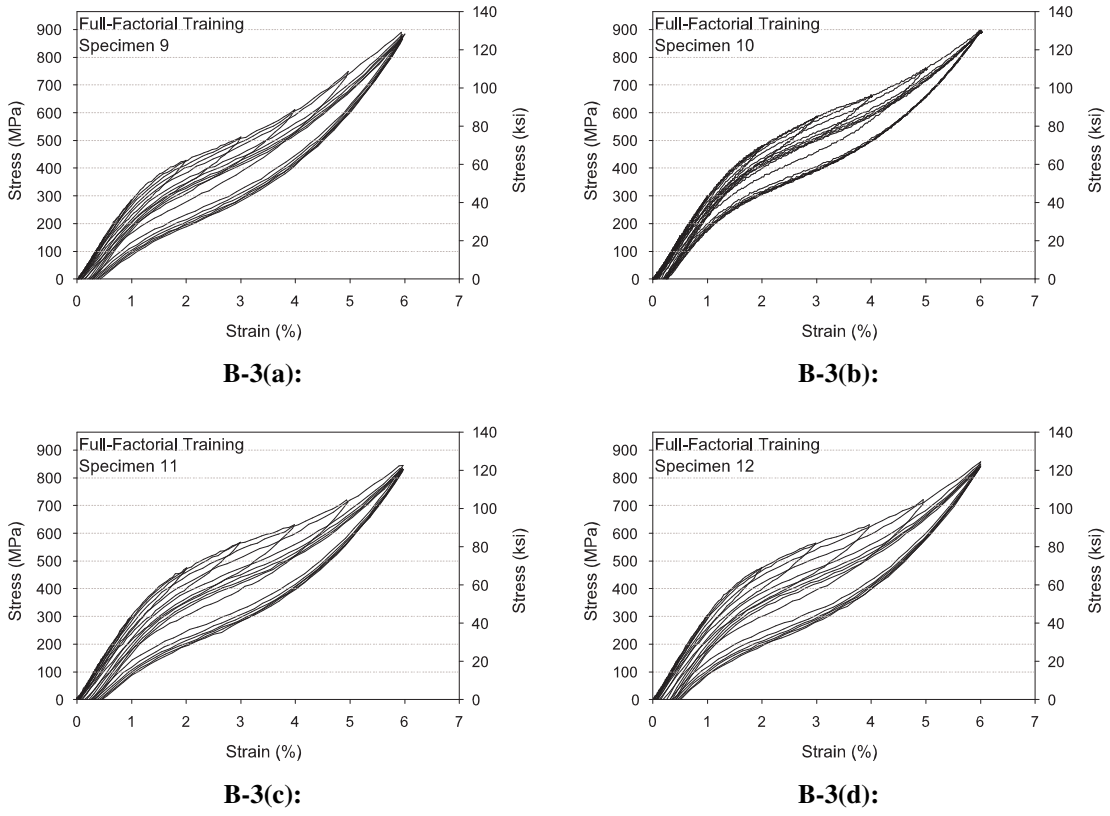

Figure B-3: Stress-strain curves for previously trained specimens from the full-factorial mechanical training study undergoing the earthquake loading protocol: (a) Specimen 9, (b) Specimen 10, (c) Specimen 11, and (d) Specimen 12.

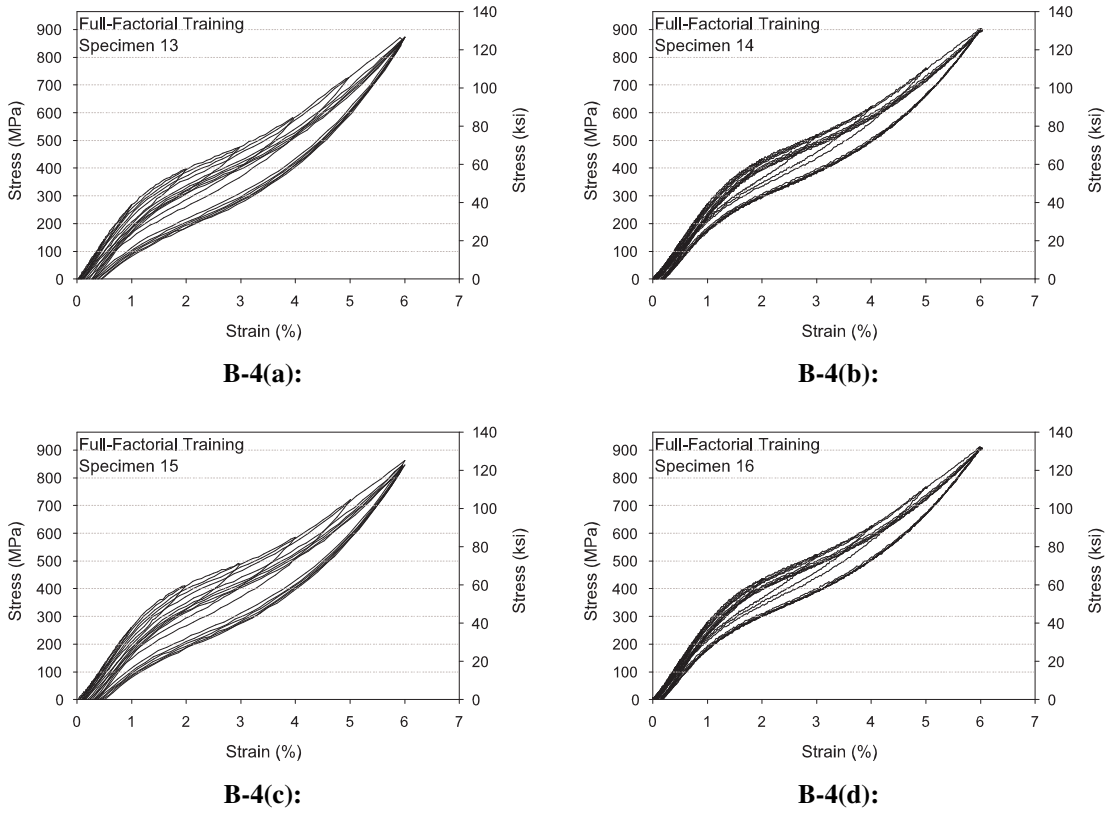

Figure B-4: Stress-strain curves for previously trained specimens from the full-factorial mechanical training study undergoing the earthquake loading protocol: (a) Specimen 13, (b) Specimen 14, (c) Specimen 15, and (d) Specimen 16.

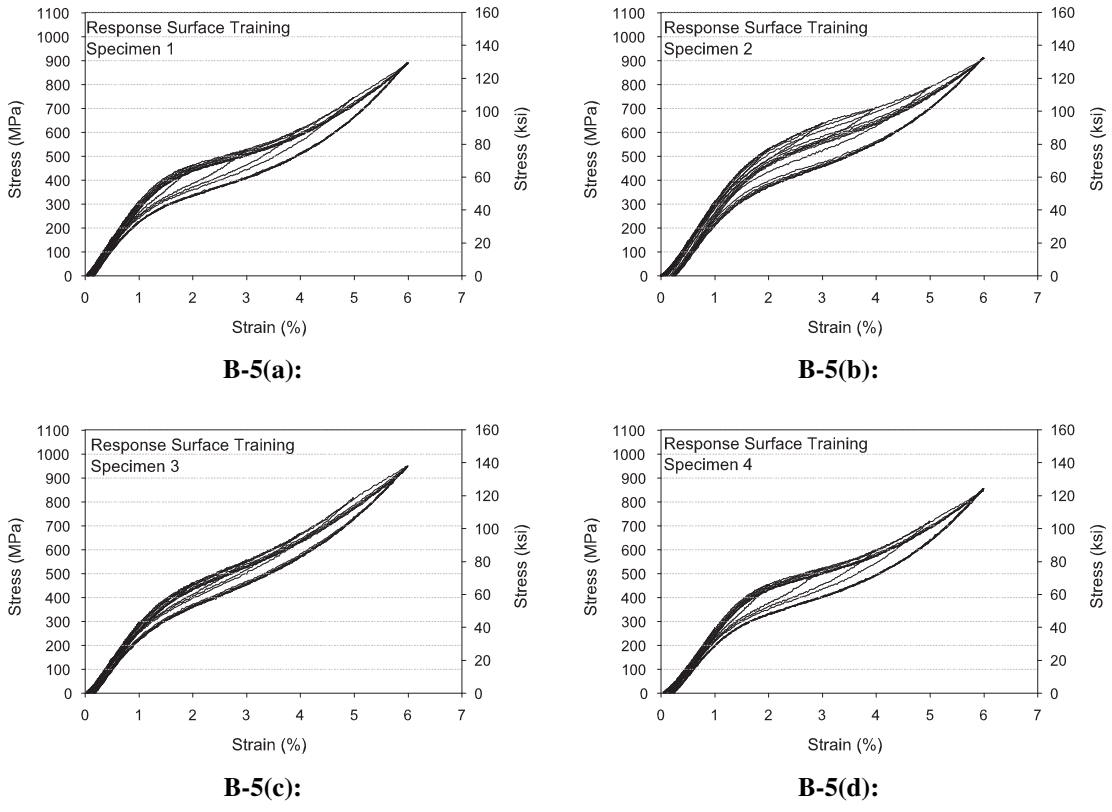

Figure B-5: Stress-strain curves for previously trained specimens from the response surface mechanical training study undergoing the earthquake loading protocol: (a) Specimen 1 (b) Specimen 2, (c) Specimen 3, and (d) Specimen 4.

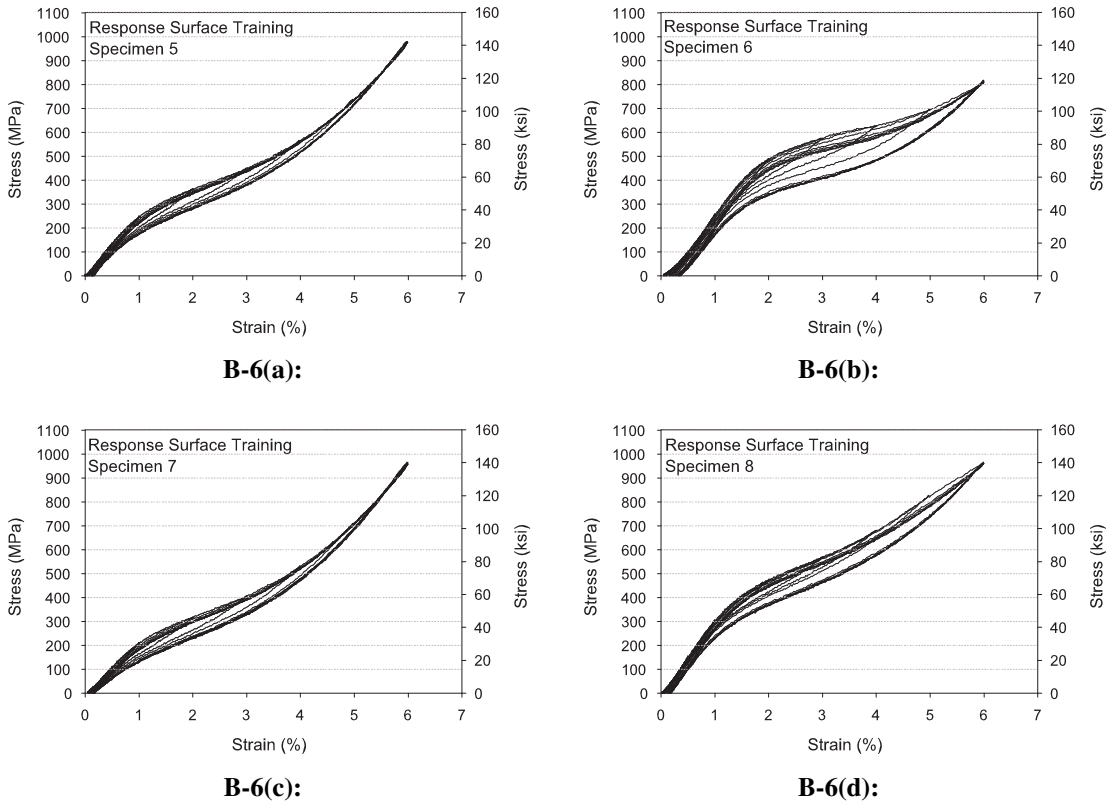

Figure B-6: Stress-strain curves for previously trained specimens from the response surface mechanical training study undergoing the earthquake loading protocol: (a) Specimen 5, (b) Specimen 6, (c) Specimen 7, and (d) Specimen 8.

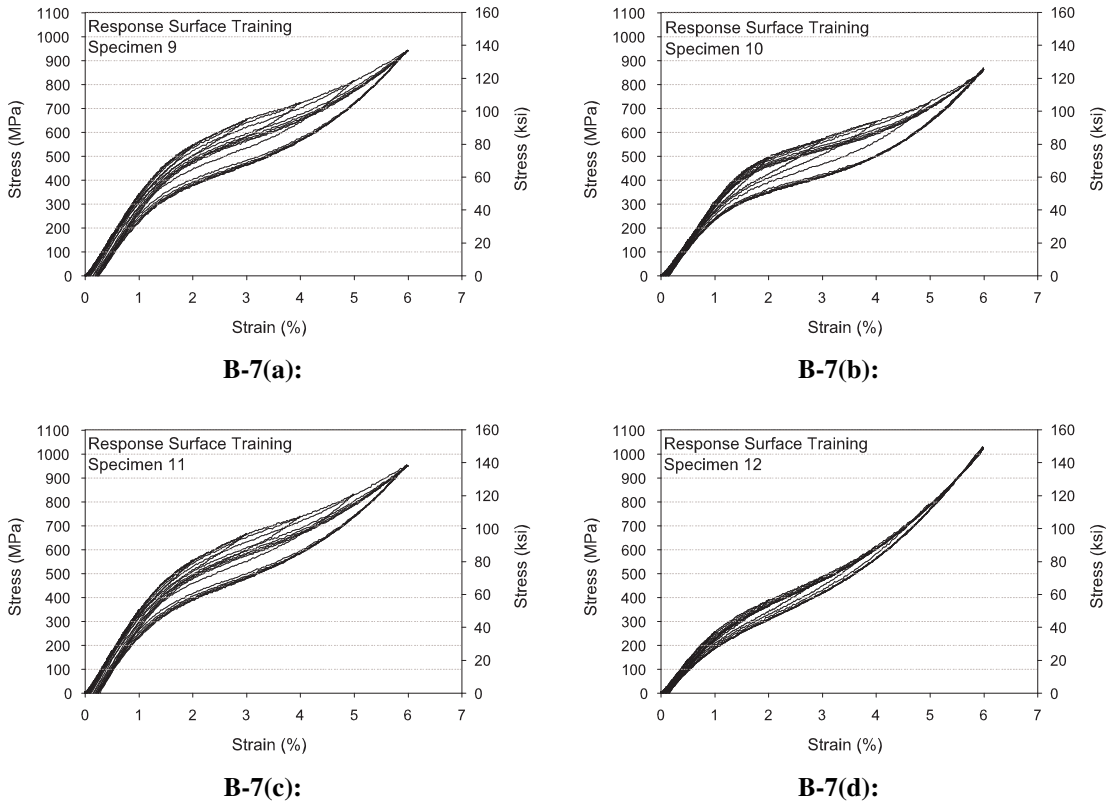

Figure B-7: Stress-strain curves for previously trained specimens from the response surface mechanical training study undergoing the earthquake loading protocol: (a) Specimen 9, (b) Specimen 10, (c) Specimen 11, and (d) Specimen 12.

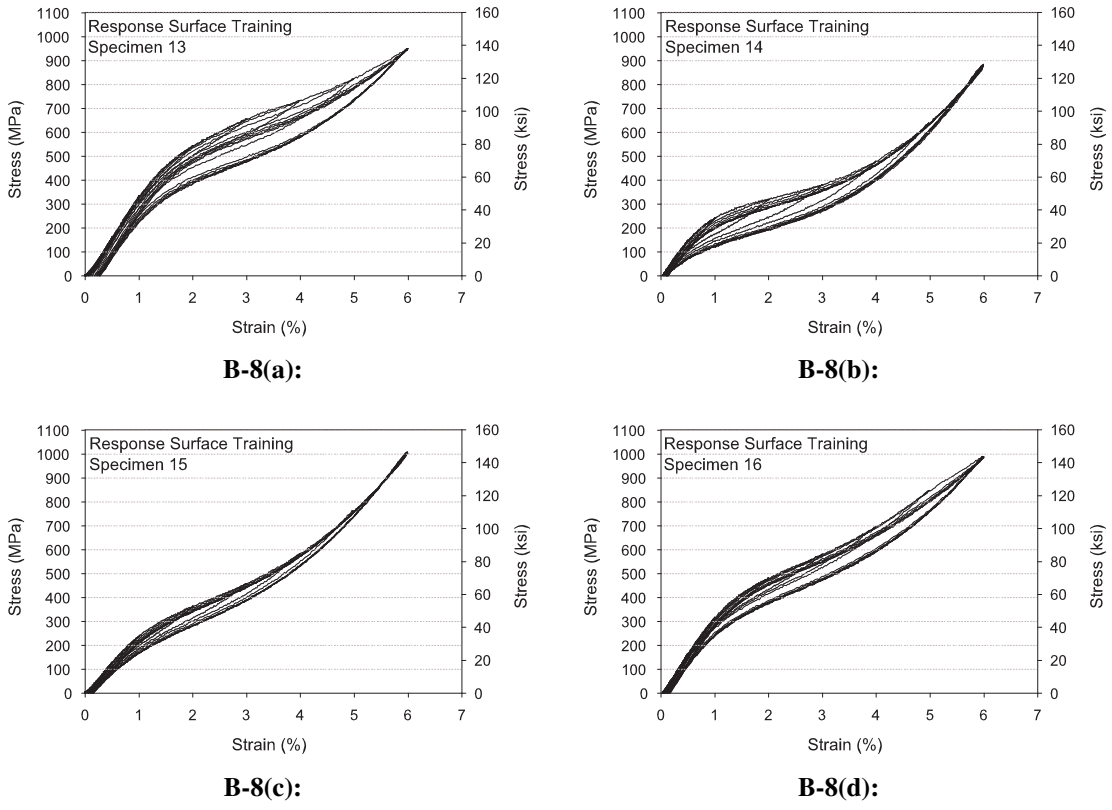

Figure B-8: Stress-strain curves for previously trained specimens from the response surface mechanical training study undergoing the earthquake loading protocol: (a) Specimen 13, (b) Specimen 14, (c) Specimen 15, (d) Specimen 16.

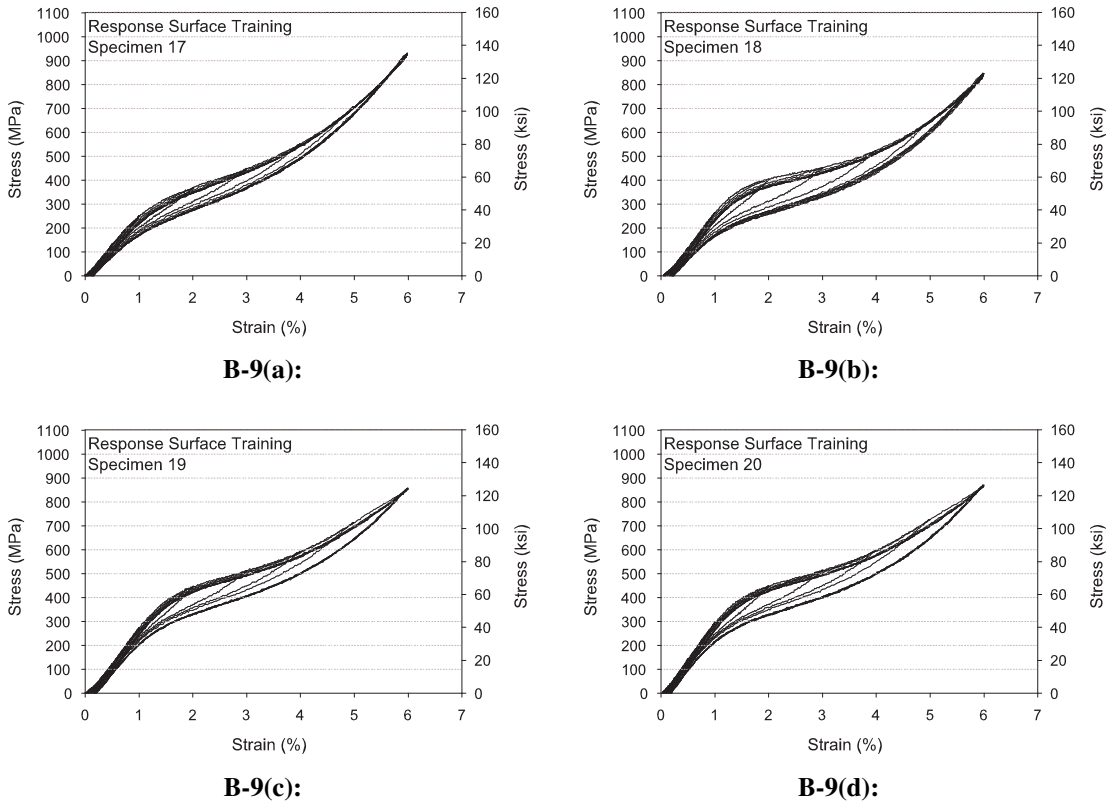

Figure B-9: Stress-strain curves for previously trained specimens from the response surface mechanical training study undergoing the earthquake loading protocol: (a) Specimen 17, (b) Specimen 18, (c) Specimen 19, and (d) Specimen 20.

APPENDIX C

NITI WIRE PRE-STRAINING RESULTS

The pre-straining study discussed in Chapter 4 provides a means of obtaining more energy dissipation capacity during small strain cycles as a result of early sub-cycling. Both constant cyclic loading tests and earthquake loading tests are conducted on the NiTi wire specimens to compare the behavior of specimens pre-strained to various levels between 1.0% and 4.0%. This appendix provides all of the tensile stress-strain curves of the NiTi wires undergoing both the cyclic loading protocol and the earthquake loading protocol. For each pre-strain level, loading type, and loading rate, a single replicate is conducted.

C.1 Cyclic Loading Study

Figures C-1 to C-7 show the corresponding stress-strain curves for the wires tested as part of the cyclic loading study. Pre-strain levels of 1.0%, 1.5%, 2.0%, 2.5%, 3.0%, 3.5%, and 4.0% are considered. All tests are conducted at a quasi-static loading rate.

C.2 Earthquake Loading Study

The earthquake loading study reduces the number of pre-strain levels to 1.0%, 2.0%, 3.0%, and 4.0%, but considers dynamic loading effects. Figures C-8 to C-11 show the stress-strain curves for each specimen cycled quasi-statically and dynamically with respect to pre-strain level.

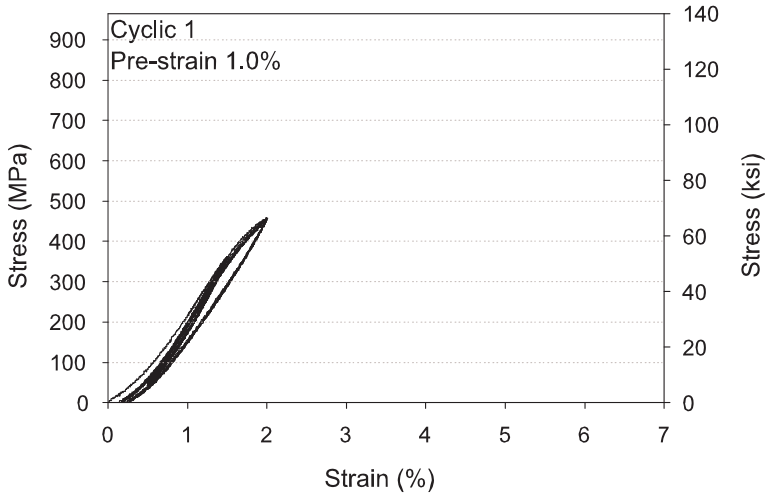

C-1(a):

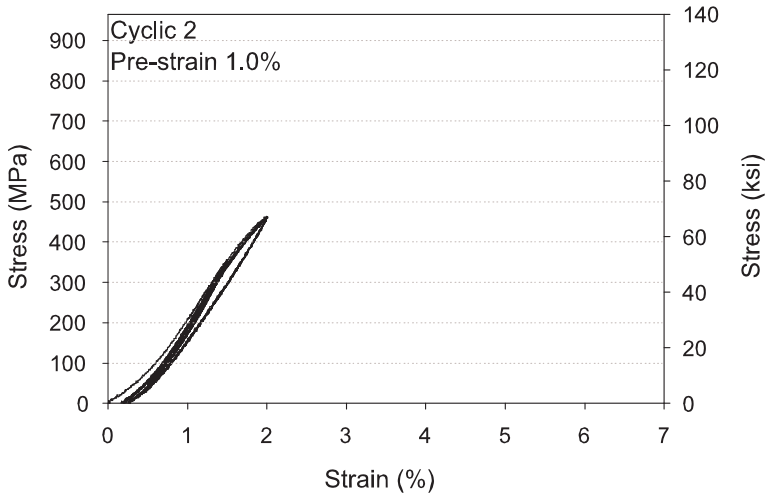

C-1(b):

Figure C-1: Cyclic loading stress-strain plots for the NiTi wire pre-strained to 1.0%: (a) test 1 and (b) test 2.

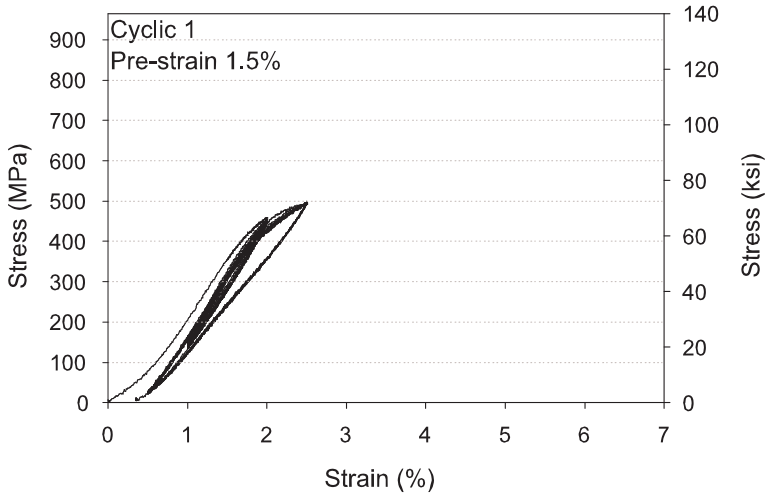

C-2(a):

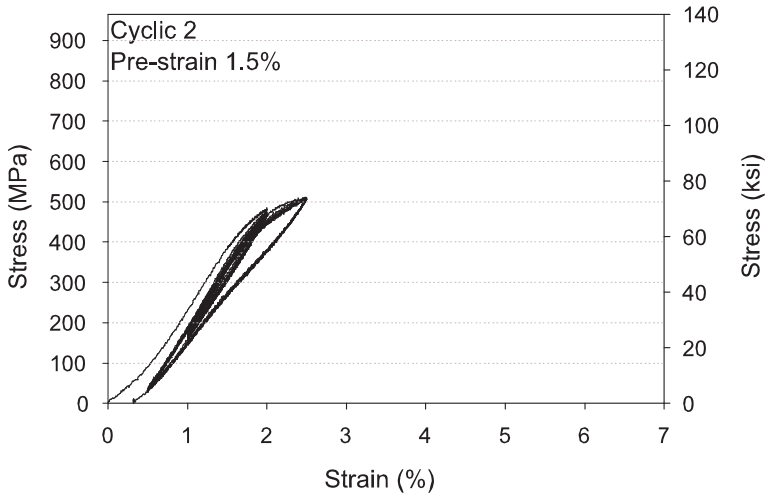

C-2(b):

Figure C-2: Cyclic loading stress-strain plots for the NiTi wire pre-strained to 1.5%: (a) test 1 and (b) test 2.

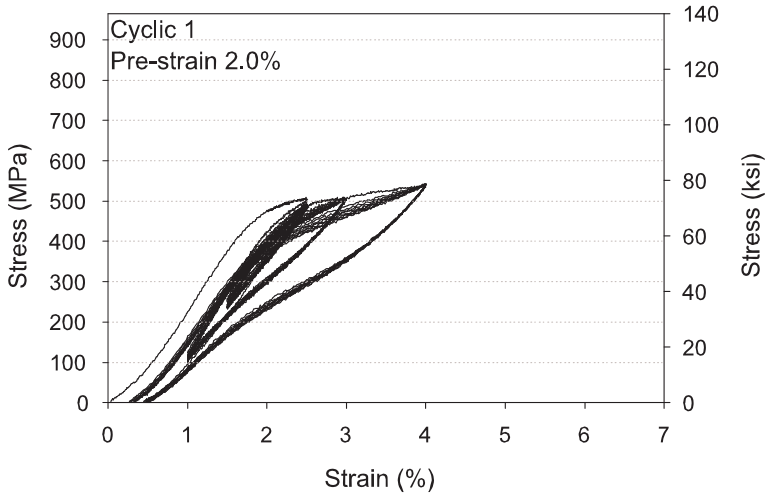

C-3(a):

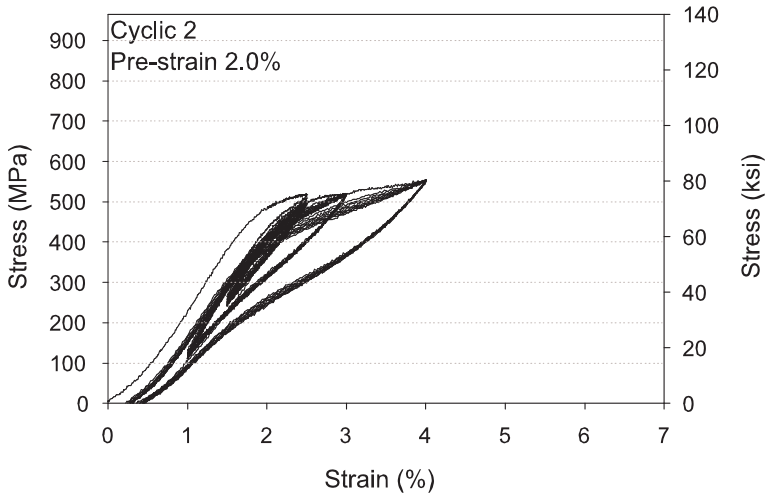

C-3(b):

Figure C-3: Cyclic loading stress-strain plots for the NiTi wire pre-strained to 2.0%: (a) test 1 and (b) test 2.

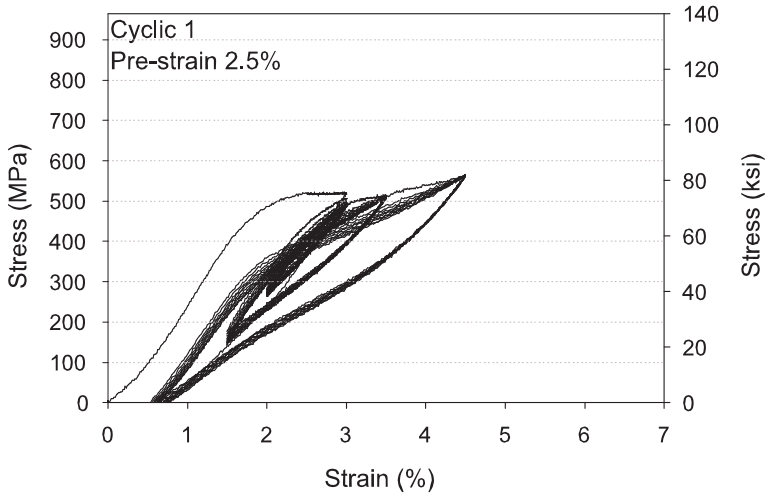

C-4(a):

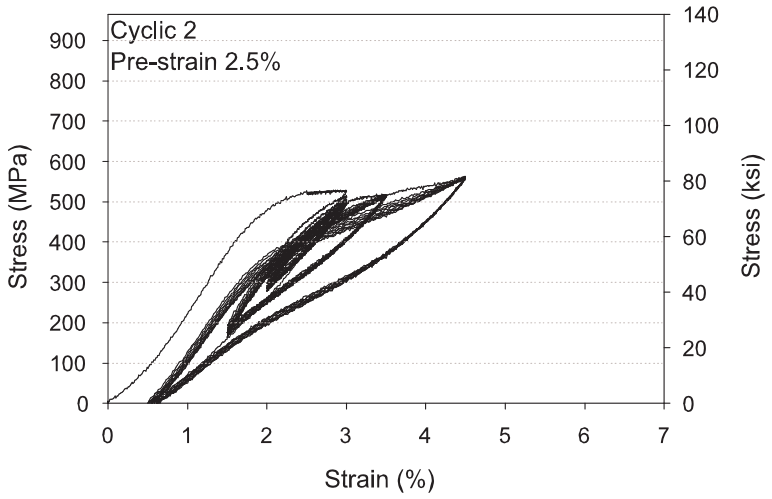

C-4(b):

Figure C-4: Cyclic loading stress-strain plots for the NiTi wire pre-strained to 2.5%: (a) test 1 and (b) test 2.

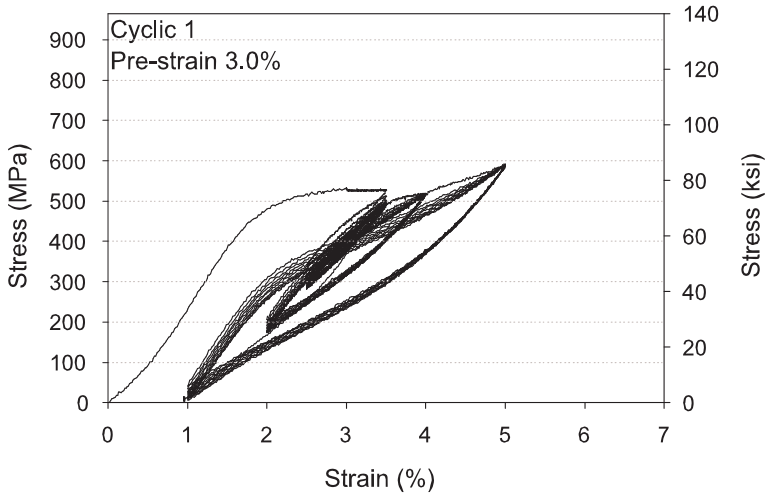

C-5(a):

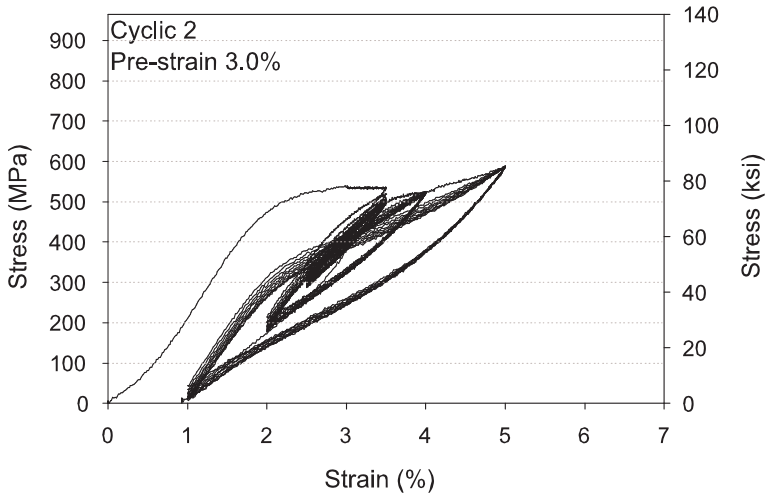

C-5(b):

Figure C-5: Cyclic loading stress-strain plots for the NiTi wire pre-strained to 3.0%: (a) test 1 and (b) test 2.

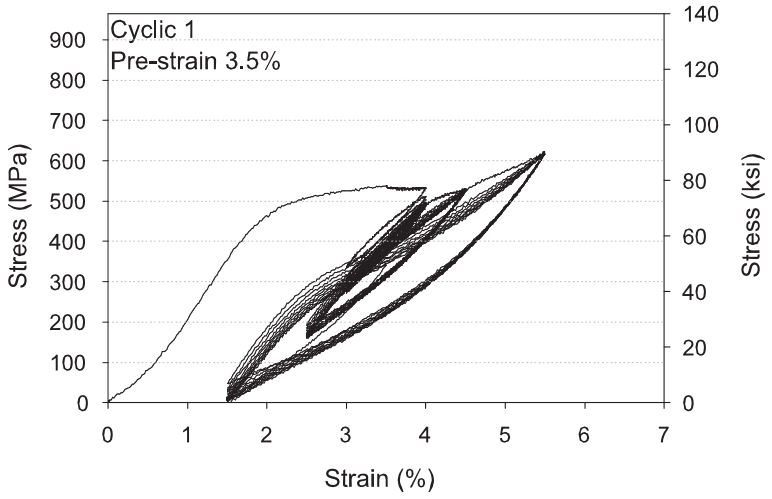

C-6(a):

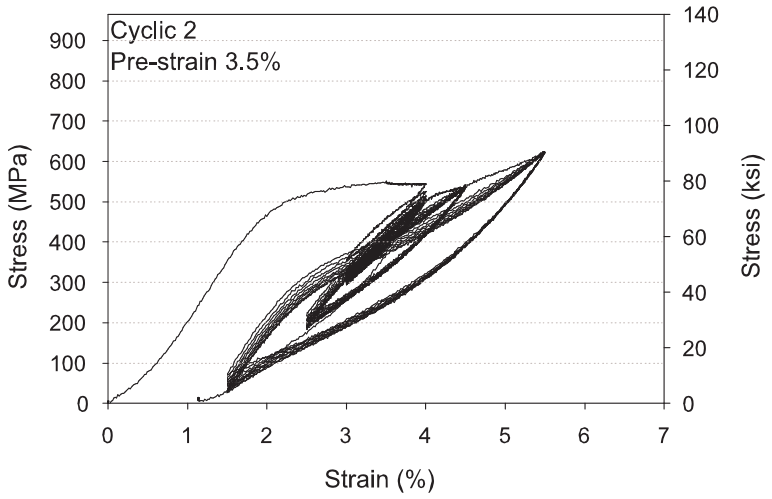

C-6(b):

Figure C-6: Cyclic loading stress-strain plots for the NiTi wire pre-strained to 3.5%: (a) test 1 and (b) test 2.

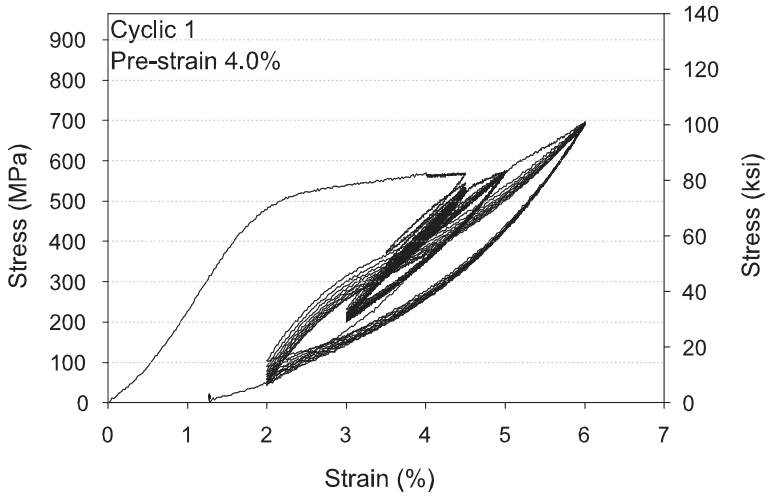

C-7(a):

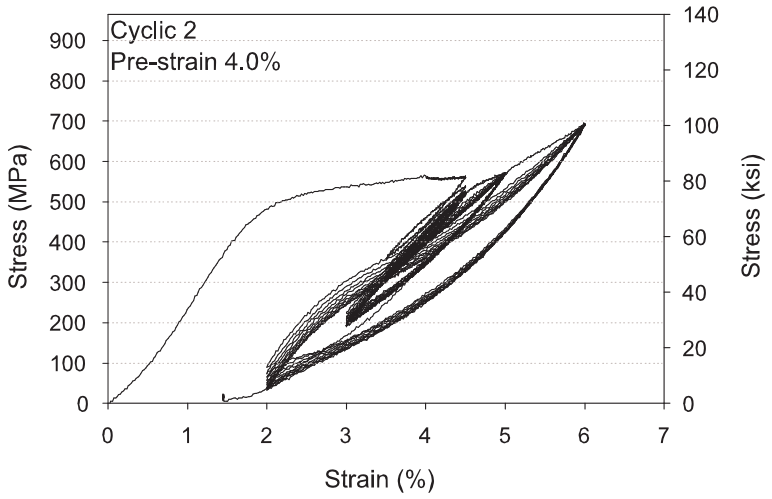

C-7(b):

Figure C-7: Cyclic loading stress-strain plots for the NiTi wire pre-strained to 4.0%: (a) test 1 and (b) test 2.

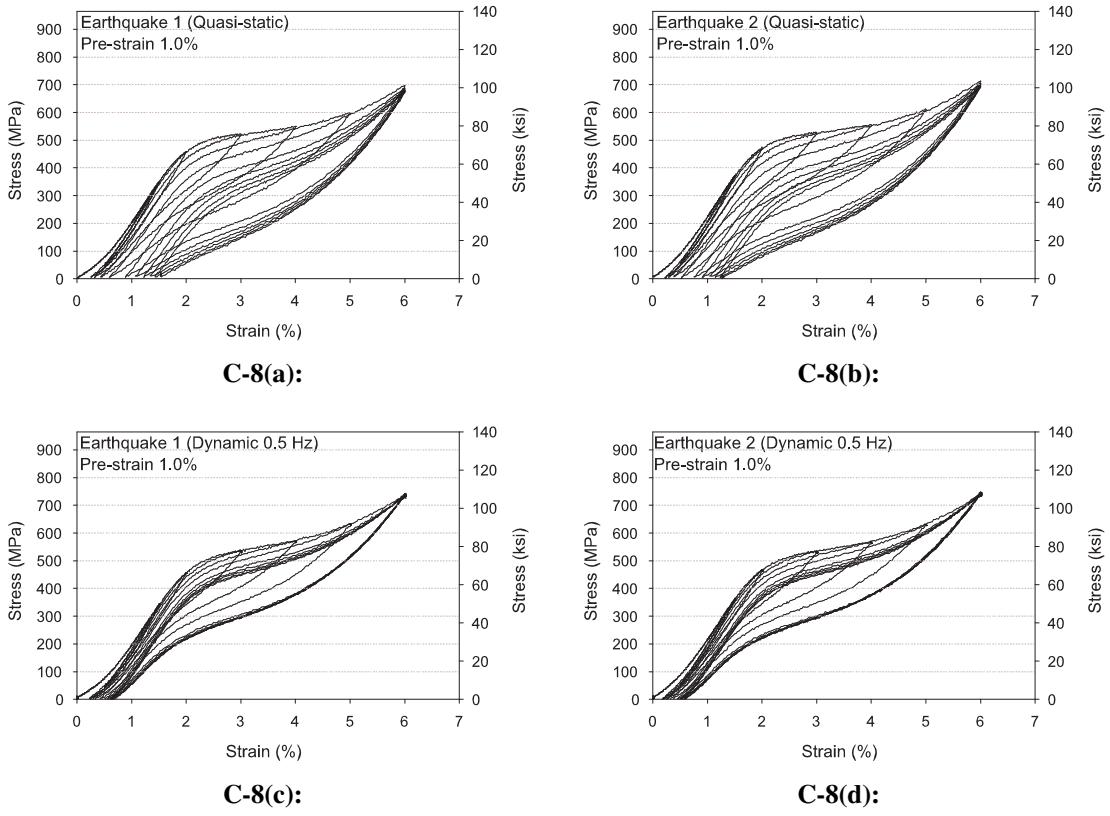

Figure C-8: Earthquake loading stress-strain plots for the NiTi wire pre-strained to 1.0%: (a) quasi-static test 1, (b) quasi-static test 2, (c) 0.5 Hz dynamic test 1, and (d) 0.5 Hz dynamic test2.

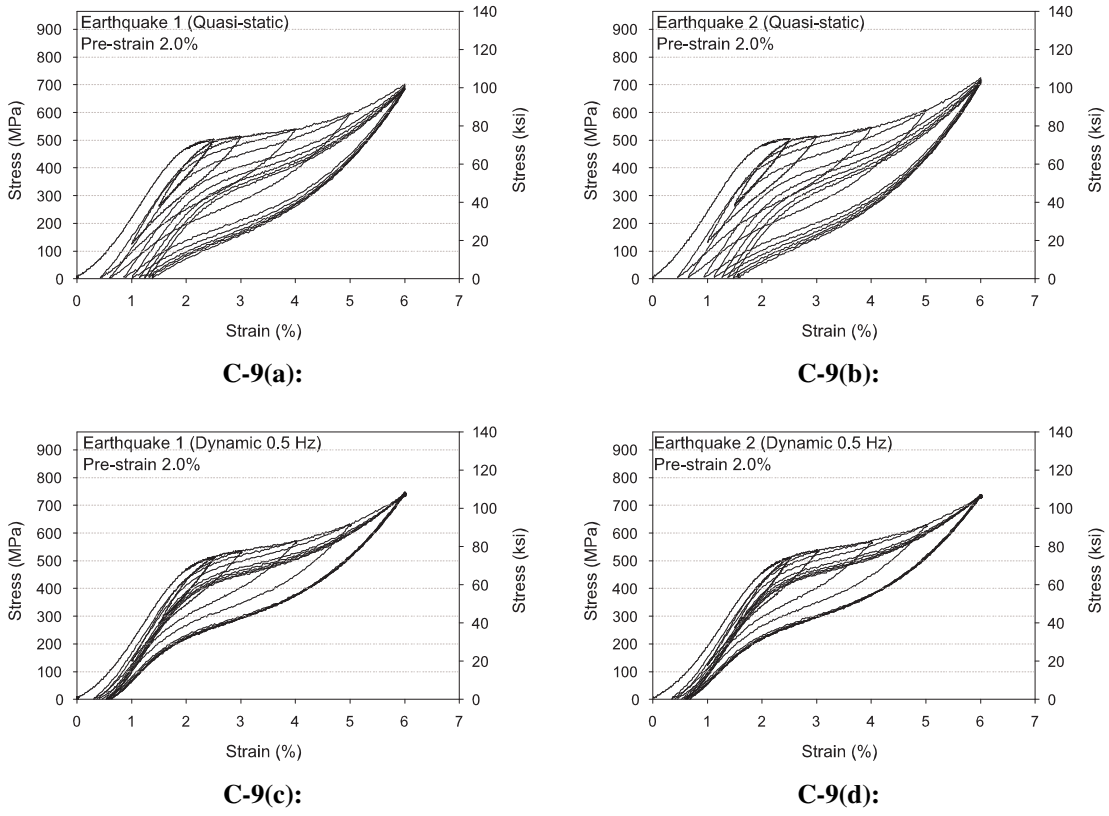

Figure C-9: Earthquake loading stress-strain plots for the NiTi wire pre-strained to 2.0%: (a) quasi-static test 1, (b) quasi-static test 2, (c) 0.5 Hz dynamic test 1, and (d) 0.5 Hz dynamic test2.

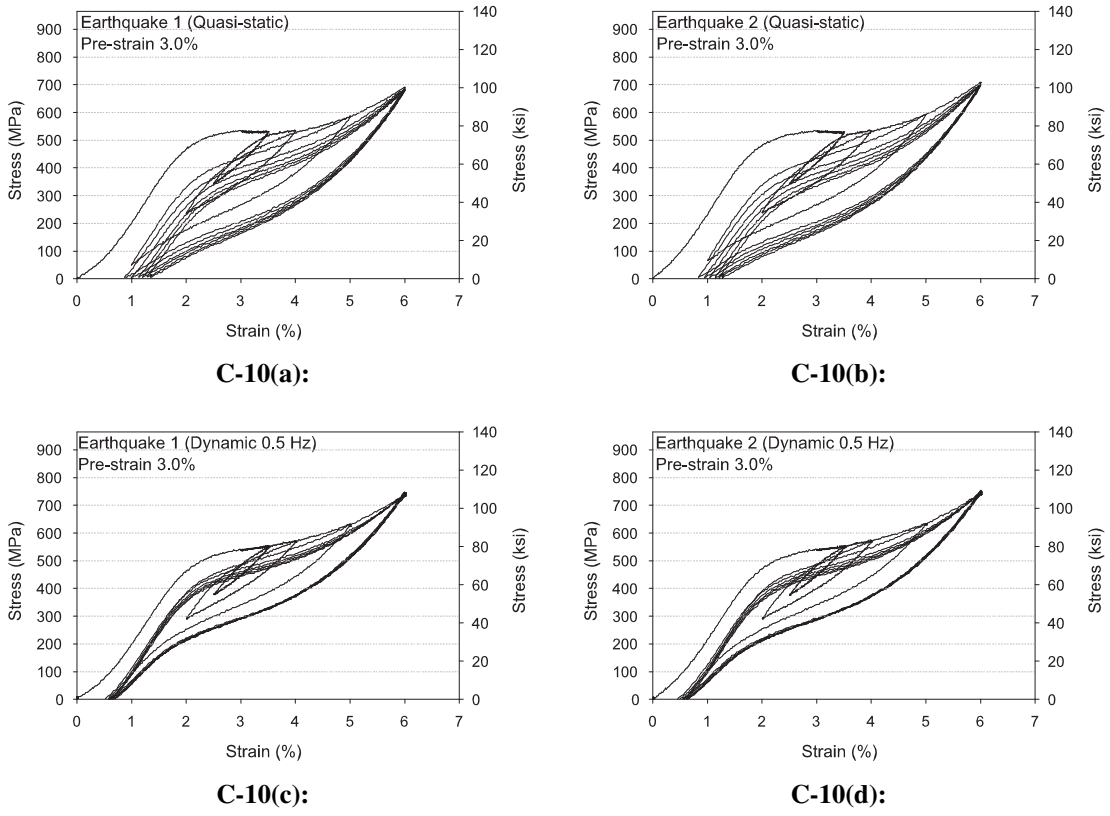

Figure C-10: Earthquake loading stress-strain plots for the NiTi wire pre-strained to 3.0%: (a) quasi-static test 1, (b) quasi-static test 2, (c) 0.5 Hz dynamic test 1, and (d) 0.5 Hz dynamic test2.

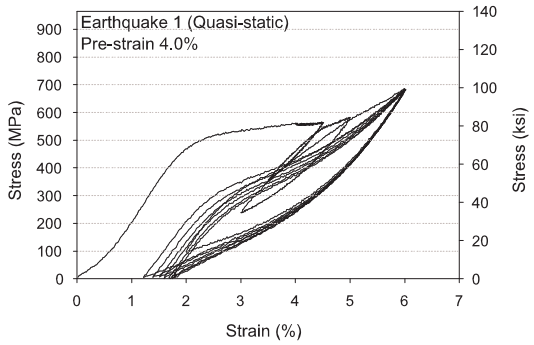

C-11(a):

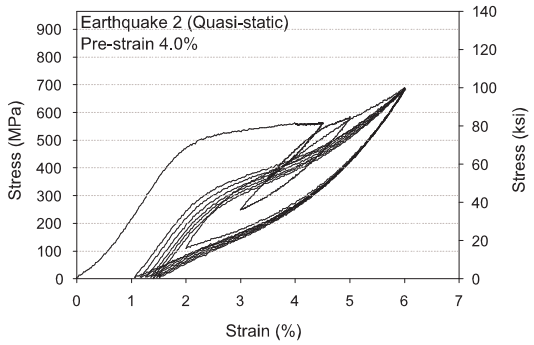

C-11(b):

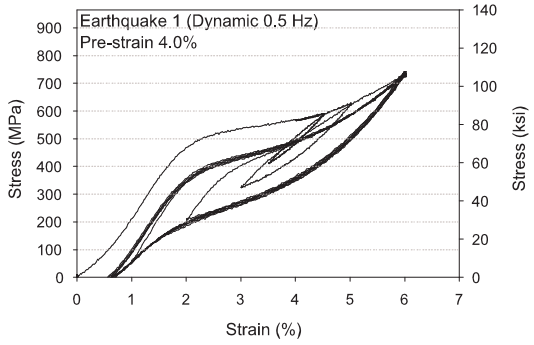

C-11(c):

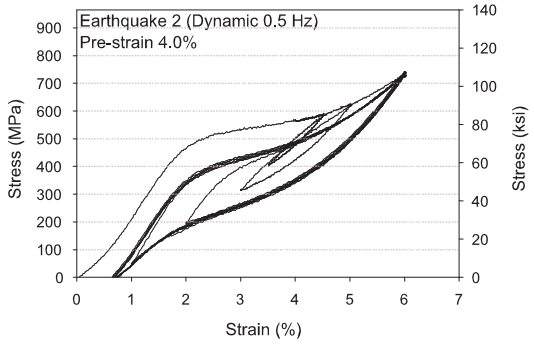

C-11(d):

Figure C-11: Earthquake loading stress-strain plots for the NiTi wire pre-strained to 4.0%: (a) quasi-static test 1, (b) quasi-static test 2, (c) 0.5 Hz dynamic test 1, and (d) 0.5 Hz dynamic test2.

APPENDIX D

NITI WIRE EARTHQUAKE TYPE LOADING RESULTS

Chapter 4 also provides a study which compares the tensile behavior of NiTi wires tested under a far-field type loading protocol consisting of gradually increasing strain cycles and under a near-field type loading protocol which contains early large strain cycles. In order to implement NiTi SMAs into seismic applications, it is important to determine if these early large strain cycles are detrimental to the superelastic cyclic properties. This appendix provides all of the stress-strain curves resulting from this loading type study. A single replicate test is performed for each loading protocol and each loading rate.

D.1 Far-field Earthquake Loading Study

Figures D-1 to D-3 provide the corresponding stress-strain curves for the wires tested under the far-field loading protocol. Specimens are tested at either a quasi-static, 0.25 Hz dynamic, or 0.5 Hz dynamic loading rate.

D.2 Near-field Earthquake Loading Study

Figures D-4 to D-6 provide the corresponding stress-strain curves for the wires tested under the near-field loading protocol. As is done with the far-field specmens, the near-field specimens are tested at either a quasi-static, 0.25 Hz dynamic, or 0.5 Hz dynamic loading rate.

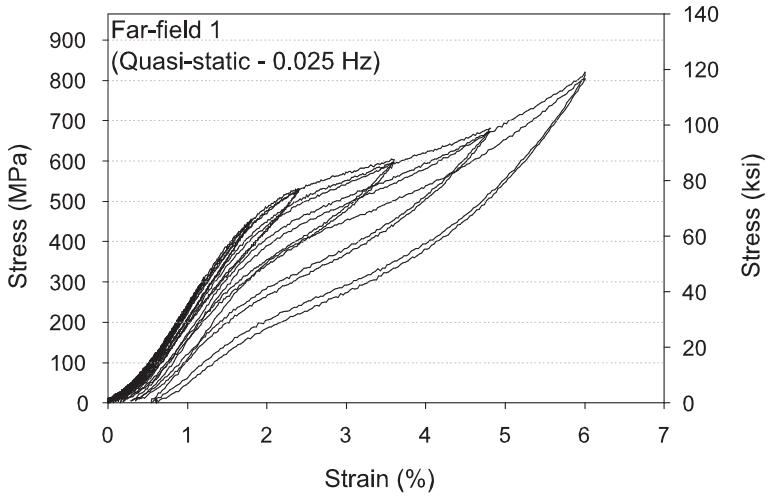

D-1(a):

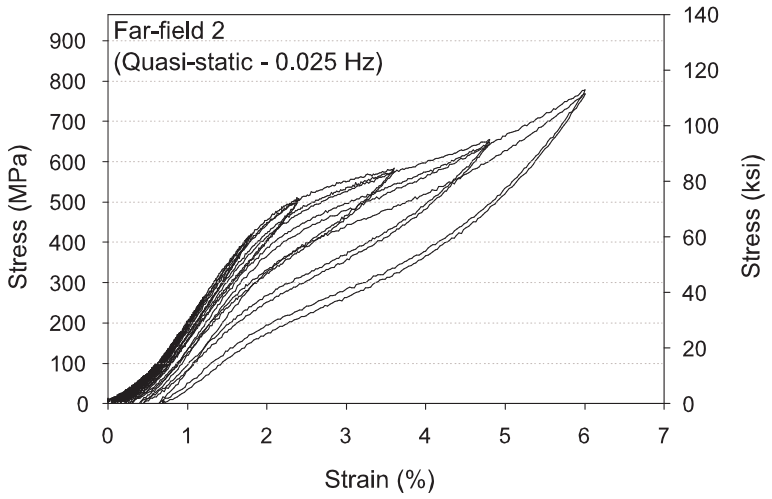

D-1(b):

Figure D-1: Quasi-static far-field loading stress-strain plot for the NiTi wire: (a) test 1 and (b) test 2.

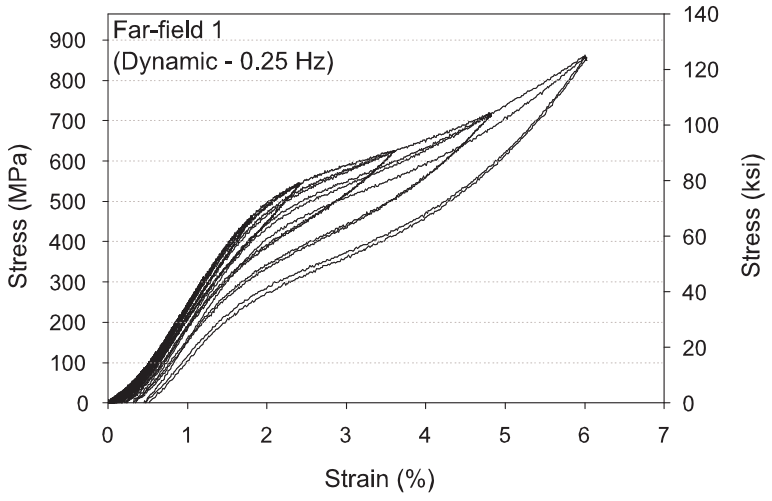

D-2(a):

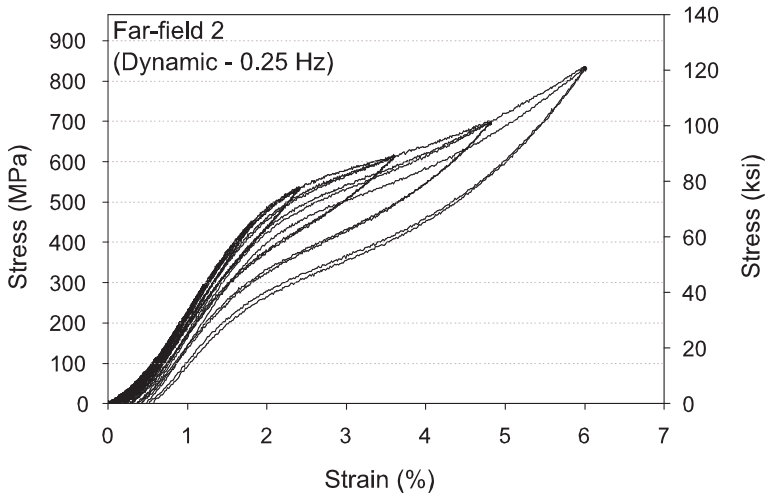

D-2(b):

Figure D-2: 0.25 Hz dynamic far-field loading stress-strain plot for the NiTi wire: (a) test 1 and (b) test 2.

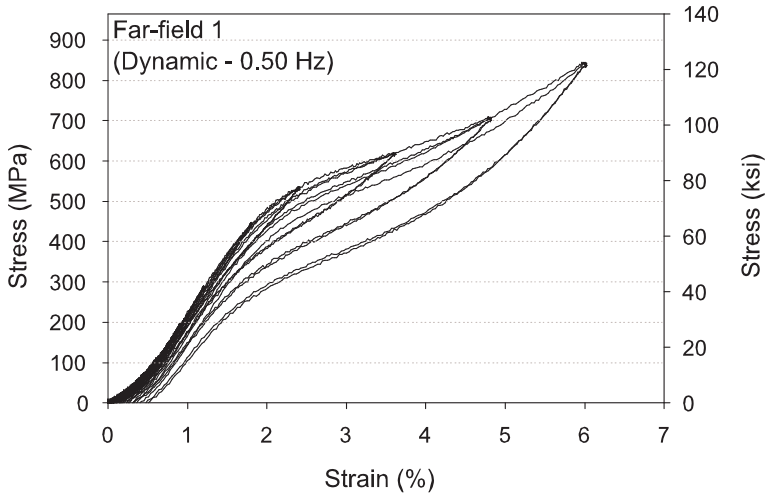

D-3(a):

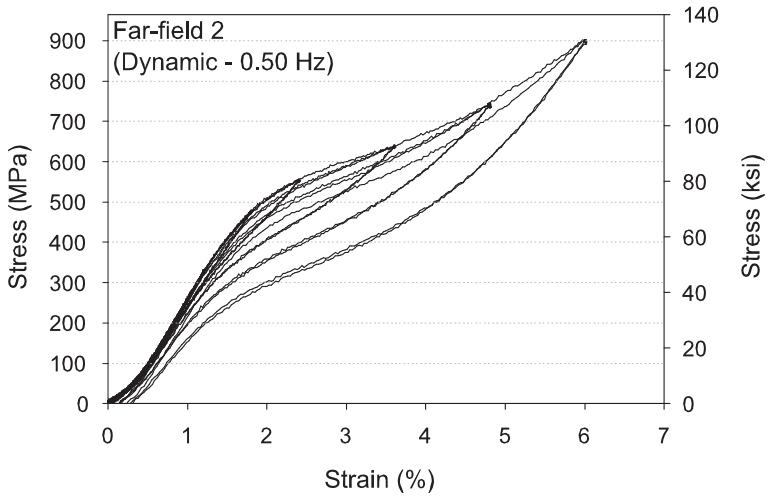

D-3(b):

Figure D-3: 0.5 Hz dynamic far-field loading stress-strain plot for the NiTi wire: (a) test 1 and (b) test 2.

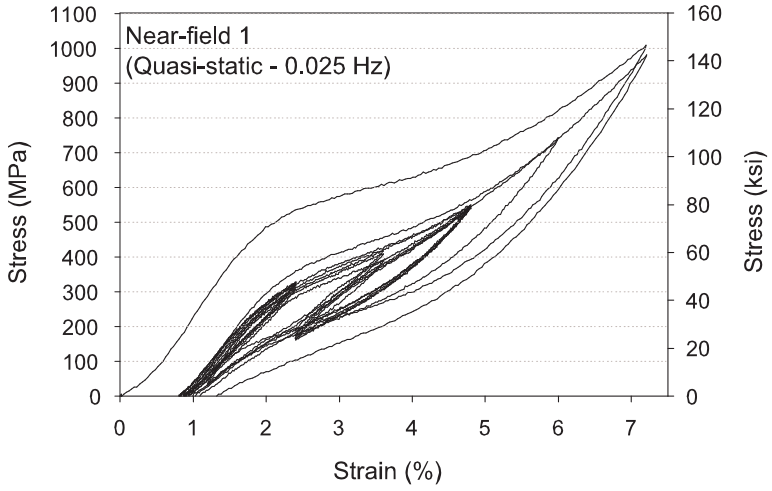

D-4(a):

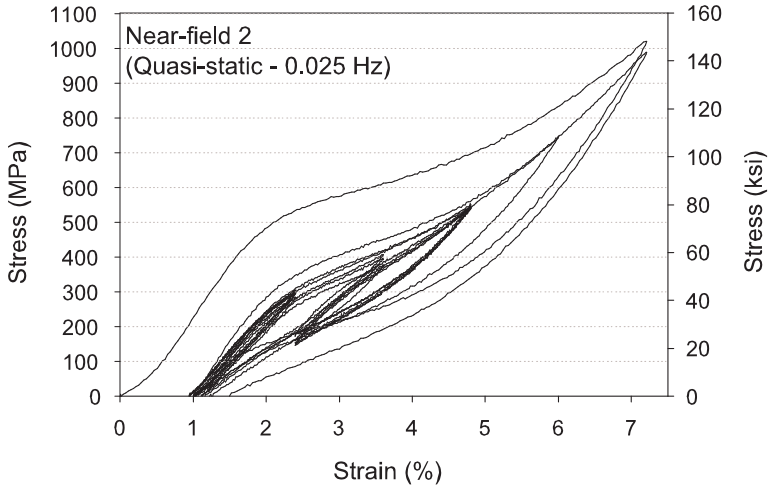

D-4(b):

Figure D-4: Quasi-static near-field loading stress-strain plot for the NiTi wire: (a) test 1 and (b) test 2.

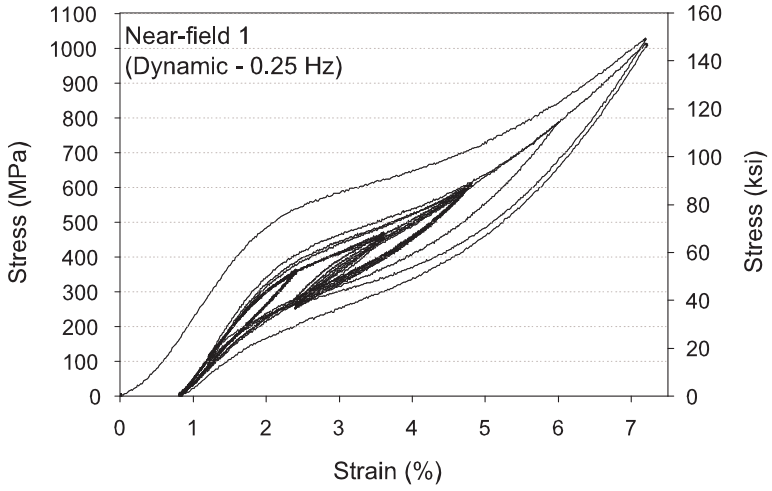

D-5(a):

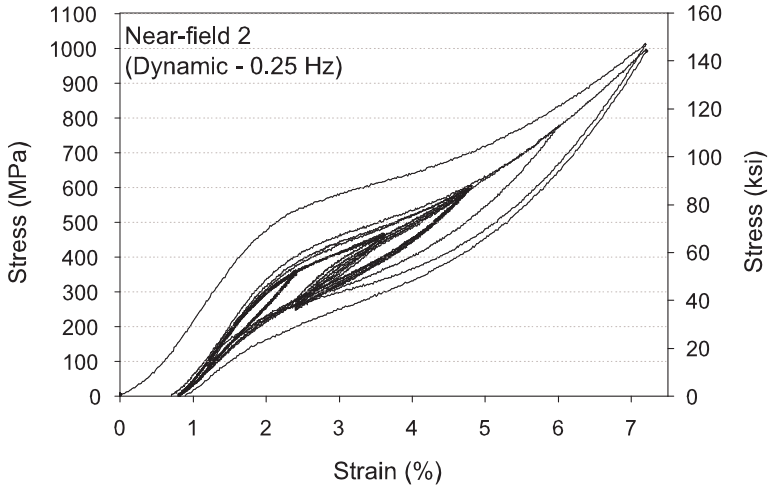

D-5(b):

Figure D-5: 0.25 Hz dynamic near-field loading stress-strain plot for the NiTi wire: (a) test 1 and (b) test 2.

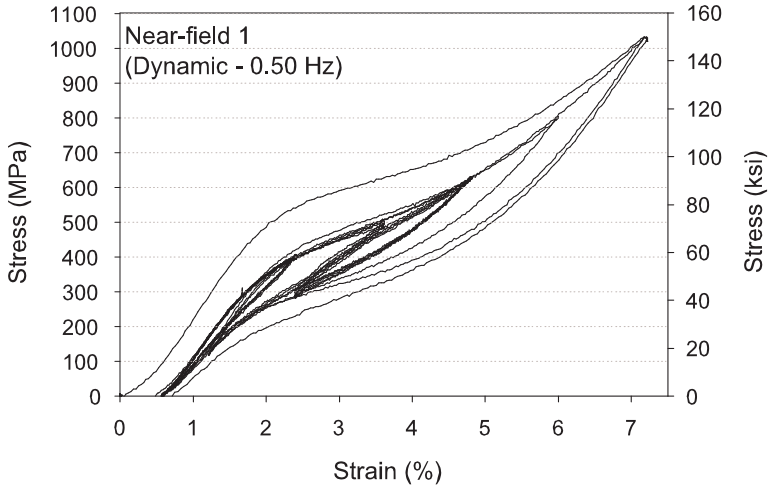

D-6(a):

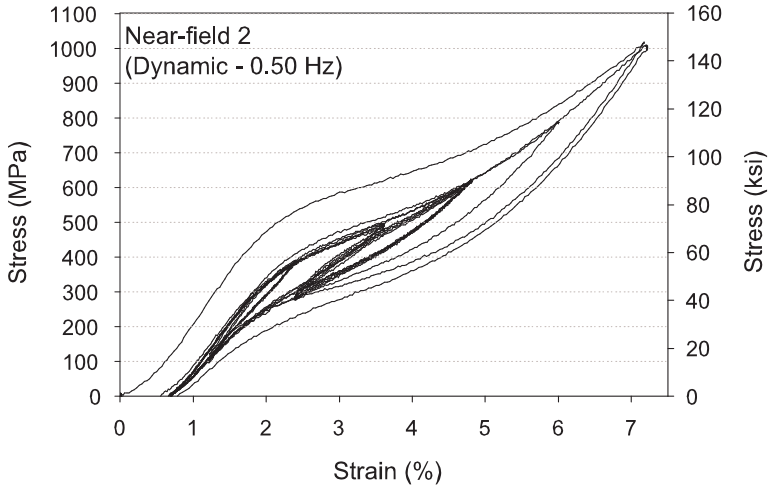

D-6(b):

Figure D-6: 0.5 Hz dynamic near-field loading stress-strain plot for the NiTi wire: (a) test 1 and (b) test 2.

APPENDIX E

STATISTICAL ANALYSIS STRESS-STRAIN RESULTS

Given the focus on performance-based seismic design in structural engineering, it is becoming increasingly more important to account for uncertainties and variabilities in structural systems. This includes the variability in material properties. In order to conduct such reliability type studies, distributions of the SMA properties need to be available. In order to address this need, Chapter 5 presents a statistics study of the cyclic properties of 30 NiTi wires specimens tested under increasing strain cycles at a loading rate of 0.5 Hz. The corresponding stress-strain curves for each of the specimens are presented in Figures E-1 to E-15. The stress-strain curves are grouped in sets of two. All specimens are tested under the same conditions.

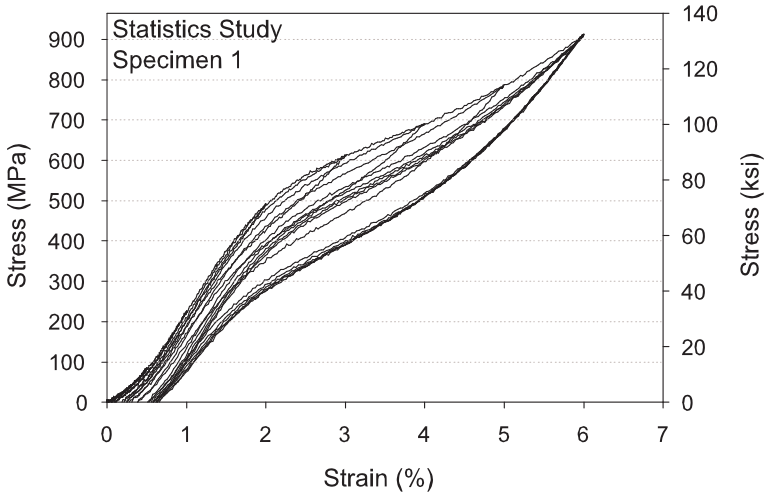

E-1(a):

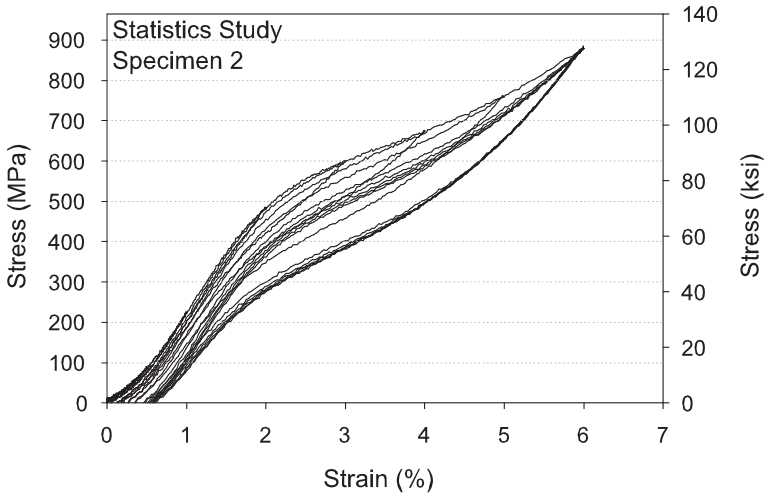

E-1(b):

Figure E-1: Statistics study stress-strain plots for the NiTi wire: (a) Specimen 1 and (b) Specimen 2.

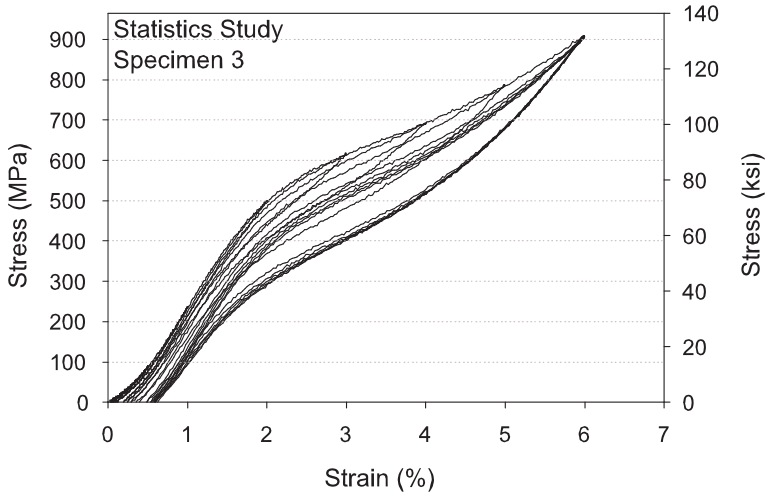

E-2(a):

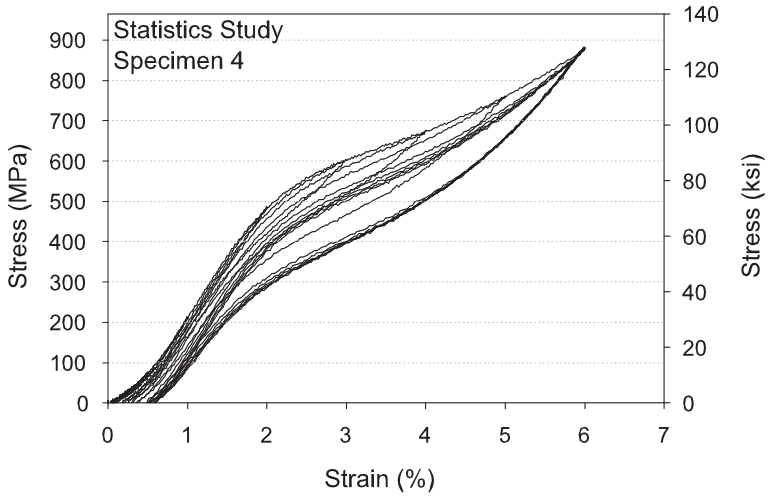

E-2(b):

Figure E-2: Statistics study stress-strain plots for the NiTi wire: (a) Specimen 3 and (b) Specimen 4.

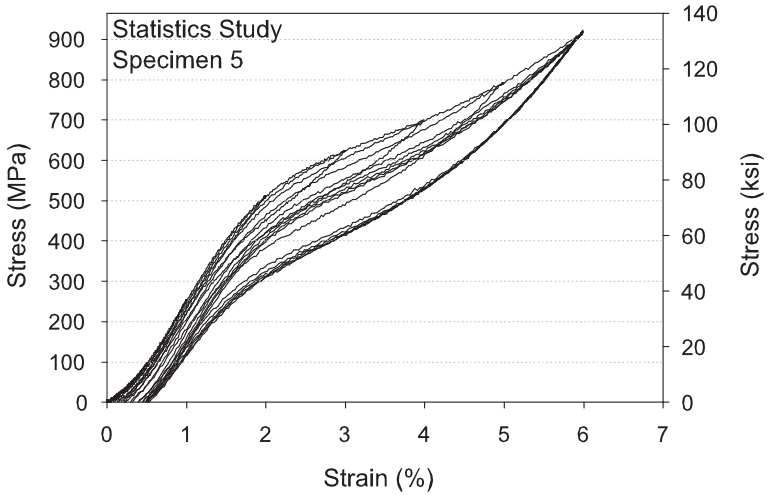

E-3(a):

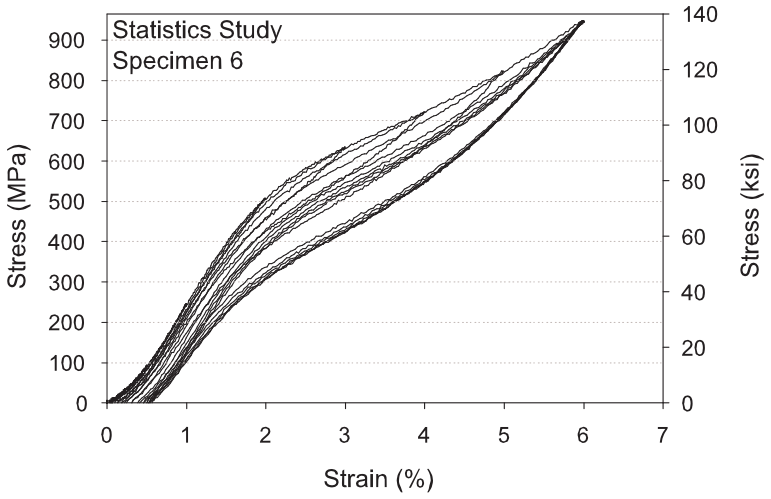

E-3(b):

Figure E-3: Statistics study stress-strain plots for the NiTi wire: (a) Specimen 5 and (b) Specimen 6.

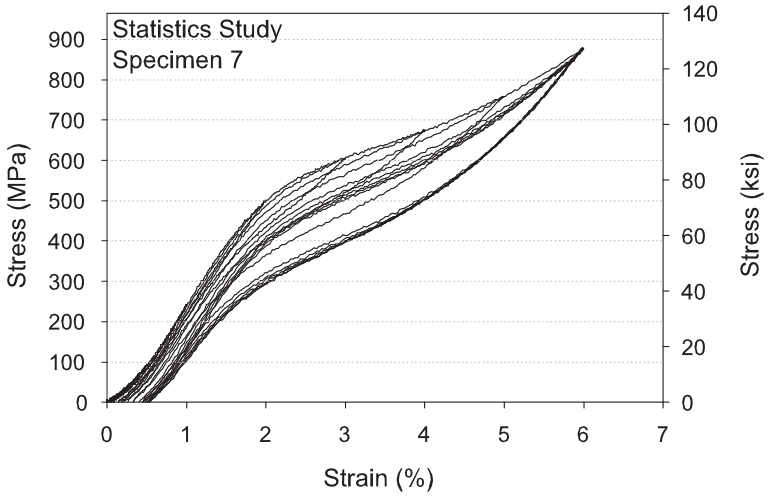

E-4(a):

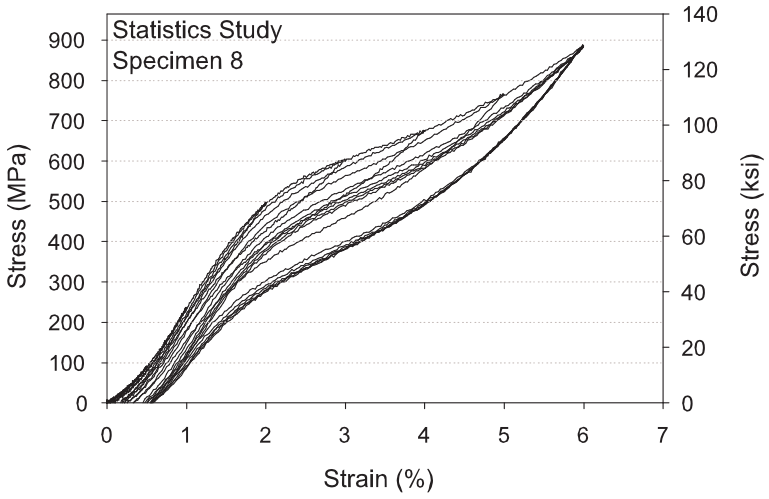

E-4(b):

Figure E-4: Statistics study stress-strain plots for the NiTi wire: (a) Specimen 7 and (b) Specimen 8.

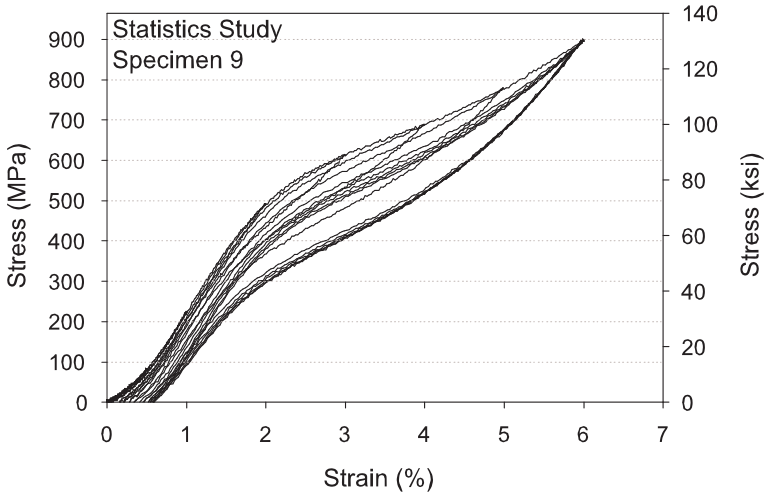

E-5(a):

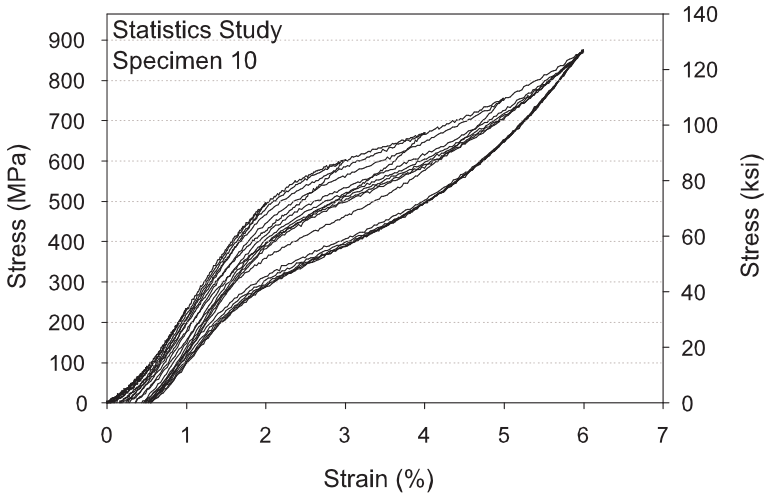

E-5(b):

Figure E-5: Statistics study stress-strain plots for the NiTi wire: (a) Specimen 9 and (b) Specimen 10.

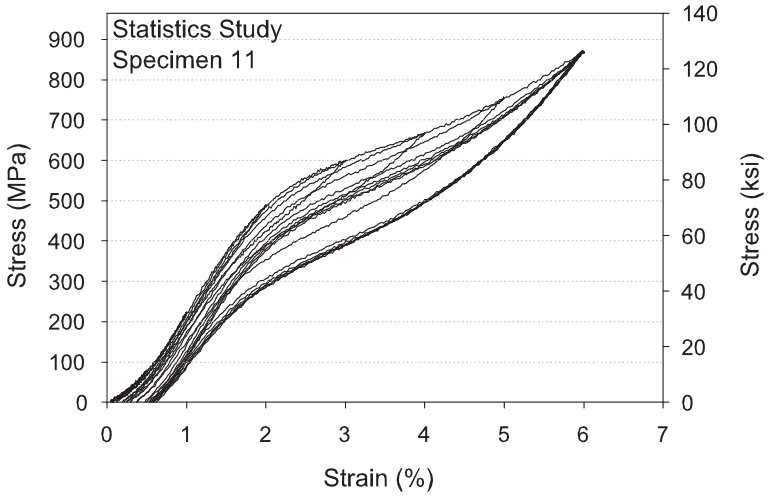

E-6(a):

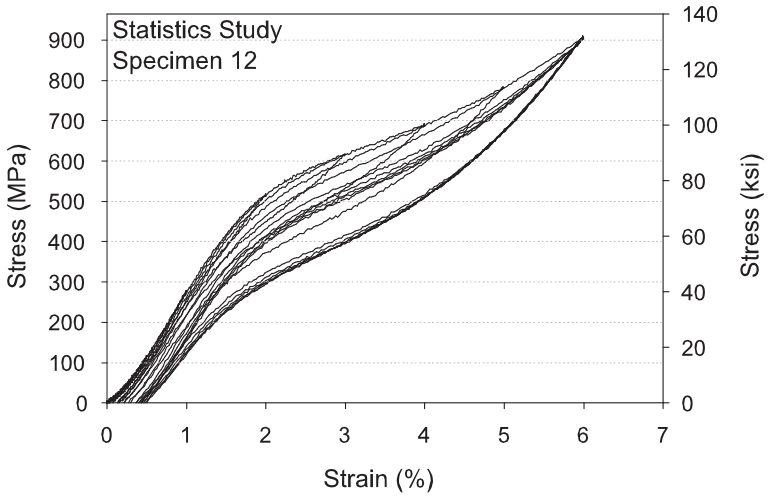

E-6(b):

Figure E-6: Statistics study stress-strain plots for the NiTi wire: (a) Specimen 11 and (b) Specimen 12.

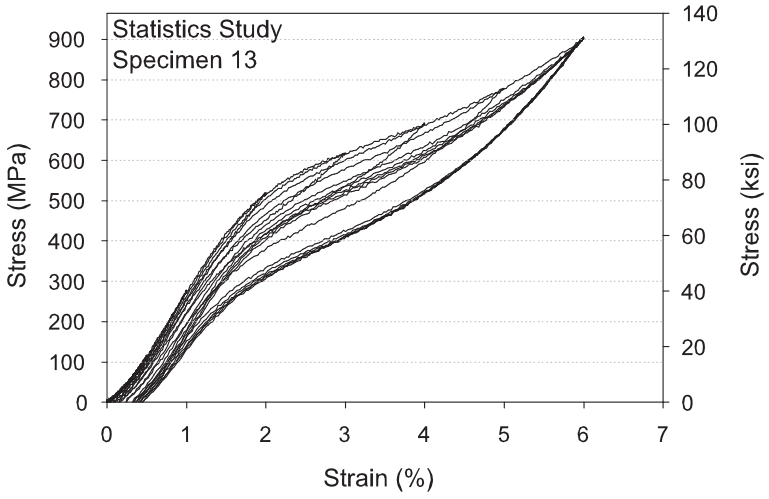

E-7(a):

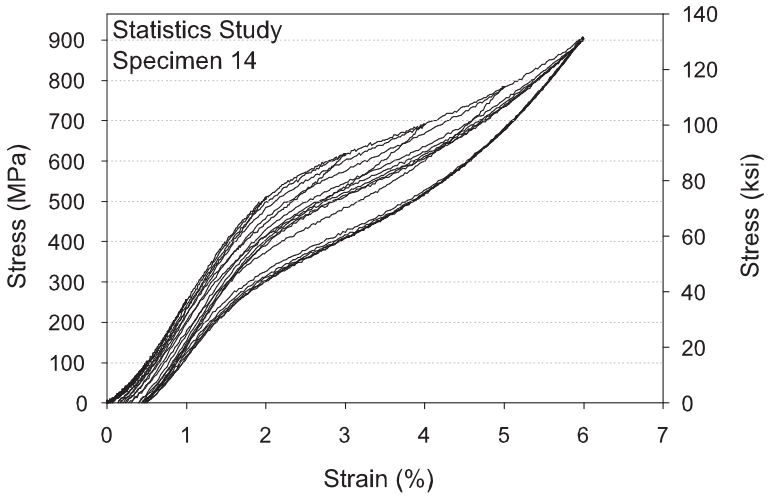

E-7(b):

Figure E-7: Statistics study stress-strain plots for the NiTi wire: (a) Specimen 13 and (b) Specimen 14.

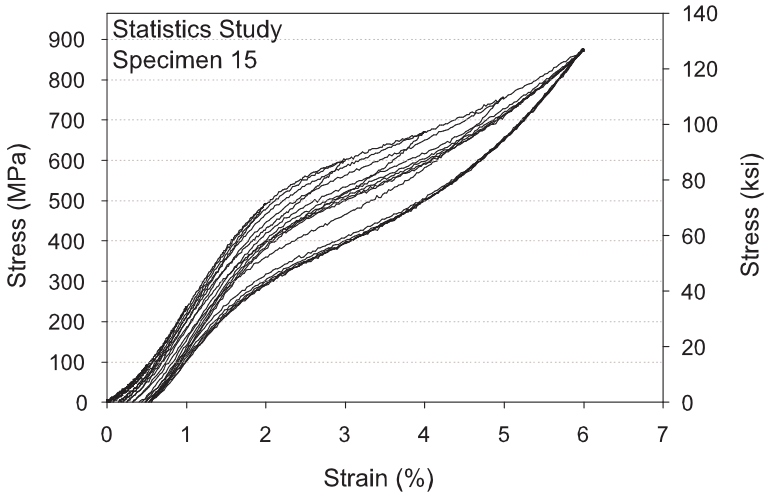

E-8(a):

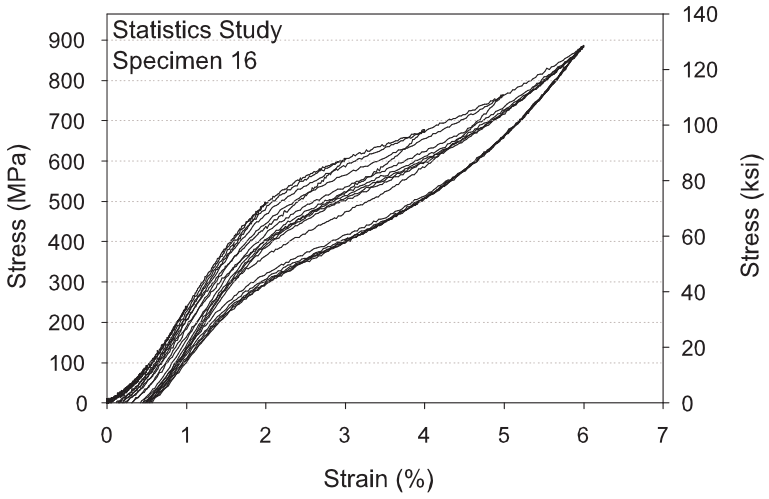

E-8(b):

Figure E-8: Statistics study stress-strain plots for the NiTi wire: (a) Specimen 15 and (b) Specimen 16.

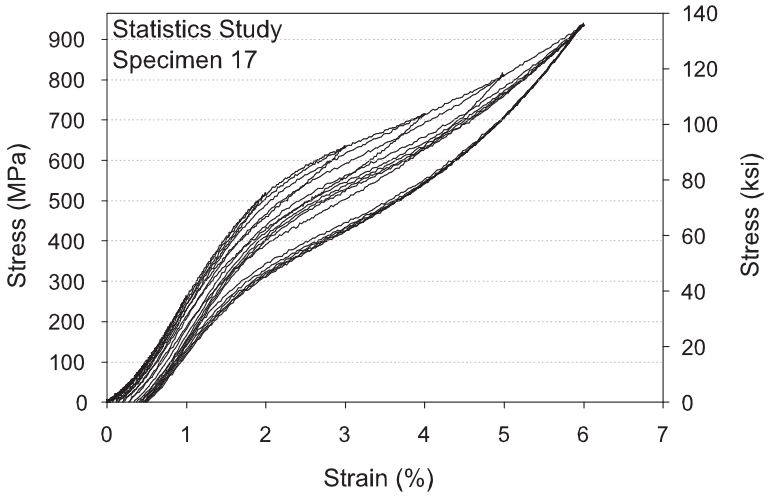

E-9(a):

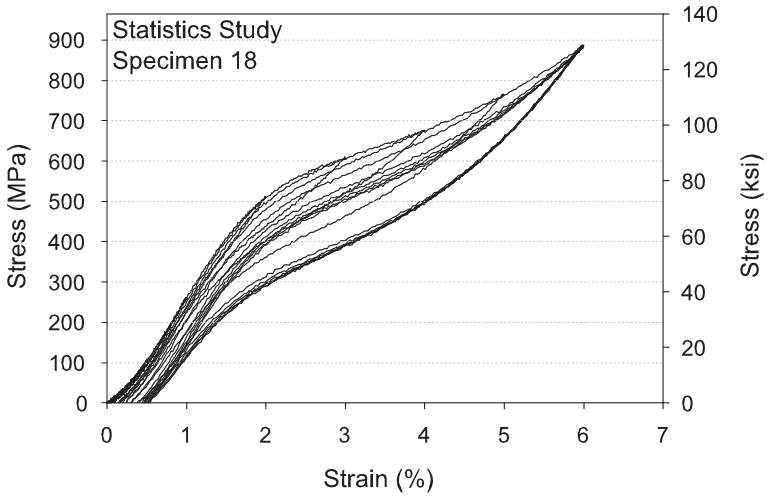

E-9(b):

Figure E-9: Statistics study stress-strain plots for the NiTi wire: (a) Specimen 17 and (b) Specimen 18.

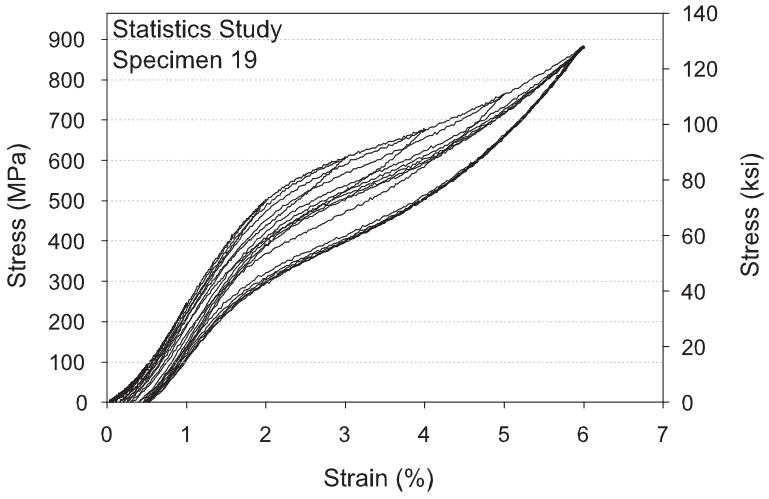

E-10(a):

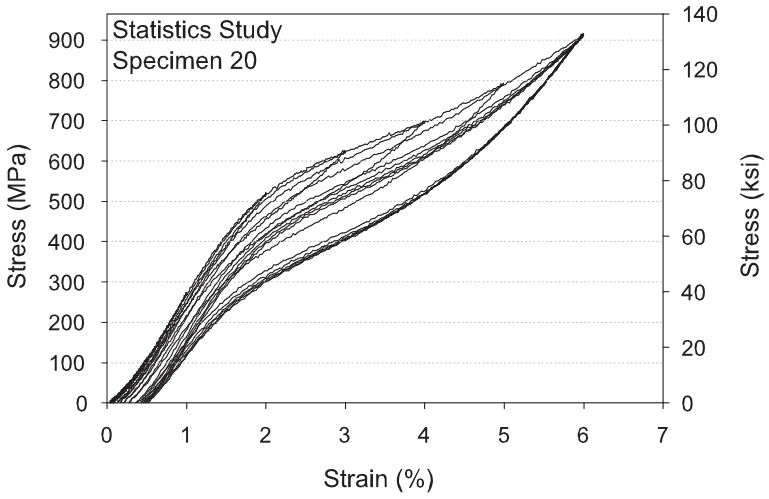

E-10(b):

Figure E-10: Statistics study stress-strain plots for the NiTi wire: (a) Specimen 19 and (b) Specimen 20.

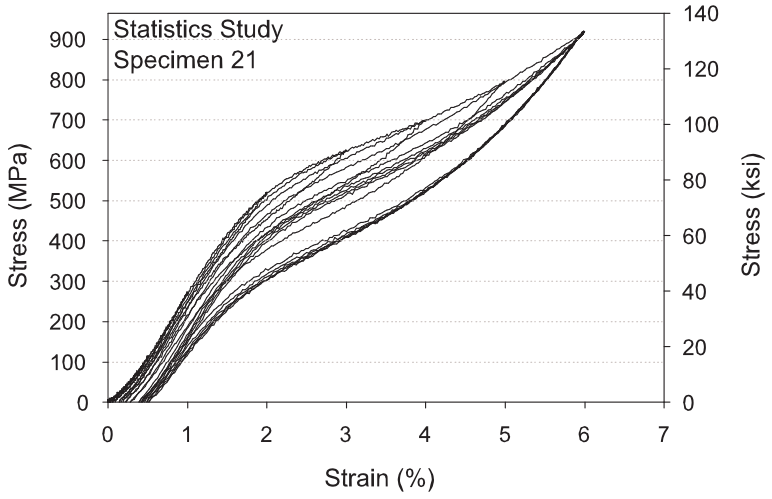

E-11(a):

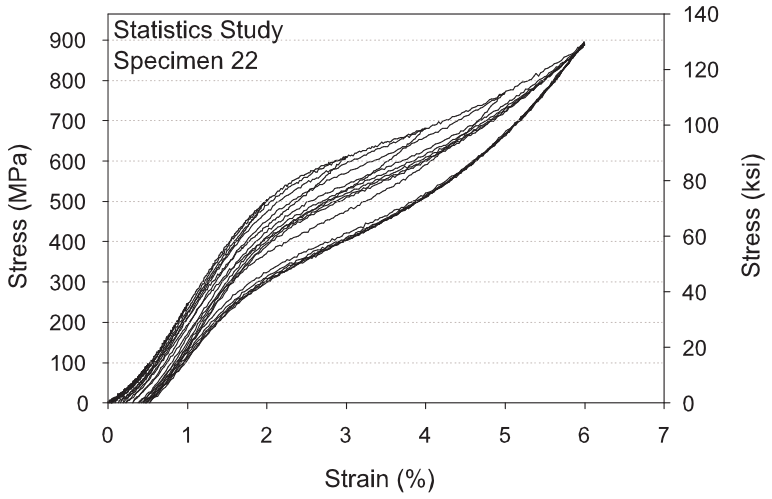

E-11(b):

Figure E-11: Statistics study stress-strain plots for the NiTi wire: (a) Specimen 21 and (b) Specimen 22.

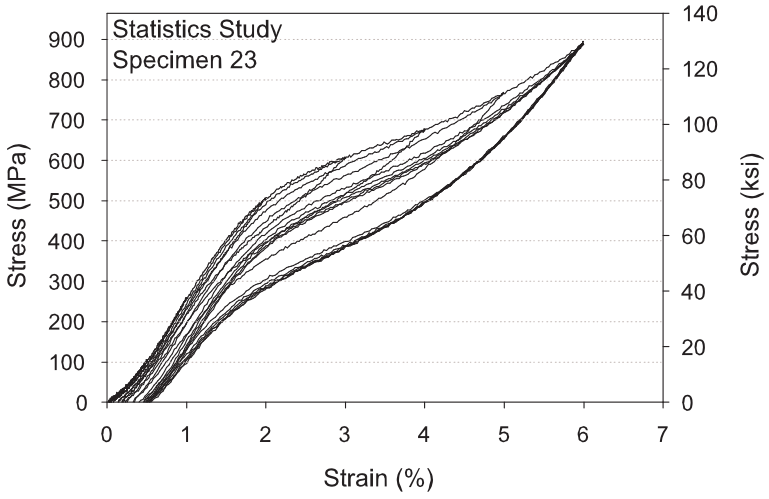

E-12(a):

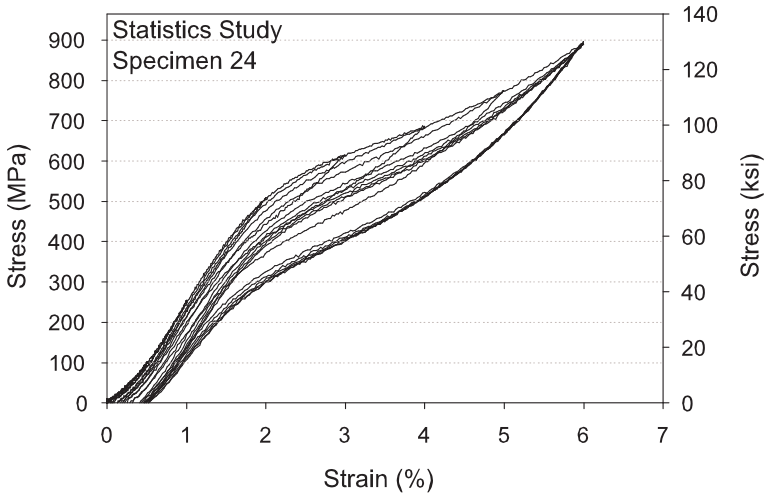

E-12(b):

Figure E-12: Statistics study stress-strain plots for the NiTi wire: (a) Specimen 23 and (b) Specimen 24.

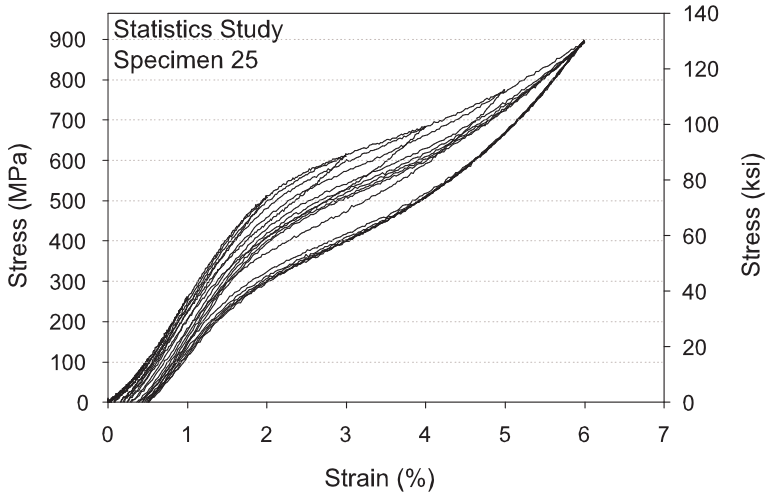

E-13(a):

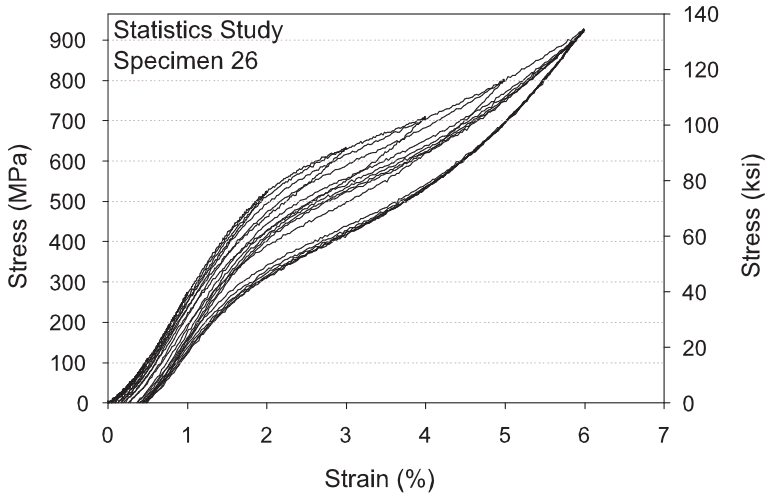

E-13(b):

Figure E-13: Statistics study stress-strain plots for the NiTi wire: (a) Specimen 25 and (b) Specimen 26.

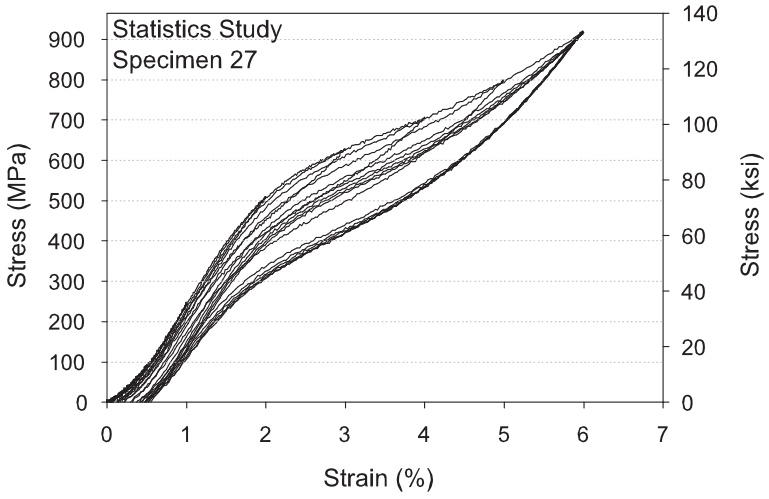

E-14(a):

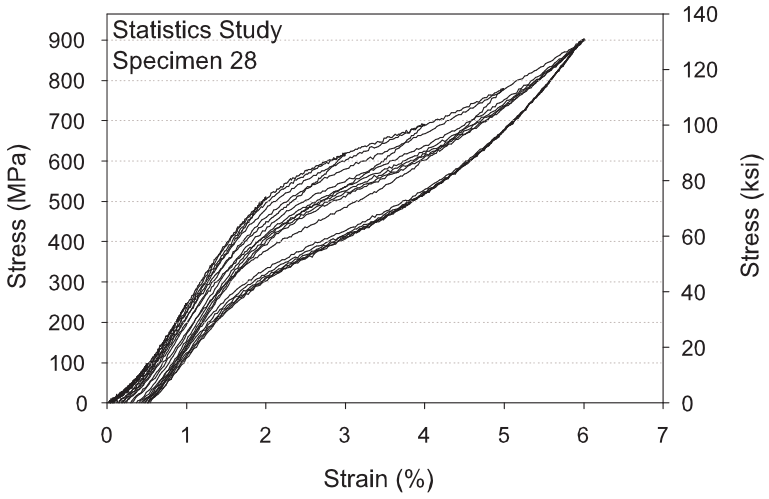

E-14(b):

Figure E-14: Statistics study stress-strain plots for the NiTi wire: (a) Specimen 27 and (b) Specimen 28.

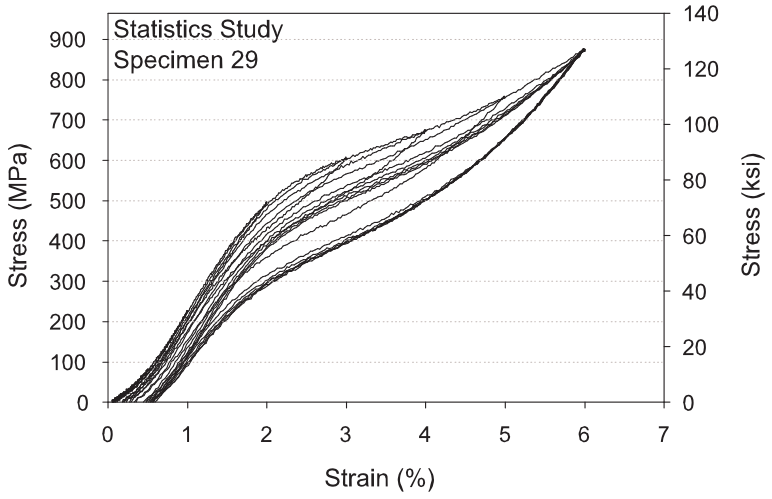

E-15(a):

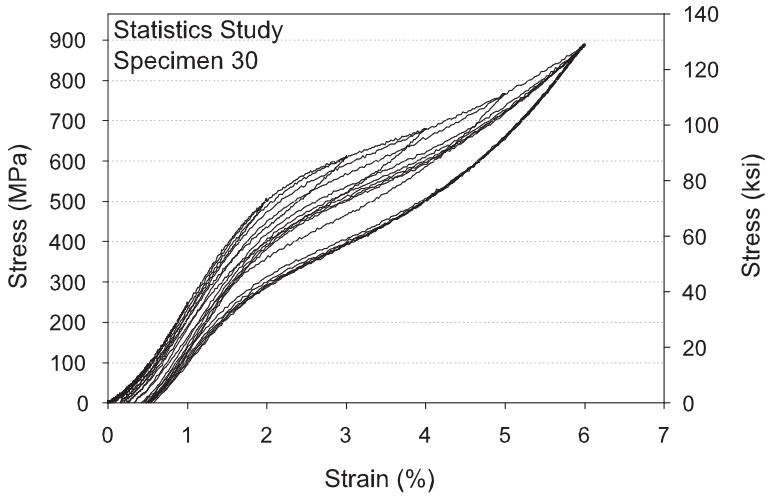

E-15(b):

Figure E-15: Statistics study stress-strain plots for the NiTi wire: (a) Specimen 29 and (b) Specimen 30.

APPENDIX F

SAC GROUND MOTIONS

Table F-1 and Table F-2 provide details on the 10% probability of exceedance in 50 year ground motions (LA 10 in 50) and 2% probability of exceedance in 50 year ground motions (LA 2 in 50) developed for Los Angles, CA as part of the FEMA/SAC steel project, respectively (Somerville et al., 1997). These motions are used in both the SDOF study used to compare the simplified SMA model to the trigger-line SMA model and the analytical study of braced frames with either steel or SMA braces discussed in Chapter 6.

Table F-1: Details in Regards to the LA 10 in 50 Ground Motions

EQ	Description	Earthquake Magnitude	Distance (km)	PGA (g)
LA01	fn Imperial Valley, 1940, El Centro	6.9	10.0	0.46
LA02	fp Imperial Valley, 1940, El Centro	6.9	10.0	0.68
LA03	fn Imperial Valley, 1979, Array #05	6.5	4.1	0.39
LA04	fp Imperial Valley, 1979, Array #05	6.5	4.1	0.49
LA05	fn Imperial Valley, 1979, Array #06	6.5	1.2	0.30
LA06	fp Imperial Valley, 1979, Array #06	6.5	1.2	0.23
LA07	fn Landers, 1992, Barstow	7.3	36.0	0.42
LA08	fp Landers, 1992, Barstow	7.3	36.0	0.43
LA09	fn Landers, 1992, Yermo	7.3	25.0	0.52
LA10	fp Landers, 1992, Yermo	7.3	25.0	0.36
LA11	fn Loma Prieta, 1989, Gilroy	7.0	12.0	0.67
LA12	fp Loma Prieta, 1989, Gilroy	7.0	12.0	0.97
LA13	fn Northridge, 1994, Newhall	6.7	6.7	0.68
LA14	fp Northridge, 1994, Newhall	6.7	6.7	0.66
LA15	fn Northridge, 1994, Rinaldi RS	6.7	7.5	0.53
LA16	fp Northridge, 1994, Rinaldi RS	6.7	7.5	0.58
LA17	fn Northridge, 1994, Symlar	6.7	6.4	0.57
LA18	fp Northridge, 1994, Symlar	6.7	6.4	0.82
LA19	fn North Palm Springs, 1986	6.0	6.7	1.02
LA20	fp North Palm Springs, 1986	6.0	6.7	0.99

Table F-2: Details in Regards to the LA 2 in 50 Ground Motions

EQ	Description	Earthquake Magnitude	Distance (km)	PGA (g)
LA21	fn Kobe, 1995	6.9	3.4	1.28
LA22	fp Kobe, 1995	6.9	3.4	0.92
LA23	fn Loma Prieta, 1989	7.0	3.5	0.42
LA24	fp Loma Prieta, 1989	7.0	3.5	0.47
LA25	fn Northridge, 1994	6.7	7.5	0.87
LA26	fp Northridge, 1994	6.7	7.5	0.94
LA27	fn Northridge, 1994	6.7	6.4	0.93
LA28	fp Northridge, 1994	6.7	6.4	1.33
LA29	fn Tabas, 1974	7.4	1.2	0.81
LA30	fp Tabas, 1974	7.4	1.2	0.99
LA31	fn Elysian Park (simulated)	7.1	17.5	1.30
LA32	fp Elysian Park (simulated)	7.1	17.5	1.19
LA33	fn Elysian Park (simulated)	7.1	10.7	0.78
LA34	fp Elysian Park (simulated)	7.1	10.7	0.68
LA35	fn Elysian Park (simulated)	7.1	11.2	0.99
LA36	fp Elysian Park (simulated)	7.1	11.2	1.10
LA37	fn Palos Verdes (simulated)	7.1	1.5	0.71
LA38	fp Palos Verdes (simulated)	7.1	1.5	0.78
LA39	fn Palos Verdes (simulated)	7.1	1.5	0.50
LA40	fp Palos Verdes (simulated)	7.1	1.5	0.63

References

Abujudom, D. N., Thoma, P. E., and Fariabi, S. (1990). "The effect of cold work and heat treatment on the phase transformations of near equiatomic NiTi shape memory alloy." *Materials Science Forum*, 56-58, 565–570.

Adachi, Y. and Unjoh, S. (1999). "Development of shape memory alloy damper for intelligent bridge systems." *SPIE Proceedings on Smart Systems for Bridges, Structures, and Highways*, Vol. 3671, Newport Beach, CA. 31–42.

Aizawa, S., Kakizawa, T., and Higashino, M. (1998). "Case studies of smart materials for civil structures." *Smart Materials and Structures*, 7, 617–626.

Allafi, J. K., Ren, X., and Eggeler, G. (2002). "The mechanism of multistage martensistic transformations in aged Ni-rich NiTi shape memory alloys." *Acta Materialia*, 50(4), 793–803.

Andrawes, B. and DesRoches, R. (2005). "Unseating prevention for multiple frame bridges using superelastic devices." *Smart Materials and Structures*, 14, S60–S67.

Ang, A. H.-S. and Tang, W. H. (1975). *Probability Concepts in Engineering Planning and Design Vol. I Basic Principles*. John Wiley and Sons, New York.

Ang, A. H.-S. and Tang, W. H. (1984). *Probability Concepts in Engineering Planning and Design Vol. II Decision, Risk, and Reliability*. John Wiley and Sons, New York.

Asai, M. and Suzuki, Y. (2000). "Applications of shape memory alloys in Japan." *Materials Science Forum*, 327, 17–22.

ASTM (2003). "Standard test methods for tension testing of metallic materials." *Designation: E8-03*, ASTM International, 1–23.

Auricchio, F. and Sacco, E. (1997). "A one-dimensional model for superelastic shape-memory alloys with different properties between martensite and austenite." *International Journal of Non-Linear Mechanics*, 32, 1101–1114.

Baratta, A. and Corbi, O. (2002). "On the dynamic behaviour of elastic-plastic structures equipped with pseudoelastic SMA reinforcements." *Computational Materials Science*, 25, 1–13.

Barbero-Bernal, L. I. (2004). "Cyclic behavior of superelastic Nickel-Titanium and Nickel-Titanium-Chromium shape memory alloys," Master's Thesis, Georgia Insitute of Technology.

Beauchamp, C. H., Nadolink, R. H., Dickinson, S. C., and Dean, L. M. (1992). "Shape memory alloy adjustable camber (SMAAC) control surface." *Proceedings of the First European Conference on Smart Structures and Materials*, Glasgow, Scotland.

Birman, V. (1997). "Review of mechanics of shape memory alloy structures." *Applied Mechanics Review*, 50(11), 629–645.

Bo, Z. and Lagoudas, D. C. (1994). "Comparison of different thermomechanical models for shape memory alloys." *Proceedings of the 1994 International Mechanical Engineering Congress and Exposition, Nov 6-11 1994*, Vol. 45 of *American Society of Mechanical Engineers, Aerospace Division (Publication) AD*, Chicago, IL, USA. ASME, New York, NY, USA, 9–19.

Bram, M., Ahmad-Khanlou, A., Heckmann, A., Fuchs, B., Buchkremer, H. P., and Stover, D. (2002). "Powder metallurgical fabrication processes for NiTi shape memory alloy parts." *Materials Science and Engineering A*, 337(1-2), 254–263.

Bruno, S. and Valente, C. (2002). "Comparative response analysis of conventional and innovative seismic protection strategies." *Earthquake Engineering and Structural Dynamics*, 31, 1067–1092.

Casciati, F. and Faravelli, L. (2004). "Experimental characterisation of Cu-based shape memory alloy toward its exploitation in passive control devices." *Journal de Physique IV*, 115, 299–306.

Castellano, M. G., Indirli, M., and Martelli, A. (2001). "Progress of application, research and development and design guidelines for shape memory alloy devices for cultural heritage structures in Italy." *SPIE Proceedings*, Vol. 4330. 250–261.

Chandra, R. (2001). "Active shape control of composite blades using shape memory actuation." *Smart Materials and Structures*, 10(5), 1018–1024.

Chopra, A. K. (2001). *Dynamics of Structures: Theory and Applications to Earthquake Engineering*. Prentice Hall, Upper Saddle River, NJ, 2nd edition.

Chorbak, D., Str, D., and Morawiec, H. (2003). "Effect of early stages of precipitation and recovery on the multi-step transformation in deformed and annealed near-equiatomic NiTi alloy." *Scripta Materialia*, 48, 571–576.

Clark, P. W., Aiken, I. D., Kelly, J. M., Higashino, M., and Krumme, R. C. (1995). "Experimental and analytical studies of shape memory alloy dampers for structural control." *SPIE Proceedings*, Vol. 2445. 241–251.

Comartin, C., Green, M., and Tubbesing, S. (1995). "The Hyogo-Ken Nanbu Earthquake." *Preliminary Reconnaissance Report*, Earthquake Engineering Research Institute, Oakland, CA.

Corbi, O. (2003). "Shape memory alloys and their application in structural oscillations attenuation." *Simulation Modelling Practice and Theory*, 11, 387–402.

Croci, G. (2001). "Strengthening the Basilica of St Francis of Assisi after the September 1997 earthqauke." *Structural Engineering International*, 3, 207–210.

Cui, L., Zheng, Y., Li, Y., and Zhao, X. (2002). "Stress-Strain characteristics of TiNi shape-memroy alloy wires after constrained thermal cycles." *Materials Science Forum*, 394-395, 261–264.

DesRoches, R. and Delemont, M. (2002). "Seismic retrofit of simply supported bridges using shape memory alloys." *Engineering Structures*, 24, 325–332.

DesRoches, R., McCormick, J., and Delemont, M. (2004). "Cyclic properties of superelastic shape memory alloy wires and bars." *Journal of Structural Engineering*, 130(1), 38–46.

Dobovsek, I. (2001). "Phenomenological modelign of shape memory effect using the concept of orientational back stress." *Journal de Physique IV*, 11(8), Pr8–59–Pr8–64.

Dolce, M. and Cardone, D. (2001). "Mechanical behaviour of shape memory alloys for seismic applications 2. Austenite NiTi wires subjected to tension." *International Journal of Mechanical Sciences*, 43, 2657–2677.

Dolce, M., Cardone, D., and Marnetto, R. (2000). "Implementation and testing of passive control devices based on shape memory alloys." *Earthquake Engineering and Structural Dynamics*, 29, 945–968.

Dolce, M., Cardone, D., Ponzo, F. C., and Valente, C. (2005). "Shaking table tests on reinforced concrete frames without and with passive control systems." *Earthquake Engineering and Structural Dynamics*, 34, 1687–1717.

Duerig, T. W., Melton, K. N., Stöckel, D., and Wayman, C. M. (1990a). *Engineering aspects of shape memory alloys*. Butterworth-Heinemann, Boston, MA.

Duerig, T. W. and Zadno, G. (1990b). "An engineer's perspective of pseudoelasticity." *Engineering aspects of shape memory alloys*, T. W. Duerig, K. N. Melton, D. Stöckel, and C. M. Wayman, eds., Butterworth-Heinemann, Boston, MA, 369–393.

Eguchi, R. T., Goltz, J. D., Taylor, C. E., Chang, S. E., Flores, P. J., Johnson, L. A., Seligson, H. A., and Blais, N. C. (1998). "Direct economic losses in the Northridge Earthquake: A three-year post-event perspective." *Earthquake Spectra*, 14(2), 245–264.

FEMA (2000). "Recommended Seismic Design Provisions for New Moment Frame Buildings." *Report No. FEMA 350*, Federal Emergency Management Agency.

Frick, C. P., Ortega, A. M., Tyber, J., A.El.M., M., Maier, H. J., Liu, Y., and Gall, K. (2005). "Thermal processing of polycrystalline NiTi shape memory alloys." *Materials Science and Engineering A*, 405, 34–47.

Frick, C. P., Ortega, A. M., Tyber, J., Gall, K., and Maier, H. J. (2004). "Multiscale structure and properties of cast and deformation processed polycrystalline NiTi shape-memory alloys." *Metallurgical and Materials Transactions A: Physical Metallurgy and Materials Science*, 35 A(7), 2013–2025.

Fugazza, D. (2003). "Shape-Memory alloy devices in earthquake engineering: Mechanical properties, constitutive modelling and numerical simulations," Master's Thesis, University of Pavia, Italy.

Gall, K. and Sehitoglu, H. (1999b). "The role of texture in tension-compression asymmetry in polycrystalline NiTi." *International Journal of Plasticity*, 15(1), 69–92.

Gall, K., Sehitoglu, H., Anderson, R., Karaman, I., Chumlyakov, Y. I., and Kireeva, I. V. (2001). "On the mechanical behavior of single crystal NiTi shape memory alloys and related polycrystalline phenomenon." *Materials Science and Engineering*, A317, 85–92.

Gall, K., Sehitoglu, H., Chumlyakov, Y. I., and Kireeva, I. V. (1999a). "Tension-Compression asymmetry of the stress-strain response in aged single crystal and polycrystalline NiTi." *Acta Metallurgica*, 47(4), 1203–1217.

Gall, K., Sehitoglu, H., Chumlyakov, Y. I., Kireeva, I. V., and Maier, H. J. (1999c). "The influence of aging on critical transformation stress levels and martensite start temperatures in NiTi: Part I - aged microstructure and micro-mechancal modeling." *Journal of Engineering Materials and Technology*, 121(1), 19–27.

Gall, K., Sehitoglu, H., Chumlyakov, Y. I., Kireeva, I. V., and Maier, H. J. (1999d). "The influence of aging on critical transformation stress levels and martensite start temperatures in NiTi: Part II - Discussion of experimental results." *Journal of Engineering Materials and Technology*, 121(1), 28–37.

Gall, K., Sehitoglu, H., Chumlyakov, Y. I., Zuev, Y. L., and Karaman, I. (1998). "The role of coherent precipitates in martensitic transformation in single crystal and polycrystalline Ti-50.8at%Ni." *Scripta Materialia*, 39(6), 699–705.

Gong, J. M., Tobushi, H., Takata, K., Okumura, K., and Endo, M. (2002). "Cyclic superelastic deformation of TiNi shape-memory alloy." *Materials Science Forum*, 394-395, 245–248.

Graesser, E. J. and Cozzarelli, F. A. (1991). "Shape-Memory alloys as new materials for aseismic isolation." *Journal of Engineering Mechanics*, 117(11), 2590–2608.

Hamburger, R. O., Foutch, D. A., and Cornell, C. A. (2003). "Translating research to practice: FEMA/SAC performance-based design procedures." *Earthquake Spectra*, 19(2), 255–267.

Han, Y.-L., Li, Q. S., Li, A.-Q., Leung, A. T., and Lin, P.-H. (2003). "Structural vibration control by shape memory alloy damper." *Earthquake Engineering and Structural Dynamics*, 32, 483–494.

Han, Y.-L., Xing, D.-J., Xiao, E.-T., and Li, A.-Q. (2005). "NiTi-wire shape memory alloy dampers to simultaneously damp tension, compression, and torsion." *Journal of Vibration and Control*, 11(8), 1067–1084.

Higashino, M., Aizawa, S., Clark, P. W., Whittaker, A. S., Aiken, I. D., and Kelly, J. M. (1996). "Experimental and analytical studies of structural control system using shape memory alloy." *Second International Workshop on Structural Control*, Hong Kong.

Hines, W. W., Montgomery, Douglas, C., Goldsman, D. M., and Borror, C. M. (2003). *Probability and Statistics 4th Edition*. John Wiley and Sons, New York.

Hodgson, D. E. (2002). "Damping applications of shape-memory alloys." *Materials Science Forum*, 394-395, 69–74.

Hori, T., Tobushi, H., Ohashi, Y., and Saida, H. (1992). "Cyclic deformation of a bias-type two-way shape memory component using TiNi alloy." *JSME International Journal*, 35(2), 179–184.

Hsu, S. E., Yeh, M. T., Hsu, I. C., Chang, S. K., Dai, Y. C., and Wang, J. Y. (2000). "Pseudo-elasticity and shape memory effect on the TiNiCoV alloy." *Materials Science Forum*, 327, 119–122.

Indirli, M., Castellano, M. G., Clemente, P., and Martelli, A. (2001). "Demo-application of shape memory alloy devices: The rehabilitation of the S. Giorgio Church bell-tower." *SPIE Proceedings*, Vol. 4330. 262–272.

Kawaguchi, M., Ohashi, Y., and Tobushi, H. (1991). "Cyclic characteristics of pseudoelasticity of Ti-Ni alloys (Effect of maximum strain, test temperature and shape memory processing temperature)." *JSME International Journal*, 34(1), 76–82.

Kolomytsev, V. and Kozlov, A. (1998). "Effect of the strain rate and sample size on features of non-linear deformation behaviour in TiNi-based ribbons and wires." *Proceeding of XXYIII Symposium of UIA*.

Krawinkler, H., Gupta, A., Medina, R., and Luco, N. (2000). "Loading Histories for Seimsic Performance Testing of SMRF Components and Assemblies." *Report No. SAC/BD-00/10*, SAC Joint Venture.

Lagoudas, D. C., Bo, Z., and Qidwai, M. A. (1996). "A unified thermodynamic constitutive model for SMA and finite element analysis of active metal matrix composites." *Mechanics of Composite Materials and Structures*, 3, 153–179.

Leo, P. H., Shield, T. W., and Bruno, O. P. (1993). "Transient heat transfer effects on the pseudoelastic behavior of shape-memory wires." *Acta Metallurgica*, 41(8), 2477–2485.

Leon, R. T., DesRoches, R., Ocel, J., and Hess, G. (2001). "Innovative beam column connections using shape memory alloys." *SPIE Proceedings*, Vol. 4330. 227–237.

Lexcellent, C., Leclercq, S., Gabry, B., and Bourbon, G. (2000). "The two way shape memory effect of shape memory alloys: an experimental study and a phenomenological model." *International Journal of Plasticity*, 16(10), 1155–1168.

Li, H., Liu, M., and Ou, J. (2004). "Vibration mitigation of a stay cable with one shape memory alloy damper." *Structural Control and Health Monitoring*, 11, 21–36.

Liang, C. and Rogers, C. A. (1997). "One-Dimensional thermomechanical constitutive relations for shape memory alloys." *Journal of Intelligent Material Systems and Structures*, 8(4), 285–302.

Malovrh, B. and Gandhi, F. (2001). "Mechanism-Based phenomenological models for the pseudoelastic hysteresis behavior of shape memory alloys." *Journal of Intelligent Material Systems and Structures*, 12(1), 21–30.

Martńez-Rueda, J. E. (2002). "On the evolution of energy dissipation devices for seismic design." *Earthquake Spectra*, 18(2), 309–346.

Masuda, A. and Noori, M. (2002). "Optimization of hysteretic characteristics of damping devices based on pseudoelastic shape memory alloys." *International Journal of Non-Linear Mechanics*, 37, 1375–1386.

Matsumoto, H. (1991). "Appearance of an intermediate phase with thermal cycling on the transformation of NiTi." *Journal of Materials Science Letters*, 10, 408–410.

McKenna, F. and Fenves, G. (2004). "OpenSees command language manual." Pacific Earthquake Engineering Research Center, Version 1.5.2.

Melton, K. N. (1990). "Ni-Ti based shape memory alloys." *Engineering aspects of shape memory alloys*, T. W. Duerig, K. N. Melton, D. Stckel, and C. M. Wayman, eds., Butterworth-Heinemann, Boston, MA, 21–33.

Melton, K. N. and Mercier, O. (1981). "The mechanical properties of NiTi-based shape memory alloys." *Acta Metallurgica*, 29, 393–398.

Michutta, J., Carroll, M. C., Yawny, A., Somsen, C., Neuking, K., and Eggeler, G. (2004). "Martensitic phase transformation in Ni-rich NiTi single crystals with one family of Ni4Ti3 precipitates." *Materials Science and Engineering*, A378(1-2), 152–156.

Miller, D. A. and Lagoudas, D. C. (2001). "Influence of cold work and heat treatment on the shape memory effect and plastic strain development of NiTi." *Materials Science and Engineering A*, 308(1-2), 161–175.

MINITAB (2004). "Meet MINITAB release 14 for windows." Minitab Inc. Release 14.

Miyazaki, S. (1990). "Thermal and stress cycling effects and fatigue properties of Ni-Ti alloys." *Engineering aspects of shape memory alloys*, T. W. Duerig, K. N. Melton, D. Stckel, and C. M. Wayman, eds., Butterworth-Heinemann, Boston, MA, 394–413.

Miyazaki, S., Imai, T., Igo, Y., and Otsuka, K. (1986a). "Effect of cyclic deformation on the pseudoelasticity characteristics of Ti-Ni." *Metallurgical Transactions A*, 17A, 115–120.

Miyazaki, S., Imai, T., Otsuka, K., and Suzuki, Y. (1981b). "Lüders-like deformation observed in the transformation pseudoelasticity of a Ti-Ni alloy." *Scripta Metallurgica*, 15, 853–856.

Miyazaki, S. and Otsuka, K. (1986b). "Deformation and transition behavior associated with the R-phase in Ti-Ni alloys." *Metallurgical Transactions A*, 17A, 53–63.

Miyazaki, S., Otsuka, K., and Suzuki, Y. (1981a). "Transformation pseudoelasticity and deformation behavior in a Ti-50.6at%Ni alloy." *Scripta Metallurgica*, 15, 287–292.

Müller, I. and Huibin, X. (1991). "On the pseudo-elastic hysteresis." *Acta Metallurgica*, 39(3), 263–271.

Nakashima, M., Inoue, K., and Tada, M. (1998). "Classification of damage to steel buildings observed in the 1995 Hyogoken-Nanbu earthquake." *Engineering Structures*, 20(4-6), 271–281.

Nakashima, M., Roeder, C. W., and Maruoka, Y. (2000). "Steel moment frames for earthquakes in United States and Japan." *ASCE Journal of Structural Engineering*, 126(8), 861–868.

Neter, J., Kutner, M. H., Nachtsheim, C. J., and Wasserman, W. (1996). *Applied linear statistical models*. WCB/McGraw Hill, Boston, 4th edition.

Nishida, M. and Wayman, C. M. (1988). "Electron microscopy studies of the 'premartensitic' transformations in an aged Ti-51at%Ni shape memory alloys." *Metallography*, 21, 255–273.

NSTC (2005). "Grand challenges for disaster reduction." *A Report of the Subcommittee on Disaster Reduction*, National Science and Technology Council: Committee on Environment and Natural Resources.

Ocel, J., DesRoches, R., Leon, R. T., Hess, G. W., Krumme, R., Hayes, J. R., and Sweeney, S. (2004). "Steel beam-column connections using shape memory alloys." *Journal of Structural Engineering*, 130(5), 732–740.

Ortega, A. M., Frick, C. P., Gall, K., Tyber, J., and Maier, H. J. (2005). "Cast NiTi shape memory alloys." *Advanced Engineering Materials*, 7(6), 492–507.

Otsuka, K. and Shimizu, K. (1986). "Pseudoelasticity and shape memory effects in alloys." *International Metals Reviews*, 31(3), 93–114.

Otsuka, K. and Wayman, C. M. (1998). *Shape memory materials*. Cambridge University Press, New York.

Perkins, J. (1981). "Ti-Ni and Ti-Ni-X shape memory alloys." *Metals Forum*, 4(3), 153–163.

Piedboeuf, M. C., Gauvin, R., and Thomas, M. (1998). "Damping behaviour of shape memory alloys: strain amplitude, frequency and temperature effects." *Journal of Sound and Vibration*, 214(5), 885–901.

Renzi, E., Ranieri, N., and DeCanio, G. (2004). "Experimental verifications of seismic protection of steel and R.C. structures at Enea-Casaccia shaking tables." *13th World Conference on Earthquake Engineering*, Vancouver, B.C., Canada. Paper No. 846.

Rogers, C. A. (1995). "Rebuilding and enhancing the nations infrastructure: A role for intelligent material systems and structures." *Journal of Intelligent Material Systemes and Structures*, 6, 4–12.

Saadat, S., Noori, M., Davoodi, H., Hou, Z., Suzuki, Y., and Masuda, A. (2001). "Using NiTi SMA tendons for vibration control of coastal structures." *Smart Materials and Structures*, 10, 695–704.

Saadat, S., Salichs, J., Noori, M., Hou, Z., Davoodi, H., Bar-on, I., Suzuki, Y., and Masuda, A. (2002). "An overview of vibration and seismic applications of NiTi shape memory alloy." *Smart Materials and Structures*, 11, 218–229.

Sabelli, R. (2001). "Research on improving the design and analysis of earthquake-resistant steel-braced frames." *The 2000 NEHRP Professional Fellowship Report*, Earthquake Engineering Research Institute.

Sabelli, R., Mahin, S., and Chang, C. (2003). "Seismic Demands on Steel Braced Frame Buildings with Buckling-Restrained Braces." *Engineering Structures*, 25, 655–666.

Sabol, T. A. (2004). "An assessment of seismic design practice of steel structures in the United States since the Northridge earthquake." *Structural Design of Tall and Special Buildings: LA Tall Buildings Structural Design Council*, 13(5), 409–423.

Scherngell, H. and Kneissl, A. C. (1999). "Influence of the microstructure on the stability of the intrinsic two-way shape memory effect." *Materials Science and Engineering A*, 273-275, 400–403.

Semba, H., Okabe, N., Yamaji, T., Okita, K., and Yamauchi, K. (2005). "Axial compressive behavior of single-stage bellows of TiNi shape memory alloy for seismic applications." *Materials Science Forum*, 475-479, 2055–2058.

Serneels, A. (1999). "Shape memory alloy characterisation and optimisation." *SMST-99: Proceedings of the First European Conference on Shape Memory and Superelastic Technologies*, Antwerp Zoo, Belgium. 6–23.

Somerville, P., Smith, N., Punyamurthula, S., and Sun, J. (1997). "Development of ground motion time histories for Phase 2." *Report No. SAC-BD-97-04*, SAC Joint Venture.

Soroushian, P., Ostowari, K., Nossoni, A., and Chowdhury, B. (2001). "Repair and strengthening of concrete structures through applications of corrective posttensioning forces with shape memory alloys." *Transportation Research Record*, 1770, 20–26.

Strnadel, B., Ohashi, S., Ohtsuka, H., Ishihara, T., and Miyazaki, S. (1995a). "Cyclic stress-strain characteristics of Ti—Ni and Ti—Ni—Cu shape memory alloys." *Materials Science and Engineering A*, 202(1-2), 148–156.

Strnadel, B., Ohashi, S., Ohtsuka, H., Miyazaki, S., and Ishihara, T. (1995b). "Effect of mechanical cycling on the pseudoelasticity characteristics of Ti—Ni and Ti—Ni—Cu alloys." *Materials Science and Engineering A*, 203(1-2), 187–196.

Sweeney, S. C. and Hayes, John R., J. (1995). "Shape memory alloy dampers for seismic rehabilitation of existing buildings." *Proceedings of the 27th Joint Meeting on Wind and Seismic Effects*, Tsukuba, Japan. 317–332.

Tadaki, T., Otsuka, K., and Shimizu, K. (1988). "Shape memory alloys." *Ann. Rev. Mater. Sci.*, 18, 25–45.

Tamai, H. and Kitagawa, Y. (2002). "Pseudoelastic behavior of shape memory alloy wire and its application to seismic resistance memeber for building." *Computational Materials Science*, 25, 218–227.

Tamai, H., Kitagawa, Y., and Fukuta, T. (2004). "Application of SMA rods to exposed-type column bases in smart structural systems." *13th World Conference on Earthquake Engineering*, Vancouver, B.C., Canada. Paper No. 1884.

Tan, G. S., Suseno, T., and Liu, Y. (2002). "Mechanical hysteresis in the pseudoelasticity of Ti-50.2at%Ni." *Materials Science Forum*, 394-395, 249–252.

Tanaka, K. (1986). "A thermomechanical sketch of shape memory effect: One-dimensional tensile behavior." *Res Mechanica*, 18, 251–263.

Terriault, P., Meunier, M. A., and Trochu, F. (1997). "Application of dual kriging to the construction of a general phenomenological material law for shape memory alloys." *Journal of Intelligent Material Systems and Structures*, 8(7), 605–618.

Thoma, P. E., Angst, D. R., and Schachner, K. D. (1995). "The effect of cold work, heat treatment, and composition on the austenite to R-phase transformation temperature of Ni-Ti shape memory alloys." *Journal De Physique IV*, 5(12), C8–557–C8–562.

Thomson, P., Balas, G. J., and Leo, P. H. (1995). "The use of shape memory alloys for passive structural damping." *Smart Materials and Structures*, 4, 36–42.

Thomson, P., Balas, G. J., and Leo, P. H. (1997). "Analysis of trigger line models for shape memory hysteresis based on dynamic testing." *Journal of Intelligent Material Systemes and Structures*, 8, 193–201.

Tobushi, H., Iwanaga, H., Tanaka, K., Hori, T., and Sawada, T. (1992b). "Stress-Strain-Temperature relationships of TiNi shape memory alloy suitable for thermomechanical cycling." *JSME International Journal*, 35(3), 271–277.

Tobushi, H., Ohashi, Y., Saida, H., Hori, T., and Shirai, S. (1992a). "Recovery stress and recovery strain of TiNi shape memory alloy (Cyclic properties under constant residual strain and constant maximum stress)." *JSME International Journal*, 35(1), 84–90.

Tobushi, H., Shimeno, Y., Hachisuka, T., and Tanaka, K. (1998). "Influence of strain rate on superelastic properties of TiNi shape memory alloy." *Mechanics of Materials*, 30, 141–150.

Torra, V., Isalgue, A., Lovey, F., Martorell, F., Molina, F., Sade, M., and Tachoire, H. (2004). "Shape memory alloys: From the physical properties of metastable phase transitions to dampers for civil engineering applications." *Journal de Physique IV*, 113, 85–90.

VanHumbeeck, J. and Liu, Y. (2000). "Shape memory alloys as damping materials." *Materials Science Forum*, 327-328, 331–338.

Vokoun, D., Sittner, P., and Stalmans, R. (2003). "Study of the effect of curing treatment in fabrication of SMA/polymer composites on deformational behavior of NiTi-5at.%Cu SMA wires." *Scripta Materialia*, 48(5), 623–627.

Wayman, C. M. and Duerig, T. W. (1990). "An introduction to martensite and shape memory." *Engineering aspects of shape memory alloys*, T. W. Duerig, K. N. Melton, D. Stckel, and C. M. Wayman, eds., Butterworth-Heinemann, Boston, MA, 3–20.

Wilde, K., Gardoni, P., and Fujino, Y. (2000). "Base isolation system with shape memory alloy device for elevated highway bridges." *Engineering Structures*, 22, 222–229.

Wolons, D., Gandhi, F., and Malovrh, B. (1998). "Experimental investigation of the pseudoelastic hysteresis damping characteristics of shape memory alloy wires." *Journal of Intelligent Material Systems and Structures*, 9(2), 116–126.

Wu, C. F. J. and Hamada, M. (2000). *Experiments: Planning, analysis, and parameter design optimization*. John Wiley and Sons, Inc., New York.

Wu, K., Yang, F., Pu, Z., and Shi, J. (1996). "The effect of strain rate on detwinning and superelastic behavior of NiTi shape memory alloys." *Journal of Intelligent Material Systems and Structures*, 7(3), 138–144.

Zhu, Y.-g., L, H.-x., and Yang, D.-z. (2002). "A new model of shape memory alloys." *Applied Mathematics and Mechanics*, 23(9), 1009–1015.

VITA

Jason P. McCormick was born on September 23, 1977 in Massachusetts. Upon graduation from High School, he entered an undergraduate 3-2 Cooperative Engineering program at Saint Anselm College in Manchester, NH. After three years at Saint Anselm College, he transferred to the Catholic University of America in Washington, DC to finish the last two years of the program. After one year at Catholic University, Jason received his Bachelor of Arts degree from Saint Anselm College in 2000. The following year, he received his Bachelor of Civil Engineering from CUA. After completion of his undergraduate degrees, Jason continued to graduate school pursuing a Masters Degree and Doctorate Degree in Civil Engineering at the Georgia Institute of Technology.